University of Nottingham
UK | CHINA | MALAYSIA

Empirical modelling of the solar spectral influence on photovoltaic devices for improved performance forecasting

Thesis submitted to the University of Nottingham for the degree of **Doctor of Philosophy, July 2023.**

Rajiv Daxini

20198035

Signature _____

Date _____ / _____ / _____

Abstract

Photovoltaic performance modelling is essential for the successful development of PV systems. Accurate modelling can inform system design and financing prior to construction, help with fault detection during operation, and improve the grid penetration of PV energy.

Whereas the models to account for the effects of broadband irradiance, temperature, and so forth on PV performance are well established, those for the influence of the solar spectrum, known as spectral correction functions (SCFs), suffer a range of limitations. Existing models are typically based on proxy variables used to represent the solar spectrum, which are restricted in the amount of information they contain on the prevailing spectral irradiance conditions. Furthermore, validation of these models is restricted to climates that are not representative of the UK, where a broader range of spectral irradiance conditions is experienced due to its high northern latitude and frequent overcast or partially overcast skies.

Some studies have explored the possibility of characterising measured spectra with parameters such as the average photon energy to develop SCFs. However, these studies are limited in terms of their validation scope, such as duration of field data and types of PV module, and extension to a predictive model. In this project, two new SCFs are developed and validated in two distinct climate regions for multiple PV technologies. The first is based on the average

photon energy alone ($f(\varphi)$), while the second is based on both the average photon energy and the depth of the 650–670nm water absorption band ($f(\varphi, \varepsilon)$). Using data from Go (Golden, Colorado, USA), the former is shown to cut the prediction error for aSi modules by around 40% relative to a single-variable air mass SCF ($f(AM_a)$) and a double-variable air mass and clearness index SCF ($f(AM_a, K_t)$). The latter, $f(\varphi, \varepsilon)$, addresses issues raised in the literature regarding the reliability of φ as a spectral characterisation index. Using the same data, $f(\varphi, \varepsilon)$ is shown to cut the prediction error by up to 60% with respect to a comparable multivariable proxy SCF based on the air mass and atmospheric precipitable water content ($f(AM_a, W)$).

These results are also validated at a new test site built at the University of Nottingham as part of this project. Although the overall errors are greater due to site-specific system characteristics, the relative improvements achieved by the APE-based models with respect to the proxy-based models are maintained in both climate regions.

The proposed spectral correction approaches can be integrated into wider PV performance models to improve their performance forecasting accuracy.

Acknowledgements

This project would not have been possible without the support of my supervisors, Professor Yupeng Wu and Professor Robin Wilson, who have guided me throughout the PhD journey. It has been a privilege to take my first steps as a researcher under your supervision.

I also wish to express thanks for the scholarship provided by the Faculty of Engineering. In addition, I am extremely grateful for the travel grants awarded to me by the University of Nottingham Faculty of Engineering, University of Nottingham Researcher Academy, and the SUPERGEN SuperSolar Hub. These grants provided me with the exceptionally invaluable experiences of presenting my research at international conferences that have truly enriched my PhD experience and my ambitions for the future.

I also appreciate the support from Sanyo Panasonic and Polysolar Ltd. who provided some of the solar cells used in the measurement campaign; in particular the team at Sanyo for their encouragement with the project.

I would also like to thank the technical staff at the University of Nottingham, in particular Karl Booker, for facilitating the construction of the new test site on the roof of our office building.

I must end by thanking my parents and friends. My parents taught me at a young age the greatest lessons of all — the importance of education, how to learn, and to pursue what I enjoy. Lastly, my incredible friend, Meruyert, thank you for always supporting me over the last three years.

Publications

Daxini, R. and Wu, Y., 2023. Review of methods to account for the solar spectral influence on photovoltaic device performance. *Energy*, p.129461.

Daxini, R., Wilson, R. and Wu, Y., 2023. Modelling the spectral influence on photovoltaic device performance using the average photon energy and the depth of a water absorption band for improved forecasting. Energy, 284, p.129046.

Theristis, M., Riedel-Lyngskær, N., Stein, J.S., Deville, L., Micheli, L., Driesse, A., Hobbs, W.B., Ovaitt, S., **Daxini, R.**, Barrie, D., Campanelli, M., et al. 2023. Blind photovoltaic modeling intercomparison: A multidimensional data analysis and lessons learned. *Progress in Photovoltaics: Research and Applications*, 31(11), pp.1144-1157.

Daxini, R., Sun, Y., Wilson, R. and Wu, Y., 2022. Direct spectral distribution characterisation using the Average Photon Energy for improved photovoltaic performance modelling. *Renewable Energy*, 201, pp.1176-1188.

Daxini, R., Wu, Y., Wilson, R. Improvement of the Average Photon Energy Spectral Correction Function for Photovoltaic Performance Forecasting, *8th World Conference on Photovoltaic Energy Conversion*. Milan, Italy, 26–30 September 2022. EU PVSEC. DOI: 10.4229/WCPEC-82022-3BV.3.49

Contents

List of Tables

List of Figures

Chapter 1

Introduction

1.1 Background

Achieving the global goal of carbon neutrality in an attempt to combat anthropogenic climate change requires the deployment of clean energy technologies at speed and at scale [19, 20]. The importance of photovoltaics in the clean energy mix is undeniable from a financial perspective considering the fact that over the last forty years the price of solar PV has fallen by two orders of magnitude [21]. The resulting annual average growth rate in installed PV capacity over the period 1996–2019 is 35%.

Despite the rapid growth of PV, even the fastest PV-deploying countries are reported not to be installing PV fast enough to avoid the worst effects of climate change [22]. The issues confronting global PV growth range from problems with waste [23] to a rise in "solar nationalism", where countries are trying to protect and grow domestic PV manufacturers [24] rather than rely on foreign companies, which are seen as a competitive threat [25]. There also exist a number of technical challenges, including the need to increase the grid penetration of solar PV and reduce curtailment [26, 27]. In 2018 alone, >1% of potential PV output

was curtailed in several key markets [28]. Various solutions to the curtailment problem are reported in the literature. An extensive review of a range of such solutions is presented in Ref. [29]. These methods include improved voltage regulation [30], energy storage [31], and PV output forecasting [32].

The third of these mitigation measures — photovoltaic performance forecasting — is one of the most important. PV forecasting can facilitate greater PV grid penetration by providing timely performance predictions so energy from different sources can be balanced for a reliable and efficient supply [33]. The accurate prediction of a PV system's performance under a certain set of technical and environmental conditions is crucial for its success [34, 35, 36]. PV performance modelling (PVPM) under real weather conditions is not only useful for increasing grid penetration, but can also aid PV system designers, investors and policy makers, and end-users [37]. For example, performance predictions can be used to calculate financial savings for the end user, and optimise system design prior to investment and construction [38]. To put the scale of the financial implications of PVPM into perspective, a 2% difference between the predicted and actual output of a 100 MW PV plant translates into an annual revenue difference of $150,000 [39]. If the plant were to be displacing carbon dioxide emissions from fossil fuel energy generation at 0.33 kg/kWh [40], the annual difference in emissions would be 990 tonnes in one year[1].

The availability of solar irradiance is one of the most obvious considerations in all PV performance models [41, 42, 43], but the spectral distribution of the available irradiance is a more subtle yet also critical parameter that must be considered when evaluating how a PV system will perform [44, 45, 46]. Neglecting the spectrum can lead to significant errors in PV performance forecasts. The magnitude of these errors is strongly correlated with the type of PV technology under investigation since the spectral response (SR) of a PV device

[1] 1500 kWh/kW/year * 100 MW * 0.33 kg/kWh * 2% = 990,000 kg, or 990 tonnes

is determined by the cell construction and semiconductor material.

In terms of semiconductor material, for example, amorphous silicon (aSi) technologies have a particularly wide band gap, and therefore narrow SR. Under realistic operating conditions (ROCs), the fraction of the spectrum that lies within the useful range of aSi modules can vary by +10% to -15% with respect to standard test conditions, which translates into deviations in performance of up to 20% [47, 48, 49]. In terms of cell construction, a higher level of sensitivity to spectral variations has also been found for double junction technologies [50], such as GaAs/Ge devices. On the other hand, the output from some PV technologies, such as multicrystalline-Si (mSi), is less sensitive to the spectral distribution of incident solar radiation [51] due to their flatter and broader spectral response. However, even these technologies can exhibit performance variation due to the spectrum, with weekly spectral-induced performance variation reaching up to 14% having been reported in Edmonton, Canada [52]. The spectral influence on PV performance is accounted for in the overall modelling pipeline through the use of a spectral correction function (SCF). An SCF describes how PV performance changes relative to its performance at standard test conditions (STC); the four key characteristics of which are $1000\mathrm{W\,m^{-2}}$ irradiance, 25°C cell temperature, normal angle of incidence, and AM1.5 spectrum.

The theory behind PVPM, as well as a range of the different PV performance models published to date, is reviewed in Section 2.2. These models typically consider the effect of environmental parameters such as device temperature, incident irradiance, angle of incidence, and the spectrum on PV performance. However, the methods by which the spectral influence is incorporated into PVPM are limited, as explained in Chapter 2.7. Therefore, the focus of this research project is to investigate the spectral influence on solar panel performance, and develop a new model to account for these effects in PVPM. This

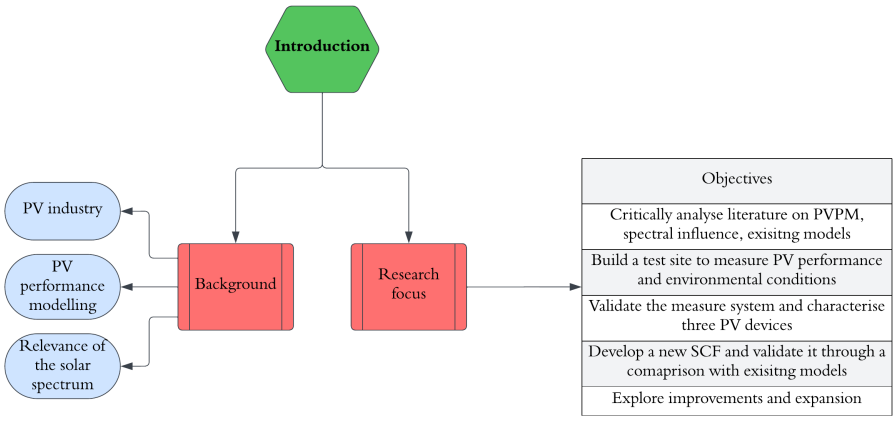

Figure 1.1: Structure of Chapter 1.

research focus and the precise objectives of this project are explained in the following subsection. A summary of the structure of this chapter is presented in Figure 1.1.

1.2 Research focus

The aim of this PhD project is to improve PV performance modelling accuracy by improving the accuracy with which the influence of the solar spectrum is accounted for in the overall performance modelling procedure. The following objectives have been set to achieve this aim:

- Critically analyse previous research on:
  - Photovoltaic performance modelling
  - The spectral influence on photovoltaic device performance
  - Existing spectral correction functions — their method, accuracy, and limitations
- Build a PV and meteorological monitoring and data acquisition system for the measurement and recording of:
  - PV performance and associated metrics, such as module temperature

  - Prevailing meteorological and spectral irradiance conditions

- Validate the reliability of the system and use it to determine the performance characteristics of several PV devices
- Develop a new SCF and validate its performance through a comparison with existing SCFs
- Explore possibilities to improve the model and extend the validation to multiple PV technologies
- Extend the validation further through assessing the generalisability of the model in a second climate.

Achieving the stated research objectives will allow this project to answer fundamental questions in the field of photovoltaic performance modelling, including: what is the motivation for using spectral proxy variables in spectral correction functions? Can metric(s) derived directly from measured spectral irradiance data offer an alternative basis for a spectral correction function? How do proxy and direct variable spectral correction functions compare in terms of accuracy? Is there value in collecting spectral irradiance data to facilitate the use of direct spectral correction functions in PV performance modelling?

1.2.1 Thesis outline

Following this introduction, Chapter 2 is a literature review in which, first, an overview of the different photovoltaic performance models and their evolution over time is presented. The key theory related to the solar energy and the spectrum, and photovoltaics, is then introduced. This is followed by an extensive review and discussion of how exactly PV performance models account for the influence of the solar spectrum in the modelling pipeline. Based on this review,

several clear gaps in the existing body of research are highlighted, discussed, and used to guide the remainder of this project.

The review in Chapter 2 finds that the applicability of spectral correction functions in environments that experience a range of non-ideal atmospheric conditions, such as variable cloud cover, aerosol optical depth, humidity, etc. is limited. However, improvements in this area through the use of measured spectral distributions have been reported in recent years. Chapter 3 describes the methodology proposed in this work through which measured spectra can be used in PV performance models to improve their accuracy. This chapter includes a description of the construction and operation of a new PV and meteorological monitoring station in the United Kingdom, methods of data acquisition, processing, and analysis, and the use of an additional PV measurement site in the USA. The methods to validate the new UK test site's reliability, and determine the electrical, optical, and thermal characteristics of the PV samples, is covered in Chapter 4

The proposed spectral correction method is first tested using data from the USA site in Chapter 5. A significant improvement in the accuracy of PV performance predictions is achieved through the proposed spectral correction model compared with existing models. However, some limitations are identified in the proposed model, which are subsequently addressed in Chapter 6 using data from the same test site.

In order to test the geographic generalisability of the proposed approach, data from the new UK test site are used to test the models that were developed and validated in Chapters 5 and 6. The results of this analysis are presented in Chapter 7.

A conclusion along with a discussion of the limitations of this project is presented in Chapter 8.

A flow chart summarising the overall structure of this thesis and the contents of each chapter is shown in Figure 1.2.

Figure 1.2: Summary of the thesis structure and contents of each chapter.

Chapter 2

Literature Review

2.1 Introduction

Traditionally, solar cell technologies has been categorised into four categories based on their performance, cost, and material construction [53]. These four categories are as follows:

1. Crystalline silicon-based PV, which have over 95% market share [54] owing in part to their low cost and relatively high power conversion efficiency (PCE) of up to 25% [55].

2. Thin film devices, the most common of which are amorphous silicon (aSi), cadmium telluride (CdTe), and copper indium selenide (CIGS). Although the production cost of this type of device is lower, the PCE of such devices is generally lower than that of the first-generation devices [56, 57].

3. Mixed polymer and semiconductors devices, including dye-sensitised organic solar PV cells (DSSC), multijunction (MJ) solar cells, and organic polymer-based solar cells [58, 59, 60]. These devices can be fabricated on flexible electrode substrates, which increases the application potential.

4. Hybrid inorganic solar cells [61], which combine the low cost and flexibility of polymer thin films with the durability of inorganic nanostructures [62].

The major factors that affect instantaneous performance of all of these types of cells are the availability of solar irradiance, operating temperature, surface reflection properties, and the solar spectrum [63, 64, 65, 66]. Over the lifetime of a PV module, degradation is the primary factor influencing performance [67].

Accounting for the effects of all of these parameters on the performance of a solar cell to make predictions of its performance is known as PV performance modelling (PVPM).

There exist several studies evaluating the different performance models that have been developed to date. For example, de la Parra et al. [68] review models in the context of providing recommendations for quality assurance and financial management. Williams et al. [69] review performance models more generally, evaluating the state of the art in Europe as of 2005.

Although there do exist some reviews of specific stages or conditions within PVPM, such as the review of 18 broadband radiative models presented in Ref. [70], there is less focus in the review literature on the spectral distribution conditions in the context of PVPM. This absence is noted in Ref. [69] in 2005 and remains the case to this day. One particular study by Duck and Fell [71] does review a selection of three prominent spectral correction methods. Their analysis of the Sandia Array Performance Model (SAPM)'s absolute air mass (AM_a) function [72], CREST model [47], and modified CREST model [73] finds the presence of site-specific errors in the AM_a approach, but also finds significant improvements relative to the AM_a and CREST approaches by using the modified CREST model. The clear focus on three models and rigorous empirical analysis makes a significant contribution to researchers' understanding of these models. What is lacking, however, is the inclusion of any methods

that use direct spectral characterisation parameters rather than only proxies, such as air mass. In addition, the scope of analysis is primarily based on the empirical work of the authors, with less of a focus on reviewing the extensive contributions of other authors' theoretical and empirical work.

In the current literature, there still lacks a wider overview of a broader set of spectral correction methods in PVPM, including a review of associated studies that critically investigate specific aspects of said models in greater detail in order to apply modifications, or investigate aspects such as applicability in different locations or climates. The main focus of this chapter is, therefore, to review a broader scope of PVPM spectral correction methods. A greater depth of analysis is presented through the review of not only the original proposals of different methods, but also further investigations and more recent developments to each of the discussed methods. Based on a comprehensive evaluation of the current state of the art, this study goes on to propose suggestions for the future development of novel spectral correction functions and their integration into PV performance models. Prior to the main review of SCFs, first, an overview of PV performance modelling is presented, which includes background information, a review of existing models, and the evolution of these models over time. The third and fourth sections of this chapter present the key theory of solar energy and photovoltaics, respectively, required to understand the topics discussed in the main review. The latter includes an explanation of how the spectrum distribution can be characterised mathematically, following which there is an explanation of how the change in PV performance due to changes in the spectrum can be characterised mathematically. The main review of spectral correction functions, which combine these two characterisation techniques, is presented across Sections 2.6 and 2.7. Finally, a summary and conclusion of the review, in addition to recommendations for further work in the area of SCFs, are presented in Section 2.8. The structure of this chapter is summarised in Figure 2.1.

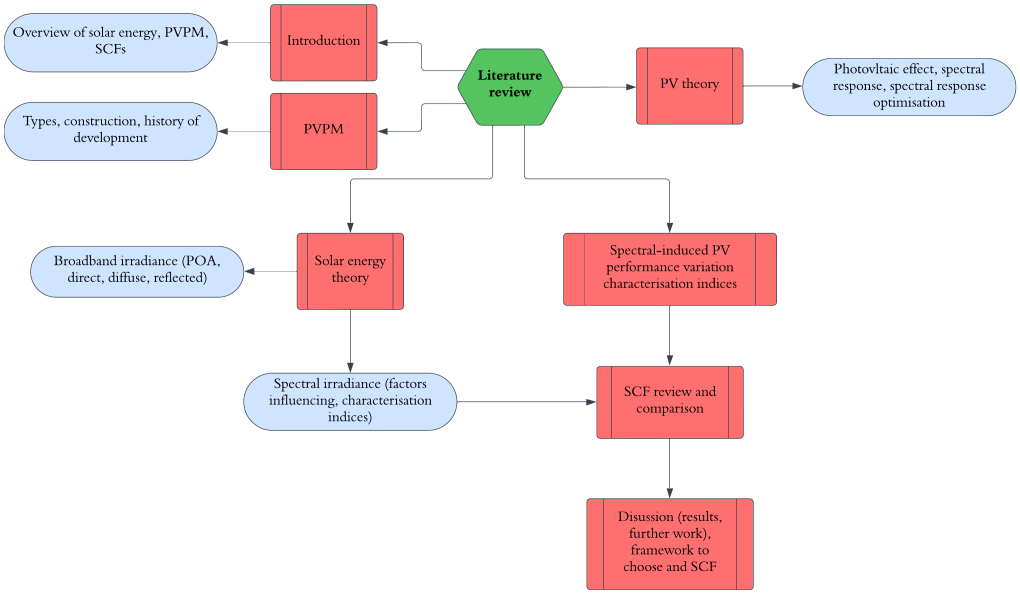

Figure 2.1: Structure of Chapter 2.

2.2 Photovoltaic performance modelling

PV performance models are used to estimate the power output of a PV system, which can consist of PV panels, inverters, charge controllers, and potentially other components such as energy storage devices. Generally speaking, there are two types of PVPM strategies — parametric modelling and non-parametric modelling. Parametric models conceive the PV system as a conglomeration of multiple sub-systems, each of which can be modelled in terms of a specified set of parameters. On the other hand, a non-parametric model does not assume any knowledge of the internal system or sub-systems, instead taking a data-driven approach by relying on a historical time series of inputs and outputs of a specific system to predict the power output of that same system. The focus of this research is on the parametric models, but a brief explanation and comparison of the two methods is presented in Section 2.2.1 for completeness. Section 2.2.2 goes on to explain the evolution of parametric performance models over the past fifty years.

2.2.1 Parametric and non-Parametric PVPM

Parametric models are the conventional model type that have been developed over the past few decades, whereas non-parametric models have undergone intensive research in more recent years.

Figure 2.2 illustrates the system conceptualisation of each method. The box in each portion of the diagram represents the PV system. This system is defined in terms of a series of sub-systems and models in the parametric method, but is blacked out in the non-parametric method as no information is known about the internal characteristics of the system, although each sub-system component does still exist. In recent years, some researchers have taken a new approach to PV performance modelling by developing non-parametric methods involving statistical models that use machine learning algorithms to predict performance based on historical data. There are a variety of forecasting methods, including neural networks, support vector regression, regression tree, random forest, gradient boosting, amongst others. As the key input to machine learning-based PV performance models, the accurate forecasting of solar irradiance is essential for accurate performance predictions [38]. There are ample studies exploring machine learning techniques for solar radiation forecasting. For example, Voyant et al. [74] and Li et al. [75] provide an extensive review of machine learning methods for solar radiation forecasting, with a specific focus on both neural networks and support vector regression. In addition, Lauret et al. [76] go on to propose a benchmarking of supervised machine learning methods for solar radiation forecasting. Each of these different machine learning methods are adopted into performance models in different ways by researchers [77, 78, 79].

The implications of these different approaches mean that parametric models provide a means by which performance may be predicted prior to or after the installation of the system, whereas non-parametric models require the system

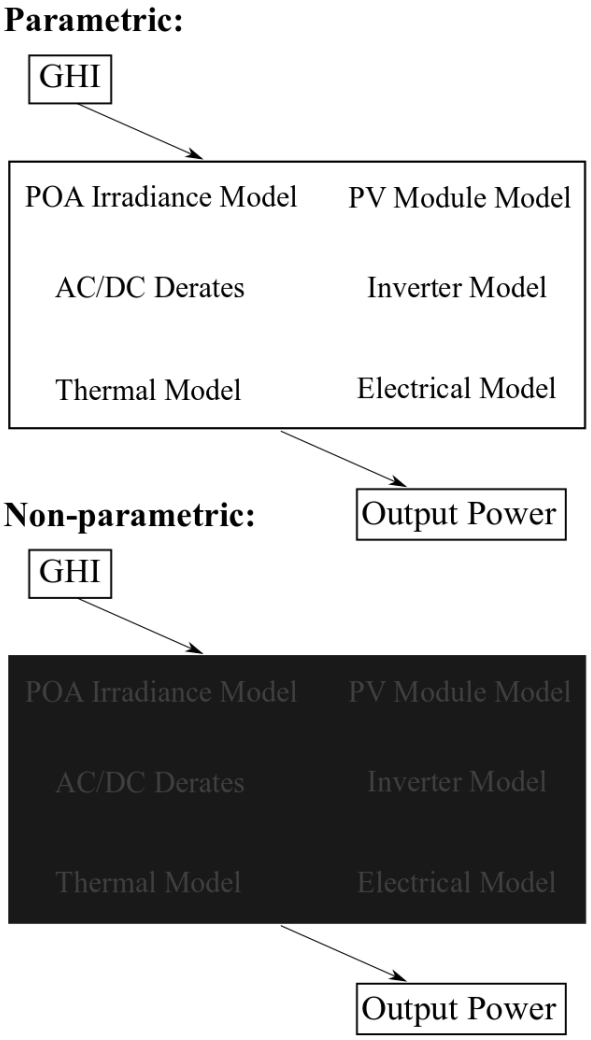

Figure 2.2: (Non-)parametric PV system conceptualisation.

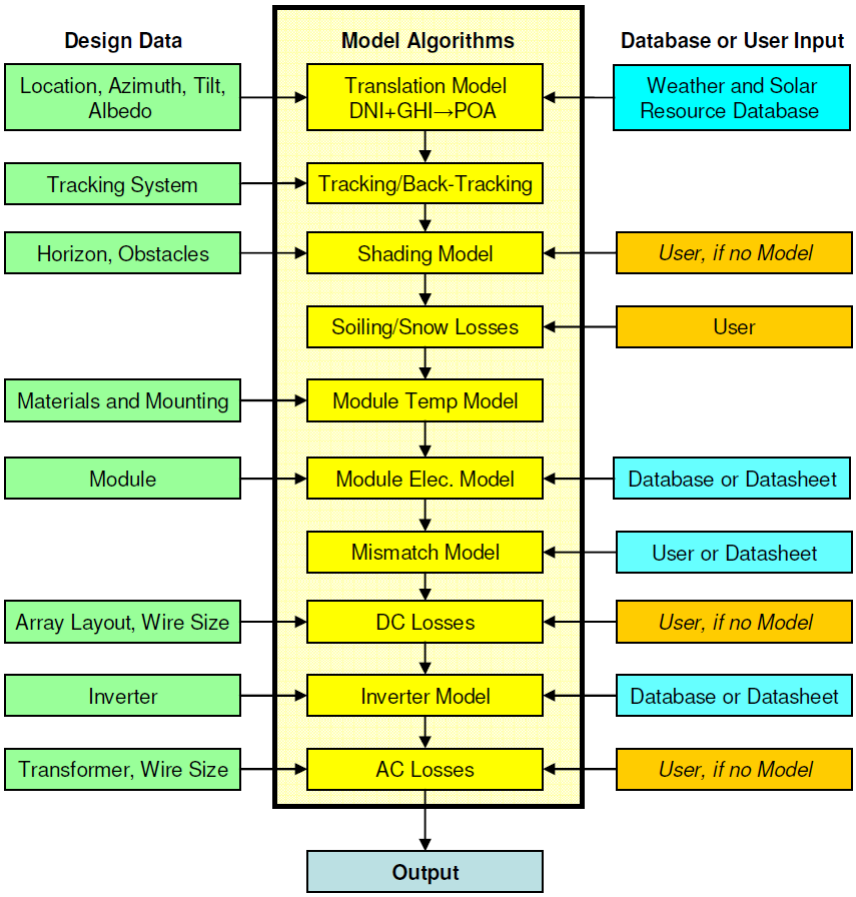

Figure 2.3: PV performance modelling process, reproduced from Ref. [8].

to have been operating for some time already in order for there to exist a sufficiently large input and output dataset.

The drawback of parametric models is that, due to the complexity of the multiple different sub-systems, it is often necessary to make assumptions and approximations about their characteristics, thus introducing significant uncertainties into the final predictions. This complexity is illustrated in Figure 2.3, which summarises the entire parametric performance modelling process. The potential variation caused by the complexity and model assumptions when different modellers attempt to model the same system is shown in Figure 2.4. It follows that the advantage of non-parametric models is that by avoiding such assumptions, the dependence of the uncertainties is shifted to the quality of the data [78]. Nevertheless, being able to predict the performance of a PV system before installation can help with key decision making processes. For

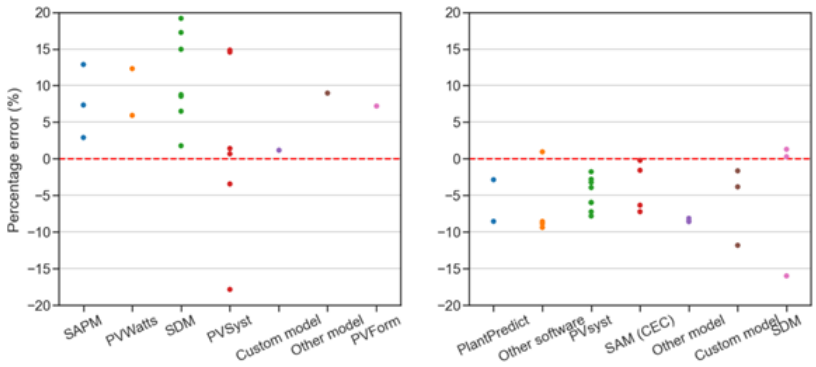

Figure 2.4: Predicted energy production of a single system by different modellers using different PV performance models [9].

example, it enables optimisation modifications to the system design to improve performance before the large financial and technical investments are made. Performance predictions in advance of system installation can also advise policy makers governing the development of PV infrastructure.

The focus of this project is on parametric PVPM as the goal is to develop a function that can account for the effect of one specific variable — the spectral distribution of solar irradiance — on PV system performance in both cloudy and clear sky conditions. Henceforth, when referring to PVPM, it may be assumed that the model type is parametric unless otherwise stated.

The various parameters incorporated into the calculations of parametric PV performance models are categorised by this study as follows: meteorological, geographic, electrical, thermal, financial, and system. It is important to emphasise that elements of these categories are fluid, with some parameters potentially crossing boundaries between different categories. For example, for a PV system with a cooling system, the chiller's performance factor may be classed as a "system" parameter but would also be a relevant input in the "thermal" category for any thermal sub-model adopted in the performance calculations.

One category may consist of multiple inputs, which may be determined either through direct measurement, indirect measurement, calculated based on other directly or indirectly measured parameters, or may be fixed values based on

the definition of the system itself. Different performance models choose to evaluate each of the different parameters in different ways, with more simplistic models making general assumptions about system components and ratings, often relying on indirect measurements and inferred values, and more complex models considering specific manufacturer parameters and empirically derived data specific to the system in question.

Over the past half-a-century or so, different attempts have been made to model the aforementioned parameters and their correlation to PV performance with greater and greater accuracy. The following subsection explains the evolution of these attempts, manifested in dozens of different performance models.

2.2.2 Evolution of PV Performance Models

This section describes the historic development of photovoltaic performance models over the past half a century, with reference to a selection of some of the most prominent models to have been developed. A summary of those models discussed here is presented in Figure 2.5. A more extensive review of a wider range of models can be found in, for example, reviews by Klise [80] and Gueymard [70].

The Sandia National Laboratory (SNL) has long pioneered the development of PV performance models, beginning in the late 1970s with PVSS — a simple model to simulate PV performance based on a variety of different system configurations for both on– and off-grid PV systems [81]. This model is no longer used, updated, or supported by SNL, but was superceded in the following years by models such as SOLCEL and PVForm.

SOLCEL uses the same equivalent circuit model as PVSS, but can model both concentrating PV (CPV) as well as flat-plate PV incorporated onto tracker or fixed arrays. Furthermore, unlike PVSS, SOLCEL is able to perform ba-

sic financial analaysis using a range of costs incorporated into two economic evaluation techniques — life-cycle costing methodology and US Department of Energy required revenue methodology — to determine the optimal configuration with the lowest life-cycle cost [82, 83]. SOLCEL is also no longer supported by SNL and relevant accessible literature is sparse.

PVForm is largely based on SOLCEL yet was built to simplify and improve it [84]. Despite only modelling flat-plate cSi technologies, arguably taking a step back from recent developments at the time, PVForm demonstrated major advances in terms of solar insolation calculations and plane of array orientations by incorporating the newly developed Perez POA model and the calculation of module temperature using a thermal model proposed by Fuentes (1987) [85]. Despite no longer being supported by SNL, elements of PVForm are used in other programs such as PVWatts, which uses the same Perez POA and array performance algorithms.

Other performance models, such as PVSYST, allow the user to adopt different irradiance models. PVSYST uses the simpler Hay and Davies model as the default option, although it does still offer the option of using the Perez model. Other key features of PVSYST include its ability to model a variety of technologies, including crystalline and thin film modules [86], a 3-D shading tool to account for potential shading impacts, air mass spectral correction for thin-film modules, comprehensive economic analysis tools that can work with different currencies, life cycle costs, and feed-in tariffs.

Another popular performance model is PVWatts, which is a web-based application developed by NREL. PVWatts can model grid-connected PV systems in a series of 239 preset locations corresponding to the 239-station Typical Meteorological Year (TMY2) database [87] for the United States and its territories. The model incorporates a comprehensive range of input parameters, including DC rating, derate factors, array type (fixed tilt, or 1– or 2-axis tracking), array

tilt, and azimuth. However, its applicability was originally restricted to cSi technologies only, in part due to its assumption of a -0.5%/°C [88] temperature coefficient. Nevertheless, in recent updates [89], three generic module categories are considered and the temperature coefficient is adjusted accordingly. PVWatts does still makes several other assumptions about the type, configuration, and operation of the system, which makes it easy to use for both experts and non-experts alike. However, consequently, the uncertainty in the annual and monthly energy totals can reach ±10% ±30%, respectively; actual performance in a specific year may deviate from the long-term average by as much as ±20% ±40% for the annual and monthly values, respectively [89]. Nevertheless, PVWatts incorporates some interesting novel features, such as the "In My Back Yard" program that allows users to zoom in on a specific site and draw the outline of the PV array for analysis.

Ultimately, these advances over the decades led to arguably the most comprehensive of performance models to be developed just after the turn of the century — the Sandia PV Array Performance Model SAPM. Where other models attempt to evaluate performance by using a mix of theoretical and semi-empirical methods, SAPM differs from these in that it is based on empirical measurements taken for a range of modules in conditions other than the manufacturer-provided standard test conditions. The model is applicable not only to standard cSi technology, but also thin films such as CdTe, CIGS, and aSi, both single and multi-junction concentrating photovoltaics (CPV/MJ CPV), and also BIPV. Although somewhat difficult to implement given that modules must undergo additional testing to obtain parameters not provided by the manufacturer, the model has demonstrated high accuracy in validation studies by the National Institute for Standards and Technology, predicting power output to within 1% of measured power for different geographic locations [90].

Despite the achievements of SAPM, the limitations with regards to obtaining

all parameters with high accuracy were part of the motivation for the development of the 5-parameter model. Originally the 4-parameter model developed by Townsend (1989) [91], the 5-parameter model, or 5-par model, was developed by De Soto (2006) following further validation and analysis [92]. The goal of this model is to predict power output under non-standard test conditions, like the Sandia Model, but to do so with only the data supplied by the manufacturers. Its simplicity and relative accuracy has led to its widespread institutional and academic use, such as in the California Energy Commission's work to estimate the system performance for its New Solar Homes Partnership Program [93]. However, it is important to note that it was found in further research by Fanney et al. (2002) that the 5-par model cannot match the SAPM's power output prediction accuracy, particularly at high AOI and low incident irradiance, and, generally speaking, the 5-par model is only used with amorphous PV technologies [94]. Furthermore, the 5-parameter model was shown to exhibit a lower reliability and precision, which was highly dependent on the user [8], as shown in Figure 2.4. Nevertheless, it is evident from the same figure that even comprehensive models such as the SAPM still exhibit substantial uncertainty. Pinpointing the dominant errors and minimising the corresponding uncertainty is the key to the future development of PV performance modelling.

Figure 2.5 provides a summary of the timeline of development of PV performance models over the years and some of the models' key characteristics.

The Sandia Array Performance Model (SAPM) is the most comprehensive model developed to date. However, the required non-trivial experiment campaign involving multiple days of outdoor and indoor experiments under stringent testing conditions means that it is not suitable for every use case. This has led to attempts to simplify the experimental methodology, such as by Hansen et al. [95] and Peng et al. [96] who have developed an indoor measurement methodology to determine the majority of parameters required in the SAPM

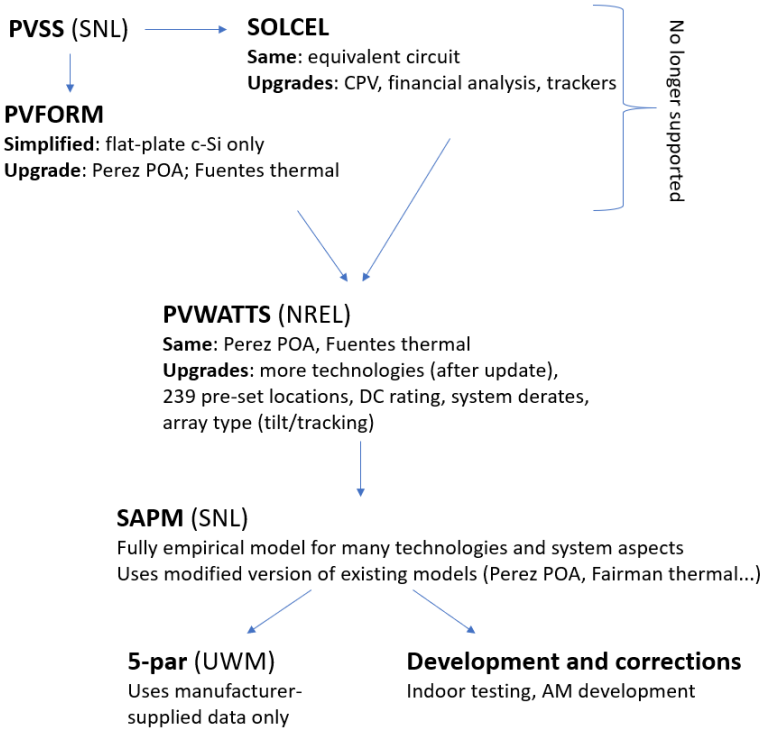

Figure 2.5: Development and key aspects of PV performance models since the 1970s.

for a variety of PV technologies. Therefore, where feasible, the SAPM is still the model of choice as it is unrivalled in its prediction accuracy and detail. Having said that, the model still suffers severe limitations, particularly in terms of capacity to make predictions in cloudy conditions given its simplified spectral correction function. In this project to develop a new spectral correction function that works in cloudy conditions, the Sandia Model will be used as a guide for the analysis. For example, when conducting tests to derive auxiliary functions required for the overall PV performance modelling, such as the angle of incidence modifier. The new spectral correction functions that result from this work will, therefore, be directly compatible with the Sandia Model and others.

2.3 Solar energy theory

This section introduces some of the key theory related to solar energy, including definitions of key terms, explanation of principles, and discussion of environ-

mental and meteorological phenomena.

2.3.1 Broadband irradiance

Irradiance is defined as the energy per unit time (power) incident on a horizontal unit area per unit wavelength, in $\mathrm{W\,m^{-2}\,nm^{-1}}$ [97]. A helpful explanation of the difference between irradiance, irradiation, insolation, and other such terms is presented in Ref. [98]. Broadband irradiance is the irradiance over all wavelengths, typically 280–4000 nm, which is calculated as the integral of irradiance with respect to wavelength. Broadband irradiance originates from the sun as what is termed global extraterrestrial radiation (GEI), which is calculated based on the Earth's position relative to the sun as follows [62, 99]:

$$\mathrm{GEI} = \frac{\mathrm{S}}{\mathbf{R}^2} \times \cos Z, \tag{2.1}$$

where the S is the solar constant, equal to 1367 $\mathrm{W\,m^{-2}}$, $\mathbf{R}$ is the Earth radius vector, and Z is the solar zenith angle.

Whereas irradiance from space (the GEI) is a function of distance from sun, the solar cycle, and cross-cycle changes [100], irradiance on the Earth depends on the tilt of the measuring surface, height of the sun above the horizon, and atmospheric conditions [101]. Radiation incident on the Earth's surface has three components: beam (or direct), diffuse, and reflected. Figure 2.6 illustrates the definitions of these three components, which are explained in more detail in the following subsections. The Plane of Array (POA) irradiance, or Global Tilted Irradiance (GTI) is used for PV performance calculations; this is the irradiance incident on a tilted plane, such as a PV module. The POA irradiance can be determined from analysis of measured irradiance component data using one of a variety of available irradiance models, or measured directly using a

pyranometer or reference module. A discussion of the differences between the latter two methods is presented in Ref. [102].

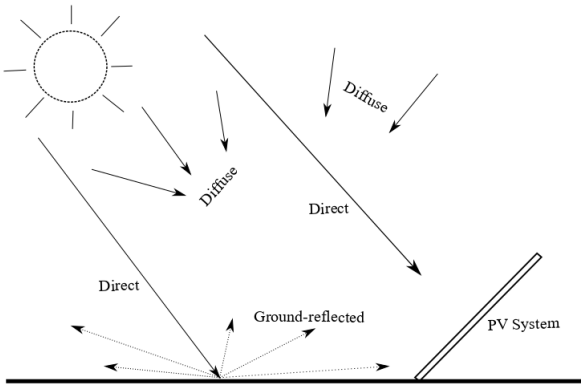

Figure 2.6: Beam, diffuse, and reflected components of solar irradiance.

Plane of Array Irradiance

The POA irradiance, or Global Tilted Irradiance (GTI) is defined as the sum of the beam (G_b), reflected (G_R), and diffuse (G_d) radiations incident on a tilted surface:

$$G_{poa} = G_b + G_d + G_R, \tag{2.2}$$

In this context, the tilted surface in question would be a solar module. To calculate the POA irradiance, it is necessary to resolve each component of the total irradiance incident onto the tilted surface. The resolution process for each component — beam, reflected, and diffuse — is explained in each of their respective sub-sections. For the beam and reflected components, this process is relatively simple. However, there exist numerous models for determine the diffuse radiation incident on a tilted surface, which are examined in 2.3.1.

Beam radiation

Beam radiation (E_b), or Direct Normal Irradiance (DNI), refers to the flux density of non-scattered solar radiation incident on a flat plane perpendicular to the

sun's rays [103]. The earliest technologies for measuring beam radiation were the Angstrom pyrheliometer and the Abbot water flow calorimeter [104]. Both of these technologies relied on the principle that an internal element would be heated by an amount proportional to the incident radiation. Pyranometers are another instrument, more commonly used today, which measure global radiation indirectly through measurements of the short-circuit current in the device, which is approximately linearly related to incident solar radiation.

The beam irradiance incident on a horizontal surface, $E_{b,h}$, is given by:

$$E_{b,h} = E_b \sin(\alpha), \tag{2.3}$$

and on a tilted surface:

$$E_{b,t} = E_b \sin(\alpha + \beta), \tag{2.4}$$

where α and β are the angles between the incident beam and horizontal, and horizontal and tilted plane, respectively. The relationship between the different beam irradiance components and these angles is illustrated in Figure 2.7.

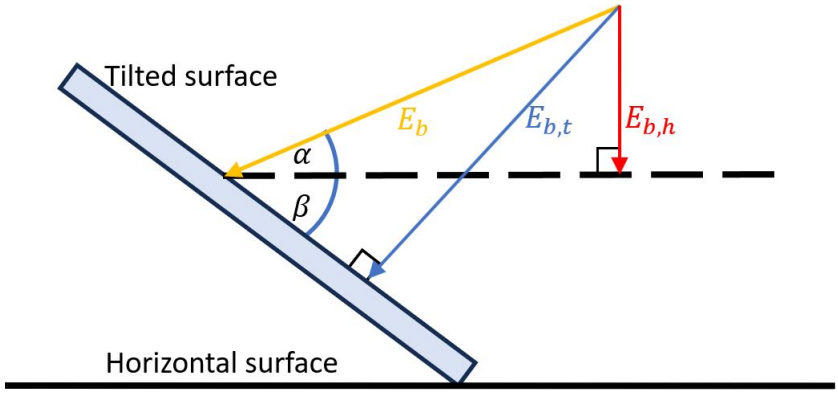

Figure 2.7: Irradiance on a tilted surface.

A generalised equation for the beam irradiance incident on any surface can hence be established as follows:

$$G_b = E_b R_B, \tag{2.5}$$

where R_B is known as the beam radiation tilt factor, defined as the ratio of $E_{b,t}$ to $E_{b,h}$.

Reflected radiation

The reflected radiation, E_R, accounts for the light reflected from non-atmospheric surfaces, such as the ground. PV systems are usually directed away from reflected radiation, hence this forms a small, if not negligible, part of the light striking their surface [105]. The reflected radiation is dependent on the albedo, ρ, of the surface from which it is reflecting [106]. Values of ρ can vary from around 0.04 for fresh asphalt [107] to 0.80 for fresh snow [108].

When determining the component of E_R incident on a tilted surface, such as a PV module, most models assume isotropic reflection from the ground, which has a diffuse reflectance given by its albedo. The tilted surface has a view factor to the ground of $R_r = \frac{1-\cos(\phi)}{2}$, where ϕ is the tilt angle of the module. Hence, the reflected radiation incident on a tilted surface is given by:

$$G_R = E_R \rho \frac{1 - \cos(\phi)}{2} \tag{2.6}$$

Diffuse radiation

Diffuse radiation (E_d) is the component of global irradiance that has had its direction changed following scattering by the atmosphere. Since the global irradiance is the sum of the beam and diffuse components, if shaded from the beam component, then a pyranometer can be used to measure the diffuse component.

There are many models available to calculate G_d, which tend to be categorised as either **isotropic** or **anisotropic** based on how they consider the distribution

Reference	Type	Note
LJ [109]	Isotropic	Simple isotropic
HD [110]	Isotropic	+circumsolar radiation
R [111]	Anisotropic	+horizon brightening
P [112, 113]	Anisotropic	Combined HDKR (K= [114])

Table 2.1: Four of the most prominent models for calculating the diffuse component of solar irradiation incident on a tilted surface

of irradiance across the sky. Four of the most prominent models are detailed in Table 2.1.

The first isotropic model was proposed by Liu and Jordan (LJ) [109], which was followed by Hay and Davies's (HD) improved isotropic model that also accounted for circumsolar radiation [110]. In later years, the anisotropic Perez Model [112, 113] and the combined Hay and Davies, Klucher [114], and Reindl et al. [111] model (HDKR) were developed. These are four of the main models used in the literature. A comprehensive, quantitative analysis of a broader selection of POA irradiance models is widely available in the literature (for example, see: [115, 116]).

2.3.2 Spectral irradiance

In this section, an explanation of what the solar spectrum is and the information it contains is presented. In addition, the key factors that affect the solar spectrum, and how these may be used as proxies to characterise it mathematically, are introduced. Figure 2.8 is a simple illustration of the effect of some of these environmental variables on the solar spectrum as measured on the Earth's surface. Other parameters of characterising the solar spectrum that are not based on proxies are also discussed. These variables are a key component of SCFs as they are used as the dependent variable in these functions.

Spectral irradiance (SI) is defined as in the previous subsection — energy

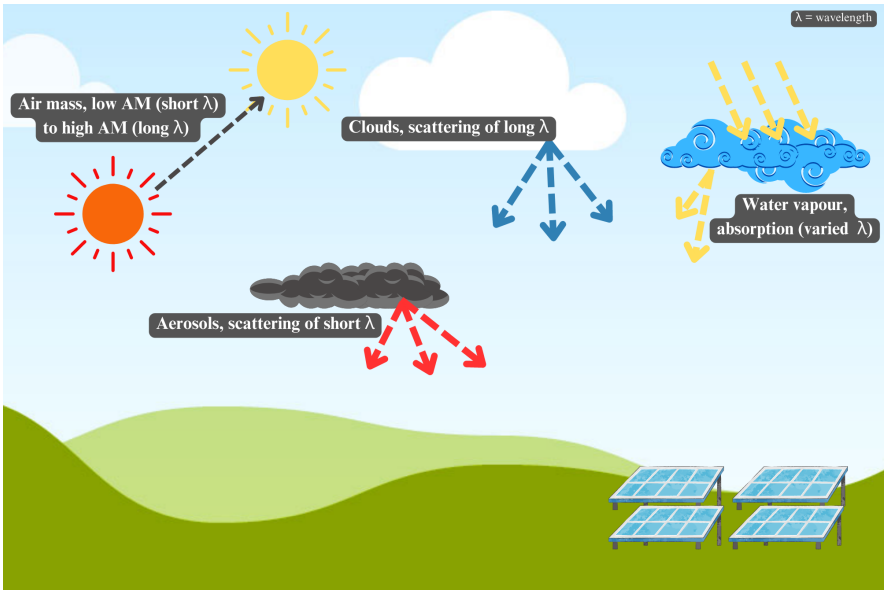

Figure 2.8: Illustration of the effects of some environmental variables on spectral irradiance incident on the Earth's surface.

incident on a horizontal unit area per unit time per unit wavelength — in $\mathrm{W\,m^{-2}\,nm^{-1}}$. The solar spectrum contains information on the distribution of irradiance across different wavelengths. Terrestrial spectral irradiance differs from that which is emitted by the sun due to two phenomena: 1) **Scattering** by air molecules, water, and dust; 2) **Absorption** by ozone (shorter wavelengths) and water vapour and carbon dioxide (longer wavelengths) [117, 62, 118]. The effects of atmospheric scattering and absorption are illustrated in Figure 2.9, which shows the extraterrestrial solar spectrum and the reference air mass (AM) 1.5 spectrum [10].

Models to forecast the solar spectral irradiance distribution exist, but are less well established that those for broadband irradiance. Historically, models based on different meteorological inputs were used, such as SMARTS and ASPIRE [119, 120], but now AI and deep learning models dominate the literature [121].

In order to analyse the effect of any particular spectral distribution on, for example, PV device performance, it is necessary to characterise the distribution numerically. There are two ways in which this is typically done. The first is to use one or a combination of environmental variables that themselves affect the

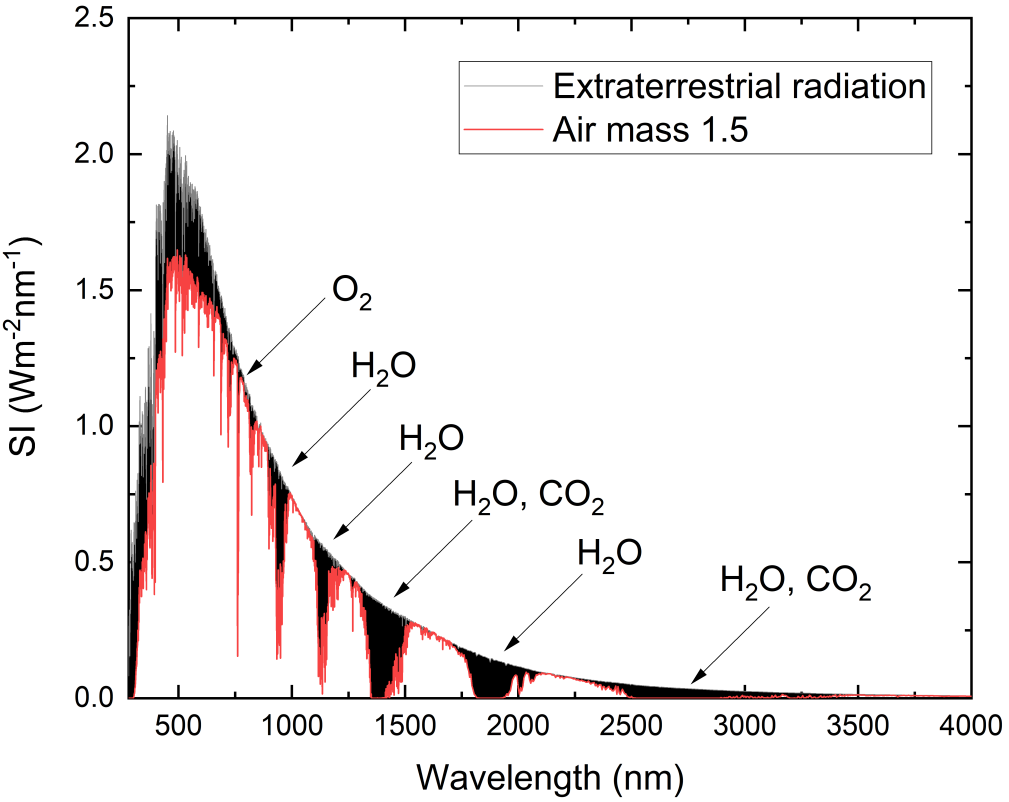

Figure 2.9: Effects of atmospheric absorption and scattering on the extraterrestrial solar spectrum. The plotted data are extracted from the ASTM standard publication [10].

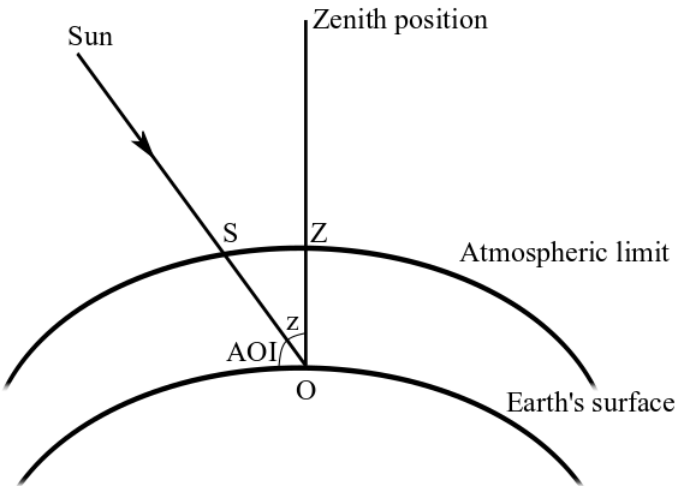

Figure 2.10: Solar geometry: Angle of Incidence (AOI), Zenith Angle (z), and air mass (SO:ZO)

solar spectrum. These variables can be used as proxies to represent the solar spectral distribution because their variation is assumed to be the primary of driver of variation in the spectrum. The second is a more direct representation through parameters derived directly from the spectral distribution. Prominent examples of both proxies and direct variables are introduced in the following subsections.

Air mass

The path length of direct radiation through air is described by air mass. This path length is calculated as the ratio of direct optical path length to the path length at the zenith (vertically upwards) [122]. This geometry is illustrated in Figure 2.10.

A first order approximation of air mass is:

$$AM = \sec Z. \tag{2.7}$$

Equation 2.7 assumes that the atmosphere is a flat horizontal layer, ignoring

its finite height, and hence predicts infinite air mass at the horizon. Therefore, Equation 2.7 hold for angles of z up to around 70°(AM=2.92) [104]. Kasten and Young propose a refined model that accounts for the curvature of the Earth [123]:

$$AM = (\cos z + 0.50572(96.07995 - Z)^{-1.6364})^{-1}. \tag{2.8}$$

As the direct optical path length increases, greater scattering of shorter wavelength (higher frequency) light occurs, resulting in a greater proportion of longer wavelength light reaching the observer [124]. As a result, changes in air mass are strongly correlated with changes in the solar spectrum [125, 126, 127]. This relationship is shown in Figure 2.11, in which the normalised spectral distributions of different air masses are plotted. The spectral irradiance curves are simulated using the SMARTS software [119, 128] The normalisation is carried out by dividing the spectral irradiance value for each wavelength by the total irradiance, which is calculated by the integral of of the spectral irradiance curve with respect to wavelength. The spectral shift associated with changing air mass has led to investigations of how air mass variation is correlated with PV performance. Passow et al. find that variation in air mass between 1.0 and 5.0 results in performance fluctuations of up to 5% in cSi modules and over 5% for CdTe modules [129]. Marion et al. (2012) report that, for several aSi-based technologies, changes in air mass alone can result in deviations from RTC performance of over 10% [130].

In certain clear sky conditions, air mass may be the dominant factor influencing the solar spectral distribution [131]. Therefore, air mass has been used in the literature to characterise the solar spectrum, since changes in AM are strongly correlated with changes in the solar spectrum [125, 126, 127]. This correlation has been used as the basis to derive air mass-based SCFs, which are discussed

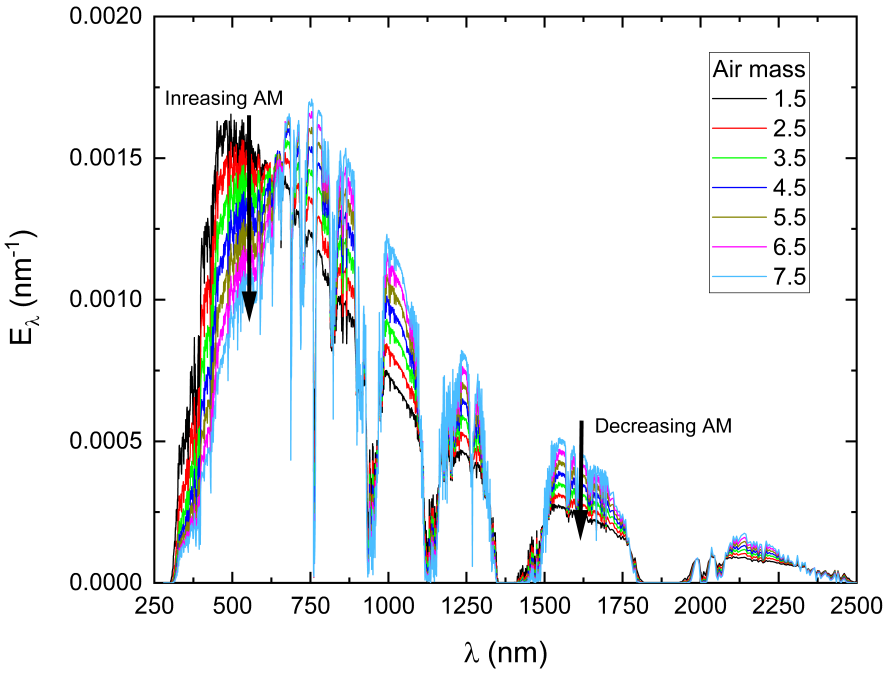

Figure 2.11: Simulated effect of air mass on the solar spectrum. Here, E_λ has been normalised by the total irradiance.

in Sections 2.6 and 2.7.

Diffuse solar radiation ratio

A more direct measure of the level of scattering is the diffuse solar radiation ratio, R_d, which is dependent on the initially available solar irradiance, atmospheric and ground conditions, and topography [132]. It is calculated simply as the ratio of horizontal diffuse irradiance to the global horizontal irradiance:

$$R_d = \frac{DHI}{GHI}, \tag{2.9}$$

where DHI is the diffuse horizontal irradiance and GHI is the total global horizontal irradiance. More information on the relationship between the different components of irradiance can be found in Ref. [109]. Albeit not widely used in

spectral characterisation, R_d has been used previously in combination with air mass to characterise the solar spectrum for PV-spectral research [133].

Clearness index

The clearness index, K_t, is an indicator of cloud cover. K_t is calculated as the ratio of the global extraterrestrial radiation (GEI) to the terrestrial global horizontal irradiance (GHI):

$$\mathrm{K}_t = \frac{\mathrm{GHI}}{\mathrm{GEI}}, \tag{2.10}$$

where GEI and GHI are defined in Section 2.3.1.

Understanding the level of cloud cover is important when analysing the spectrum since longer wavelength irradiance tends to be scattered as it passes through clouds, resulting in a higher prevalence of shorter-wavelength irradiance reaching the Earth's surface [134, 135, 136]. The clearness index, K_t, therefore, offers an opportunity to characterise the spectrum of solar irradiance. An extensive review of the cloud effects on solar irradiance is provided by Calbó et al. [137].

Although clouds result in a drop in overall irradiance, and therefore lower PV output [138], cloud-induced spectral shifts can result in certain PV technologies operating more or less efficiently in cloudy conditions [139]. For example, aSi-based PV technologies have been found to operate approximately 2% more efficiently in overcast conditions (K_t=0.2) compared to clear sky (K_t=0.8) conditions [140]. This is due to aSi having a higher spectral response at shorter wavelengths. On the other hand, CdTe, mSi, and cSi PV technologies were all found to operate less efficiently in overcast conditions, in the same study. Ishii et al. (2013) attribute ±10% performance fluctuations in hydrogenated

aSi (aSi:H) PV to cloud cover [141]. Other studies also affirm the importance of clouds on the spectrum, and hence the output of aSi [47] and cSi [73] devices in particular.

Atmospheric precipitable water content

As discussed in Section 2.4.2 and illustrated in Figure 2.9, water vapour content in the atmosphere is responsible for significant scattering of solar irradiance in specific wavebands. One measure of water vapour content in the atmosphere is the atmospheric precipitable water vapour (W). W, usually measured in centimetres, is the height that would be reached if all of the water vapour in a column from the Earth's surface to the troposphere were to condense. A comprehensive discussion of W characteristics around the world is presented in Ref. [142] and real-time measured precipitable water data are publicly available for many locations around the world [143].

In the absence of measured data, W[cm] may easily be estimated from relative humidity and temperature using the following relationship [144]:

$$W = 0.1 H_\nu \rho_\nu, \tag{2.11}$$

where H_ν[km] is the apparent water vapour scale height, ρ_ν[g m^{-3}] is the surface water vapour density, and the coefficient 0.1 is necessary to reconcile units. H_ν is a function of temperature and is calculated as follows:

$$H_\nu = 0.4976 + 1.5265\beta + \exp(13.6897\beta - 14.9188\beta^3), \tag{2.12}$$

where $\beta = T/T_0$ and $T_0 = 273.15$K. Meanwhile, ρ_ν is a function of relative humidity (R_H), temperature, T[K], and saturated water vapour pressure, e_s[mb],

which is a function of temperature [145]:

$$\rho_\nu = 216.7 \cdot \frac{R_H e_s}{T}, \tag{2.13}$$

where:

$$e_s = \exp a_0 + a_1 T_0^{-1} + a_2 T_0^{-1} + a_3 T_0^{-1}. \tag{2.14}$$

There exist many other models to estimate e_s, for example Refs. [146, 147, 148, 149, 150]. The cited models, among others, are analysed extensively in Ref. [145]. The approach reported here for reference is used in Ref. [151].

Given the significant W-induced spectral irradiance absorption around the peak response of CdTe devices, a notable correlation between variation in W and CdTe performance has been highlighted in the literature. Nelson et al. [152] find a $\pm 6\%$ variation in CdTe performance due to variation between in W between 0.1 cm and 10 cm, when other variables (e.g. pressure, ozone, irradiance, etc.) are held constant.

Aerosol optical depth

Atmospheric aerosols are are suspensions of liquid, solid, or mixed particles with highly variable chemical composition and size distribution [153]. Aerosol optical depth (AOD) is the dimensionless measure of extinction of beam irradiance caused by these aerosols. Global aerosol data is available from a variety of sources [154, 155].

The impact of AOD on spectral irradiance can be estimated using the Ångstrom turbidity formula [156]:

$$AOD = AOD_{500} \left(\frac{\lambda}{0.5} \right)^{-\alpha}. \tag{2.15}$$

AOD_{500} accounts for the quantity of aerosols in a column of the atmosphere at 500 nm, and λ and α are the wavelength and the Angstrom exponent, respectively. AOD scattering primarily affects the UV-visible range of the solar spectrum [157, 158], hence the impact of its variability is particularly significant for wide bandgap PV technologies such as CdTe and Perovskite [159]. AOD-induced spectral shifts have also been found to be responsible for performance changes of around 4% for concentrating triple junction PV devices [160].

Besides the impact of aerosols on the spectrum, absorption and enhanced levels of diffuse irradiance due to aerosols have also been studied more broadly in terms of their effects on PV power generation. During extreme weather events such as wildfires and smog, PV power generation has been found to be reduced by up to 40% as a result of increased AOD [161, 162].

Average photon energy and an absorption band

Unlike the other parameters discussed thus far, the average photon energy (APE, φ) is not an environmental variable that affects the spectrum. Rather, the average photon energy is a value extracted directly from a solar spectral distribution that can be used to characterise it. The APE has been used widely in the Physics literature since the 1900s [163, 164, 165, 166], but its application to characterising spectral irradiance measured on the Earth's surface, in particular for PV applications, was proposed in Ref. [167]. The APE originates from considering the inverse relationship between photon wavelength (λ) and energy (E):

$$E = \frac{hc}{\lambda}, \tag{2.16}$$

where h is Planck's constant, c is the speed of light in a vacuum, and E is

the photon energy. If one considers the mean energy of all photons in a solar spectral distribution, this value gives an indication of the overall shape of the distribution. This mean value is calculated by dividing the total energy in the spectrum by the number of photons it contains [167]:

$$\varphi[\mathrm{eV}] = \frac{1}{q}\left(\frac{\int_a^b E_\lambda \, d\lambda}{\int_a^b \Phi_\lambda \, d\lambda}\right). \tag{2.17}$$

Here, $E(\lambda)$ [$\mathrm{W\,m^{-2}\,nm^{-1}}$] is the spectral irradiance, $\Phi(\lambda)$ [$\mathrm{m^{-2}\,nm^{-1}}$] is the spectral photon flux density, q [C] is the electron charge, and a [nm] and b [nm] are the upper and lower wavelength limits, respectively, of the considered waveband.

When the mean is calculated between limits a and b, theoretically there exists the possibility that increases in spectral irradiance at one wavelength may be countered by a decreases at another another wavelength, thus leading to the same average photon energy but a different shape of the spectrum. If this were the case, two spectral distributions would have the same average photon energy but different shapes, and hence different effects on PV performance. In order to validate the reliability of the APE parameter to represent solar spectral distributions, Minemoto et al. [168] find that a single APE value yields a spectral irradiance distribution with a relatively small standard deviation. They conclude that the APE is a bijective index that can uniquely represent different solar spectral distributions. The APE parameter has been used extensively in subsequent research to characterise the spectral irradiance distribution [169, 170, 171, 172]. Unlike the proxy variable methods, rather than taking one variable that affects the spectrum to represent it, the APE is extracted directly from the spectrum after all possible factors have already influenced it. Therefore, it is argued widely in the literature that the APE contains information on the dominant environmental conditions influencing PV performance and is

therefore capable of effectively characterising the shape of the incident spectral distribution [51, 173, 174].

Adopting the same methodology as Minemoto et al., but analysing the spectra using the coefficient of variation rather than the standard deviation, Nofuentes et al. [175] argue that the APE is in fact not a unique characteristic of the spectral distribution. They find that in the 450–900 nm waveband, the CV remains below 3.3%, which is acceptable, but outside of this waveband the CV reaches values of up to 5–11%. Between 350–450 nm, the CV lies around 5–6%, and reaches 6–11% for the 900–1050 nm waveband. They conclude that the APE may only be considered approximately unique within this mid-range waveband of 450–900 nm for the climate considered in their study, but otherwise the APE is not a unique characteristic of the spectrum. They attribute the spread about the mean predominantly to experimental uncertainty for wavelengths below 450 nm, which could be mitigated in future work, but attribute it to a mixture of experimental uncertainty and the direct effects of aerosols and water vapour for wavelengths longer than 900 nm.

Much of the existing PV-APE research [176, 177, 178, 179] tends to focus on thin-film PV devices, in particular aSi technologies. Given that the spectral response of thin-film devices is narrow, with aSi cutting off at around 750 nm to 800 nm, the issues raised by Nofuentes et al. [175] for spectral effects beyond 900 nm may not have been a problem.

Ishii et al. [11] find that the primary driver for changes in the shape of spectra that maintain the same APE are the negatively correlated depths of water absorption bands and atmospheric windows. This principle is illustrated in Figure 2.12. They show that a solar spectral distribution may therefore be characterised uniquely for all wavelengths with both the APE and an additional index, namely the depth of a water absorption band or an atmospheric window, ε. The use of ε as part of spectral distribution characterisation methods does

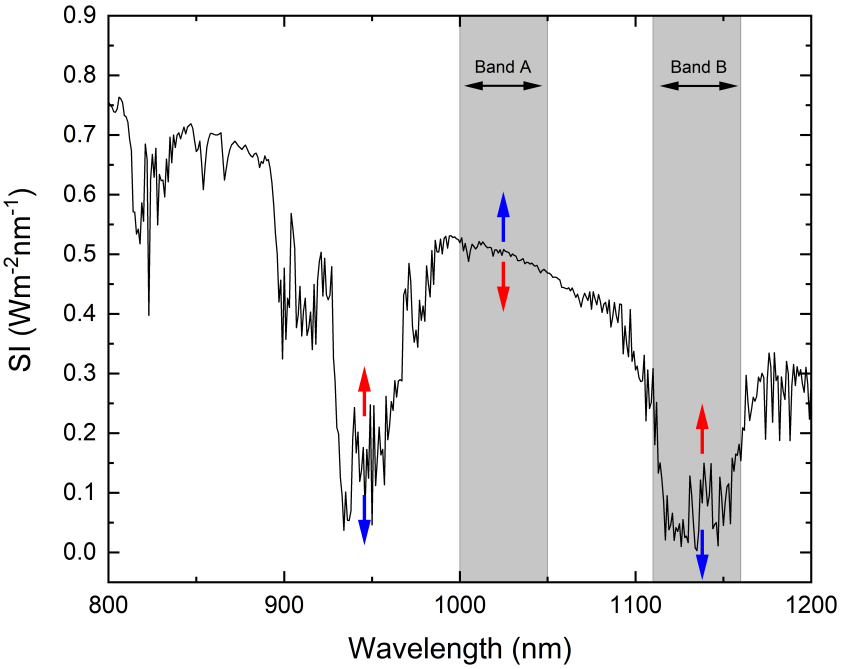

Figure 2.12: (Colour) Atmospheric window (Band A, 1000–1050 nm) and water absorption band (Band B, 1110–1160 nm) as highlighted in [11]. The red and blue arrows indicate a higher and lower SI in bands A and B, respectively. SI data were measured at the University of Nottingham.

not appear to have been adopted in the literature, but it forms a significant part of this project and has led to a publication as of 2023 [1].

The depth of one of these spectral bands, ε, can be calculated by integrating the spectral irradiance with respect to wavelength within the wavelength limits of the band in question:

$$\varepsilon = \int_c^d E_\lambda \, d\lambda. \tag{2.18}$$

Summary of spectral characterisation indices

The spectral characterisation indices discussed in this section are summarised in Table 2.2. One of the main differences between the parameters is the balance they strike between simplicity and accuracy, which is determined primarily by the data requirements for their calculation. In Table 2.2, the data "level"

refers to how complex and/or affordable the required data acquisition is for the direct measurement or calculation of the parameter in question. Overall, it appears as though the characterisation of spectral effects on the PV performance through the use of proxy variables is simpler but less accurate, while the direct characterisation through the use of spectral data requires a more complex measurement but is more accurate. The simulation of spectral irradiance data to calculate parameters such as the average photon energy could mitigate the measurement issue but validation of such methods in conjunction with PV performance forecasting is not currently presented in the existing literature.

Index	Eqns.	Type	+	−	Refs.
AM_a	2.7, 2.8	Proxy	Simple calculation, low-level data	No diffuse irradiance	[123]
R_d	2.9	Proxy	Simple calculation, medium-level data, diffuse effects included	Diffuse irradiance only best used with other parameters	[109, 133]
K_t	2.10	Proxy	Cloud effects included, medium-level data	Limited information on complex scattering	[118]
W	2.11	Proxy	Accurate measure of a specific atmospheric phenomenon, simple estimation	High-level data (unless estimated), best used with other parameters	[145, 151]
AOD	2.15	Proxy	Accurate measure of a specific atmospheric phenomenon	High-level data	[156]
φ	2.17	Direct	Single number with info on multiple E_λ features and atmospheric phenomena	High-level data	[140, 180]
ε	2.18	Direct	Accurate measure of a specific atmospheric phenomenon	High-level data	[11, 1]

Table 2.2: Summary of the indices used to characterise the prevailing spectral irradiance conditions. The data "level" refers to the requirement for data of different levels of accessibility or complexity. For example, irradiance data would be considered medium level due to the need for non-trivial, but still relatively simple and common measurements at any established PV or meteorological monitoring station.

2.4 Photovoltaic theory

In this section, the physics underpinning the photovoltaic effect and how these principles relate to the spectral response of a PV device is explained.

2.4.1 Photovoltaic effect

Some materials, such as Silicon and Germanium, are intrinsic semiconductors. The addition of an impurity into one of these bulk (host) materials, known as doping, that has more valence electrons than the host results in an n-type semiconductor. A dopant with fewer electrons than the host results in a p-type semiconductor. When p– and n-type semiconductor layers are brought into contact, an electric potential is created between the p– and n-type layers. In this construct, an electron can move from an energy level in the valence band to the conduction band, which are the energy bands closest to the Fermi level, leaving a hole in its place. The separation of these charges creates an electric field across the depletion zone (between the layers), which provides the force to drive the current through an external circuit. Whether the device has a single p-n junction, or an insulating layer is introduced to form a p-i-n junction, or there are multiple junctions, the electrical behaviour is similar. The relationship between the current, I, and voltage, V, is as follows [181]:

$$I = I_0 \left[\exp\left(\frac{qV}{nkT} \right) - 1 \right] - I_L. \tag{2.19}$$

Equation 2.19 is the standard diode equation. I_L is the light-generated current, n is a diode factor, which is related to the recombination mechanisms in the cell, I_0 is the reverse saturation current, T is the temperature in Kelvin, B is Boltzmann's constant, and q is the electron charge. For a real (non-ideal) device, it is necessary to include the effects of resistance (shunt, R_{sh}, and series

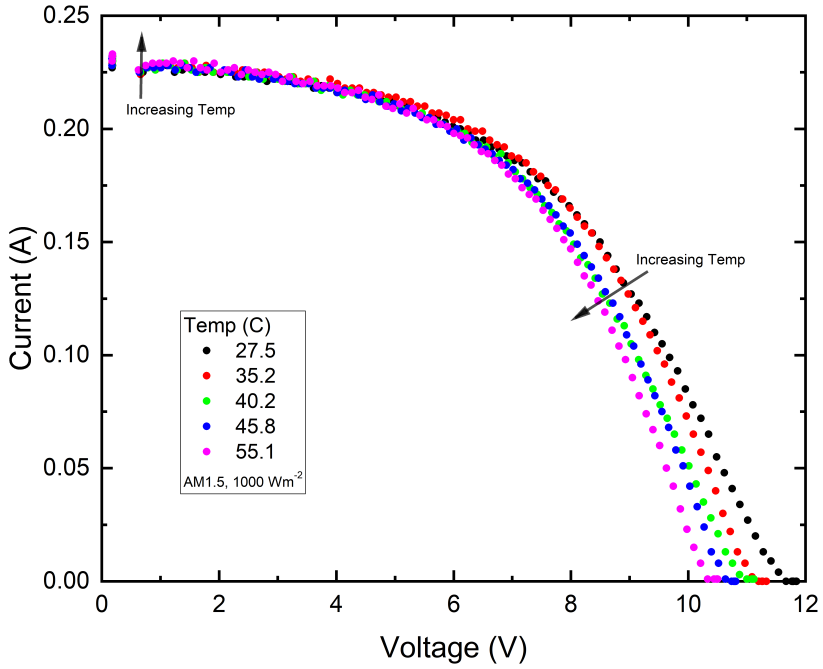

Figure 2.13: Example I-V curves for a CdTe device used in this project.

R_s) resulting from aspects such as the front and rear contacts, carrier transport within the semiconductor, etc.:

$$I = I_L - I_0 \left[\exp\left(\frac{q(V + IR_s}{nkT} \right) - 1 \right] - \frac{V + IR_s}{R_{sh}}. \tag{2.20}$$

The resulting I-V characteristics of a PV cell operating at arbitrary operating conditions are shown in Figure 2.13. The effect of cell temperature is also shown as an example of how certain environmental variables can influence the I-V characteristics. These data were measured at the University of Nottingham using the CdTe module introduced in Chapter 3. The following parameters, which can all be extracted directly or calculated from the I-V curve, are typically used to describe the electrical performance of a solar cell [182]:

- I_{sc} — short-circuit current; this is the current at $V = 0$ when there is zero resistance between the terminals. It is the maximum possible current for the specific operating conditions of the device.

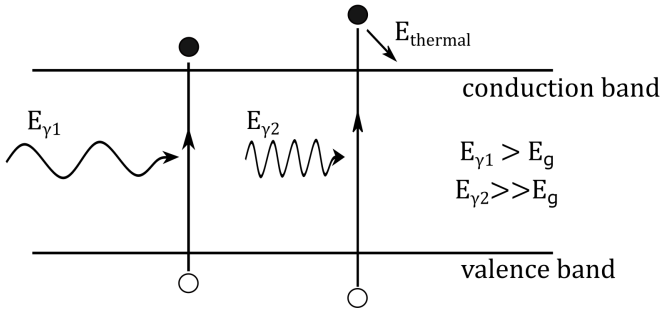

Figure 2.14: Illustration of the photovoltaic effect.

- V_{oc} — open-circuit voltage; voltage across the device terminals in open circuit when $I = 0$. It is the maximum voltage for the specific operating conditions.

- MPP — maximum power point; the point along the I-V curve at which maximum power ($I \times V$) is obtained.

- I_{MPP} — Current at MPP; the current value for which $I \times V$ is maximum.

- V_{MPP} — Voltage at MPP; the voltage value for which $I \times V$ is maximum.

- FF — Fill Factor; the ratio of the product of I_{MPP} and V_{MPP} to the product of I_{sc} and V_{oc}.

In a photovoltaic device, it is an incident photon that provides the energy required to excite an electron from the valence to the conduction band, leaving a hole in its place, and generate a current. This entire process is known as the photovoltaic effect and is illustrated in Figure 2.14. The size of the gap between the valence and conduction bands is known as the band gap, E_g, and a photon (γ) must transfer an energy (E) of $E_\gamma \geq E_g$ to generate an electron-hole (e-h) pair. Any excess energy is converted into a thermalisation loss, $E_{thermal}$. How the size of the band gap relates to the performance of a PV device is described in the following subsection.

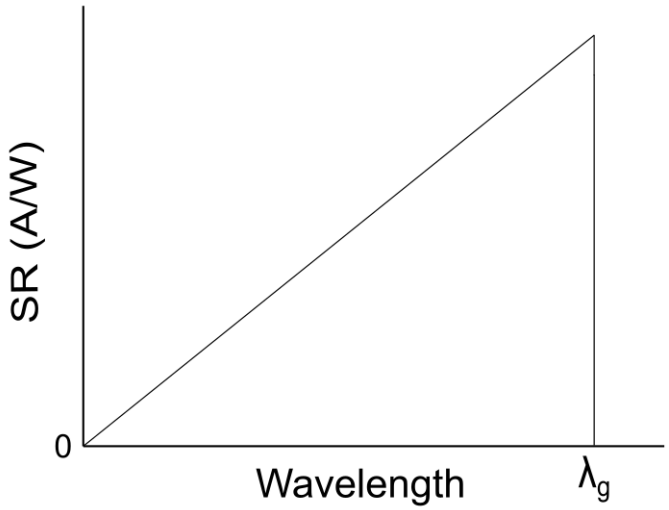

Figure 2.15: Ideal spectral response of a PV device.

2.4.2 Spectral response

The spectral response of a PV device describes how efficiently the device converts incident photons of different wavelengths into electron-hole (e-h) pairs. The wavelength, λ[nm] of a photon is inversely proportional to its energy, E_γ[eV], where the constant of proportionality is the product of Plank's constant, h, and the speed of light in a vacuum, c:

$$E_\gamma = \frac{hc}{\lambda}.$$

This equation is the same as Equation 2.16 but is repeated here for clarity. If the spectral response (SR) is defined as the current generated by a PV device per incident watt of power, one would expect the SR to increase linearly with decreasing photon energy (increasing photon wavelength) as the photon energy tends towards the band gap energy and thermalisation losses are reduced. Beyond the cut off energy, equal to the band gap, $E_\gamma < E_g$ and PV device SR drops to zero. This yields the theoretical ideal spectral response curve for a PV device shown in Figure 2.15. Given that the size of the semiconductor band gap determines the photon energy required to generate a photocurrent, the different

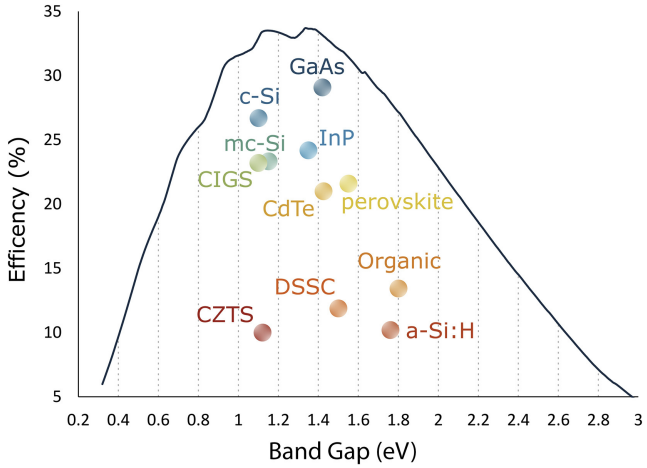

Figure 2.16: Band gaps of several common PV devices. Image reproduced from Ref. [12].

E_g values of different PV devices means that they each respond differently to different wavelengths of light. Typical E_g values of several common PV devices are summarised in Figure 2.16. In reality, SR curves are more complex, owing to the interplay of various material parameters of the PV device. In a PV device, electron and holes can recombine prematurely to generate heat or light, which leads to inefficiency in the power generation of the PV device. There are different types of recombination that occur in different locations of the PV material, such as the surface layer, emitter layer, etc., and are driven by different factors such as diffusion length, defect density, etc. [183]. A brief overview of the factors affecting the SR of a PV device is presented in Figure 2.17. Front surface recombination will typically affect short-wavelength light more, while rear-surface recombination will typically affect long-wavelength light more, which all contributes to the response of a PV device to different wavelengths of light. The spectral responses of some common PV technologies are shown in Figure 2.18. In the background of the SR curves, the STC AM1.5G spectrum, normalised between 300 nm and 1200 nm, is plotted between for reference.

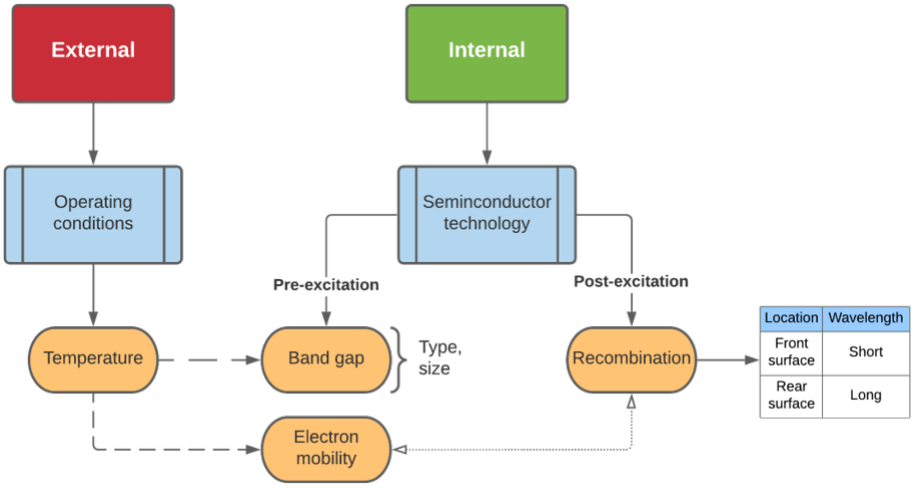

Figure 2.17: Summary of the factors influencing the PV device spectral response.

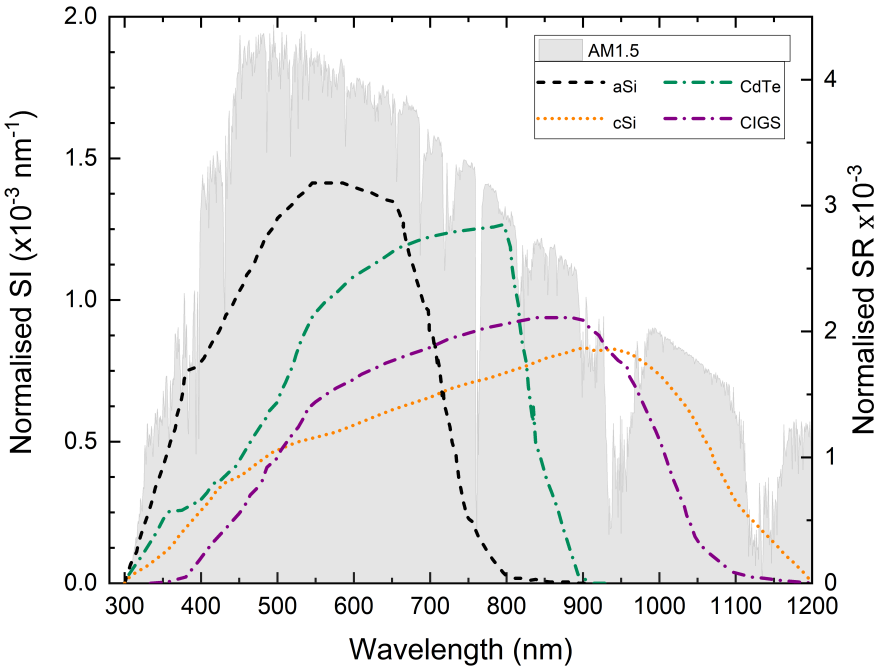

Figure 2.18: Spectral responses of several common PV technologies, namely amorphous silicon (aSi), Cadmium Telluride (CdTe), crystalline silicon (cSi), and Copper Indium Gallium Selenide (CIGS). The SR curves are plotted using data published in Ref. [13] (mSi and CdTe) and Ref. [14] (aSi-T). The AM1.5 reference spectrum, normalised between 300 nm and 1200 nm, is plotted in the background for comparison.

2.4.3 Developments in SR optimisation

There have been many developments in the field of photovoltaics related to optimising device spectral response and, therefore, improving overall device efficiency. These methods include combining cells with different SRs into one device [184], applying coatings to devices to reshape the incident spectrum [185], and directly tuning the band gaps of PV devices [186]. These developments are reviewed briefly in this section to provide the reader with a broad contextual background to the research field of photovoltaics and the spectral response.

In a multijunction (MJ) device, multiple p-n junctions made of different semiconductor materials are combined into a single solar cell. Combining materials of different band gaps in this way reduces thermalisation losses and thus increases efficiency [187]. As of 2022, the highest recorded efficiency of an MJ device is 47.6% [188, 189], which far exceeds that of single-junction devices. Although the SR of an MJ device is wider, since the SRs of each device are combined, the construction of multijunction devices is such that the junctions may be considered as cells connected in series. Therefore, the current flowing through each junction must be equal, which limits the overall device current to that of the least productive junction. Therefore, multijunction devices still exhibit a strong spectral dependence [174, 190] due to the particular spectral response characteristics of the individual subcells (junctions). A detailed discussion of how this mismatch can be mitigated through power and current matching in MJ devices is presented in Ref. [191].

Another way to increase the efficiency of a PV device through consideration of the module spectral response is through spectral shaping, whereby the energy of incident photons is changed to improve their utilisation rate and efficiency by the solar cell [192]. A layer can be added to rear surface of a solar to increase the energy of sub-E_g energy photons (up conversion) [193] to maximise the

solar cell's use of the incident irradiance. A front surface layer can also be used to split high energy photons into multiple lower energy photons, thus reducing thermalisation losses and increasing efficiency. Efficiencies of up to around 63% and 39% have been calculated as limits for solar cells with up and down converters, respectively, depending on the precise device construction and converter layer properties [194]. A review of the materials developed for down shifting over thirty years until 2009 is presented in Ref. [195], while more recent developments in the field of down shifting are reported in Ref. [196]. However, minimising degradation of up– and down-conversion layers in the field is still an area under research [197, 198]

Up and down conversion focus on shifting the energy of the incident photons, band gap tuning is a method of adjusting the solar cell receiving those photons. Another approach is to modify the solar cell spectral response itself through band gap tuning, or band gap engineering. Band gap tuning is a powerful technique that can create new semiconductor materials with variations in band gap that are best suited to optimise electron and hole transportation for the desired application [199]. An overview of recent advances in band gap engineering to improve efficiency, with a particular focus on perovskite solar cells, is presented in Ref. [186, 200]. This technique is particularly useful for adjusting materials such as $Cu_2ZnSn(S,Se)_4$ that have desirable characteristics such as high absorptivity, but a sub-optimal band gap for photocurrent generation [201]. Relative improvements in efficiency of over 90% have been reported in the literature as a result of band gap engineering applied to thin film PV technologies [202].

In summary, as the importance of the solar spectrum for PV performance has been recognised, a significant amount of academic and industrial effort has been made to optimise solar cell design to maximise efficiency with respect to utilisation of the incident irradiance. It is evident that there are not only various parameters related to the environment that influence the solar spectrum, but

also those related to the PV cell design and construction that influence the cell's response to the incident spectrum. In order to understand the behaviour of different PV cells in response to different spectra, it is necessary to isolate the effects of the spectrum on PV performance by removing the influence of other parameters such as irradiance, temperature, etc. There exist various mathematical characterisations of the variation in PV performance solely due to variation in the spectrum, which can be used for such analysis. The most commonly used of these parameters are introduced in the following subsection.

2.5 Characterising spectrum-induced variation in PV performance

Several methods of characterising the solar spectral distribution were discussed in Section 2.3.2. In order to analyse the relationship between the spectrum and PV performance, it is also necessary to characterise variation in PV performance as a result of variation in the solar spectrum. Several different approaches extracted from the existing literature are presented in this section.

2.5.1 Useful and Weighted Useful Fraction

The useful fraction (UF) is the ratio of irradiance that falls within the spectral response of a PV device to the total available irradiance. It was originally termed "available spectrum" by Hirata and Tani (1995) who first proposed it [49], but has since become known as the Useful Fraction. The UF is calculated as follows [49, 203]:

$$\mathrm{UF} = \frac{1}{G} \int_0^{\lambda(E_g)} E(\lambda)\, d\lambda, \tag{2.21}$$

where G is the total irradiance and the interval of integration is from zero to the band gap, E_g, expressed as a wavelength (λ). Although the UF (dimensionless) has been used in previous publications [204, 205, 206], one of its significant limitations is that it assumes a constant (100%) spectral response across all wavelengths. An alternative is the weighted useful fraction (WUF), which weights the fraction calculated at each wavelength by the module spectral response at that wavelength [207]. The WUF (dimensionless) is calculated as follows:

$$\mathrm{WUF} = \frac{\int_{\mathrm{cell-min}}^{\mathrm{cell-max}} E_\lambda \mathrm{SR}_\lambda \, d\lambda}{\int_{\mathrm{G-min}}^{\mathrm{G-max}} E_\lambda \, d\lambda}. \tag{2.22}$$

Since the true module SR is never 100% at any wavelength, the UF is always greater than the WUF. The overestimate of useful irradiance by the UF would lead to an overestimate of PV power output. One mutual limitation of the UF and WUF is that they both require knowledge of the module spectral response, which can only be acquired through a non-trivial measurement. Another limitation is that these parameters are device dependent.

2.5.2 Normalised short-circuit current

The solar spectral influence on PV performance may also be characterised through the direct use of performance measurements. The short-circuit current of a PV device, I_{sc}, is subject to the effects of many different variables, including the spectrum. However, the dominant of these are the broadband irradiance and PV cell temperature. By isolating the non-spectral effects from the measured short-circuit current, any remaining deviation from an RTC performance can be attributed to variation in the incident solar spectrum from the reference spectrum. Other effects considered dominant for the DUT may also

be taken into account, such as the angle of incidence.

The normalisation process is as follows. I_{sc}, which is measured at arbitrary irradiance and temperature, is translated to a reference temperature, T_r, and reference irradiance, G_0, to give and intermediary current value, I'_{sc}:

$$I'_{sc} = \frac{I_{sc}}{1 + \hat{\alpha}_{I_{sc}}(T_c - T_r)} \left[\frac{G_0}{G_{poa}}\right]. \tag{2.23}$$

$\hat{\alpha}_{I_{sc}}$ [°C^{-1}] is the short-circuit current temperature coefficient, T_c [°C] is the measured (or modelled) cell temperature, and G_{poa} [W m^{-2}] is the measured (or modelled) plane of array irradiance.

The normalised short-circuit current, I_{scn}, is then found by dividing I'_{sc} by the reference short-circuit current, I_{sc0}, which is the current measured at the reference test conditions (T_r, G_0, and $\mathrm{E}_{\lambda,0}$):

$$I_{scn} = \frac{I'_{sc}}{I_{sc0}}. \tag{2.24}$$

The normalisation principle here is a standard mathematical technique and is widely known for its use in the Sandia model [131, 208], and has also been adopted in other SCF literature [1, 133, 3, 180].

I_{scn} is a device-independent parameter, thus making it easier to understand and use to compare the spectral effects on different devices. $I_{scn} > 1$ indicates higher performance under the prevailing spectrum with respect to the performance under the reference conditions, $I_{scn} < 1$ indicates decreased performance, while $I_{scn} = 1$ indicates there is no difference between the performance under the prevailing spectrum and under reference conditions.

2.5.3 Spectral or mismatch factor

The spectral mismatch factor (SF), also known as the mismatch factor (M), is calculated based on the differences between the responses of the PV device under test (DUT) and a reference device, to both the incident spectral irradiance and a reference spectrum. It is calculated as follows [209]:

$$M = \frac{\int E_{\lambda,0} SR_{\lambda,0} d\lambda \int E_{\lambda,meas} SR_{\lambda,sample} d\lambda}{\int E_{\lambda,meas} SR_{\lambda,0} d\lambda \int E_{\lambda,0} SR_{\lambda,sample} d\lambda}, \tag{2.25}$$

where the first subscript, λ, denotes the functional dependence, and the second, ref, $meas$, or $sample$, indicates the reference value, measured value, or sample (DUT) value, respectively.

The calculation of M requires knowledge of the module spectral response, which, as highlighted in the discussion on UF, is a non-trivial measurement. However, the M is in fact analogous to I_{scn} [210, 211]. The final output is also a ratio with values greater than, less than, or equal to unity indicating increased, decreased, and the same performance under the prevailing spectrum relative to performance under the reference spectrum. Both M and I_{scn} are ratios of performance under prevailing conditions to reference conditions, albeit calculated in different ways.

M has been used widely in the literature to understand differences between measured spectra and reference spectra, for example when calibrating solar simulators [212], testing new PV materials [213], and for PV performance analysis under varying spectral irradiance conditions [214, 215, 216].

Variants of the spectral factor exist, with some studies using its inverse for PV-spectral analysis [173, 217]. Another variant used in the literature [218, 219] is the weighted average spectral factor, which is calculated by weighting the

instantaneous M_i values with the broadband irradiance G_i over a period of time:

$$\langle M \rangle = \frac{\sum_i G_i M_i}{\sum_i G_i}. \tag{2.26}$$

However, the issue regarding the requirement for knowledge of the module spectral response, and the complexity of solving the integral at multiple time steps, persists.

2.5.4 Summary

Table 2.3 summarises the indices used to characterise the shift in PV performance resulting from shifts in the prevailing spectral irradiance conditions. There is less variety in these methods compared with the methods of characterising the solar spectral distribution. I_{scn} appears to be the best approach given that it is a device-independent parameter, unlike the UF and WUF, and it offers a similar accuracy to M without the need for spectral irradiance and spectral response (SR) measurements. However, where such measurements are available, M may be a better choice. Furthermore, I_{scn} does still require module-level performance measurements.

Index	Eqn.	+	−	Refs.
Useful fraction (UF)	2.21	Simple calculation	Device dependent, high-level data	[49, 204]
Weighted UF	2.22	Accounts for variable SR	High-level data	[207]
Normalised I_{sc} (I_{scn})	2.24	Device-independent, simple calculation, intuitive representation	Multiple measurements (various levels)	[208]
Mismatch factor (M)	2.25	High accuracy, intuitive representation	Complex calculation, high-level data (SR)	[209]
M variants	2.26	As above, some extra information included	Complex calculation, high-level data (SR)	[218, 219]

Table 2.3: Summary of parameters used to characterise the shift in PV performance due to spectral variation. The data "level" refers to the requirement for data of different levels of accessibility or complexity. For example, spectral response (SR) data would be considered high level due to the need for complex measurements.

2.6 Review of spectral correction functions

To account for the influence of the spectrum in photovoltaic performance modelling (PVPM), a spectral correction function (SCF) is used to translate the PV output known at a set of reference spectral irradiance conditions to the performance under arbitrary spectral irradiance conditions. Such functions consist, in principle, of two components — one component is the mathematical characterisation of the solar spectrum, while the second is the characterisation of the PV performance under the influence of variable spectral irradiance conditions. Sections 2.3.2 and 2.4 have explained the parameters that can be used to represent the solar spectrum, as well as its effect on PV performance, respectively. By understanding the relationship between the two, a spectral correction function can be derived. In this section, ten such spectral correction functions (arising from combinations of eight unique spectral characterisation parameters) are introduced and explained. In section 2.7, the following section, these SCFs are compared and their respective merits and drawbacks, in isolation and relative to one another, are critically analysed.

2.6.1 Air mass function

The air mass spectral correction function was first proposed by King et al. (1997) [220], and later integrated into many photovoltaic performance models such as the Sandia Array Performance Model (SAPM) [221] and the five-parameter model [92].

The air mass function uses air mass to characterise the incident solar spectrum. As an example, in the SAPM, I_{scn} is analysed as a function of a pressure-corrected value for the air mass, commonly referred to as the "absolute air mass", AM_a. The pressure correction is required to account for the decreased density of air molecules at different elevations [222]. The air mass is calculated

using the Kasten and Young (1989) model [123] (Equation 2.8), and a linear pressure correction is applied by the ratio of the site pressure, P, to the pressure at sea level, P_0. The correction can be calculated based on measurements of on-site pressure, or estimated using:

$$\frac{P}{P_0} \approx e^{-0.0001184 \cdot h}, \tag{2.27}$$

where h is the altitude in metres.

The functional form of $I_{scn} = f(AM_a)$ is a fourth order polynomial, the coefficients of which are dependent on the PV technology being used. The model is as follows:

$$I_{scn} = f(AM_a) = \sum_{n=0}^{4} a_n \cdot \varphi^n, \tag{2.28}$$

where a_{0-4} are the PV technology-dependent coefficients. An open-access database of all of the SAPM coefficients for a variety of common PV technologies has been developed by the Sandia National Laboratory and can be found in the PVLIB Python library [223]. A comprehensive guide to determining the coefficients empirically is presented in Ref. [208].

2.6.2 Precipitable water content function

Due to the specific susceptibility of CdTe module performance to changes in atmospheric precipitable water content, W, Nelson et al. (2012) proposed an alternative to $f(AM_a)$ based on W [152]. The function was primarily targeted at, and hence validated only for, CdTe PV technology.

Using the simple model of the atmospheric radiative transfer for sunshine

(SMARTS) [119], in combination with Typical Meteorological Year 3 (TMY3) files for specific locations [224] as an input, the authors first show that W is a dominant parameter when determining M for CdTe PV systems. Furthermore, a model to predict M is derived, and validated in eleven locations. The final predictive model for M is as follows:

$$M_{CdTe} \approx 0.632 + 0.134 \cdot \exp(0.976(W + 0.05)^{0.079}) \tag{2.29}$$

Although the results reported in Ref. [152] have been used to guide further work in the field of CdTe spectral modelling [218, 225], the proposed SCF has not been widely adopted. Instead, a modified version of the model to include the effects of air mass, which is discussed in the following section, has superceded the single-variable precipitable water approach.

2.6.3 Air mass, precipitable water function

Although W is the primary driver for changes in M for CdTe PV modules, improvements in predictive accuracy of $M = f(W)$ have been achieved through the inclusion of an additional index. Lee and Panchula (2016) proposed a two-parameter spectral correction function based on both W and AM_a [2]. Their model, which is commonly referred to as the First Solar (spectral correction) model, is validated for both CdTe and cSi PV technologies, and shows an improvement when compared to both the W and AM_a single-variable SCFs.

The derivation of $f(AM_a, W)$ follows a similar procedure to that which is used to derive $f(W)$. The SMARTS model is used to correlate spectral variation, characterised using the spectral shift (M), with W and AM_a. The 3D surface plot is parameterised, resulting in the following predictive equation for M:

	b0	b1	b2	b3	b4	b5
CdTe	0.7946	-0.05423	-0.01319	0.1724	0.08372	-0.004376
mSi	0.8409	-0.02754	-0.00792	0.1357	0.03802	-0.002122
aSi-T	0.928	-0.103	-0.0597	0.0939	0.166	0.00656

Table 2.4: $f(AM, W)$ model coefficients for an aSi-T [1], CdTe, and mSi module [2]

$$M = b_0 + b_1 \cdot AM_a + b_2 \cdot W + b_3 \cdot \sqrt{AM_a} + b_4 \cdot \sqrt{W} + b_5 \cdot \frac{AM_a}{\sqrt{W}} \tag{2.30}$$

The module-specific coefficients, b_{0-5}, for the CdTe and mSi devices investigated by Lee et al. [2] are presented in Table 2.4. As part of a comparison with another SCF discussed later (Section 2.3.2), Daxini et al. [1] publish the $f(AM_a, W)$ model coefficients for a triple junction amorphous silicon device. These are also included in Table 2.4, however, the data source and filtering conditions used to derive the coefficients are different. Unlike Ref. [2] in which a mixture of simulated and measured spectra are used, Ref. [1] uses a full year of measured spectral irradiance data for the model development and validation.

2.6.4 Air mass, clearness index function

One issue with the SCFs presented so far is that they do not explicitly consider the effects of cloud cover on the solar spectrum. As highlighted in the discussion in Section 2.3.2, clouds have a significant impact on the efficiency of photovoltaic devices. Gottschalg et al. (2004) present a correlation between the air mass, clearness index, and the UF [47], hereinafter referred to as the CREST model. In later work, Huld et al. (2009) from the European Joint Research Centre (JRC) present a model based on AM_a and K_t to estimate the spectral influence

Module	mSi	CdTe
k_1	0.00172	6.43×10^{-4}
k_2	5.08×10^{-4}	1.30×10^{-4}
k_3	3.57×10^{-6}	1.08×10^{-5}

Table 2.5: Fitted coefficients for the Huld et al. [3] spectral correction model.

on photovoltaic device performance [3]:

$$I_{scn} = k_1(e^{-K_t} - e^1) + k_2(K_t - 1) + k_3(AM - 1.5). \tag{2.31}$$

The JRC model coefficients, k_{1-3}, are determined through fitting to measured data. The measurement campaign took place in Ispra, Italy. The multicrystalline module data were measured over a one-year period during 2003, while the CdTe data were measured from November 2008 to June 2009. The resultant model coefficients for each module are listed in Table 2.5.

Another model based on air mass and clearness index is the PVSPEC model, which correlates these two variables with the spectral mismatch factor, M [15]:

$$M = a_1 K_t^{a_2} AM^{a_3}. \tag{2.32}$$

In their analysis, they use the ESRA clear sky model [226] with monthly Linke turbidity values from [227] as inputs, while air mass is calculated using the Kasten and Young model presented in Equation 2.8 in Section 2.3.2 [123]. The PVSPEC model coefficients for a range of PV technologies are summarised in Table 2.6:

The $f(AM_a, K_t)$ approach is a popular method that has been explored widely in the literature through the examination of different parameterisations and application in different locations and for different PV technologies [118, 228, 229].

Table 2.6: Summary of the PVSPEC model coefficients

PV Technology	a1	a2	a3
mSi	0.9847	-0.05237	0.03034
mono-Si	0.9845	-0.05169	0.03034
FS4-2	1.002	-0.07108	0.02465
FS4-1	0.9981	-0.05776	0.02336
aSi	1.051	-0.1033	0.009838
CIGS	0.9791	-0.03904	0.03096

	Correction for:		
	AM_a	AOD	W
SF1	$ax^4 + bx^3 + cx^2 + dx + e$	$a \ln x + b$	$a \ln x + b$
SF2	$ax^4 + bx^3 + cx^2 + dx + e$	$ax^2 + bx + c$	$ax + b$
SF3	$ax^4 + bx^3 + cx^2 + dx + e$	$a \ln x + b$	$a \ln x + b$

Table 2.7: Spectral correction model for a 3T GaInP/GaInAs/Ge CPV device based on AM_a, AOD, and W.

2.6.5 Air mass, aerosol, precipitable water function

The SCFs introduced thus far are either single– or double-variable functions. The dependent variables in these models are environmental proxies for the spectrum. Given the many environmental variables that affect the spectrum, naturally these functions are likely to exclude the effects of certain environmental parameters. This can be problematic when applying such SCFs to different climate regions around the world. In different climate regions, the relative significance of the impact of different environmental parameters on the spectrum may vary.

Theristis et al. (2016) incorporate a broader scope of spectral variables by building an SCF based on air mass, aerosol optical depth, and atmospheric precipitable water content [230]. They propose a set of analytical equations to account for the spectral influence on each sub-cell of a triple-junction GaInP/-GaInAs/Ge concentrating photovoltaic (CPV) system. The proposed spectral corrections for each subcell are presented in Table 2.7.

	Correction for:		
	AM_a	AOD	W
aSi	$ax^4 + bx^3 + cx^2 + dx + e$	$ax^2 + a_x + a$	$a \ln x + b$
Perovskite	$ax^4 + bx^3 + cx^2 + dx + e$	$ax^2 + a_x + a$	$a \ln x + b$
CdTe	$ax^4 + bx^3 + cx^2 + dx + e$	$a \ln x + b$	$a \ln x + b$
mSi	$ax^4 + bx^3 + cx^2 + dx + e$	$ax + b$	$a \ln x + b$
Mono-Si	$ax^4 + bx^3 + cx^2 + dx + e$	$ax + b$	$a \ln x + b$
CIGS	$ax^4 + bx^3 + cx^2 + dx + e$	$ax + b$	$a \ln x + b$

Table 2.8: Spectral correction model for six PV materials based on AM_a, AOD, and W.

Caballero et al. (2018) expand on the CPV spectral correction model by developing a similar SCF, based on the same dependent variables of AOD, W, and AM_a, for six single-junction PV devices [231]. By expressing the effects of AOD and W on PV performance as different functions of AM_a, a set of spectral corrects are proposed for the six PV material types (Table 2.8).

For each of the six PV materials, the R^2 values for $f(AOD)$ and $f(W)$ are greater than 0.97 and 0.98, respectively. The model was validated through an outdoor experiment campaign in Jaén, Spain, from March 2016 to February 2017, inclusive. Correlations between the predicted and modelled mismatch factor yielded R^2 values from 0.87 (mSi) to 0.92 (aSi), indicating a high prediction accuracy.

2.6.6 Air mass cumulative distribution function

Although the triple-variable method introduced in Section 2.6.5 is capable of including the spectral effects of more environmental factors in PV performance modelling, the method is relatively complex. In order to maintain a high level of inclusion of factors, but reduce the number of variables to retain the simplicity of the other methods, Peng et al. (2019) propose a modified air mass function [133]. They argue that the effects of aerosol, precipitable water vapour content, cloud cover, etc. cannot be ignored, but their effects can be summarised in

a single parameter. Aerosol is known to increase the diffuse fraction of total irradiance [232, 233, 234], as do W [235] and cloud cover [236]. Therefore, Peng et al. combine an "air mass cumulative distribution function" (AMCDF) with the diffuse solar radiation ratio (R_d) to form a new method of accounting for the spectral influence on the performance of PV devices. Around one week of data were extracted from a four month measurement campaign for the final analysis. The resultant model is a piecewise function dependent on the value of R_d:

$$\begin{cases} f(AM) = y = 1697 \cdot AM^{-1.987} + 1836 & R_d \leq 0.7 \\ f_2(AM) = -8.76e-016y^5 + 3.745e-0.12y^4 - 5.942e \\ -009y^3 + 4.254e-006y^2 - 0.001341y + 1.137 \\ I_{sc} = \frac{I_{sc0} \cdot f_2(AM)}{1+\alpha_{Isc}(T_c - T_0)} \cdot \frac{G}{G_0} \\ f(R_d) = 0.8381R_d + 0.1244 & R_d > 0.7 \\ I_{sc} = \frac{I_{sc0} \cdot f(R_d)}{1+\alpha_{Isc}(T_c - T_0)} \cdot \frac{G}{G_0} \end{cases} \tag{2.33}$$

This model does not appear to have been adopted for spectral correction purposes by industry or other researchers in their analysis of PV performance under the influence of the solar spectrum. In addition, the proposed model is not validated through an analysis of its predictive accuracy. As a result, the AMCDF model is not included in the comparison of SCFs in the next subsection as no suitable data are available to enable a meaningful comparison. However, the model description is still presented here for completeness of the review.

2.6.7 Average photon energy

As explained in Section 2.3.2, the average photon energy is a useful way of characterising the solar spectrum and has been used as such in the existing literature. Takei et al. use the APE and module temperature to predict the energy output of three PV modules and compare these values to the measured output and those predicted using air mass and clearness index [4]. However, they do not go on to establish a validated spectral correction function that can be integrated into broader PV performance models. In the development of a new PV performance model, Williams et al. [174] propose a spectral loss factor based on the APE that is analogous to a spectral correction function. The loss factor, r_φ, is a dimensionless spectral correction that is calculated as follows:

$$r_\varphi = \frac{1}{\eta_{STC}}(B_0 + B_1 \cdot \varphi_{eff} + B_2 \cdot \varphi_{eff}^2). \tag{2.34}$$

The terms φ_{eff} and φ_{eff}^2 are calculated on the basis of a time series as follows:

$$\varphi_{eff} = \frac{C_0 \cdot S_{G1\varphi} + C_1 \cdot S_{G2\varphi} + C_2 \cdot S_{G3\varphi}}{C_0 \cdot S_{G1} + C_1 \cdot S_{G2} + C_2 \cdot S_{G3}} \tag{2.35}$$

and

$$\varphi_{eff}^2 = \frac{C_0 \cdot S_{G1AP2} + C_1 \cdot S_{G2\varphi 2} + C_2 \cdot S_{G3\varphi 2}}{C_0 \cdot S_{G1} + C_1 \cdot S_{G2} + C_2 \cdot S_{G3}}. \tag{2.36}$$

The underlying sums are:

$$\begin{aligned} S_{G\varphi} = \sum G \cdot \varphi; S_{G2\varphi} = \sum G^2 \cdot \varphi; \\ S_{G3\varphi} = \sum G^3 \cdot \varphi; S_{GU\varphi 2} = \sum G \cdot \varphi^2; \\ S_{G2U\varphi 2} = \sum G^2 \cdot \varphi^2; S_{G3\varphi 2} = \sum G^3 \cdot \varphi^2. \end{aligned} \tag{2.37}$$

It is not possible to determine the reported spectral loss factors for each PV

device due to the low resolution of the presented bar chart (Figure 5 in [174]) but the overall power prediction model is reported to be accurate to within 7% of the measured performance values.

Overall, the use of the APE as a basis for a spectral correction function as part of a PV performance model is limited. A spectral correction function using the APE has not been developed and validated in the literature with publicly available model coefficients for different PV technology types. Therefore, this is one of the main areas of investigation for this project.

2.7 Comparison of SCFs

The previous sections show the high level of diversity in methodologies used to model the spectral influence on PV performance and incorporate this influence into forecasts of PV performance. In this section, a critical comparison is made between the different methods in terms of their underlying principles, such as which parameters are used to characterise the spectrum, and the differences in their predictive performance.

Starting with $f(AM_a)$, this is the most widely-known SCF and the model coefficients have been published for dozens of PV technologies from a range of manufacturers. The free and ready availability of model coefficients make $f(AM_a)$ and obvious choice for PV performance modellers. The ease with which AM_a can be calculated accurately in the field, without the need for specialist equipment and measurements, also makes deriving new coefficients for novel technologies relatively easy. However, air mass is defined by the path length of direct irradiance only, hence spectral effects linked to diffuse irradiance are omitted. Zanesco and Krenzinger (1993) highlight that spectral variations are due not only to air mass, but also atmospheric precipitable water, Angstrom's turbidity coefficient, and aerosol particle size distribution [237]. In environ-

Site: module	$f(W)$, $f(AM_a)$	$f(AM_a, W)$
Cocoa: CdTe	$\text{MAE}_W = 0.0169$ $R^2 = 0.494$	$\text{MAE} = 0.0157$ $R^2 = 0.705$
Cocoa: mSi	$\text{MAE}_A = 0.0130$ $R^2 = 0.428$	$\text{MAE} = 0.00749$ $R^2 = 0.724$
Eugene: CdTe	$\text{MAE}_W = 0.0188$ $R^2 = 0.445$	$\text{MAE} = 0.638$ $R^2 = 0.598$
Eugene: mSi	$\text{MAE}_A = 0.00406$ $R^2 = 0.696$	$\text{MAE} = 0.767$ $R^2 = 0.817$
Golden: CdTe	$\text{MAE}_W = 0.00827$ $R^2 = 0.712$	$\text{MAE} = 0.7266$ $R^2 = 0.706$
Golden: mSi	$\text{MAE}_A = 0.00955$ $R^2 = 0.001$	$\text{MAE} = 0.561$ $R^2 = 0.356$

Table 2.9: Linear regression of outdoor testing data measured for a CdTe and mSi panel in Cocoa (Florida), Eugene (Oregon), and Golden (Colorado) [2]. Subscript W indicates the use of $f(W)$, while subscript A indicates the use of $f(AM_a)$.

ments where only the effects of air mass dominate, $f(AM_a)$ may sufficiently capture the majority of the spectral effects on PV performance [220]. However, Hansen et al. (2014) find a systematic error in the air mass function where, at the same air mass, the spectral effects on I_{sc} vary depending on the time of day [238]. Klise et al. (2015) attribute uncertainty in Sandia Model PV performance predictions, which use $f(AM_a)$, in different geographic locations, to the effect water vapour content and atmospheric turbidity on the spectral distribution [239].

With all SCFs, quantification of their uncertainties for comparison is difficult due to the differences in the methodologies and datasets used to derive them. Elements of comparison using standardised methods exist in some publications, typically when new models are compared to existing models. In addition, some indication of relative performance may be gleaned from analysing model fitting statistics in the context of the methods through which they were derived. In their proposal of $f(AM_a, W)$, Lee and Panchula (2016) compare linear regression results of outdoor testing data for $f(AM_a)$, $f(W)$, and $f(AM_a, W)$. These results are summarised in Table 2.9.

The absolute values of fitting statistics and errors in Table 2.9 are not comparable with those of other publications that process their data differently, for example by using different irradiance filtering conditions. However, the rela-

tive performance $f(AM_a)$, $f(W)$, and $f(AM_a, W)$ is a meaningful result from Ref. [2]. The combined AM_a, W model decreases the MAE in two of the three locations studied, namely Cocoa (Florida), and Eugene (Oregon). Considering their relative proximity to the sea, in contrast to the continental location of Golden, increased humidity may result in the marked benefit of including W in the SCF. On the other hand, in Golden, the R^2 for $f(AM_a, W)_{mSi}$ is an order of magnitude greater than for the single-variable SCF, yet the MAE value is still higher. This could suggest that the proposed parameterisation for this model is prone to overfitting. Since a mixture of simulated and measured spectra are used, the model development dataset may not be representative of the model validation dataset [52]. Another possibility is that the model-specific coefficients may in fact have a location-specific element to them [71].

None of the three models discussed thus far consider the effects of clouds on the spectrum, and therefore PV performance. $f(AM_a)$ is only defined in clear sky conditions and previous research has shown that it results in high PV performance prediction uncertainty in cloudy conditions. $f(W)$ and $f(AM_a, W)$ are derived using the Simple Model of the Atmospheric Radiative Transfer of Sunshine (SMARTS), which is well-renowned and widely used model [119, 240, 241], but SMARTS does not account for the influence of cloud cover on the solar spectrum. Furthermore, the field data used for model validation omit cloud cover through the data filtering conditions of $0.7 \leq K_t \leq 1.0$. In environments where air mass and water vapour are the dominant drivers of spectral changes, the omission of clouds may not be significant. However, in countries such as the United Kingdom, the effects of cloud cover and non-negligible, as discussed quantitatively in Section 2.3.2.

$f(AM_a, K_t)$ is an alternative method that explicitly includes the effects of cloud cover in the spectral correction. Previous work has shown the benefit of including the K_t variable in spectral corrections, compared with the single-variable air

mass approach, due to its ability to improve predictions of I_{scn} values greater than unity for amorphous silicon devices [180]. Despite this SCF now omitting the explicit inclusion of atmospheric precipitable water content effects, the PVSPEC parameterisation of $f(AM_a, K_t)$ (Equation 2.32) is shown to exceed the accuracy of the $f(AM_a, W)$ SCF (Equation 2.30) by reducing the root mean square error (RMSE) for all six of the PV technologies tested, which are listed in Table 2.6. The results of this comparison are presented in Figure 2.19. The absolute error of each model is presented in Figure 2.19(a), which shows that the PVSPEC model outperforms the $f(AM_a, W)$ model for all technologies save for CIGS. The fact that the RMSE for the JRC model is still lower despite the slightly higher absolute error suggests that $f(AM_a, W)$ may model M with a larger errors, but less frequently, since the RMSE is weighted by the square of the error hence there is a greater penalty for larger errors. Figure 2.19 also show that the PVSPEC model is more accurate than the JRC parameterisation of $f(AM_a, K_t)$ (Equation 2.31), which suggests that the PVSPEC parameterisation is a better choice for the PV technologies studied.

The question of choosing between W and K_t as a secondary variable in the AM_a SCF is addressed by Duck and Fell [242], who show that applying a correction for precipitable water to $f(AM_a, K_t)$ can improve the accuracy with which M values are predicted. However, the scale of this improvement is not quantified in their study. In addition, as the PVSPEC model was released later than the analysis by Duck and Fell, whether a precipitable water content correction can improve the PVSPEC model has not been investigated.

The $f(AOD, W, AM_a)$ model attempts to maximise the inclusion of spectral proxies in the correction function. The regression statistics for the correlations between modelled and measured M values are greater than 0.8 for all PV devices [231]. Using the same dataset and data processing, Caballero (2018) show that the root mean squared errors (RMSE) for predictions of M is lower

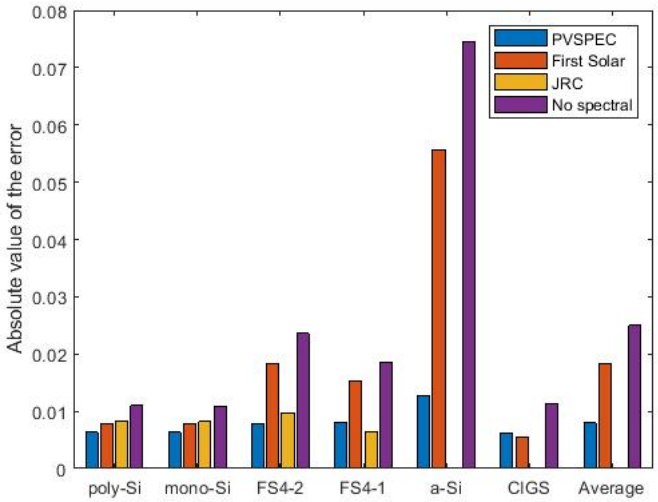

(a)

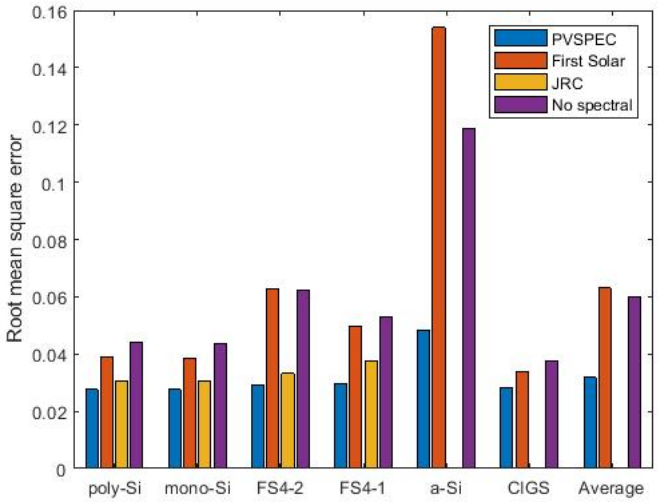

(b)

Figure 2.19: Absolute error (a) and root-mean-squared error (b) values for the spectral mismatch prediction of six different PV panels using three different models. Images reproduced from [15].

using $f(AOD, W, AM_a)$ than when using $f(AM_a)$ for all PV devices investigated. However, no comparison is drawn between $f(AOD, W, AM_a)$ and other multivariable functions, such as $f(AM_a, W)$ and $f(AM_a, K_t)$. Therefore, the increased complexity of including a third variable is not evaluated against any improvement in accuracy, if any is observed. The existing literature has established the geographic dependence of the prevalence of of atmospheric precipitable water [243, 244], aerosols [245], and other atmospheric components that influence the solar spectrum. Therefore, the worldwide generalisability of proxy-based SCFs is not certain. Duck and Fell (2015) suggest that it is this geographic variation in spectral irradiating conditions that leads to the difference they observe between predicted and measured values of M, where the predictions are computed from an SCF derived a site different to that where the measurements are made [71].

The average photon energy spectral correction function offers a simpler single-variable approach to modelling the spectral influence on PV performance. As it is derived directly from the solar spectrum, the APE is also thought to contain information on all relevant spectrum-influencing variables, including air mass, clearness index, aerosols, atmospheric precipitable water. However, a spectral correction function based on the APE has not yet been published. Although Takei et al. [4] focus on overall PV system output estimation rather than a specific spectral correction function, their work offers a helpful comparison between the strength of the correlations between PV output and both spectral proxies and a spectrum-derived parameter. The results of their analysis using APE and module temperature to predict the energy output of three PV modules and compare these values to the measured output and values predicted by air mass and clearness index are summarised in Table 2.10.

The accuracy of the spectral loss factor based on the APE, proposed by Williams et al. [174], cannot be compared to other SCFs due to the absence of specific

Year	Module	K_t and AM_a	$\varphi$and T_{mod}
		Error (%)	Error (%)
2006	mSi	0.9	0.6
	Tandem	0.9	1.3
	Triple	0.1	-0.8
2007	mSi	2.4	2.9
	Tandem	2.0	3.1
	Triple	1.8	1.4

Table 2.10: Output energy prediction errors for microcrystalline (mcSi), tandem, and triple-junction modules in 2006 and 2007 using 1) AM_a and K_t, and 2) APE and T_{mod} [4].

analysis of the loss factor in isolation from the other components of the proposed PV performance model. However, the use of the APE parameter is encouraged in this study and their PV performance model is reported to be accurate to within 7% of the measured performance. One limitation of the study, besides the absence of model coefficients for the spectral loss factor function, is the data collection period, which spans only the winter period from October 2002 to April 2003. This relatively short data collection period may limit the seasonal generalisability of the model. Finally, it may be argued that the time series analysis used is somewhat more complex than some of the simpler approaches, for example the polynomial parameterisation of $f(AM_a)$ or even two-variable surface parameterisation of $f(AM_a, W)$, without the accuracy being reported to justify it.

2.8 Summary and scope for further work

The solar spectrum is an environmental variable that has a non-negligible impact on the performance of all PV devices, including those with a broader and flatter spectral response range, such as mSi. The SCFs discussed in this chapter all use proxy variables to characterise the spectrum, primarily due the ease with which they can be calculated from measurements that are widespread in

the field or can easily be calculated. A summary of these SCFs and their key attributes is presented in Table 2.11.

The proxy-based SCF approach is based on the idea that in locations where one or two particular variables are responsible for the majority of variation in the solar spectrum, these variables can be used as proxy indicators of the prevailing spectrum. However, it will be shown in Chapters 5 and 6.5 that this simplification results in a significantly increased uncertainty in PV performance forecasts. Furthermore, the narrow selection of proxy variables hinders generalisability of such functions in environments where the relative dominance of the influences of different atmospheric or meteorological parameters on different PV technologies or on the spectrum in different locations may vary. An ideal SCF would be one with as few variables as possible containing the maximum amount of information on the dominant factors affecting the spectrum, whatever they may be.

One candidate parameter on which such an SCF could be based is the Average Photon Energy (APE). The APE provides a direct quantitative characterisation of the final spectral distribution once it has already been influenced by all of the relevant environmental parameters in the region under investigation, whether it be air mass, clouds, precipitable water content, or anything else. This is in contrast to the traditional approaches that take one or two factors that can influence the spectrum and then use them as proxies for the total spectral influence on PV output. By definition, the APE should contain information on all parameters affecting the spectrum as it is a numerical representation of a measured spectral distribution after the photons in that distribution have already been affected by all environmental phenomena. Although the APE has been used previously in analysis of the spectral effect on PV performance, a spectral correction function with publicly available model coefficients for a range of PV types has not yet been developed and validated.

One of the primary objectives of this project is to develop a new SCF based on the APE parameter and validate the proposed model using empirical data from two distinct climate regions and multiple PV panel technologies. Part of this validation procedure also includes a comparative analysis of the proposed SCF performance against that of other published SCFs. Chapter 3 presents the methodology behind this work to derive an APE SCF, $f(\varphi)$. Chapter 5 demonstrates and validates one APE-based approach using the APE parameter alone for a single location and PV technology. Chapter 6 builds on the work in Chapter 5 by exploring the application of $f(\varphi)$ for additional PV technologies and, based on an analysis of the uncertainty in the SCF, presents a modified approach that offers a significant improvement in accuracy and reliability. Throughout chapters 5 and 6, the accuracy of any approach proposed is compared with that of existing SCFs that have been published previously in the literature.

Refs.	PV index	Spectral index	Type	Model form	Data type	Coefficient availability
[220]	I_{scn}	AM_a	Single proxy	4^{th} polynomial	Field	Multiple
[152]	M	W	Single proxy	Exp1D	SMARTS+TMY simulation, field data	CdTe
[2, 1]	M	AM_a, W	Double proxy	Poly2D	SMARTS+TMY simulation, field data	CdTe, mSi, aSi-T
[3]	I_{scn}	AM_a, K_t	Double proxy	NL Poly2D	Field	mSi, CdTe
[47]	UF	AM_a, K_t	Double proxy	n/a	Field	n/a
[15]	M	AM_a, K_t	Double proxy	Power	Field	Multiple
[231, 230]	M	AM_a, W, AOD	Triple proxy	4^{th} polynomial+log	SMARTS, measured	Multiple
[133]	I_{scn}	AM_a, R_d	Double proxy	Piecewise	One week field	aSi
[180]	I_{scn}	φ	Single direct	4^{th} polynomial	One year field	aSi
[1]	I_{scn}	φ, ε	Double direct	Poly2D	One year field	CdTe, mSi, aSi-T

Table 2.11: Summary of the SCFs reviewed in this study.

Chapter 3

Methodology

3.1 Introduction

This chapter gives a description of the methods used to execute the project and the two test sites at which the meteorological stations and PV systems were deployed for the experiment. Grid-connected PV systems accounted for 99% of the worldwide installed PV capacity in 2015 [246], but stand-alone systems exist where the power generated from the module(s) is used directly to meet a specified load, for example water pumping, refrigeration systems, etc. In this study, the focus is the performance of a module under various meteorological conditions, and therefore a stand-alone system is adopted. In this case, the module performance can be measured in isolation from the grid and analysed with respect to the prevailing weather conditions. In this way, complex variables such as inverter performance are removed from the modelling analysis.

There are two test locations in this study. The first of these is Golden, which is in Colorado, USA. The data from this site are part of a publicly available dataset published by the National Renewable Energy Laboratory. The second location is at the University of Nottingham in Nottingham, United Kingdom,

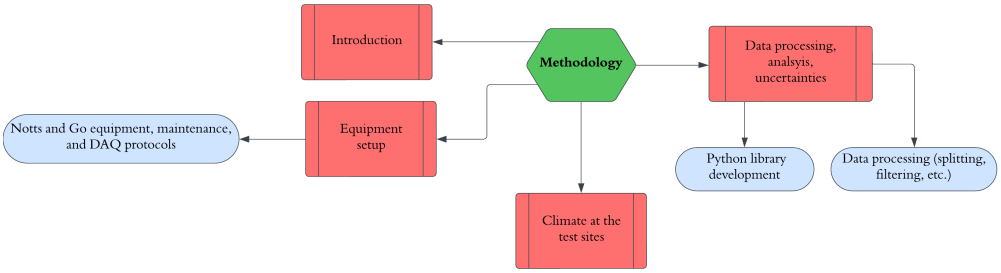

Figure 3.1: Structure of Chapter 3.

where a new test site has been built as part of this project. Conducting the investigations of this project at two locations with distinct climate characteristics enables a more rigorous investigation of the spectral influence on PV performance and how different models, including those which are developed in this project, perform in different climates.

The standard test conditions (STC) at which PV module performance is typically characterised by manufacturers (1000 $\mathrm{W\,m^{-2}}$, AM1.5G, 25°C) rarely occurs in field. At the Notts test site, the STC combination did not occur once. In fact, only around 5% of the entire one-year dataset had at least one of the three parameters to within 1% of its STC value. Therefore, characterisation in the field is an essential way to understand and analyse PV performance for practical applications. Nevertheless, STC performance metrics offer a useful way in which PV devices can be compared and their field performances contextualised against a baseline.

The following section in this chapter describes the equipment and data acquisition protocols used in the experiment to measure the prevailing environmental conditions and resultant PV performance. The data processing and analysis methods, including the uncertainty analysis, are then explained. Finally, the climatic conditions at each of the two test sites are analysed and compared to provide an environmental context through which the results of the main SCF analysis in this project may be analysed. Figure 3.1 summarises the structure of this chapter.

Figure 3.2: OTF at NREL in Golden, Colorado, USA [16].

3.2 Equipment and DAQ

In this section, the equipment set up and data acquisition (DAQ) protocols at each of the test sites ups are described. The site maintenance procedures undertaken to ensure reliability of the long-term measurements are also described.

3.2.1 Golden, Colorado, USA

The data used for the model development and validation in Chapters 5 and 6 are sourced from the National Renewable Energy Laboratory (NREL) in Golden, Colorado, USA. The PV performance and meteorological data are sourced from the NREL Outdoor Test Facility (OTF) [6], while the spectral irradiance (SI) data are sourced from the Measurement Instrumentation Data Centre at NREL [5]. Full descriptions of the test sites, measurement protocols, etc. are provided in the cited publications and, therefore, these details are only summarised here for completeness. An aeriel view of the OTF is presented in Figure 3.2.

A summary of the PV module specifications used in the investigations of this

Parameter	DUT			
	aSi	aSi-T	CdTe	mSi
Database identifier	aSi03038	aSiTriple28325	CdTe75669	mSi0251
I_{sc} (A)	0.7683	4.386	1.144	2.668
V_{oc} (V)	223.7	23.22	85.15	21.90
P_{mpp} (W)	101.45	58.67	65.77	43.88
$\alpha_{I_{sc}}$ (%°C^{-1})	0.001096	0.000981	0.00051	0.00057

Table 3.1: Technical specification and database identifier of the three DUTs as detailed in the NREL database [5, 6, 7].

Figure 3.3: PV panels being measured at the NREL OTF [17].

project are summarised in Table 3.1. The initial investigation to develop the APE SCF, $f(\varphi)$, focuses on an amorphous silicon PV device only as an example to demonstrate the method. Despite exhibiting a waning mainstream market share compared to crystalline silicon devices, aSi silicon devices are still particularly relevant for applications with a large future growth potential such as building integrated photovoltaics [247, 248, 249].

Table 3.2 summarises the parameters measured and the devices used to measure them at the Go test site. Figure 3.3 shows the physical set up of the PV panels at the OTF.

Parameter	Instrument
Wind speed/direction, precipitation, temperature, relative humidity, pressure	Vaisala WCT529 sensor
Plan-of-array irradiance	Kipp & Zonen CMP22 pyranometer
Datalogger	Campbell Scientific CR1000
Data Logger Communications	RAVEN XE-EVDO
PV module IV curve	Daystar MT5 multi-tracer
Module back surface temperature	Omega CO1-T Style I thermocouple

Table 3.2: Equipment at the Go test site.

3.2.2 Nottingham, United Kingdom

The test site based at the University of Nottingham in Nottingham, United Kingdom, was built for the purposes of this study and hence is described in more detail. First, the physical test rig is introduced. Second, the specific equipment used for the different measurements is introduced, followed by a summary of the measurement protocols.

Test rig

The test rig was built on the roof of the Energy Technologies Building, which is a research facility on the Jubilee Campus of the University of Nottingham. The elevation above sea level of the test rig is approximately 42 metres and the latitude and longitude coordinates are 52.9523, -1.1838. The high elevation of the roof with respect to its surroundings helps minimise shading by trees and surrounding buildings, especially during winter when the solar elevation is low. Such obstructions not only reduce irradiance levels, but can also change shift the solar spectrum due to their colour, façade construction, etc. as shown in Figure 3.4. Not all obstructions are avoided, for example, the 60-metre tall Aspire Sculpture on Jubilee Campus. Figure 3.4 shows the variation in broadband irradiance and APE on 22nd November 2021, which was a clear sky day. As the sun passes behind the sculpture, between an azimuth angle (γ_s)

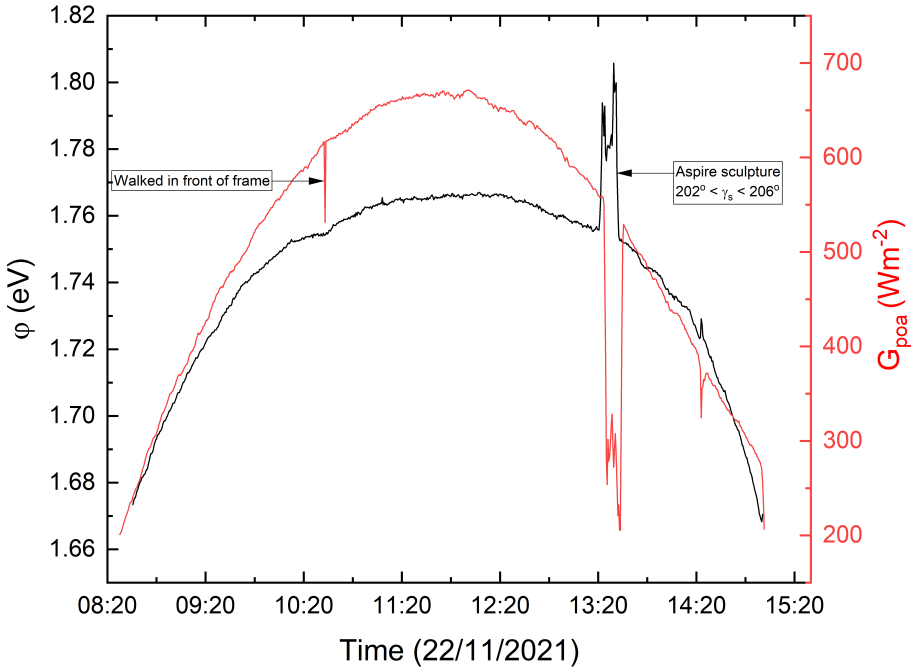

Figure 3.4: Effect of the Aspire sculpture on spectral and broadband irradiance measurements.

of 202° and 206°, the global plane-of-array irradiance drops, while the APE spikes.

For reference, the aspire sculpture is shown in Figure 3.5a. This image also shows the bare red frame that was present at the test site prior to this project. This frame was moved to the East side of the roof (rightwards in the image) into the vicinity of mains power supplies.

Another aspect of the test rig is the mounting for the PV devices and other meteorological sensors. PV modules in are typically tilted to maximise the collection of solar irradiance throughout the day [250] and minimise obstruction from buildings [251]. Many studies have investigated optimum tilt angles [252, 253, 254, 255, 256] for improving PV output. The key criteria for this investigation is that the measurements are consistent so, for example, the irradiance measurements are either made at or translated to the plane of the PV panel. A typical tilt angle for the United Kingdom is around 35° [257, 258] and this is the angle used for all PV panels and irradiance sensors. This is also

roughly in line with some simple rule of thumb calculations based on latitude-tilt relations [259, 260, 261].

Figure 3.5b is a photograph of the test rig. The tilt angle of the inclined plane is 35°. The silver enclosure contained within the red frame is use as ventilated housing for the IV-loads that form part of the EKO PV blocks system described in Section 3.2.2.

The final aspect of the test rig is a separate device used to control the AOI of affixed sensors and PV panels — a two-axis sun tracker. This sun tracker was assembled at the test site and was used in the IAM investigation described in Chapter 4. A mounting frame and mounting plates for the devices were designed in Rhinoceros 5 [262], the CAD model of which is shown in Figure 3.6a. The PV devices were mounted onto the frame using custom 3D printed brackets, an example of which for the mSi module is pictured in Figure 3.6b. The same design as that which is shown in Figure 3.6a is used for the fixed-plane test rig frame but with different dimensions. The centres of both frames (Figures 3.6a and 3.5b) are filled with aluminium struts that can easily be moved from left to right to accommodate different device sizes and mounting requirements.

PV performance measurement

The initial set up featured a Keithley 2420 source-measure unit (SMU) with two channels shared among the three PV devices (aSi, CdTe, and mSi) from November 2021 to May 2022. The system was upgraded after around eight months to an EKO PV blocks measurement system with six channels. Whereas the Keithley device operates on the basis of a four-quadrant power supply system, the EKO system is based on a set of variable resistors. A comprehensive review of the different types of IV measurement systems is presented in Ref.

(a) Bare frame on top of which the fixed-plane test rig was constructed. The Aspire sculpture is in the background.

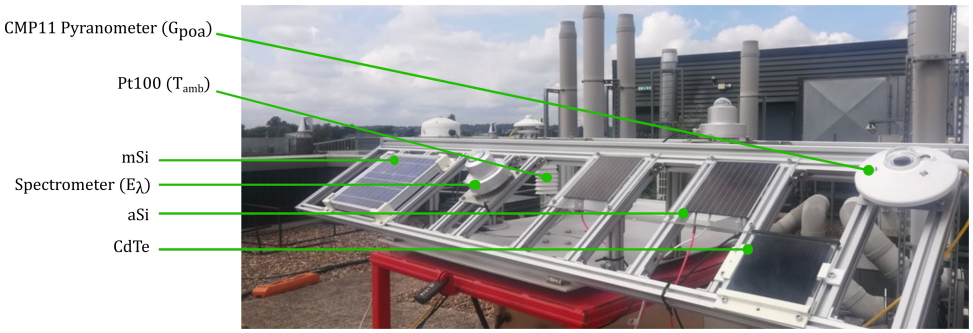

(b) Test rig for the PV devices and irradiance sensors on the inclined plane, and the PT100 T_{amb} sensor at the rear of the frame.

Figure 3.5

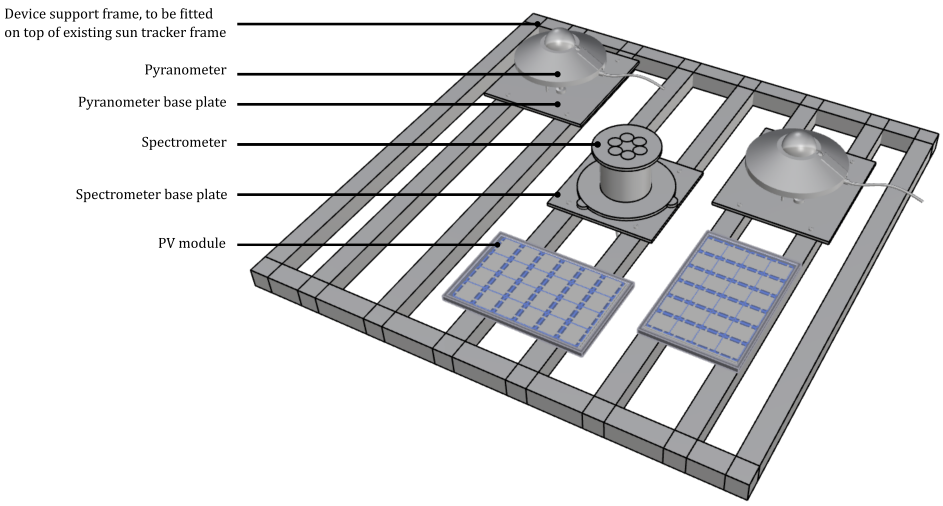

(a)

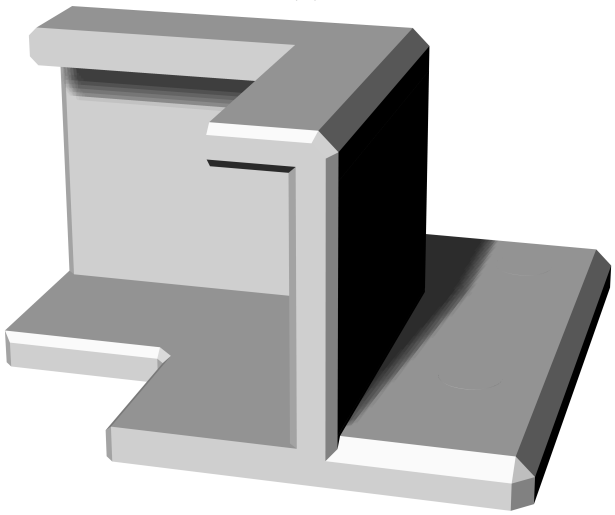

(b)

Figure 3.6: CAD models for the sun tracker frame (a) and the 3D-printed mSi PV device mounting bracket (b).

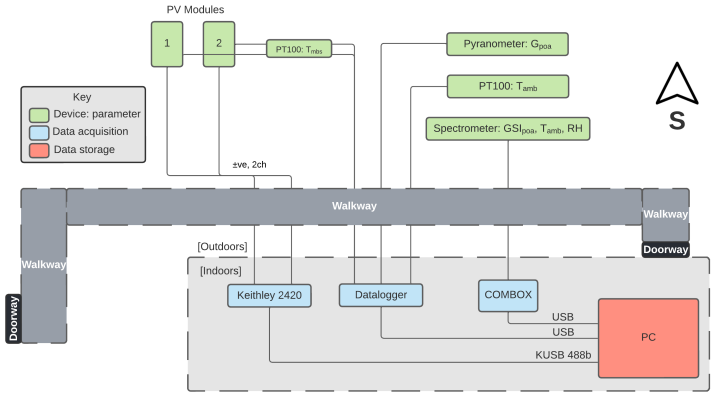

(a)

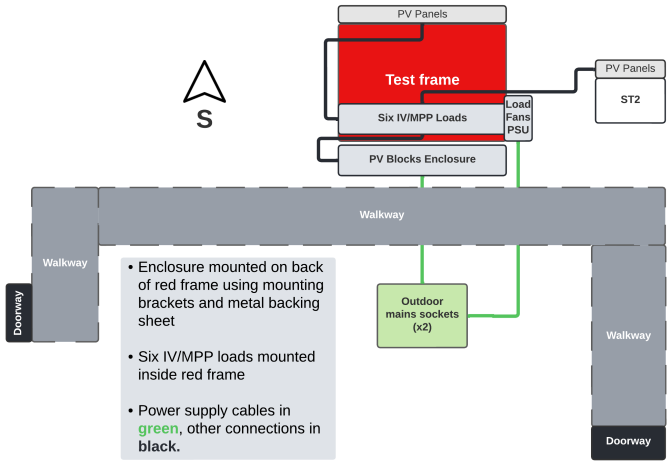

(b)

Figure 3.7: Outdoor testing arrangement. The EKO equipment shown in panel (b) replaced the Keithley PV measurement system shown in panel (a). All other devices and connections remained the same.

[263]. The layout of both systems is shown in Figure 3.7.

The Keithley 2420 SMU measures an IV curve by sourcing a programmed series of voltages at predefined time intervals to the PV device, and measuring the resultant current. On the other hand, the EKO equipment measures the device current at different voltages by dissipating the power output of the device through variable resistors within the "load" component of the set up. The main reason for changing the equipment was to increase the number of channels of the measurement system. Whereas the Keithley SMU only had two channels through which only sequential measurements were supported, the EKO system was set up with six channels capable of simultaneous measurements across

the different channels. Another benefit of the new system is its capacity to include non-PV measurement devices (such as pyranometers, spectrometers, temperature sensors, etc.) to the system via additional blocks (channels). All measurements can then be controlled, monitored, and recorded through one streamlined data acquisition system. Two disadvantages of the EKO measurement system are that the highest measurement frequency is one IV curve per minute; the load ratings are also relatively high compared to the PV device ratings, hence the sensitivity of the measurements is reduced. These aspects of the system are discussed in greater detail in Section 7.7 in the context of the data analysis and limitations of the test site.

All PV measurements were made using four-wire measurements to isolate the cable resistance from the measurement. 24 solar cables in total for the two PV measurement systems were cut to length, fitted with solar connectors, and trailed underground through conduit for protection against UV radiation, waterproofing, and electrical insulation. Solar connectors are used as they offer a low-resistance, waterproof, and safe method of connecting the PV panels to the measurement system. The Keithley system required the cables to lead to the SMU inside the building, so the eight cables (two channels each protected by separate conduit) were merged in a custom-made waterproof junction box and fed through a hole in the exterior building wall to reach the SMU. The EKO system required the cables to connect the panels to the load component, and then these loads were each connected to a measurement channel, and finally all channels were connected and controlled by the "PV Link" computer. The computer is powered by a power supply unit (PSU) connected to an outdoor mains power supply. A local area network connection was set up between the PV Link computer and a Windows PC located indoors in order to transfer data, which was done hourly under the control of a Python script. Although the loads are kept outside, mounted on a metal mounting plate, the PV Link computer and block channels were installed inside an enclosure and mounted

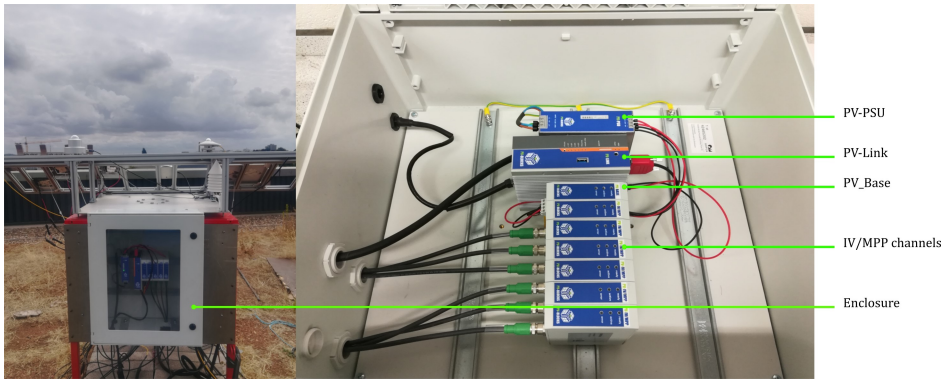

Figure 3.8: Set up of the PV Link computer, PSU, base, and IV/MPP measurement channels.

on DIN rails. The final component of the EKO system is a PSU for the cooling fans on the loads. This PSU is connected in chain to all of the loads and is used to power the fans contained in the loads, which operate only when overheating is detected. The enclosure is pictured in Figure 3.8. A schematic of the EKO equipment set up and wiring configuration is shown in Figure 3.7b.

Meteorological measurement and DAQ

A wide range of meteorological variables are measured at the test site. These are listed, along with their respective measurement device(s), in Table 3.3. The CMP10 pyranometer (serial number 211490) was mounted on an aluminium plate and levelled horizontally prior to affixing the mounting plate to the tilted frame. ISO 17025 device calibration was carried out by Kipp and Zonen in August 2021 and is valid for two years. The white sun screen on the device prevents external heating of the pyranometer housing, which could interfere with the measurement. The pyranometer operates on the principle of the Seebeck effect [264] whereby a voltage is induced by the temperature gradient within the thermopile inside the pyranometer.

The PT100 used for ambient air temperature measurement was mounted within a 3D printed Stevenson screen, pictured in Figure 3.9. The Stevenson screen

Figure 3.9: 3D printed Stevenson screen used to shield the PT100 sensor for the ambient air temperature measurement.

shades the sensor from sunlight and rainfall whilst still allowing air flow over the sensor so that the ambient air temperature can be measured. The PT100s used to measure the module back surface (MBS) temperature were attached to the module surface using lightly-adhesive reflective tape. The reflective tape prevents irradiance incident on the sensor from heating it and ensures that the temperature measurement is of the module back surface only. These sensors were checked regularly as it is not uncommon for such sensors to come loose or detach entirely from the module back surface [208]. All PT100s were calibrated by the manufacturer (Alphatemp Tech) at the time of order (2021).

The data acquisition system was set up to enable collection, sorting, and cloud synchronisation of the data. Remote access to the cloud storage was secured with Microsoft's two-factor authentication and only devices that had been manually authorised by the system administrator (the author) could access the remote network. The PT100 temperature sensors and CMP10 pyranometer were connected to a DataTaker DT85 Series 4 datalogger. The DT85 datalogger converts a voltage signal from the pyranometer, and a resistance signal from the PT100, to a reading in $\mathrm{W\,m^{-2}}$ and °C based on predefined conversion values. The timing of all measurements was synchronised to the University of Nottingham time server via the PC, which was connected to the university network.

The spectrometer was supplied with a Combox that serves the same purpose as the datalogger, powering the device and converting the measured channel

currents into a usable *.csv* data file. A total of nine channels measure the spectral irradiance at nine wavelengths, and a software package uses a model to estimate the full spectral irradiance measurement [265]. The spectrometer provides measurements of global plane-of-array spectral irradiance between 280 nm and 1100 nm, relative humidity, air pressure, and ambient air temperature. The measurement frequency for all measurements made by the spectrometer was also five seconds.

Parameter	Sensor	Measurement uncertainty
Ambient air temperature	PT100, Spectrafy SolarSIM-G	-
Module back surface temperature	PT100	1.9 °C
Global plane-of-array broadband irradiance	Kipp and Zonen CMP10	1.44
Global plane-of-array spectral irradiance	Spectrafy SolarSIM-G	5% per wavelength
Air pressure	Spectrafy SolarSIM-G	-
Relative humidity	Spectrafy SolarSIM-G	-

Table 3.3: Summary of the meteorological and MBS temperature measurements, and their respective sensors. The datalogger's voltage measurement uncertainty is 0.28% was added in the final calculations to measurements made using the datalogger to account for the voltage reading uncertainty.

Device	Parameter	Acquisition interval
Spectrafy SolarSIM-G	P, RH, $E_{\lambda,poa}$, T_{amb}	5s
Kipp and Zonen CMP10	G_{poa}	5s
PT100	T_{mbs}, T_{amb}	5s
Keithley 2420 SMU	I_{sc}	30s

Table 3.4: Summary of the measurements made at the outdoor test site.

Device	Function
DT-85 datalogger	Data acquisition
Conduit	UV, water, etc. protection
MC4 connectors	PV↔cable and cable↔DAQ connections
Class 5 tinned copper cable	All PV↔ system cabling

Table 3.5: Additional summary of key equipment at the outdoor test site.

Summary of equipment and protocols

Table 3.4 presents a full summary of all measurement devices used in the outdoor experiment campaign, the parameters they measure, the measurement frequency, and any additional notes about the devices or measurement. Table 3.5 is an extended summary of the equipment used that includes non-measurement devices such as the DAQ equipment, such as the datalogger, and system peripherals such as cables.

Site maintenance

An online spreadsheet was created to to log the access to the roof by any person. The PV devices and irradiance sensors were cleaned daily to mitigate the effects of soiling and increase the reliability of the long-term measurements [266, 267]. Soiling is known to decrease performance by up to 40% in extreme cases [268, 269] and cleaning protocols are therefore an essential part of long-term site maintenance [270]. Another benefit of regular cleaning is to remove dew and water droplets, which can shade the devices, shift the incident spectrum, as well as lead to the cementation of dust soiling [271]. During the winter,

Figure 3.10: Example dust soiling on the measurement devices.

periods of snow also resulted in full coverage of the measurement devices. During periods of severe icing, the ice was left to melt naturally so as to protect the fragile surface of the modules from potentially abrasive deicing methods. Measurements during these periods of extreme weather were discarded from the dataset due to the near-zero irradiance measurements. Figures 3.10, 3.11, and 3.12 show examples of water, dust and snow deposits covering the irradiance sensor glass domes and the PV panel surfaces.

3.3 Data processing and analysis

The NREL data used in Chapters 5 and 6 are published in a processed format. A few small data processing measures were applied to the NREL data. A more rigorous processing procedure is applied to the raw data measured in

Figure 3.11: Example water droplet coverage on the measurement devices.

Figure 3.12: Example snow coverage of the measurement devices.

Filter action	Explanation
Irradiance >200 W m^{-2}	Reduce noise but retain overcast conditions
Time 0800h–1600h	Retain daylight hours only
Manual I_{scn}	Example: $I_{scn,CdTe} = 0.17$, all other $I_{scn} > 0.8$

Table 3.6: Additional data processing measures undertaken for the NREL data measured in Golden, Colorado, USA. The $I_{scn} = 0.17$ example point occurred on 2013-01-02 at 1045h.

the UK to bring it to the level of the NREL data and ensure consistency in the analysis. A full description of the data processing and analysis methods applied to both datasets is presented in this section. In addition, some of the algorithms developed in Python for the data analysis, as well as the surface fitting and uncertainty analysis calculations, are introduced and explained.

3.3.1 Data processing

All details of the Golden (Go) site, including data measurement and processing, are explained in the database's associated publications [5, 6, 7]. The Go E_λ data have a one-minute resolution between the hours of approximately 0600h and 1800h, while the PV and meteorological (PVM) data have a fifteen-minute resolution between similar hours. A subset of these data between the hours of 0800h and 1600h was extracted to ensure a focus on daylight hours only. In total, around 200,000 spectral distributions and 11,000 PVM measurements were obtained. Measurements obtained under conditions with less than 200 W m^{-2} were omitted to reduce noise whilst still retaining measurements made in heavily overcast conditions [141, 73]. Some measurements were missing from the different datasets due to external factors such as instrument downtime. Therefore, only measurements of one parameter for which there existed a concurrent measurement of all other required parameters were retained. After processing, a final dataset of approximately 6,300 measurements of each parameter was used. These data processing actions are summarised in Table 3.6.

For the Notts test site data, a simpler data processing methodology was adopted. The goal was to achieve in one procedure the same combined effect the steps adopted by the authors of the NREL dataset and those taken in this thesis. The approach adopted is an irradiance regression threshold filter. The relationship between irradiance and current is known to be linear, hence this can be used to identify anomalous data [272, 273, 274]. I_{sc} is normalised for the effects of temperature and angle of incidence to give I^*_{sc}, which is plotted against G_{poa}. A linear function is fitted to the data and a tolerance of 30% either side of the regression curve is used to filter out anomalous data. This tolerance level is consistent with previous studies [275] and the expected magnitude of spectral variations unaccounted for in the normalisation of I_{sc}, which is addressed in this study through the development of an SCF. The filtering analysis is presented in Figure 3.13 for the aSi, CdTe, and mSi modules. This single process achieves the same effect as the other steps whereby I_{sc} measurements under very low irradiance conditions, rapidly changing irradiance conditions, or other non-physical readings, are filtered out. The normalisation procedure to calculate I^*_{sc} is as follows:

$$I^*_{sc} = \frac{I_{sc}}{1 + \hat{\alpha}_{I_{sc}}(T_c - T_r)} \cdot f(\theta), \tag{3.1}$$

where $f(\theta)$ is a fifth order polynomial angular of incidence correction function, the coefficients of which were determined following the procedure described in the following Chapter. The temperature coefficient, $\alpha_{I_{sc}}$, for the aSi and CdTe devices was determined following the procedure described in Chapter 4. For the mSi device, the commonly reported value of $0.005°C^{-1}$ was used [223].

Just as with the NREL data, some manual filtering is used with the UK data. For example, unrealistic values of I_{sc}, such as those that exceeded I_{sc0} under low levels of irradiance, or near-zero measurements under sunny conditions, were

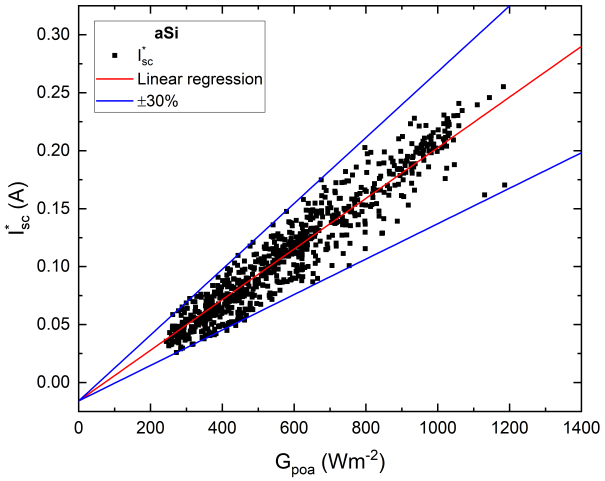

(a)

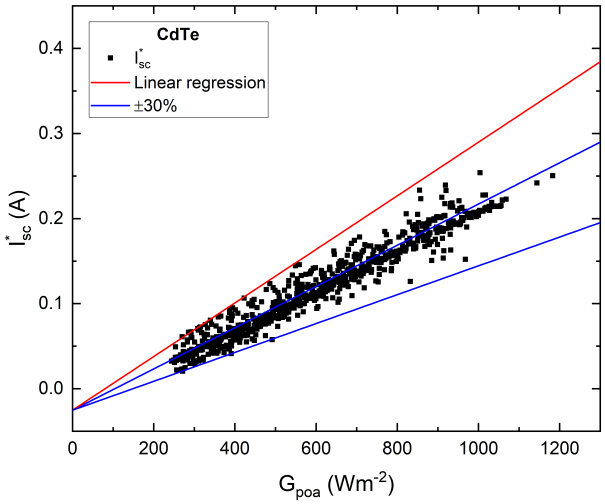

(b)

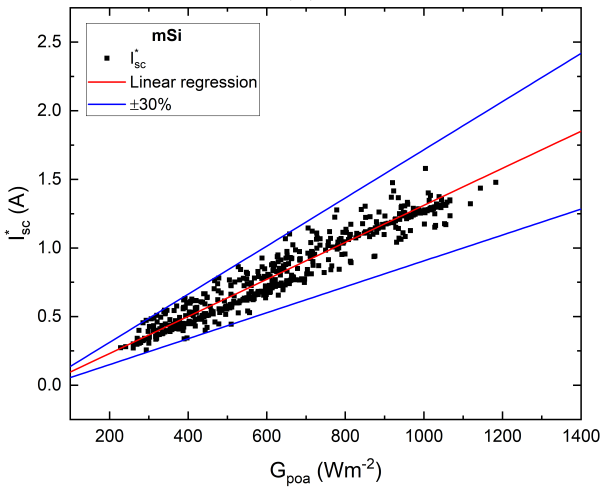

(c)

Figure 3.13: Data filtering process using the linear regression method for the aSi (a), CdTe (b), and mSi (c) devices deployed at the Notts test site.

filtered from the dataset manually. The causes of some of these readings are not related to the investigation, hence the removal of these points is justified. For example, excessive reflection, directed only at certain devices, from surrounding metallic objects under specific irradiance and AOI conditions could lead to the aforementioned type of unrealistic measurement. Another potential cause is partial shading [276], which could result from atmospheric debris, soiling, and the site-specific issue of bird flyovers. Birds that had made nests around the ventilation units on the building roof would frequently fly over, circle, and sometimes land on the test rig.

Resampling the data is the final data processing operation. The UK data were resampled to a fifteen-minute time interval to match that of the NREL data and enable a comparison between the results from the two test sites. The resampling improves the reliability of the data by smoothing out uncertainty that can arise from the different response times of the devices to rapid changes in meteorological conditions.

3.3.2 Splitting the dataset

In Chapters 5, 6, and 7 the dataset is divided into two parts — a model development subset and a model validation subset. In doing so, it is essential to maintain sufficient data in both sets to ensure they are representative of real operating conditions [277, 278, 279]. In this project, two methods are adopted. In the first, the data in Chapter 5 are divided based on a time series variation in average photon energy throughout the year, whereby it is ensured that the full range of APE that occurs during the year is present in both datasets. This is a fast and simple approach made possible by the symmetrical nature of the annual APE variation. The method is validated through a statistical comparison of regression coefficients derived for the full-year dataset and subset is made to ensure the former is representative of the latter and is not likely to result in

over– or under-fitting of the data. This was the first approach developed and published in Ref. [180]. An alternative approach was adopted in Chapters 6 and 7. Due to the asymmetrical and noisier nature of the annual climatic conditions at the Nottingham test site, the one-year dataset was sorted chronologically and sliced at a ratio of 2:1 to form the model development and validation datasets. This means that for every three measurements of the required parameters (SI, G_{poa}, I_{sc}, etc.), one was extracted to form the model validation dataset while the remaining two were retained for the model development. The advantage of this method is that data from every month of the full year are used in each of the two datasets, but a suitable split between the model development (larger) and validation (smaller) datasets is still achieved. This method was backtested on the data used in Ref. [180] and the same conclusions regarding the benefits of the proposed APE-based SCF were found.

3.3.3 Python library

The data processing protocols were implemented in Python. Two Python function libraries were developed, one of which contains functions for specific test site-related operations, while the other was for general data analysis operations. An example of the former is the function to read the spectral irradiance files, which are stored as a single *.csv* file per measurement, contained within a subfolder for the day of the year. Reading these data requires Python to import every *.csv* file from every subfolder, concatenate all of the E_λ data into a single dataframe, and append the measurement date and time (contained in the filename) to the series header of the respective E_λ measurement. It is also necessary to append the wavelength data to the final dataframe as these data are not included in the measured data because doing so would unnecessarily increase the size of the data files with repeated wavelength information. An example of a general data processing function is the calculation of the average

photon energy. This is a more generalised function that can work with any spectral irradiance file provided certain criteria, not specific to the UK test site datasets, are met. For example, wavelengths must be specified alongside their irradiances. The function includes a range of conditional IF statements to ensure that these requirements are met and, if not, messages to the user that describe the issue are printed. These two function libraries work together and, as an example, a flow chart illustrating the calculation of APE values following the import of the E_λ files measured at the test site is presented in Figure 3.14. The blue squares represent functions, within which multiple operations take place. The square on the left is the UK site-specific function to read the E_λ files as generated by the SolarSIM-G on the UK test site, while the two blue squares on the right are general functions to calculate the APE values (upper blue square) and resample the data (lower blue square).

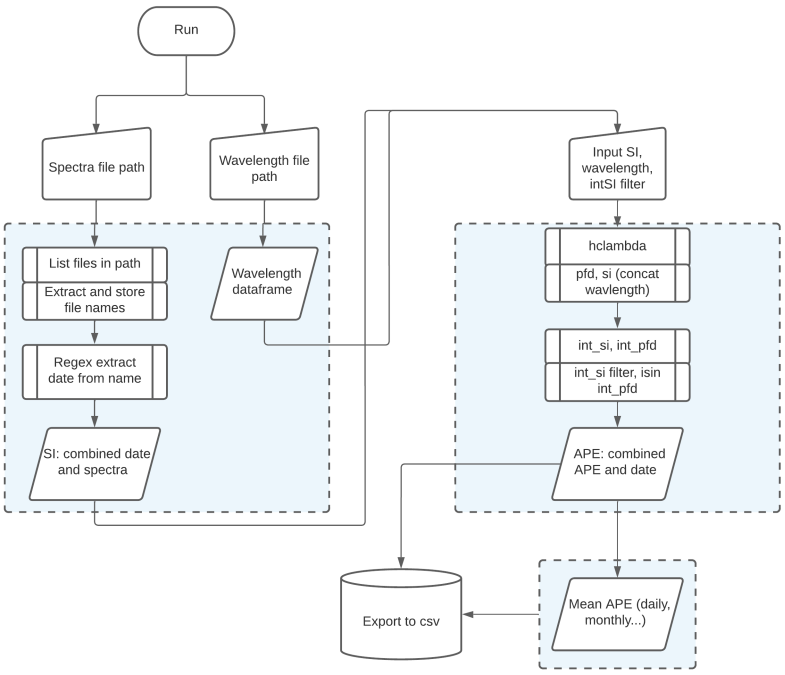

Figure 3.14: Steps to import and process E_λ files measured at the UK test site and their respective APE values. These steps were implemented in Python. `hclambda`, `int_si`, `int_pfd`, etc. refer to different variables associated with the APE calculation process. `isin`, `concat`, etc. refer to various functions used in the calculation process.

3.4 Uncertainty analysis and fitting

The methodology for determining the uncertainties on all of the measured parameters for the NREL dataset is explained in detail in Appendix B of the NREL database's associated user's manual [6]. At the UK test site, similar procedures are adopted but with some differences due to the different levels of information availability and differences in the device set up.

For the Notts test site, the dominant measurement uncertainties arise from those of the temperature, irradiance, and angle (for the AOI testing), and short-circuit current. For the temperature, the 1.9°C error is adopted from [6]. The irradiance uncertainty is based a combination of the pyranometer sensitivity (1.44%) and the voltage measurement sensitivity of the datalogger (0.28%). The angle of incidence uncertainty is set as 1° based on the resolution with which the sun tracker could be controlled. Finally, the uncertainty in the I_{sc} measurements are set as 0.28% based on the Keithley SMU. It was assumed the sensitivity of the EKO IV tracer would be lower due to its inability to set the current range automatically based on the DUT, but this 0.28% value was not increased for the EKO data analysis because any increase would have had to have been determined arbitrarily. This is likely to have led to an underestimate in the overall uncertainty of I_{sc}.

The uncertainty values on each variable are propagated through to the calculated variables using either a simple calculus-based approximation or a functional approach, depending on the complexity of the function, as described in Ref. [280]. The general equations for each of these approaches are set out as follows:

Calculus-based approach:

$$\alpha_Z^2 = \left(\frac{\partial Z}{\partial A}\right)(\alpha_A^2) + \left(\frac{\partial Z}{\partial B}\right)(\alpha_B^2) + \left(\frac{\partial Z}{\partial C}\right)(\alpha_C^2) + ... \tag{3.2}$$

Functional approach:

$$\alpha_Z^2 = (\alpha_Z^A)^2 + (\alpha_Z^B)^2 + (\alpha_Z^C)^2 + ..., \tag{3.3}$$

where:

$$\begin{aligned}\alpha_Z^2 = &\left[f\left(\bar{A}+\alpha_A, \bar{B}, \bar{C}, ...\right) - f\left(\bar{A}, \bar{B}, \bar{C}, ...\right)\right]^2 \\ &+ \left[f\left(\bar{A}, \bar{B}+\alpha_B, \bar{C}, ...\right) - f\left(\bar{A}, \bar{B}, \bar{C}, ...\right)\right]^2 \\ &+ \left[f\left(\bar{A}, \bar{B}+\bar{C}+\alpha_C, ...\right) - f\left(\bar{A}, \bar{B}, \bar{C}, ...\right)\right]^2\end{aligned} \tag{3.4}$$

where α_Z is the uncertainty in the variable Z, and Z is a function of variables A, B, C, etc. The best estimate of Z is $\bar{Z} = f(\bar{A}, \bar{B}, \bar{C}...)$.

The final error bars generated are used to apply an instrumental weighting to each data point in the fitting procedure for all graphs. For the non-linear curve fits, the Levenberg-Marquardt iteration algorithm is used [281].

3.5 Climate conditions at the test sites

In this section, the climates of the OTF at NREL in Golden (Go), and the test site at the University of Nottingham in Nottingham (Notts), are introduced. This provides some context for the analysis in the remainder of this thesis. In Chapters 5 and 6, data from the Go site are used for analysis. In Chapter 7, the application of the proposed SCFs is investigated at the Notts test site, and the results are compared with those of the Go site. A range of environmental variables are used here to describe the climate conditions at the test site. In terms of the spectrum, parameters such as APE indicate changes in the spectral irradiance, with higher values representing blue-shifted spectra and lower values representing red-shifted spectra [167]. Parameters such as AM_a, K_t, and W are

measures of environmental variables that influence the spectrum by changing how and by how much the incident spectral irradiance is scattered [47, 152, 220]. Meteorological parameters such as temperature and irradiance are simple representations of the prevailing climate conditions that are also responsible for changes in PV performance [42].

3.5.1 Golden, Colorado, USA

The test site is at an elevation above sea level of approximately 1800 m. The monthly variation in irradiance and ambient temperature at the site are shown in Figure 3.16. The climate is a typical mild-to-cold winter (mean temperature 10 °C) and warm–hot summer (mean temperature 30 °C). The monthly mean irradiance on the plane of the PV test array varies between approximately 600 $\mathrm{W\,m^{-2}}$ and 700 $\mathrm{W\,m^{-2}}$ throughout the year between 0800h and 1600h.

Figure 3.15 presents the variation in the monthly mean values of several meteorological parameters related to the spectrum, namely AM_a (a), APE (b), W (c), and AOD at 500 nm (d). Meanwhile, Figure 3.16 presents the annual variation in G_{poa} and the ambient air temperature, T_{amb}. The air mass follows a seasonal sinusoidal trend that is dictated by the change in solar elevation over the course of one year, which is as expected. Atmospheric water vapour follows a similar but inverted sinusoidal pattern, which is similar to that of the annual ambient air temperature variation. Increased temperatures in the summer lead to increased surface water evaporation and the greater capacity of warmer air to hold moisture [282, 283] The range of these parameters is between around 1.0–2.5 and 0.5–2.0 cm, which are typical of this region. The AOD levels break the sinusoidal trend with an atypical spike in April. Historical weather data from a variety of meteorological stations and airports, compiled in Ref. [284], report unstable conditions during April of 2013. Most days during this period featured one or a combination of rainfall, haze, and dust. The latter two in

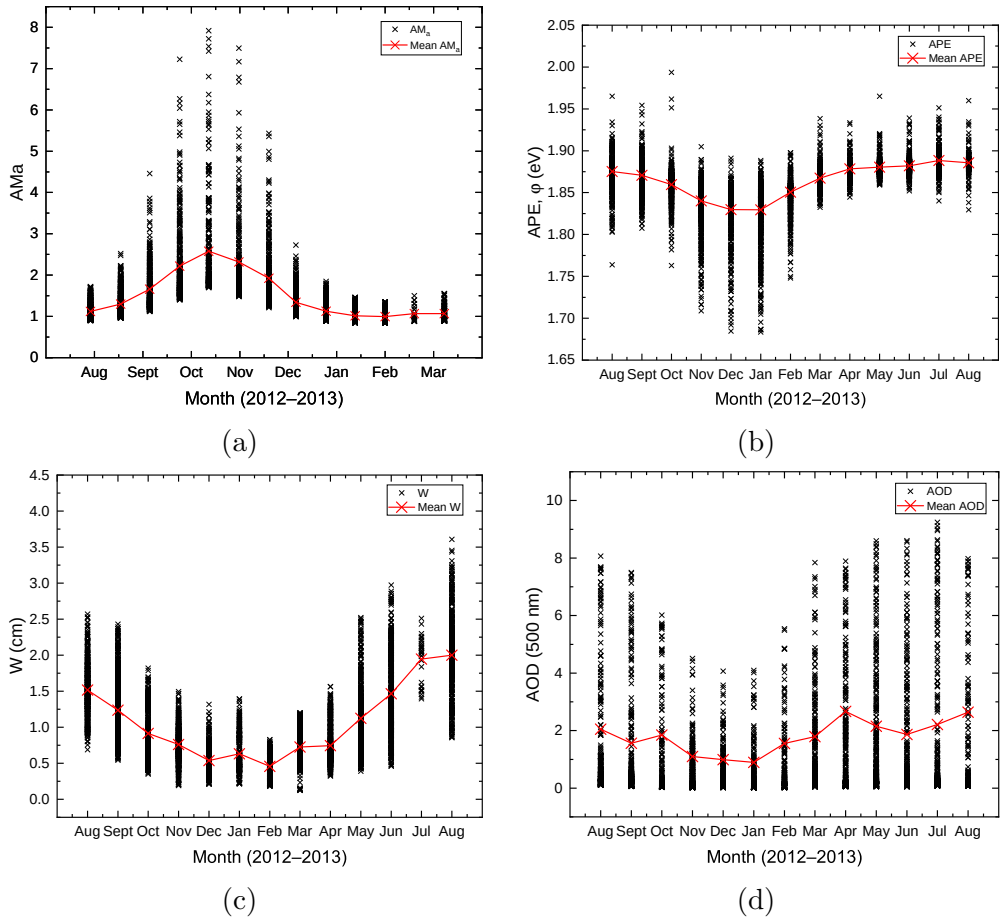

Figure 3.15: Annual variation in four spectral parameters at the OTF in Golden, Colorado. In order from a–d these are AM_a, φ, W, and AOD at 500nm. Each black cross represents the daily mean value for each parameter, while the red line-cross trend indicates the monthly mean value.

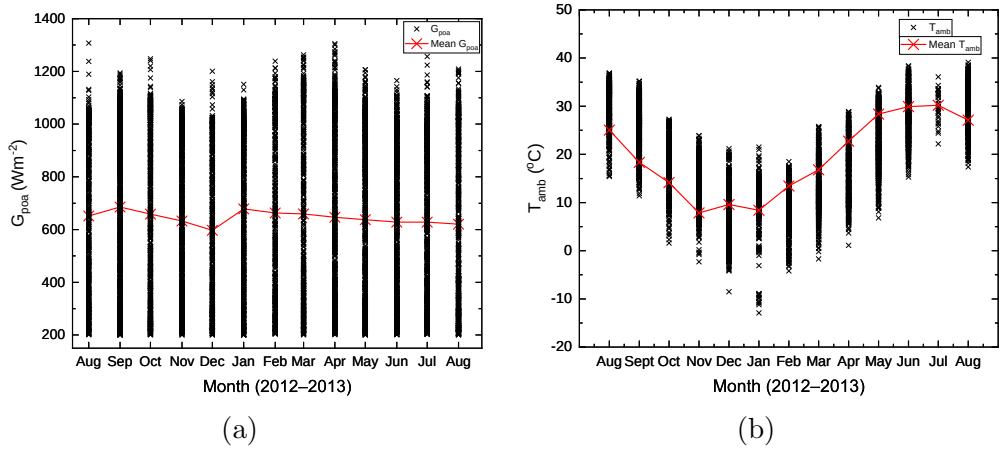

Figure 3.16: Annual variation in the global POA irradiance and the ambient air temperature at the OTF in Golden, Colorado. Each black cross represents the daily mean value for each parameter, while the red line-cross trend indicates the monthly mean value.

particular may have contributed to the increase in aerosol optical depth during the month of April 2013.

Figure 3.16b shows the annual variation in APE at the OTF. The variation in APE also exhibits a sinusoidal pattern with a decrease in the winter months relative to the summer months. For reference, between 350–1050 nm, $\varphi = 1.88$eV for AM1.5 [285]. Relative to the AM1.5 reference spectrum, the summer months tend to experience slightly blue-shifted spectra, on average, while the winter months tend to experience red-shifted spectra. This red shift in winter results from shorter-wavelength radiation being more strongly affected by Raleigh scattering when the solar elevation is lower. This pattern is in line with the trends observed in Figure 3.15 where atmospheric variables that result in greater scattering of longer-wavelength light, resulting in a blue-shifted spectrum, are more prevalent in summer months, during which time the solar elevation (air mass) is also higher (lower).

3.5.2 Nottingham, UK

The overall climatic conditions at the Nottingham test site are described in this section. The meteorological data plotted in Figure 3.17 are broadly indicative of a warm summer and cold winter climate. The atmospheric precipitable water content levels are relatively low in comparison to the global average (2.16 cm [286]) and USA average (1.75 cm [287]). The air mass and APE plots in Figures 3.17a and 3.17b follow a parabolic trend with a peak in the winter for the former and in the summer for the latter. In terms of air mass, the lower solar elevation in the winter increases the path length of light, and therefore the air mass. This increase in path length typically leads to an increase in the scattering of shorter-wavelength radiation, known as Raleigh scattering, thus decreasing the average APE value at this time of the year. Although less distinct, the trend in K_t over the year appears to follow that of the average photon energy, which

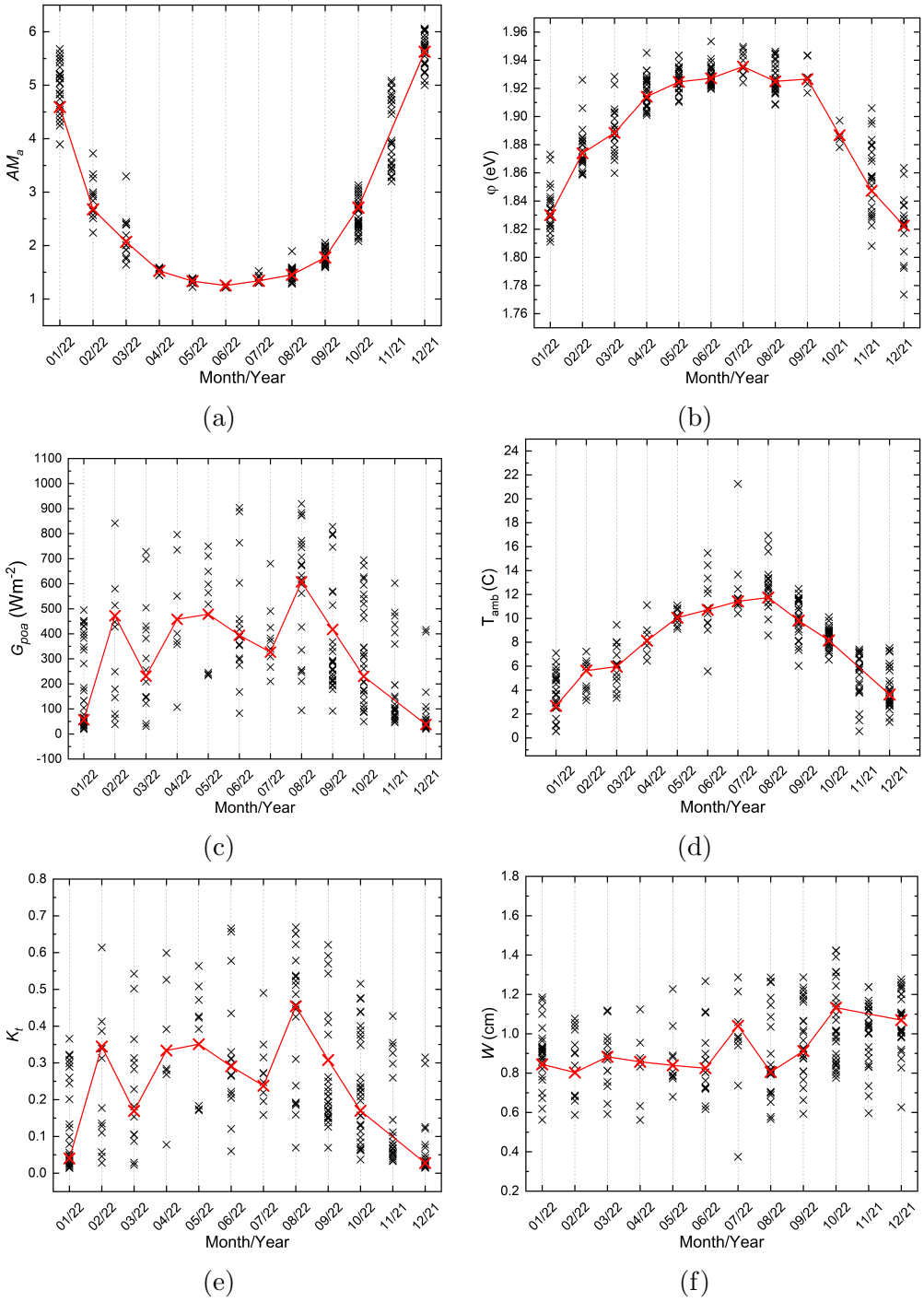

Figure 3.17: Annual variation in several key meteorological parameters in Nottingham, UK. Scatter points show the daily median for each day of the month while the line shows the monthly median. For the month of November in all Figures except 3.17b, a mean of November 2021 and November 2022 is plotted. The daily averages for both years are plotted for the month of November in these figures. In figure 3.17b, only data from 2021 are available for November, hence only data from this year are plotted.

could indicate that cloud cover is one of the dominant factors influencing the solar spectrum throughout the year. Another characteristic of the K_t data is that the daily average K_t rarely exceeds 0.6. This is not to say that there were never clear skies at the test site during the measurement period, but that such days are few and far between. Furthermore, the high frequency of daily mean K_t values between 0.2 and 0.4 suggests that partially overcast skies are a cloud cover pattern that are a frequent occurrence at the test site. The daily and monthly average K_t values in Figure 3.17e are therefore biased by low K_t values on partially cloudy days, which brings down the overall K_t average even on days where there are periods of high irradiance.

3.5.3 Climate comparison

Weather data from multiple weather stations around each of the two locations investigated in this study — Golden (Colorado) and Nottingham (UK) — are presented in this section. This section provides a broad comparison between the two areas where the test sites are located.

Figures 3.16 and 3.17 show that the temperature and irradiance conditions are lower at the Notts site than at the Go site. In terms of the spectral irradiance conditions, there is a notable shift towards not only higher average photon energy values, but also a greater range of APE values, at the Notts site. This could have implications for the thin film PV devices considering their relatively narrow spectral response that is concentrated at shorter wavelengths. The cause of these spectral irradiance conditions is investigated in more detail in Chapter 7, but the annual variation in K_t at each of the test sites suggests that cloud cover may be responsible. At the Go site, there is a high frequency of days with K_t>0.6, and the mean clearness level is relatively stable throughout the year residing at just over 0.6. On the other hand, at the Notts site the monthly mean K_t only exceeds 0.4 in one month of the year — August —

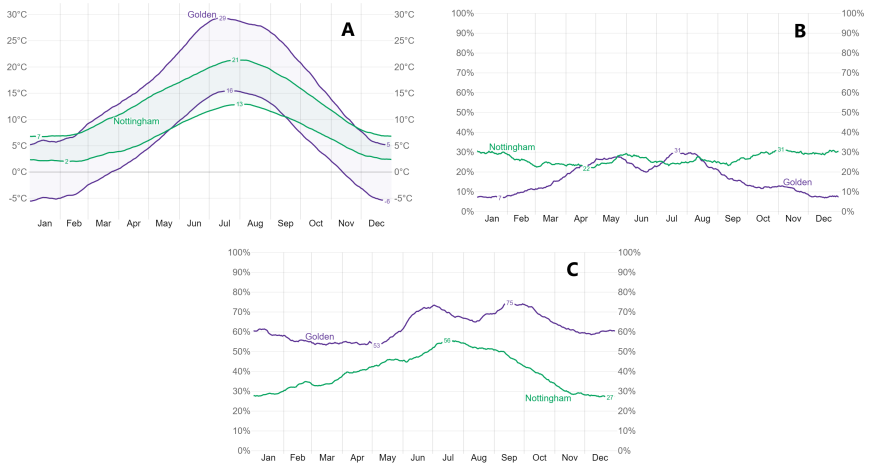

Figure 3.18: Annual climate data comparison between Golden and Nottingham [18]. Panels A, B, and C, show the average monthly minimum and maximum temperature, daily chance of precipitation, and the chance of clear skies, respectively.

while remaining below 0.4 in all other months. The annual variation in K_t also exhibits a strong seasonal trend, with clearer days in the summer, which is in contrast to the relatively stable cloud cover conditions throughout the year at the Go test site.

Data from Ref. [18] also support the discussion so far. The three panels, A, B, and C in Figure 3.18 show the average monthly minimum and maximum temperatures, daily chance of precipitation, and the chance of clear skies, respectively. The average temperatures are for two metres above the ground; the chance of clear skies is defined as the percentage of time the sky is clear, mostly clear, or partly cloudy (<60% of the sky is covered by clouds); and the daily chance of precipitation is defined as the percentage of days in which precipitation is observed, excluding trace quantities. Figure 3.18 shows that the climate in Golden is generally warmer in the summer and colder in the winter, drier all year round, and has a greater prevalence of clear skies.

The difference in cloud cover is the most important distinction between these two test sites and its relevance to the spectrum has been reported in the literature for several decades [288, 289]. As clouds are formed of water droplets

or ice crystals, radiation is scattered when passing through them. This has a particular effect on UV radiation at the shorter-wavelength end of the solar spectrum. Increased scattering can lead to an enhancement in ground-level UV radiation [290, 291, 292, 293]. However, cloud cover can also lead to the attenuation of global UV reaching the ground, with a 25–30% reduction in the annual mean UV dose relative to the dose received in clear-sky conditions being reported in New Zealand [294, 295]. The attenuation (or enhancement) resulting from clouds is related to their physical properties such as cloud amount, thickness, type, height, position relative to the sun, etc. [137]. The relationship between cloud cover and the solar spectrum has implications for PV device performance in the field [296], with technologies such as hydrogenated amorphous silicon (aSi:H) exhibiting performance fluctuations of ±10% as a result of cloud-induced spectral variation [141]. Other studies have also reported on the importance of the effect of clouds on the spectrum, and hence the performance of aSi [47] and cSi [73] PV devices.

The effects of cloud cover on the spectrum are visualised in Figure 3.19, where panel 3.19b shows the clear sky spectrum while panel 3.19a shows the cloudy sky spectrum. These data are sourced from the NREL spectral solar radiation database [297]. Each spectral distribution is divided into 13 40 nm wavebands of spectral irradiance. The percentage contribution to the total irradiance (PCTTI) for each waveband is calculated as follows:

$$\text{PCTTI}(\%) = \frac{\int_a^b E_\lambda d\lambda}{\int_c^d E_\lambda d_\lambda} \cdot 100\%, \tag{3.5}$$

An example (band 4) is highlighted on Figure 3.19b; the percentage contribution of band 4 to the total irradiance for the clear sky day is:

$$\text{PCTTI}_{Band4}(\%) = \frac{\int_{480}^{560} E_\lambda d\lambda}{\int_{300}^{1080} E_\lambda d_\lambda} \cdot 100\% = 12.61\%. \tag{3.6}$$

The PCTTIs for each waveband on each day are summarised in Tables 3.7 and 3.8. These percentags are plotted in Figure 3.19c. This analysis shows that, on cloudy days, the shorter wavelength irradiance contributes more to the total irradiance than the longer wavelength irradiance. The level of blue shift in the spectrum can be quantified by the APE, which is 0.06 eV higher on the cloudy day compared with the clear day.

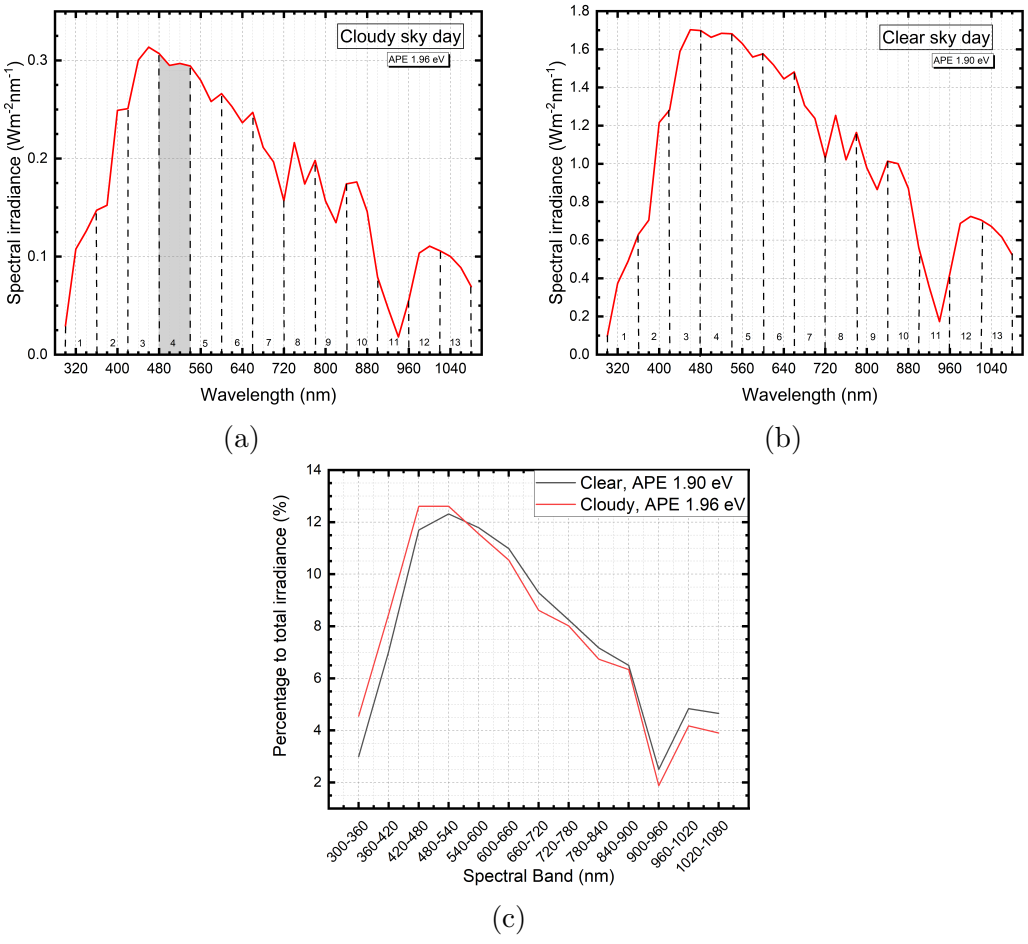

Figure 3.19: Spectral distributions on clear and cloudy days. The percentage contributions of the 13 spectral bands are shown in Tables 3.7 and 3.8.

Spectral Band (nm)	Irradiance ($W\,m^{-2}$)	PCTTI (%)
1. 300-360	6.439	4.55
2. 360-420	12.010	8.48
3. 420-480	17.857	12.61
4. 480-540	17.849	12.61
5. 540-600	16.36	11.55
6. 600-660	14.919	10.54
7. 660-720	12.196	8.61
8. 720-780	11.353	8.02
9. 780-840	9.546	6.74
10. 840-900	8.973	6.34
11. 900-960	2.658	1.88
12. 960-1020	5.901	4.17
13. 1020-1080	5.528	3.90

Table 3.7: Irradiance in each of 13 spectral bands and their respective percentage contribution to the total irradiance of the single measured spectral distribution on a cloudy sky day.

Spectral Band (nm)	Irradiance ($W\,m^{-2}$)	PCTTI (%)
1. 300-360	24.526	2.998
2. 360-420	57.553	7.036
3. 420-480	95.643	11.692
4. 480-540	100.725	12.313
5. 540-600	96.372	11.781
6. 600-660	89.853	10.984
7. 660-720	75.995	9.290
8. 720-780	67.438	8.244
9. 780-840	58.659	7.170
10. 840-900	53.202	6.503
11. 900-960	20.466	2.501
12. 960-1020	39.546	4.834
13. 1020-1080	38.031	4.649

Table 3.8: Irradiance in each of 13 spectral bands and their respective percentage contribution to the total irradiance of the single measured spectral distribution on a clear sky day.

3.6 Summary

The equipment and data acquisition processes at two test sites — Golden (USA) and Nottingham (UK) — have been introduced in this section. The former is part of an external project that has generated publicly available data while the latter was built at the University of Nottingham for this investigation and will remain in operation for future research. One year of meteorological and PV performance data from each of the two test sites has been measured for the purpose of developing and validating a new spectral correction methodology that is based on the use of the average photon energy and the depth of a spectral band to characterise the prevailing spectral irradiance conditions. The climates at the two test sites have been shown to be substantially different, primarily in terms of the levels of cloud cover, which provides an opportunity for more rigorous validation of the proposed method. The data analysis methods used to achieve the aforementioned goal of developing and validating a new SCF have also been introduced.

In the following chapter, the STC performance characteristics of the PV devices deployed at the Notts test site are derived using the outdoor measurements. This includes, mainly, the IAM function and the reference short-circuit current. Chapters 5, 6, and 7 then use the Go data to demonstrate the proposed APE method, advance the single-variable method through the inclusion of an additional parameter in the model, and then investigate the applicability of the method in a secondary climate — Notts, UK.

Chapter 4

UK PV device characterisation

4.1 Introduction

In this chapter, some of the results from the test site are used to determine the STC performance characteristics of the UK PV devices. These characteristics are used in the analysis in Chapter 7. In addition, the results of simple validation test of the EKO equipment is presented. For all three devices, I_{sc0} was determined outdoors. For the aSi and CdTe devices, $\alpha_{I_{sc}}$ was determined indoors. Figure 4.1 summarises the content of this chapter.

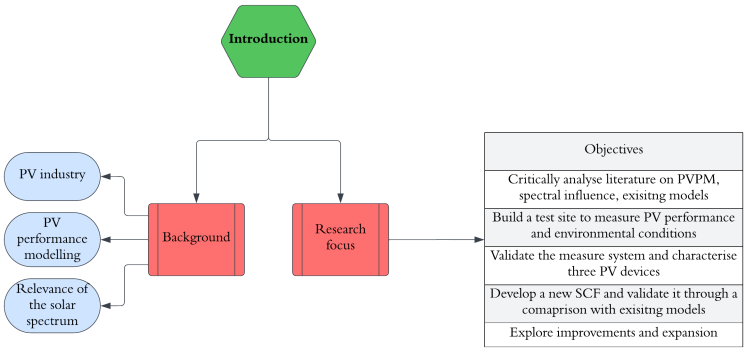

Figure 4.1: Structure of Chapter 1.

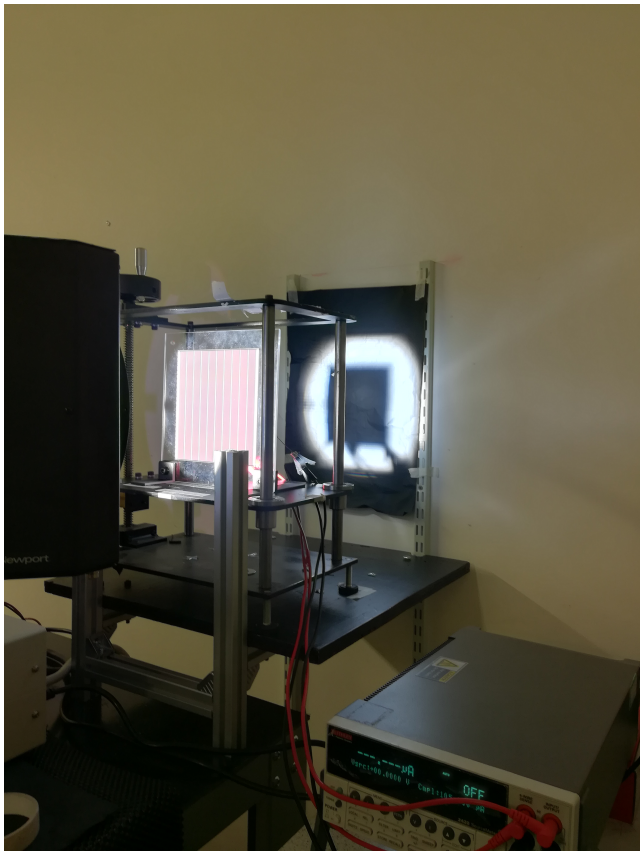

Figure 4.2: Set up to determine the STC performance of the aSi device.

4.2 Indoor characterisation

Prior to deployment in the field, the CdTe and aSi devices were tested indoors to determine the short-circuit current temperature coefficients. These tests also provided an opportunity to test the custom-made cables, connectors, brackets, etc. to ensure all are working correctly. The mSi device was not tested due to the illumination area of the solar simulator being too small.

The aSi PV device was mounted as shown in Figure 4.2. One PT100 sensor was attached to the rear surface to measure the module back surface temperature, T_m, which was converted into the cell temperature, T_c, using a one-dimensional thermal conduction model as follows [221]:

$$T_c = T_m + \frac{G_{poa}}{G_0}\Delta T. \tag{4.1}$$

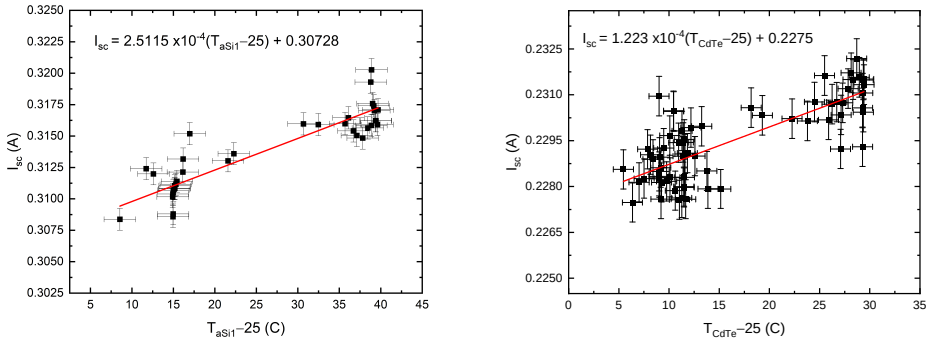

(a) (b)

Figure 4.3: Linear regression of the temperature-current relationship as measured indoors for the aSi and CdTe PV devices.

ΔT is the temperature difference between the module and cell and is determined based on the structure of the DUT. ΔT is set as 3°C in this study based on the structure of the three modules tested [131]. Measurements of the module short-circuit current were made every five seconds while temperature measurements were made every two seconds. No temperature control function was available in this set up, but the solar simulator provides a constant illumination of 1000 W m^{-2} of the shape of the standard AM1.5 reference spectrum. Under illumination, the cell temperature increases. If a linear equation of the form $y = mx + c$ is fit to a plot of the short-circuit current measured at G_0 against $T_c - T_0$, it can be seen from rearranging Equation 2.23 as follows:

$$I_{sc} = I'_{sc} + I'_{sc} \cdot \hat{\alpha}_{I_{sc}}(T_c - T_0) \tag{4.2}$$

that the short-circuit temperature coefficient can be determined by the ratio of m/c, which is the gradient divided by the intercept.

Figure 4.3 shows the regression resulting from the measurements described in this section. From this regression, $\hat{\alpha}_{I_{sc}}$ is equal to 0.000817°C^{-1} for the aSi module and 0.000538°C^{-1} for the CdTe device. The former is in agreement with the manufacturer's datasheet, which is the only datasheet that was available.

4.3 Outdoor characterisation and system validation

This section consists of two components — one is an investigation of the new test site to validate its reliability and accuracy, while the second is the use of the new test site to use outdoor field data to determine the STC performance characteristics of the aSi, CdTe, and mSi devices.

4.3.1 System validation

The results from the indoor tests in Section 4.2 showed that the short-circuit current values of the two aSi devices were statistically similar. One feature of the EKO measurement system is its ability to measure PV devices connected to multiple channels simultaneously. As a simple test to check the reliability of the measurements from different channels, two aSi devices were monitored over a period of two days. Figure 4.4a shows the measured short-circuit currents of both aSi devices as a function of time across the 25th and 26th July 2022, while Figure 4.4b shows a linear regression between the measured currents for each device over the same period. The relatively high frequency changes in

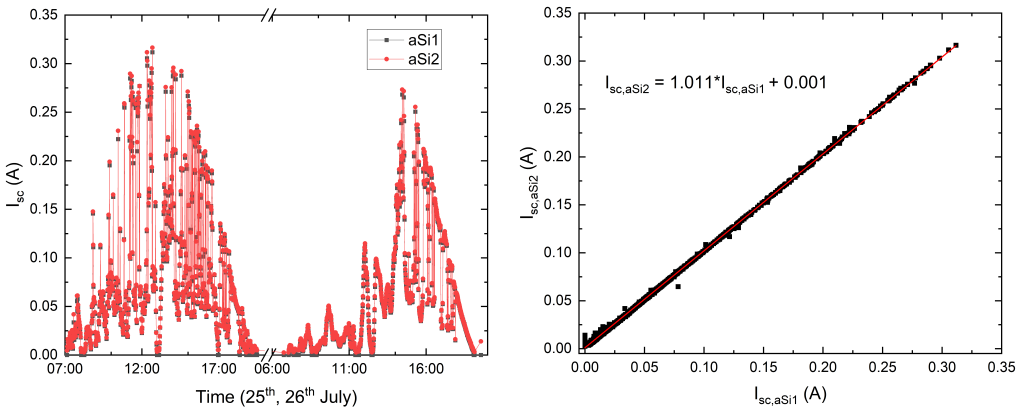

(a) (b)

Figure 4.4: Simultaneous I_{sc} measurements of two identical aSi devices using the EKO IV tracer system.

the current, visible in Figure 4.4a, result from fast-changing cloud cover (and thus irradiance) patterns over these two days. Such conditions are ideal for this investigation as they enable a test of the responsivity and sensitivity of the measurement system and PV panels. It is evident from inspection that the two measurements are closely matched, although aSi2 does appear to produce a slightly higher current for each measurement. This small difference is quantified by the regression in Figure 4.4b as about 1%. This difference comprises a random error and a systematic error, but the systematic error is an order of magnitude lower than the random error cited in Section 3.4. The Pearson's r, and coefficient of determination (R^2) values for the linear regression are 0.9999 and 0.9997, respectively, which are indicative of an extremely strong positive correlation between the two measured currents.

4.3.2 Outdoor STC characterisation

I_{sc0} is the main STC performance parameter required in this work. The method adopted to determine I_{sc0} is based on a modified version of the Sandia model method described in Ref. [208]. The Sandia model requires a two-axis tracking system to be used for all measurements during the I_{sc0} determination process to eliminate the effect of the angle of incidence. To minimise disruption to the fixed-plane long-term testing, which is collecting data for the main analysis, the fixed-plane data are used in conjunction with an incident angle modifier to correct for the AOI effects. The first step in determining I_{sc0} is translate the measured I_{sc} values to 25°C, 1000W m^{-2}, and 90° AOI. The equation for the translated current follows Equation 2.23 but with the inclusion of $f(\theta)$:

$$I'_{sc} = \frac{I_{sc}}{1 + \hat{\alpha}_{I_{sc}}(T_c - 25)} \frac{1000}{G_{poa}} \cdot f(\theta), \tag{4.3}$$

where $f(\theta)$ is a fifth order polynomial IAM. I'_{sc} is then correlated with AM_a

and a fourth order polynomial function, $f(AM_a)$, is fitted to the data. I_{sc0} is then determined by evaluating $f(AM_a = 1.5) = 1$. The process and results of the IAM testing are described in the following section, after which the results of the I_{sc0} analysis are presented in Section 4.5.

4.4 Incident angle modifier

This section presents the method and the results for the test used to determine the incident angle modifier (IAM) for the aSi device. As with other corrections such as the spectral correction used to translate measurements to their equivalent under the reference spectrum, the IAM, or angle of incidence correction, is used to translate measurements to their equivalent under a reference AOI. The reference is defined as 0°, where the irradiance is normal to the surface of the device.

Different models exist to account for AOI losses. Arguably the simplest of these is the Souka and Safwat model [298]:

$$IAM(\theta) = 1 - b_0 \left(\frac{1}{\cos\theta} - 1 \right). \tag{4.4}$$

In Equation 4.4, b_0 is a PV module-specific empirical parameter, but a default value of 0.07 is typically used [299]. This model has been adopted by the American Society of Heating, Refrigeration, and Air Conditioning [300], although not specifically for PV applications. However, the model suffers a discontinuity at 90° and is inaccurate for high angles of incidence ($\theta \geq 80°$) [301]. While many other models exist, such as the Physical IAM model [92], and Martin and Ruiz [302], there is no uniformly accepted standard [303]. Nevertheless, a widely known and relatively simple model is the Sandia IAM presented as part of the Sandia PV Array Performance Model (SAPM) [221]. Other components

of this PV performance model have underpinned the fundamentals behind this research project and, therefore, in part for continuity and simplicity in the overall modelling procedure and principles, it is this IAM model that has been adopted. Furthermore, a database of model coefficients for a range of PV devices is available for all coefficients in the sub-models of the SAPM (including the IAM). This allows for consistency in the analysis in this project where the coefficients are determined empirically for some PV devices but are sourced from the literature for others. The Sandia National Laboratories (SNL) have suggested in their work to use a fifth order polynomial function to represent the angular losses on I_{sc}:

$$IAM = f(\theta) = b_0 + b_1\theta + b_2\theta^2 + b_3\theta^3 + b_4\theta^4 + b_5\theta^5. \tag{4.5}$$

The method used to determine the IAM coefficients $b_{0–5}$ is presented in the following section.

4.4.1 Method to determine the IAM

The SNL has published a full guide to determining the coefficients of the SAPM, including $b_{0–5}$ [208]. The exact procedure was not followed due to limitations of the equipment and prevailing meteorological conditions. For example, only around 400 minutes of clear-sky weather occurred during the experiment campaign, which is lower than the 600 minutes (required) and 1200 minutes (preferred) values for the test. These limitations affect the reliability of the results but, as the IAM only forms a small part of the subsequent spectral correction analysis, and the results are consistent with expectations according to the literature, the prevailing conditions and available equipment are deemed acceptable for the purposes of this investigation.

Figure 4.5: Set up for the AOI testing on a clear-sky day in August 2022.

An aSi module and Kipp and Zonen CMP11 pyranometer were installed on the sun tracker on 10th August 2022, which was a completely clear-sky day. This set up is shown in Figure 4.5.

There are three key stages to each measurement at each angle. These are as follows:

1. Measurement normal to the sun ($\theta = 0$) as reference measurement 1 (RM1).
2. Measurement some angle θ away from the sun as the main measurement.
3. Measurement normal to the sun ($\theta = 0$) as a reference measurement 2 (RM2).

In all three steps, the "measurement" is of I_{sc}, G_{poa}, and T_{mbs}. The first measurement establishes the reference performance and conditions (RM1), the second provides the performance and conditions at a new value of θ, and finally the third enables a comparison of the test-end reference conditions (RM2) to the test-beginning conditions to verify these have been stable throughout the test.

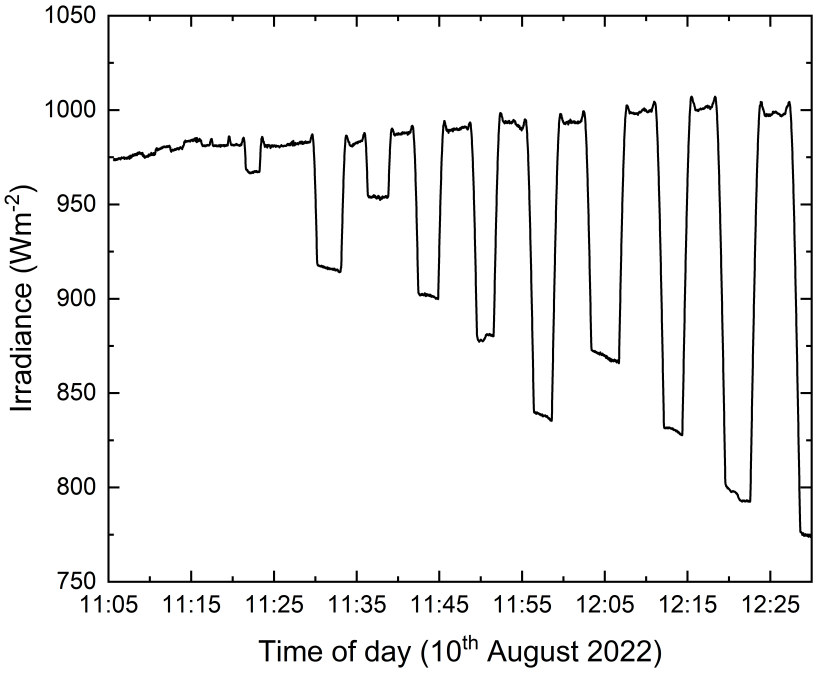

Figure 4.6: Change in irradiance during the AOI testing.

If the difference between RM1 and RM2 is greater than 3% [208], the entire three-step measurement is discarded. At each of the three stages, five repeat measurements are made over the course of around 70–80 seconds. In addition, there is a delay of approximately 30 seconds between each of the three stages to allow for thermal stabilisation of the PV cell as the irradiance incident on the device changes significantly, especially for large values of θ. This change in irradiance that occurs at different angles is shown in Figure 4.6. All measurements of I_{sc} are normalised for irradiance and temperature following the procedure described in equation 2.23. This normalisation enables an isolation of the AOI effects on the PV device.

In this investigation, θ was increased in increments of approximately 5° [208]. The angular sweep was conducted in both directions to verify that the surrounding features of the test site (e.g. buildings) were not interfering with the measurements. The results for both tests yielded the same results and therefore the results of only one sweep are presented in the following section.

Coefficient	Value
b_0	0.9993
b_1	-0.004180
b_2	2.978×10^{-4}
b_3	-1.433×10^{-5}
b_4	2.251×10^{-7}
b_5	-1.186×10^{-9}

Table 4.1: Sandia IAM coefficients for the aSi module

4.4.2 Results

Figure 4.7 shows the fifth order polynomial regression curve derived from the results of the AOI test described in the previous section. The R^2 value for the fit is 0.99651, indicating an extremely high goodness of fit for the IAM. The model coefficients for the fifth order polynomial IAM (Equation 4.5) are presented in Table 4.1.

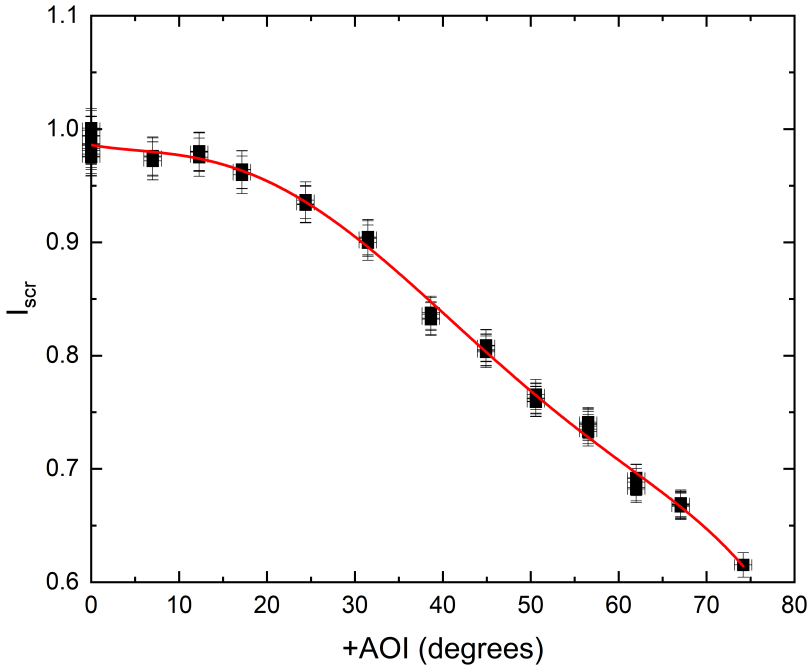

Figure 4.7: Fifth order polynomial IAM regressed between angle of incidence and the normalised short-circuit current of an aSi module.

The IAM model summarised in Equation 4.5 and Table 4.1 is used to apply a correction to the short-circuit current in the subsequent analysis of the UK test site data.

4.5 Reference current

Following the steps outlined in Section 4.3.2, Figure 4.8 presents the results of the analysis to determine I_{sc0} for the aSi (Figure 4.5a), CdTe (Figure 4.5b), and mSi (Figure 4.5c) PV devices. For the thin film modules, two distinct trends in the data are observed in Figure 4.8. These two trends correspond to different times of the year, namely the autumn–winter period (black) and the spring–summer period (red). The latter appears to be caused by a restriction in the AM_a variation corresponding to a similar I'_{sc} variation across the seasons, meaning that multiple unique I'_{sc} values are being attributed to the same AM_a values. In terms of PV device behaviour, the existence of different reference current values for the thin film modules in different seasons may be attributed to the effects of light soaking and temperature on the bond structure and degradation of the module [304, 305, 306, 307, 308, 309]. For the purpose of determining I_{scn}, two polynomial functions have been fit to each of the aSi and CdTe performance curves. In the main analysis, a different value of I_{sc0} is applied in the calculation of I_{scn} depending on the time of year in which the measurement was made. The final I_{sc0} values for each PV device are summarised in Table 4.2.

	I_{sc0}	
	W	S
aSi	0.2095	0.1808
CdTe	0.1826	0.1962
mSi	1.26	

Table 4.2: I_{sc0} values for the three PV modules, including separate values for the autumn-winter (W) period and spring-summer (S) period for the thin film devices.

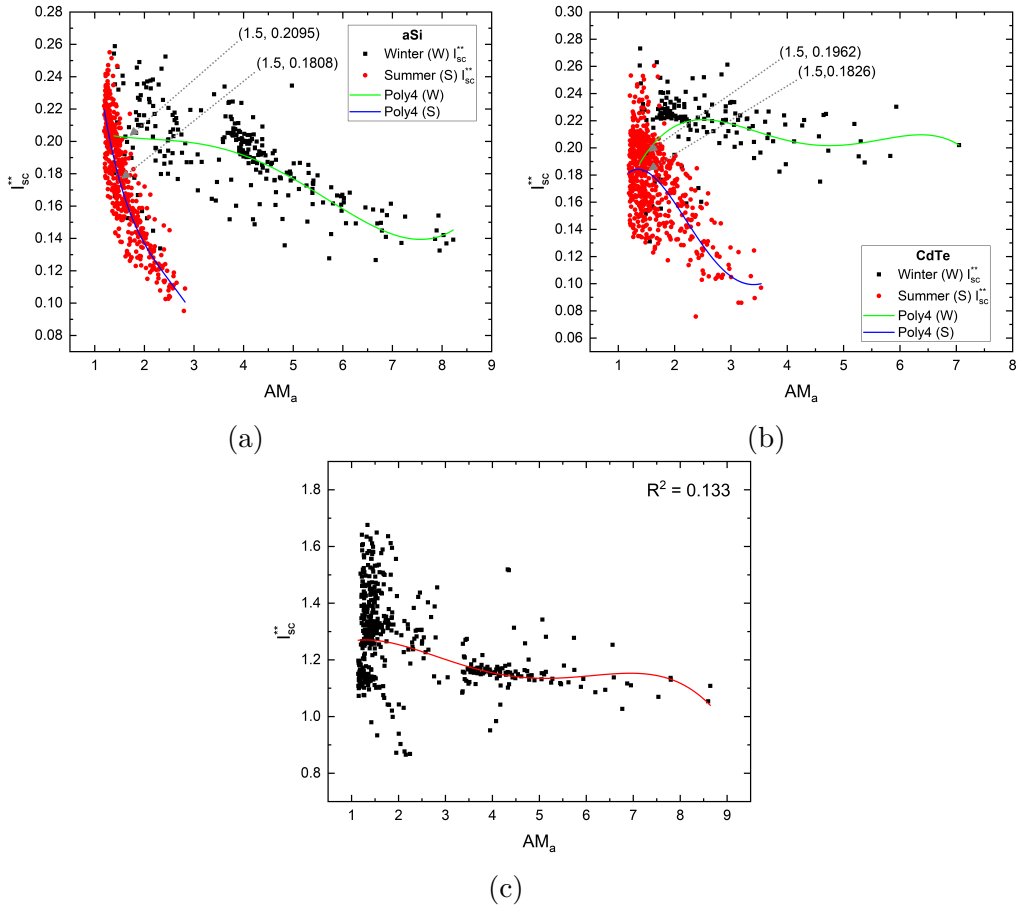

Figure 4.8: Determination of I_{sc0} for the three PV devices. Separate I_{sc0} values for the thin film devices are calculated for the autumn–winter and spring–summer periods due to the distinct behaviour of the devices in each of these periods.

4.6 Summary

The measurement equipment has undergone some simple testing procedures to ensure its reliability, and preliminary data from the outdoor test site as well as an indoor setup have been used to determine the STC performance characteristics of the PV devices. The short-circuit temperature coefficients of the thin film have been determined indoors and the reference short-circuit currents of all three devices have been determined outdoors. For the thin film devices, two values for the reference short-circuit have been derived for use at the different stages of the experiment. For the mSi module, only a single value is required. Furthermore, IAM coefficients based on the Sandia angle of

incidence correction function has been derived for the aSi device using outdoor measurements. For the CdTe and mSi devices, typical values from the Sandia coefficient database are been used.

In the next chapter, Chapter 5, the proposed APE-based SCF is tested using data from the first test site in Golden, Colorado. Following further development of the model in Chapter 6, data from the three PV devices tested in this chapter are analysed.

Chapter 5

APE spectral correction

5.1 Introduction

Parameters derived from the measured spectral distribution, such as APE, are being used more in recent years [310, 311] as outdoor spectrometer devices are becoming more widely available, in particular due to technological developments leading to decreasing costs [312, 313]. The APE in particular has been used extensively to characterise spectral irradiance distributions [169, 170, 171, 172, 314] and has been shown to be correlated with other spectral characterisation parameters such as the Useful Fraction (UF) [167]. However, the APE possesses certain advantages over other indicators. Compared to AM_a for example, the APE can represent spectral conditions in both clear and cloudy skies.

The relationship between the APE parameter and PV performance has been discussed in the existing literature. Cornaro and Andreotti [169] present a detailed characterisation of their test site using the APE, but the data sample used for PV analysis spans only two summer months — June and July — thus restricting the applicability of the findings to other times of the year. A similar

limitation is faced by the work of Williams et al. [174], which only presents results for the winter months. The analysis in Section 3.5 shows the importance of considering the seasonal variation in the spectrum across the year, in particular for the UK climate. Other work has shown the strong correlation between the APE and various PV (spectral) performance indicators, and thus the benefit of using the APE parameter to understand PV spectral efficiency [177, 178, 179]. However, the analysis of the relationship between the spectrum and PV performance is not extended to the development and validation of a predictive model of performance that incorporates into it the spectral effects discussed in these studies.

In summary, existing spectral correction functions are based on proxy variables and suffer from various limitations, the most significant of which is their inability to model spectral influences accurately in situations where the relative influences of different parameters on the spectrum may vary. Several studies have attempted to use measurements of the spectral distribution to understand the spectral effects on PV performance, in particular through use of the APE parameter. However, these studies are often limited in terms of data sample size, extension to a predictive model, and validation.

In the remainder of this chapter, a new spectral correction function based on the average photon energy is derived and validated using using 12 months of outdoor performance data for an amorphous silicon PV device. The proposed SCF is validated in all sky conditions and its performance is compared to that of two commonly used spectral correction methods from the existing literature. The potential limitations of the model are also discussed, which forms the basis of the analysis in the following chapters. A summary of the structure is presented in Figure 5.1.

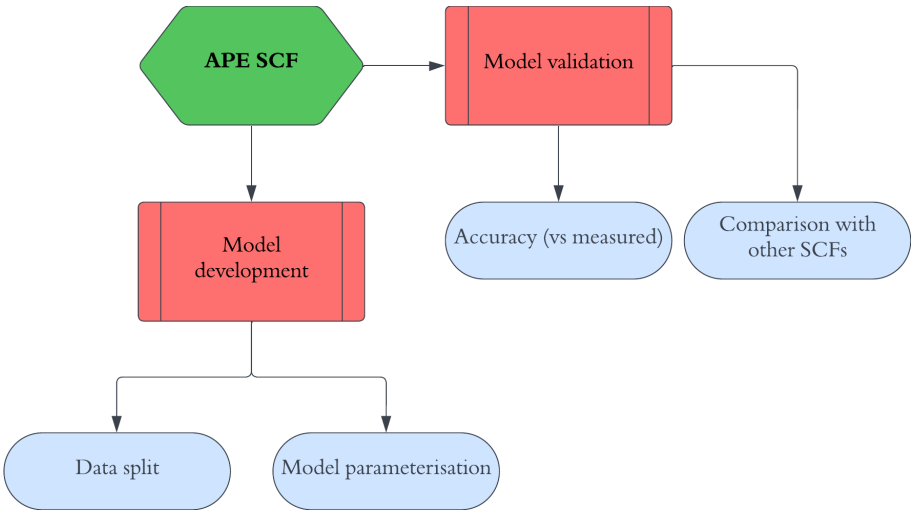

Figure 5.1: Structure of Chapter 5.

5.2 Derivation of the APE SCF

The model development and validation datasets have been defined as January–August 2013 and August–December 2012, respectively, based on the goal of including in each dataset the full range of possible PVM and SI values. As a secondary check of the representability of the model development data, the model derived from these data is compared to one derived from a full year of data.

The correlation between the APE and normalised short-circuit current, I_{scn}, for August 2012–August 2013 is presented in Figure 5.2. Several parameterisations were tested and the optimal form was found to be a fourth order polynomial function:

$$I_{scn} = f(\varphi) = \sum_{n=0}^{4} a_n \cdot \varphi^n, \tag{5.1}$$

The same correlation is presented for the sub-sample of data between January and August of 2013 in Figure 5.3. The R-square coefficient of determination (R^2) for the proposed spectral function derived from the January–August data is 0.870. This value of R^2 is close to that of the function derived from the

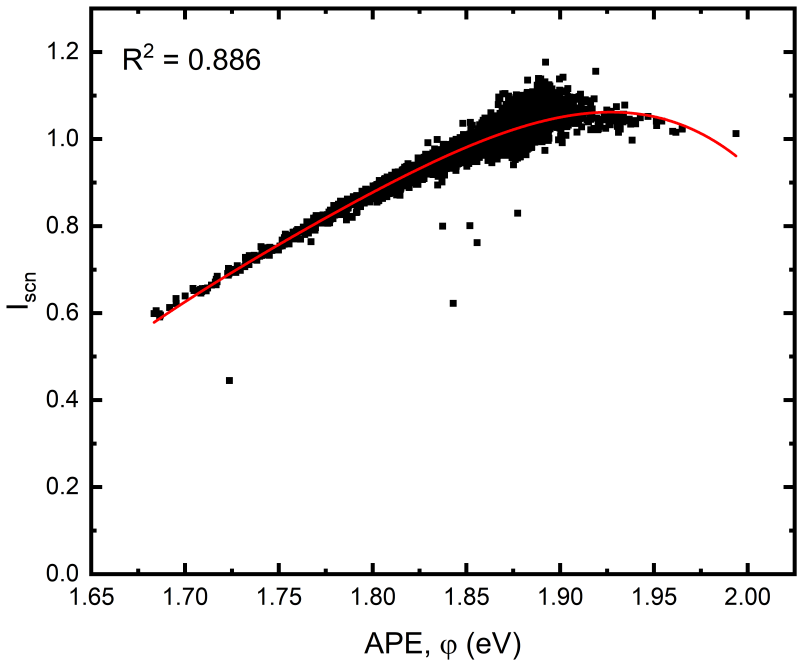

Figure 5.2: Fourth order polynomial APE spectral correction function based on one year of data from August 2012 to August 2013 measured at Golden, Colorado.

full year of data, 0.886, indicating a high similarity between the sub-sample and the full sample. For comparison, the same order polynomial plotted for September 2012–February 2013 yielded an R^2 value of 0.925, which suggests that this sample is not representative of the overall population data (the full-year dataset), which may be a result of over fitting.

From considering the annual range of APE values and this comparison of R^2 values, it may be concluded that the January-August sub-sample is representative of a typical annual dataset and may therefore be used to derive a general model for forecasting at any point during the year.

For the January–August sample plotted in Figure 5.3, there is still a high goodness of fit of $f(\varphi)$ to the data, with almost 90% ($R^2 = 0.886$) of the variability in I_{scn} being described by the dependent variable, APE. The majority of the uncertainty in the fit appears to be around the 1.88 eV–1.90 eV where there is a higher variability in I_{scn} for the same APE values. Beyond 1.88 eV, the trajectory of increase in I_{scn} changes as I_{scn} plateaus off. This plateau

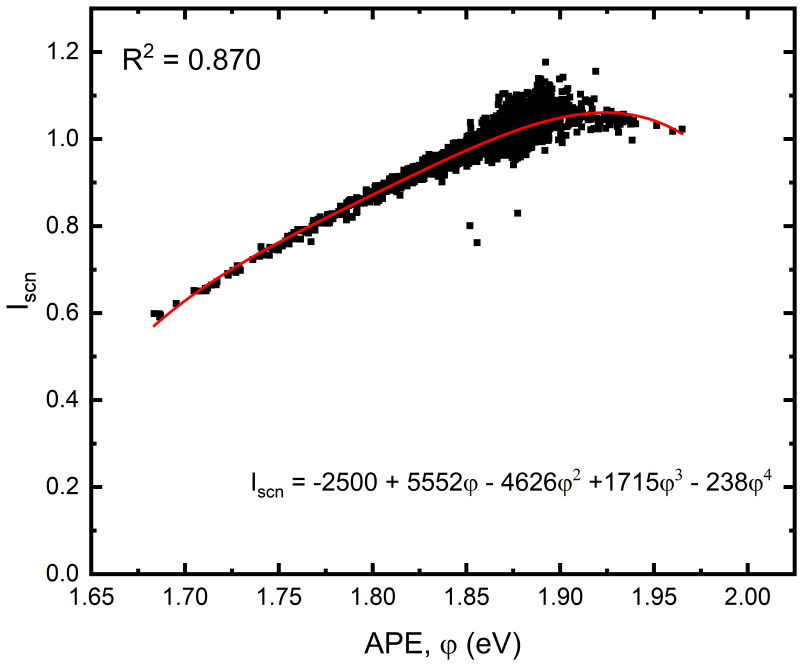

Figure 5.3: Fourth order polynomial APE spectral correction function based on data from January 2013 to August 2013 measured at Golden, Colorado.

	a_0	a_1	a_2	a_3	a_4
Value	−2500.0015	5552.1598	−4626.8451	1714.6741	−238.3416

Table 5.1: Polynomial coefficients for the APE spectral correction function derived from January 2013–August 2013 data (Figure 5.3, Equation 5.1).

may be a result of the finite spectral response range of the aSi module. The coefficients for the January–August 2013 model are presented in Table 5.1.

5.3 Model validation and discussion

The proposed model is validated using new data from August–December 2012. The normalised measured current from this period, hereinafter denoted "measured current" ($I_{scn,meas}$) for simplicity, is compared to the normalised current calculated using the proposed $f(\varphi)$ model, denoted $I_{scn,\varphi}$. In addition, the prediction accuracy of $f(\varphi)$ is compared to that of the absolute air mass function, $f(AM_a)$, which is the traditional spectral correction approach used in the Sandia Array Performance Model [221]. A comparison is also made with a

modified version of the AM_a function, originally published in [47], which adds the spectral effects of cloud cover into $f(AM_a)$ by means of the clearness index, K_t.

The predictive accuracy is analysed in two ways. One is by directly comparing the predicted values with the measured values to analyse the error in the prediction at different APE ranges. Another involves plotting the data as a time series to identify any temporal phenomena underlying the deviations between the measured and predicted values, and to evaluate the temporal resolution at which accurate predictions of I_{scn} are possible.

5.3.1 Predictive accuracy of the APE SCF

Figure 5.4 shows the predicted and measured normalised current values as a function of time, for the period from August to December 2012. The predicted values are calculated by substituting only the APE values for this period into the model presented in Figure 5.3. There is a high degree of matching between the predicted and measured values of PV performance, both for values of I_{scn} greater than and less than unity, throughout the year. There appear to be two main types of temporal fluctuations in the data. One is the high frequency (15-minute) fluctuations happening throughout each day, while another is the overall drop in $I_{scn,meas}$ as the seasons progress from summer to winter. The APE function is able to forecast accurately both the high frequency (15-minute) fluctuations and the long-term seasonal shift in PV performance.

Figure 5.5 presents the correlation between $I_{scn,meas}$ and $I_{scn,\varphi}$. The regression in Figure 5.5 indicates that $f(\varphi)$ is an accurate and reliable predictor of I_{scn}. Firstly, the Pearson's r value of 0.969 indicates a very strong positive relation between the predicted and measured values of I_{scn}. Secondly, the R^2 of 0.940 substantiates the positive correlation between the two, and affirms the high

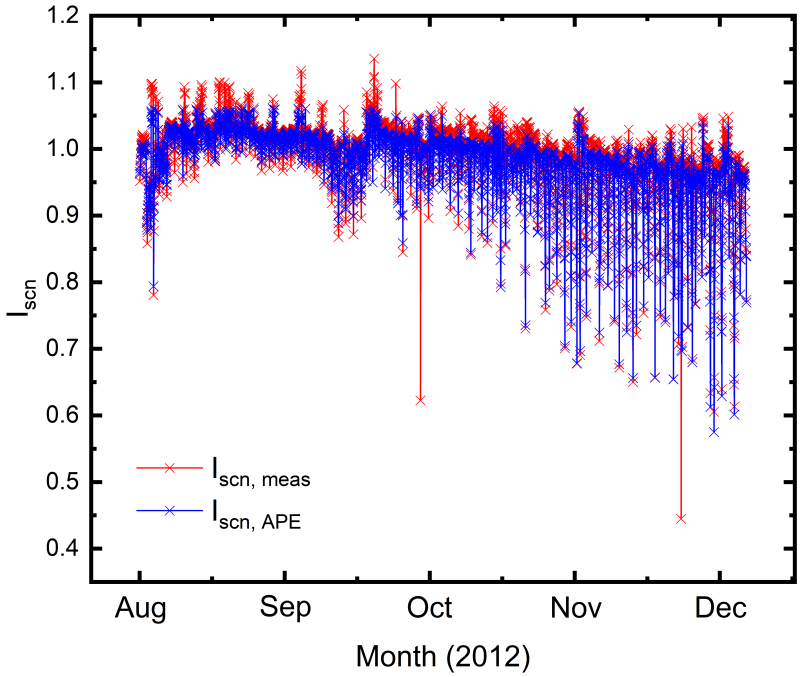

Figure 5.4: Time series validation of $f(\varphi)$ for August 2012–December 2012

degree to which the modelled current matches the measured current. As a measure of the variability between the measured values and those predicted by the proposed model, the Mean Absolute Error (MAE) is found to be only 0.014, which indicates a high degree of matching between the measured and predicted values. Finally, the regression equation in Figure 5.5 also indicates a low random and systematic error present in the data from the low uncertainty in the intercept and gradient.

There appears to be a slight drift in the data away from the line of best fit in Figure 5.5 at I_{scn} values less than 0.65. This drift may be a result of less data in the low APE value range used to derive the model. When comparing the data subset (Figure 5.3) with the annual dataset (Figure 5.2), in the data subset there are less data at low APE values in particular. The reduction may not only be responsible for the slightly lower R^2 value for the subset $f(\varphi)$ fit, but also increased uncertainty and therefore more likely natural fluctuation in the spread of data in Figure 5.5 at lower APE values.

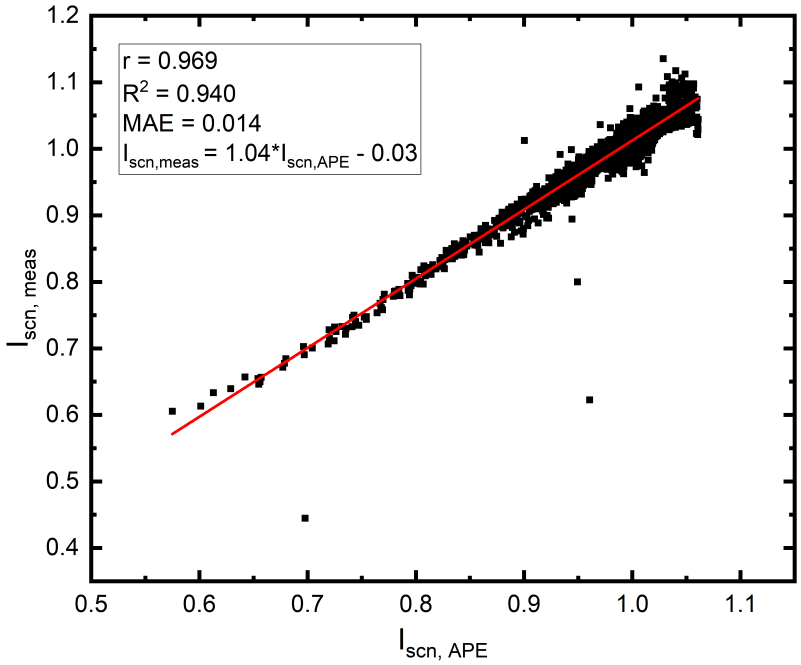

Figure 5.5: Validation of $f(\varphi)$ for August 2012–December 2012

5.3.2 Comparison with existing functions

This section of the analysis compares the predictive accuracy of the derived APE function to that of $f(AM_a)$ and $f(AM_a, K_t)$. The same methods of analysis are used — absolute predictive accuracy and time series analysis.

Existing functions: Air mass and clearness index

Model coefficients for the AM_a and AM_a-K_t spectral correction functions, which were introduced in Chapter 2, have been derived from the same NREL data used to derive $f(\varphi)$. Figure 5.6 shows the plots for each of these functions.

Comparison between the SCFs

The R^2 values show that the correlation is strongest for the $f(\varphi)$ SCF compared with the $f(AM_a)$ and $f(AM_a, K_t)$ SCFs. In terms of the predictions of I_{scn} made by these models, the correlations between the predicted and calculated

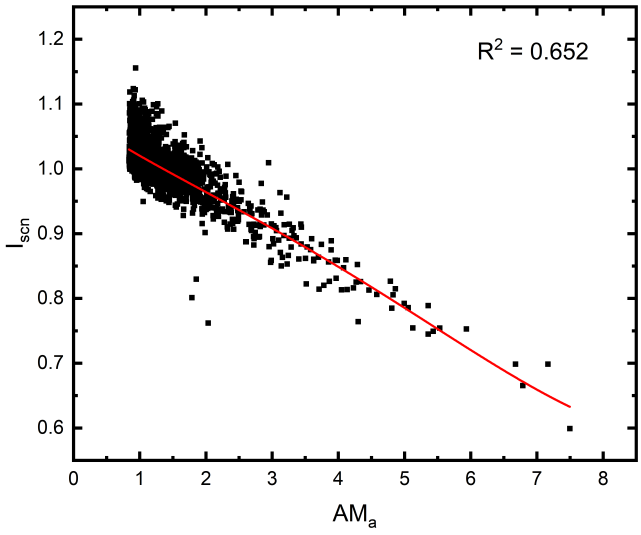

(a)

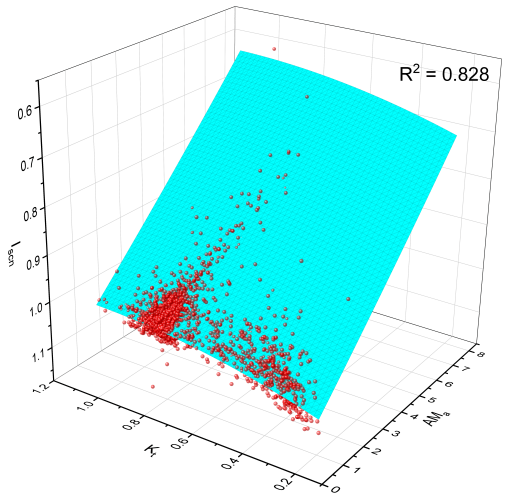

(b)

Figure 5.6: $f(AM_a)$ and $f(AM_a, K_t)$ for January 2013–August 2013.

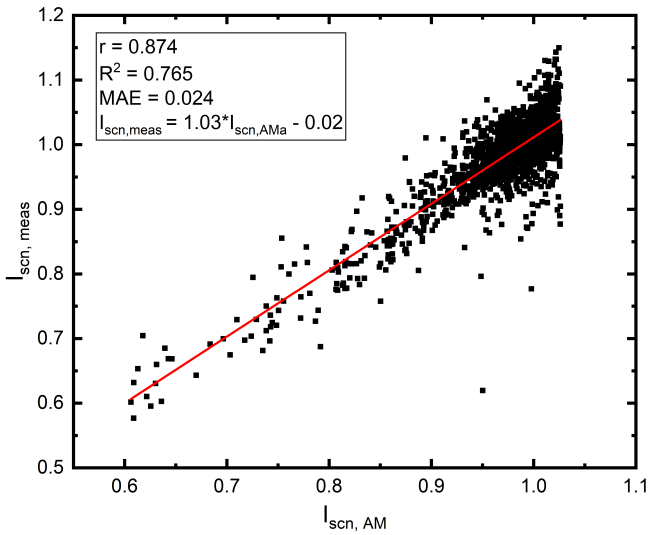

(a)

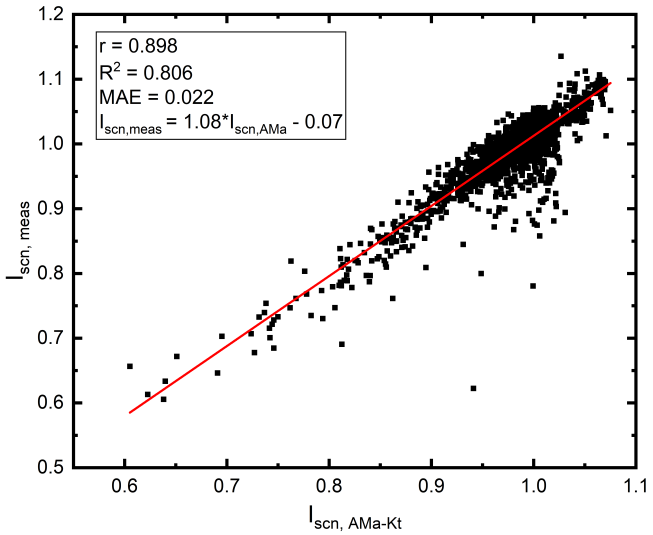

(b)

Figure 5.7: Validation of $f(AM_a)$ and $f(AM_a, K_t)$ for August 2012–December 2012.

values of I_{scn} using both $f(AM_a)$ and $f(AM_a, K_t)$ are plotted in Figures 5.7a and 5.7b, respectively. The weakness of the AM_a-I_{scn} correlation in Figure 5.6a translates into a weaker predictive power of the AM_a function in Figure 5.7a. The AM_a-K_t function offers a more reliable prediction of I_{scn} than the AM_a function, evident from the reduced spread in data, but there is still significant variability in the prediction when compared to the spread of data in the APE function in Figure 5.3. Although the proportion of explained variation in I_{scn} increases by around 5% (82% to 87%) for $f(\varphi)$ compared with $f(AM_a, K_t)$,

Correlation	Statistic		
	r	R^2	MAE
$I_{scn,meas}(AM_a)$	0.874	0.765	0.024
$I_{scn,meas}(AM_a, K_t)$	0.898	0.806	0.022
$I_{scn,meas}(\varphi)$	0.969	0.940	0.014

Table 5.2: Fit statistics for the AM_a, K_t, and φ spectral correction functions absolute predictive accuracy test.

	SCF		
	$f(AM_a)$	$f(AM_a, K_t)$	$f(\varphi)$
Matching (%)	77	81	94

Table 5.3: Degree of matching, as indicated by the R^2 value, between the measured and predicted values of I_{scn} for each of the proposed APE function and two traditional functions, $f(AM_a)$ and $f(AM_a, K_t)$.

this improvement translates into a larger improvement in prediction accuracy of almost 15% as indicated by the MAE. This highlights the importance of using multiple metrics in the model validation as improvements in model fitting (R^2) do not always linearly translate to better predictive accuracy on individual data points (MAE). Nevertheless, the overall improvements in both R^2 and MAE show the ability of $f(\varphi)$ to incorporate not only the effects of cloud cover and air mass on the spectrum, and therefore PV performance, but also additional effects from other atmospheric parameters. A comparison of all of the fit statistics for each of the functions is presented in Table 5.2.

In terms of the time series analysis, the measured and calculated normalised short-circuit currents are plotted against time for $f(AM_a)$ and $f(AM_a, K_t)$ in Figures 5.8 and 5.9, respectively. The time series analysis shows that all three functions are capable of capturing the overall seasonal trend in I_{scn} from August to December, where I_{scn} exhibits a continual decrease in magnitude and increase in variability. However, $f(\varphi)$ has a significantly greater predictive accuracy, compared to $f(AM_a)$ and $f(AM_a, K_t)$, across the full duration of the investigation. The degree of matching between each of the three SCFs is summarised quantitatively in Table 5.3.

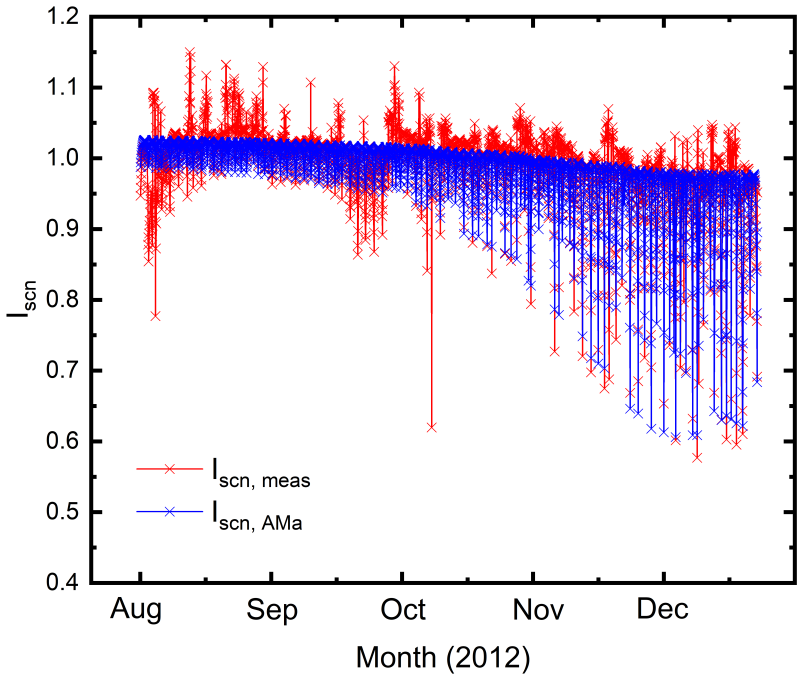

Figure 5.8: Time series validation of $f(AM_a)$ for August 2012–December 2012

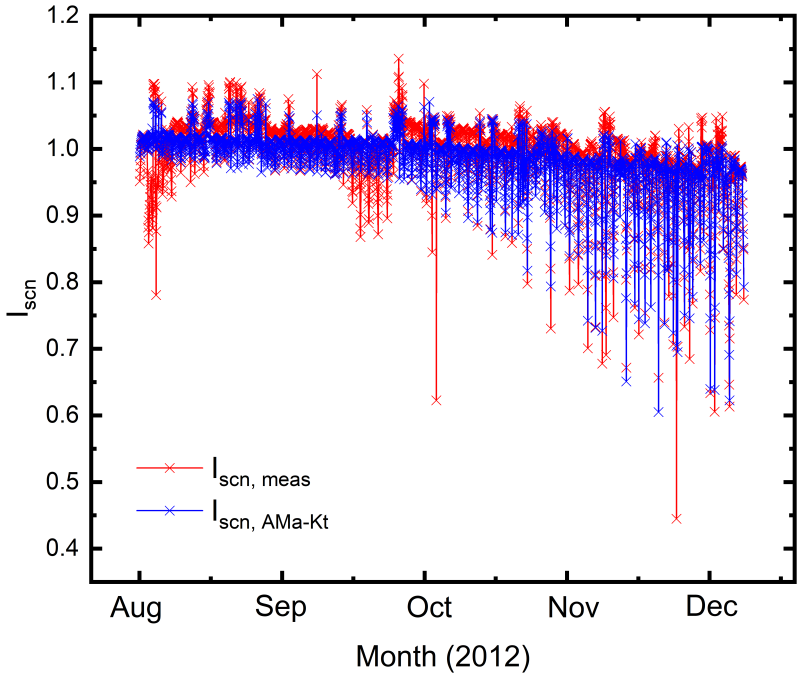

Figure 5.9: Time series validation of $f(AM_a, K_t)$ for August 2012–December 2012

Deviations of the predicted from the measured values for all three functions tend to be underestimates, which was expected following the gradients generated in the absolute predictive accuracy analysis being > 1. However, the deviations in the case of $f(AM_a)$ are visibly greater than those for $f(\varphi)$. Furthermore, the temporal resolution at which $f(\varphi)$ is able to capture the variations in I_{scn} is far beyond that of $f(AM_a)$. The ability of $f(\varphi)$ to model fluctuations at a 15-minute time resolution, which is the limit of the measured data in this study, means that the applicability of the function is greatly enhanced. The reason for this improved modelling at shorter time intervals is down to the APE's higher sensitivity to changes in the spectrum. Changes in air mass are driven only by the sun's position in the sky, which changes slowly, therefore high frequency changes in the spectrum resulting from high frequency changes in the sky conditions and atmospheric composition cannot be captured by using changes in the air mass as a proxy. Furthermore, an APE value can be derived from a spectrum, measured at any time, almost instantaneously.

This point regarding the temporal resolution at which the different functions can capture changes in the spectrum also relates to the fact that although $f(AM_a)$ and $f(AM_a, K_t)$ are able to capture situations where $I_{scn} < 1$ in the winter months, they are incapable of doing so in the summer months. This is in contrast to $f(\varphi)$, which captures both $I_{scn} < 1$ and $I_{scn} > 1$ throughout the year. The reason for this difference lies in the factors affecting the spectrum in different months. The shift in I_{scn} to lower values over the course of the year is primarily a result of the changing solar elevation, which is lower in winter months. Therefore, air mass exhibits a dominant role in the long-term seasonal variation in the spectrum, hence AM_a-based models are capable of accurately modelling this variation. On the other hand, high frequency dips in I_{scn} in the summer months are not driven by changes in air mass, but rather atmospheric composition. For example, changes in atmospheric turbidities and the distributions of different gases such as ozone and sulphur dioxide. There-

fore, instantaneous characterisation of the spectrum to determine the spectral influence on PV performance using $f(\varphi)$ is more accurate both in the short and long term.

In terms of how each individual function compares to the others for different ranges of I_{scn}, it can be seen that $f(AM_a, K_t)$ offers an improved prediction compared to $f(AM_a)$, in particular in terms of its ability to predict I_{scn} values greater than 1. This is as expected for aSi modules since such modules tend to operate more efficiently in cloudier conditions, the effects of which are modelled more accurately in $f(AM_a, K_t)$ than $f(AM_a)$ due to the inclusion of the clearness index parameter. However, $f(\varphi)$ still outperforms $f(AM_a, K_t)$, generating either a similar or better forecast of I_{scn}. The most notable improvements that are achieved by $f(\varphi)$ over $f(AM_a, K_t)$ are for I_{scn} values less than 1. This indicates that although K_t can improve the prediction accuracy of $f(AM_a)$ by incorporating the effects of cloud cover, hence for $I_{scn} > 1$, the APE function is able to account not only for the effects of air mass and cloud cover, but also the effects of other parameters omitted by the AM_a-K_t function, which also impact the spectrum.

Finally, whether the high predictive accuracy of $f(\varphi)$ is maintained for other PV technologies is yet to be tested. Questions have been raised in the literature about the uncertainty in the φ as an index of the spectrum due to the absence of a bijective relationship between the two [175]. Therefore, it is necessary to validate the proposed methodology for other PV technologies, in particular those with a wider spectral response range than aSi. Crystalline silicon (c-Si) PV would be a good starting point as this technology maintains a response at longer wavelengths than aSi. In addition, c-Si has dominated the PV market in recent years, in particular for residential rooftop applications [315, 316].

5.4 Analysis summary

The proposed methodology for analysing the spectral influence on PV performance has been used to derive an APE spectral correction function from eight months of empirical data measured in Golden, Colorado. The derived function has been validated using the remaining four months of data from the year to compare the predicted and calculated values of I_{scn}, and to compare its performance to that of the traditional air mass model and a modified air mass model that includes the effects of cloud cover. Up to 30% absolute percentage improvement in predictive accuracy can be achieved through the use of the derived APE function, which improves on traditional models both in terms of absolute prediction accuracy and the temporal resolution at which accurate predictions are achieved. These improvements have been quantified using a range of statistical parameters, namely the Pearson's correlation coefficient (r), coefficient of determination (R^2), and the mean absolute error (MAE). In all statistical tests, the APE function outperforms the air mass-based functions by a significant margin.

5.5 Conclusion

PV performance modelling is essential for the success of PV systems. Traditional approaches to account for the spectral influence on PV performance and predictions thereof have been dominated by the use of proxy variables, in particular the air mass parameter. The majority of such functions suffer from increased uncertainty due to their limited scope of inclusion of factors that affect the solar spectral distribution.

The APE is shown in this work to be a single parameter capable of accurately characterising spectral distributions for effective use in computing the effect

of the spectrum on PV performance. The spectral correction methodology presented in this chapter, which is validated using an aSi PV module deployed in Golden, Colorado, shows significant improvements in prediction accuracy and forecasting time resolution when compared to two air mass-based approaches. The greatest improvement is found with respect to $f(AM_a)$, but even after the inclusion of the clearness index in $f(AM_a)$ to account for the spectral effects of cloud cover, $f(\varphi)$ still more accurately models I_{scn} for values both greater than and less than unity.

Although aSi performance is most susceptible to spectral changes, further work is still required to validate the proposed methodology for a range of PV technologies. Finally, validation of the model in different climatic regions is necessary to test the worldwide generalisability of the proposed methodology. These aspects of the project are investigated in the forthcoming chapters.

Chapter 6

Combined APE and spectral band SCF

6.1 Introduction

The $f(\varphi)$ model is shown in Chapter 5 to reduce the mean absolute prediction error by almost 50% with respect to $f(AM_a)$ and almost 40% with respect to $f(AM_a, K_t)$. However, the proposed model is only validated for a single amorphous silicon PV device and therefore it is necessary for future work to validate the model with different types of PV technology.

Another limitation of $f(\varphi)$ presented in Chapter 5, as well as previous APE-PV studies [169, 170, 171, 172, 203, 310, 317], centres on the uniqueness of the APE parameter in terms of its ability to represent solar spectra. It is explained in Chapter 2 how dips in spectral irradiance in one particular waveband may be countered by increases in irradiance in another waveband, leading to two differently shaped spectra but the same average photon energy. Although some studies argue that the APE is a unique representation of the solar spectrum based on statistical analysis [168] and outdoor field measurements, for example

across multiple sitesin Japan [318], other research has argued otherwise [319, 320, 175]. For example, Nofuentes et al. [175] analyse the coefficient of variation of the APE parameter, rather than the standard deviation as used in Ref. [168], and find that APE values used to represent the spectrum have an uncertainty of over 3% between 450–900 nm, and 5–11% outside of this range. They conclude that the APE is not a bijective index and cannot be used reliably for spectral analysis. Since the model presented in the previous chapter only demonstrates the proposed methodology for aSi PV devices, which have a spectral response range below 900 nm, the bijectivity issue highlighted in [175] may not have been a problem. Two research gaps in the existing literature are clear:

1. The use of the APE parameter to derive an SCF for PV devices with wider spectral responses.

2. Uncertainty in the APE parameter when analysing spectral effects on PV devices, in particular those with wider spectral responses.

Ishii et al. [11] show that the primary driver for changes in the shape of spectra that maintain the same APE are negatively correlated depths of water absorption bands (ε_w) and atmospheric windows (ε_a), hereinafter collectively referred to as "spectral bands", or ε. It is suggested that a solar spectral distribution may therefore be characterised uniquely for all wavelengths with both the APE and an additional index, namely the depth of one such spectral band.

In this chapter, an SCF based on the APE parameter is derived and validated for a range of different PV technologies, including those with a spectral response beyond 900 nm. Based on an analysis of the uncertainty in the single-variable APE SCF, an advanced model based on both the APE and the depth of a spectral band is proposed to address the uncertainty in $f(\varphi)$ caused by the uncertainty in the φ. The new model is developed and validated using empirical data for three PV technologies — multicrystalline, cadmium telluride,

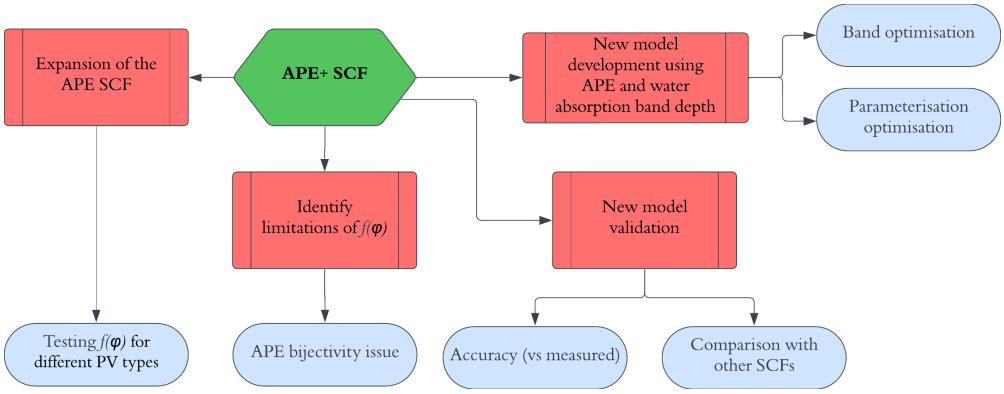

Figure 6.1: Structure of Chapter 6.

and triple-junction amorphous silicon. The combined φ-ε model addresses the bijectivity issue of the APE parameter whilst still retaining the higher accuracy achieved through the use of direct representation of the spectrum rather than the traditional proxy representation. As part of the model validation, the predictive accuracy of the proposed model is compared to that of the APE spectral correction and a proxy-variable function. New model coefficients are derived for the latter, which represent an additional contribution of this work to the literature. The overall structure of this chapter is summarised in Figure 6.1.

6.2 Analysis framework

Figure 6.2 is a flow chart illustrating the research framework and overall processes undertaken to achieve the main aims of this study, which are to validate the $f(\varphi)$ SCF for different PV technologies, and develop and validate a new SCF based on two spectral indices — the average photon energy (φ) and the depth of a water absorption band (ε).

The first stage of the work is to derive the $f(\varphi)$ model coefficients for three PV technologies not previously examined in the literature. Then, based on an analysis of the uncertainty in the $f(\varphi)$ correlation for these technologies, and published spectral irradiance analysis, four spectral bands are determined as

potential candidates for ε in the proposed $f(\varphi, \varepsilon)$ spectral correction model. An iterative algorithm is used to fit different surface functions to a correlation of I_{scn}=$f(\varphi, \varepsilon)$, for each ε band and for each device under test (DUT). In this stage, the optimal fitting function is determined for each ε band, for each DUT. The best fitting function for each ε band is then used to make predictions of I_{scn}, which are compared with measurement-derived values of I_{scn}, to determine the optimal ε band for each DUT. This leads to a final model of $f(\varphi, \varepsilon)$ with the optimal ε band and functional form. The final $f(\varphi, \varepsilon)$ SCF for each DUT is then validated through a comparison of its fitting and I_{scn} prediction accuracy with those of existing SCFs, namely $f(\varphi)$, and $f(AM_a, W)$. For each

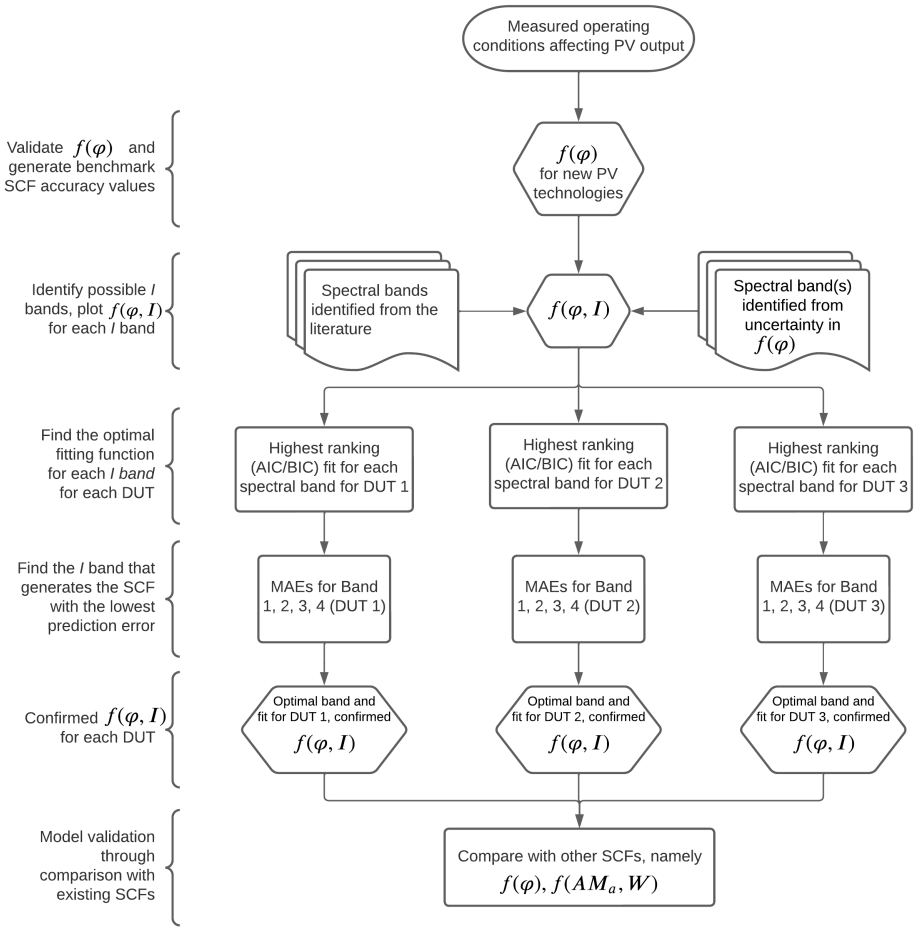

Figure 6.2: Outline of the research framework.

spectral band used in the new model, the surface functions fitted to the data are ranked according to their Bayesion and Akaike Information Criterion (BIC,

AIC) scores to determine the best fit function for each spectral band. The BIC and AIC yield a rating that balances accuracy and complexity of the model [321], although the BIC involves a greater penalty for increased complexity due to the higher weighting of the term for the number of model parameters. The coefficient of determination, R^2, is calculated for the best fit surface function for each spectral band to enable a comparison of fitting accuracy between the models. A higher R^2 indicates that the surface function explains more of the variation in the dependent variable. However, a higher R^2 value does not necessarily mean a better prediction model as there is always a risk of overfitting to the data used to develop the model [322, 323]. Therefore, in the validation stage, the optimal parameterisation, according to the BIC/AIC scores, for all four spectral bands is used to predict values of I_{scn}.

The prediction accuracies of the models based on different spectral bands are then compared to determine the optimal ε band. In addition, comparing this ε-band optimisation result to the ε band ranking according to the R^2 values will give an indication of whether any overfitting exists in the model parameterisation.

The prediction accuracy of $f(\varphi, \varepsilon)$, using the optimal φ band and functional form, is then compared to the accuracy of existing SCFs, namely $f(\varphi)$ and $f(AM_a, W)$ to test whether there is any benefit of using the new model. Finally, the sensitivity of the prediction accuracy to the functional form of $f(\varphi, \varepsilon)$ is then analysed to determine the flexibility of the model for different use cases that could impose varying levels of computational resources or requirements.

6.3 Spectral dependence of PV performance

In this section, the spectral response and how this influences the performance of each device under test (DUT) is discussed. The spectral response curves

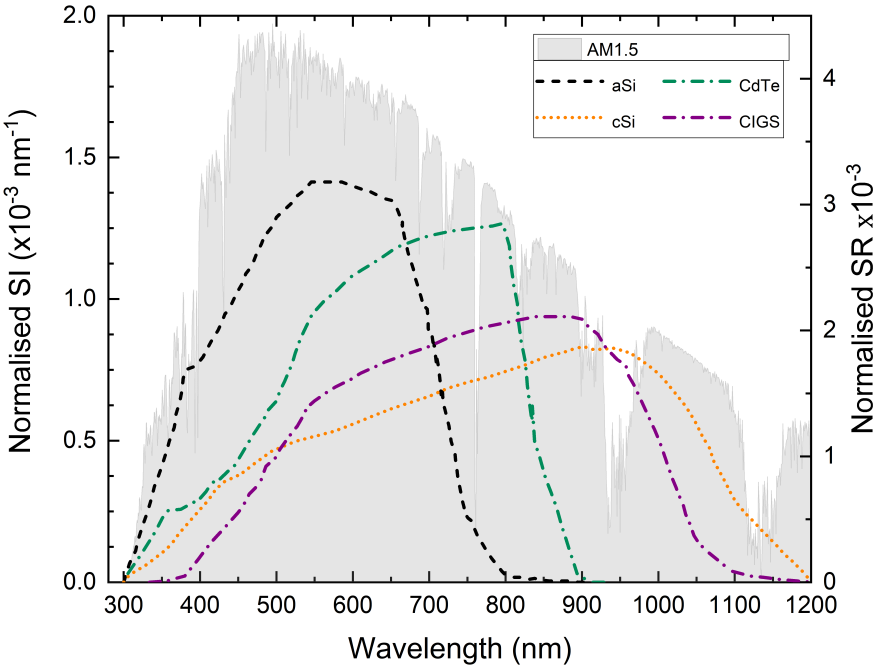

Figure 6.3: Normalised spectral response (SR) of the three PV technologies investigated in this study. Behind the spectral response curves is the spectral irradiance (SI) for the AM1.5 reference spectrum, normalised between 280 and 1200 nm. SR data are sourced from Ref. [13] (mSi and CdTe) and Ref. [14] (aSi-T)

of the DUTs in this study are presented in Figure 6.3. CdTe has the narrowest spectral response and exhibits sharp cut off wavelength at around 900 nm, which corresponds to its band gap of around 1.5 eV [324]. The wide band gap (narrow spectral response range) results in a relatively strong spectral dependence of CdTe performance as CdTe PV devices can only utilise a relatively small proportion of the available spectral irradiance. The other two devices — aSi-T and mSi — all have much broader spectral response ranges. For the mSi device, this results in a reduced spectral dependence. However, this is not the case with aSi-T, which is a triple-junction device. In a multijunction device, the spectral responses of each junction are combined to provide a wider overall spectral response range for the device. However, the construction of multijunction devices is such that the junctions may be considered as cells connected in series. Therefore, the current flowing through each junction must be equal, which limits the overall device current to that of the least productive junction.

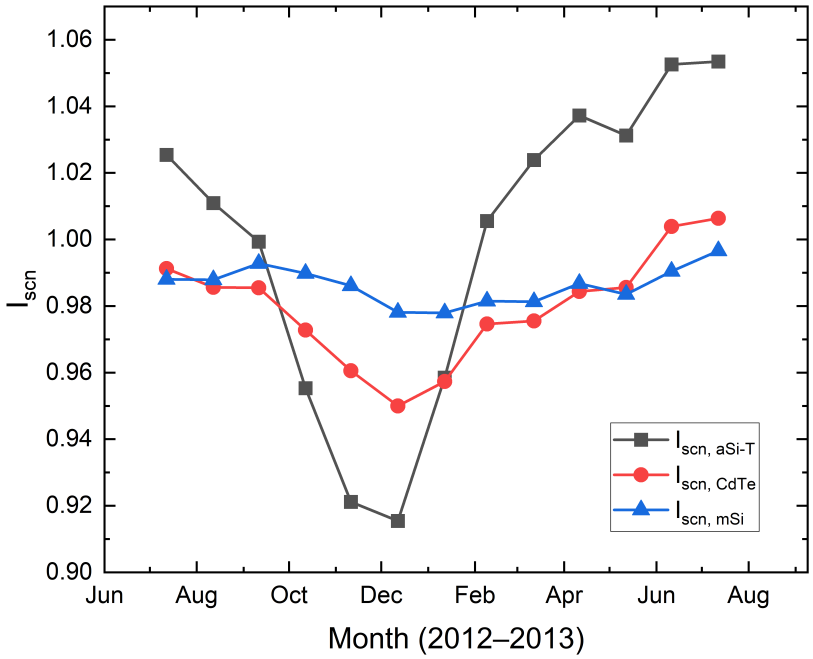

Figure 6.4: Annual variation in monthly mean I_{scn} for the three DUTs — aSi-T, CdTe, and mSi.

Therefore, multijunction devices exhibit a strong spectral dependence [174, 190] due to the particular spectral response characteristics of the individual subcells (junctions).

To understand the spectral response behaviour of the DUTs quantitatively in the field, Figure 6.4 shows the annual variation of I_{scn} for the devices. I_{scn} is an indicator of the purely spectral influence on the short-circuit current of a PV module, as defined in Section 2.5.2. Values of $I_{scn} > 1$ indicates higher performance under the prevailing spectrum with respect to the performance under the reference conditions, $I_{scn} < 1$ indicates decreased performance, while $I_{scn} = 1$ indicates there is no difference between the performance under the prevailing spectrum and under reference conditions.

As expected, the performances of the wider band gap (CdTe) and multijunction (aSi-T) devices have a stronger spectral dependence than the narrower band gap single-junction device (mSi). With respect to RTC (where $I_{scn} = 1$), the monthly mean variations plotted in Figure 6.4 show variation of up to -9%, $+6\%$ for aSi-T, -5%, $+1\%$ for CdTe, and -2%, $+0\%$ for mSi. The maximum

observed variations on the 15-minute-averaged timescale of the original dataset are −40% to +20% for aSi-T, −20% to +10% for CdTe, and around ±5% for mSi. It is important to note that I_{scn} for the aSi-T device may be influenced by non-spectral effects that are not accounted for in the normalisation process. In the summer in particular, thermal annealing of the device may lead to an increase in efficiency [325, 326], which could in part be responsible for the significant rise in I_{scn}, in particular when compared with the mSi and CdTe devices.

Variation in I_{scn} for all three devices follow a seasonal sinusoidal pattern over the year. The reduction in I_{scn} in the winter months may be attributed to an average drop in the solar elevation during this time of the year. The resultant increase in solar air mass shifts the solar spectrum to longer wavelengths on average, which results in a reduction in the efficiency, especially for the CdTe and aSi-T devices. This change in the solar spectrum is also indicated by a drop in the average photon energy at the same time, which is shown in Figure 3.17b.

6.4 APE spectral correction

In this section, the coefficients of $f(\varphi)$ are derived for each of the three DUTs, which expands on Ref. [180]. An analysis of the uncertainty in $f(\varphi)$, in addition to a review of existing studies, informs the selection of the spectral band used for ε in the main analysis of this study where a new SCF based on the APE and ε is presented.

6.4.1 APE spectral correction

Based on the discussion in Section 6.3, the correlation between I_{scn} and φ for the mSi device would be expected to be weak compared to the same correlations for the aSi-T and CdTe devices. This estimation is borne out in the results shown in Figure 6.5c. The coefficients of determination, R^2, for each of the fits are listed in Table 6.1.

DUT	R^2
aSi-T	0.90
CdTe	0.54
mSi	0.10

Table 6.1: R^2 values for the fourth order polynomial fits of $I_{scn} = f(\varphi)$ for each DUT.

All three devices show an increase in efficiency with the average photon energy, although the rate of increase is greatest for the aSi-T and CdTe modules. For the CdTe module, which has a relatively wide band gap, the blue-shifted spectra (higher APE) contain a larger proportion of photons with sufficient energy to generate a photocurrent. For the aSi-T module, a similar principle applies but in this case it is the top junction (wide band gap) out of the module that is engaged more effectively in the overall current generation by the blue-shifted spectra. Generally speaking for both the CdTe and aSi-T modules, the active region for these thin-film technologies is typically within the first micrometer of the cell (top-cell in the aSi-T case). This improves their spectral response to shorter-wavelength irradiation as irradiance in the blue-visible range is typically absorbed within 0.1–1 µm of cell depth [327]. Although the mSi data also show an increase in I_{scn} with APE, the correlation is weak and the fit is unreliable as evidenced by the extremely low R^2. The increased uncertainty in the mSi fit may be attributed in part to the wider and flatter spectral response range of the module, which means that the device performance has a greater dependence on APE values that have a higher uncertainty.

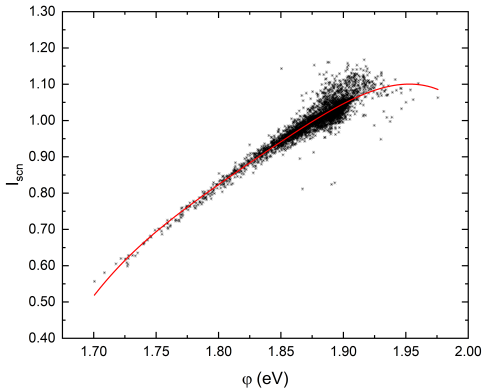

(a) $I_{scn} = f(\varphi)$ SCF for the aSi-T device. The coefficient of determination, R^2 is high, at around 0.90.

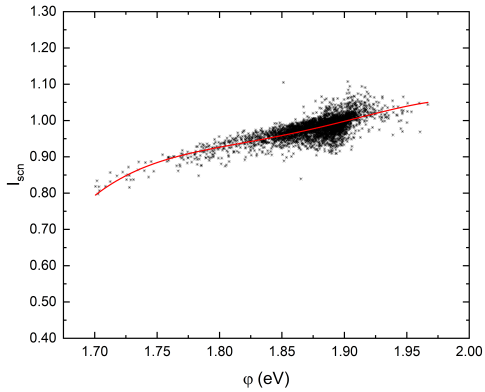

(b) $I_{scn} = f(\varphi)$ SCF for the CdTe device. The coefficient of determination, R^2 is medium-high, at around 0.54.

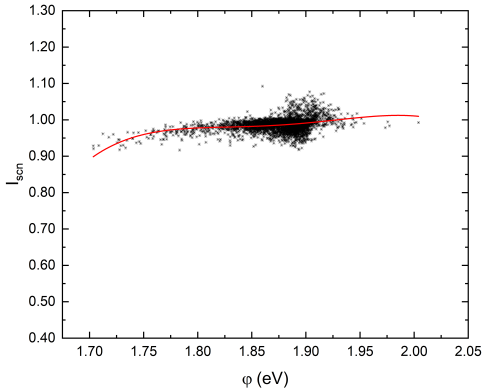

(c) $I_{scn} = f(\varphi)$ SCF for the mSi device. The R^2 value is low, at around 0.1.

Figure 6.5: Comparison of measured and predicted values for the three PV devices.

The aSi-T data show the least variability of the three PV devices, with the tightest correlation and highest R^2. However, one notable feature across all devices is that in the range of approximately 1.85eV $\leq \varphi \leq$ 1.90eV there is a larger spread in I_{scn} relative to the variation in φ, when compared to other values of φ. In this φ range, the same or similar values of φ yield different values of I_{scn}. This means that spectra resulting in different levels of PV performance possess APE values that are insufficiently different to represent the change in I_{scn} to which they lead. This observation substantiates previous work that argues the APE index is incapable of uniquely representing solar spectral

distributions [175, 320]. Improvement in the reliability and prediction accuracy of $f(\varphi)$ is likely to be achieved through attributing the different I_{scn} values to unique value(s) representing the spectrum. Previous research has identified variation in atmospheric water vapour to be the driver of uncertainty in the APE value [175, 11]. Several studies have also found that atmospheric water vapour has a significant impact on the performance of solar panels, in part through its effect on the solar spectrum [328, 65]. These studies find a high variation in PV output due to variable atmospheric precipitable water content levels, in particular for CdTe modules. Guechi et al. [329] find that the short-circuit current of a CdTe module can vary by over 3% as a result of variation in W from 0.5 to 4.0 cm, while a hydrogenated silicon device is found to vary by less than 2.5%. Passow et al. [129] report a more significant variation in CdTe performance of -4% to $+5\%$ when W ranges between 0.5–5.0 cm.

Four 20 nm-wide wavebands centred about 660 nm, 720 nm, 815 nm, and 940 nm, which are identified in [330, 329], are used as the positions of water absorption bands in the subsequent analysis. Through comparing the SCFs derived from multiple wavebands, it is possible to determine whether the uncertainty around $1.85\text{eV} \leq \varphi \leq 1.90\text{eV}$ can be resolved through the inclusion of a water absorption band in the $f(\varphi)$ SCF — $f(\varphi, \varepsilon)$.

In this section, model coefficients for $f(\varphi)$ have been derived for the three PV technologies investigated in this study — aSi-T, CdTe, and mSi. $f(\varphi)$ coefficients for these three PV types have not previously been published in the literature. Furthermore, analysis of the uncertainty in $f(\varphi)$ for each of these three devices, in addition to a review of existing literature, has helped identify four spectral bands as candidates for ε in the $f(\varphi, \varepsilon)$ SCF. The following section presents the new model, $f(\varphi, \varepsilon)$, which addresses the uniqueness issue of the APE parameter that is responsible for the high degree of uncertainty in $f(\varphi)$.

Device	Coefficient				
	a_0	a_1	a_2	a_3	a_4
aSi-T	-2681.4825	5873.6537	-4828.0300	1764.8774	-241.9810
CdTe	-1745.5747	3752.4391	-3022.5415	1081.5722	-145.0411
mSi	-1469.6501	3139.0754	-2511.0929	892.1727	-118.78122

Table 6.2: Fourth order polynomial coefficients for $f(\varphi)$ for each PV device. The fits to which these values refer are shown in Figures 6.5a, 6.5b, and 6.5c for the aSi-T, CdTe, and mSi devices, respectively.

6.5 APE-ε spectral correction

In this section, an additional index is added to the APE spectral correction, $f(\varphi)$. The index is the depth of a water absorption band, ε, which is calculated as the area beneath the spectral irradiance curve within the wavelength range of the specified waveband. The purpose of this additional index is to help distinguish observations that have similar APE values but different values of I_{scn}, in particular in the range of 1.85eV $\leq \varphi \leq$ 1.90eV where this phenomenon is prevalent. Based on the analysis in Section 6.4.1, the following four wavebands are used: 650–670 nm, 710–730 nm, 810–830 nm, and 930–950 nm. For each combination φ-ε, the optimal surface fitting function is determined for further analysis.

6.5.1 Parameterisation of the I_{scn}-φ-ε correlation

For each waveband, the 22 default surface fitting functions available in OriginLab [331] were fit to the data. Typically, around eight fits converged for each waveband. The highest ranking fit for each waveband, according to the BIC and AIC values, was selected for further analysis. These fits for each waveband are summarised in Tables 6.3, 6.4, and 6.5 for the aSi-T, CdTe, and mSi modules, respectively. The extent to which each surface function explains the variability in I_{scn} is characterised by the coefficient of determination, R^2, the

values of which are also included in the aforementioned tables.

ε	R^2	Function
650–670	0.915	LogNormal2D
710–730	0.913	ExtremeCum
810–830	0.912	ExtremeCum
930–950	0.913	ExtremeCum

Table 6.3: R^2 values for the highest ranking surface fit to the data for each of the four wavebands tested for the aSi-T device.

ε	R^2	Function
650–670	0.584	Poly2D
710–730	0.604	RationalTaylor
810–830	0.571	Parabola2D
930–950	0.596	DoseResp2D

Table 6.4: R^2 values for the highest ranking surface fit to the data for each of the four wavebands tested for the CdTe device.

ε	R^2	Function
650–670	0.295	RationalTaylor
710–730	0.242	ExtremeCum
810–830	0.237	LogNormal2D
930–950	0.269	LogNormal2D

Table 6.5: R^2 values for the highest ranking surface fit to the data for each of the four wavebands tested for the mSi device.

For all three devices, an improvement in fitting accuracy is achieved relative to $f(\varphi)$ model regardless of the waveband chosen for ε. The improvement in the SCF achieved through the inclusion of ε is not only apparent in the R^2 value, but also visually evident in the correlations plotted for each device in Figures 6.6a, 6.6b, and 6.6c. In these three graphs, the correlations using the 650–670 nm spectral band are presented as an example, although the described effect is present for all spectral bands. The grouping of observations around the $1.85\text{eV} \leq \varphi \leq 1.90\text{eV}$ range for all PV devices, which was discussed in Section 6.4.1, is spread out into the third dimension created by the additional index. As a result, different values of I_{scn} that were originally attributed to the same

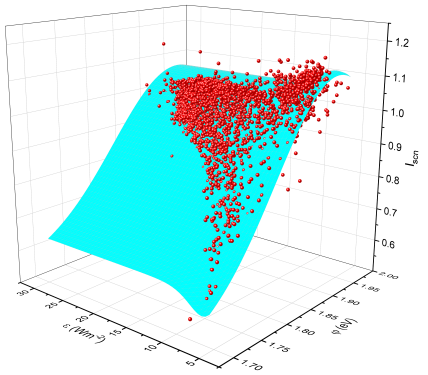

(a) $I_{scn} = f(\varphi, \varepsilon)$ for the aSi-T device, where ε is set as the 650–670 nm band.

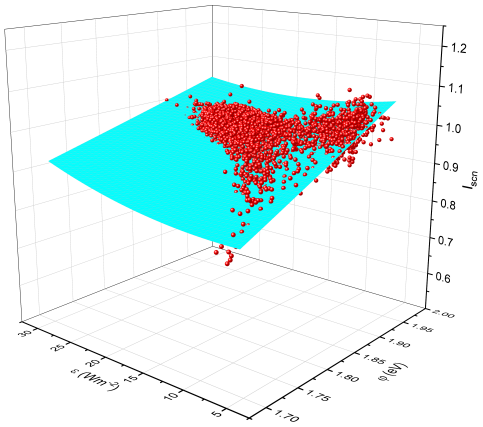

(b) $I_{scn} = f(\varphi, \varepsilon)$ for the CdTe device, where ε is set as the 650–670 nm band.

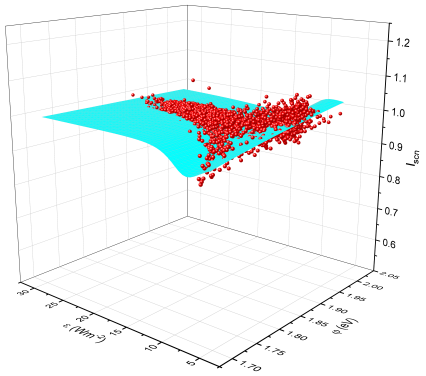

(c) $I_{scn} = f(\varphi, \varepsilon)$ for the mSi device, where ε is set as the 650–670 nm band.

Figure 6.6: $f(\varphi, \varepsilon)$ SCF for the three PV devices, where ε is calculated for the 650–670 nm band.

or similar values of APE are now attributed to unique combinations of APE and ε.

For the aSi-T device, the improvement in R^2 (Table 6.1 vs. 6.3) is relatively small (<0.02) and the fitting accuracy of all wavebands is similar. In contrast, the differences between the R^2 values for the different wavebands is more distinct for the CdTe device, as shown in Table 6.4. The range in R^2 is around 0.04 ($0.56 < R^2 < 0.60$), which is greater than the range for the aSi-T device. This may be due to the higher susceptibility of CdTe performance to changes in atmospheric water vapour content, hence $f(\varphi, \varepsilon)$ could be more sensitive to the water absorption band (ε) selection. Furthermore, the relative improvement of

the spectral correction function through the inclusion of the additional index is higher for CdTe than for the aSi-T device. Comparing $f(\varphi)$ for both devices (Figures 6.5a and 6.5b), the variation in I_{scn} for similar values of APE is significantly greater for the CdTe module than for the aSi-T device, in particular between $1.85\text{eV} \leq \varphi \leq 1.90\text{eV}$. This was to be expected given the wider spectral response of the CdTe module, compared with a single-junction aSi module (discussed in [180]), and the issues discussed earlier regarding the uncertainty in APE values for analysing spectra at longer wavelengths. Therefore, the inclusion of an additional index that helps to distinguish between different performance observations that are matched to the same APE would be expected to benefit the CdTe model more than than the aSi-T model.

For the mSi module, the variation in I_{scn} about the 1.85–1.90 eV band reaches up to around $\pm 10\%$, which is even greater than that of the CdTe module. Hence, it would be expected that the attribution of these different performance observations to uniquely characterised spectra, as opposed to similarly characterised spectra as in Figure 6.5c, would increase the model accuracy significantly. The additional index increases the value of R^2 for the spectral correction function by around 300% (a factor of three). All R^2 values for the mSi module are significantly lower than those resulting from the fits for the other PV devices, but this is to be expected given that the mSi device has a flatter spectral response (weaker spectral dependence of performance) and a higher spectral response within the wavelength range (longer wavelengths) where the APE has a higher characterisation uncertainty, compared with the aSi-T and CdTe modules, as discussed earlier. What is more important than the absolute value of the R^2 coefficient is its relative increase through the inclusion of an additional index in the spectral correction model, which shows degree to which this index mitigates the uncertainty issue of APE.

The variation in the highest ranking spectral band for each device, according

to the R^2, means that no single spectral band can be declared optimal for all devices at this stage of the analysis. The 650–670 nm ranks highest for the aSi-T and mSi devices, although by only a small margin for the former. For the CdTe module, the 650–670 nm band ranks third highest. Moreover, R^2 is only an indicator of how well the surface function fits to the plotted data points, but provides no information on whether the resulting model is a good predictor of the dependent variable when supplied with an arbitrary set of data as an input. A high R^2 value could result from overfitting to the model development dataset and the derived model may not provide accurate predictions when supplied with new data. Therefore, in the following section, the predictive accuracies of the SCFs derived for all four ε bands are analysed.

In this section, the optimal parameterisation of the 3D correlations for each combination of φ-I_w has been determined by ranking different models according to their information criteria. In addition, the R^2 values for each surface fit provide a general indicator of fitting accuracy and show an improvement of $f(\varphi, \varepsilon)$ relative to $f(\varphi)$. In the following section, the optimal waveband, ε, is determined.

6.5.2 Optimisation of ε

The highest ranking parameterisations for each ε band are used to predict I_{scn} values for each DUT using a new dataset, which is the validation dataset described in Section 3.3.2. A simple calculation of the annual Mean Absolute Error (MAE) is used here to compare the prediction accuracies of each SCF for each PV device. First, as an overall indication of accuracy, the annual mean MAE is examined. A more detailed analysis of the MAE on different timescales throughout the year is presented in the Section 6.6.1, where the proposed SCF is validated.

Device	ε	MAE
aSi-T	650–670	0.0134
	710–730	0.0156
	810–830	0.0134
	930–950	0.0134
CdTe	650–670	0.0149
	710–730	0.0149
	810–830	0.0152
	930–950	0.0150
mSi	650–670	0.0101
	710–730	0.0107
	810–830	0.0107
	930–950	0.0106

Table 6.6: MAE values calculated from predictions of I_{scn} that result from using different spectral bands in the $f(\varphi, \varepsilon)$ SCF.

Table 6.6 shows the MAE values calculated using the best fit function, as identified in Section 6.5.1, for the aSi-T, CdTe, and mSi devices. The results in Table 6.6 show that the wavebands that yielded SCFs with the highest R^2 value do not necessarily result in the lowest MAE. This may be a sign of overfitting in some of the models. The 650–670 nm waveband consistently results in the lowest MAE for each of the DUTs. However, for aSi-T device, the 810–830 and 930–950 wavebands result in the same MAE as the 650–670 waveband. For the CdTe device, the 710–730 waveband results in the same MAE as the 650–670 waveband. Despite these similarities, given that the 650–670 waveband is the most consistent across all three devices, the 650–670 band is considered to be the best choice for further analysis.

The fact that the same waveband gives the lowest prediction error for all three devices suggests that the optimum band selection to characterise the solar spectrum may depend on a fundamental property of the spectrum rather than a device-specific response to the spectrum. None of the three panels have any particular spectral response characteristics between 650–670 nm. Taking the CdTe device as an example, Figure 2.18 shows that its peak spectral response

is at around 900 nm. therefore, one may have expected that a water absorption band closer to this peak response wavelength, such as 930–950 nm, would have been a better choice for ε. Although the waveband 930–950 nm generates a relatively low MAE, it ranks third highest out of the four wavebands. This may indicate that the optimal waveband selection is a particular characteristic of the spectral distribution rather than a device-dependent parameter.

This section has optimised the band selection for ε in the final $f(\varphi, \varepsilon)$ SCF. The 650–670 nm has been concluded to be the optimal waveband for each of the three PV devices and will be used in the final validation of $f(\varphi, \varepsilon)$ in the following section.

6.6 Validation of the APE-ε SCF

The prediction accuracy of the highest ranking surface fits for each PV device are tested in this section in order to validate each model. Following on from the analysis in the previous sections, ε is set as 650–670 nm. The prediction accuracy of the proposed model is determined by comparing values of I_{scn} predicted by $f(\varphi, \varepsilon)$, $I_{scn,f(\varphi)}$, with values of I_{scn} derived from measured data, $I_{scn,meas}$. The prediction accuracy of the proposed model is then compared to that of the single-variable APE spectral correction and a traditional proxy-variable approach based on air mass and atmospheric precipitable water content.

6.6.1 Time series analysis

In this section, the temporal trends in the prediction accuracy and associated uncertainty of the proposed model is analysed. Figures 6.7a, 6.7b, and 6.7c show time series plots of $I_{scn,calc}$ and $I_{scn,meas}$ for the aSi-T, CdTe, and mSi devices, respectively. For these figures, $I_{scn,calc}$ is calculated using $f(\varphi, \varepsilon)$ and

is hence denoted $I_{scn,f(\varphi,\varepsilon)}$.

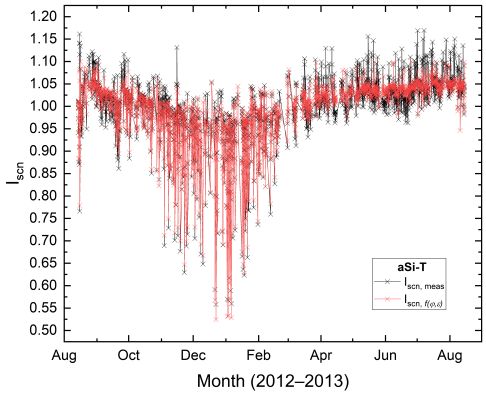

(a) Comparison of the measured and predicted values of I_{scn} (using $f(\varphi,\varepsilon)$) as a function of time for the aSi-T device.

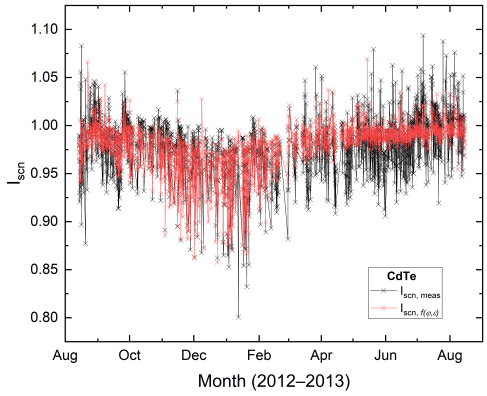

(b) Comparison of the measured and predicted values of I_{scn} (using $f(\varphi,\varepsilon)$) as a function of time for the CdTe device.

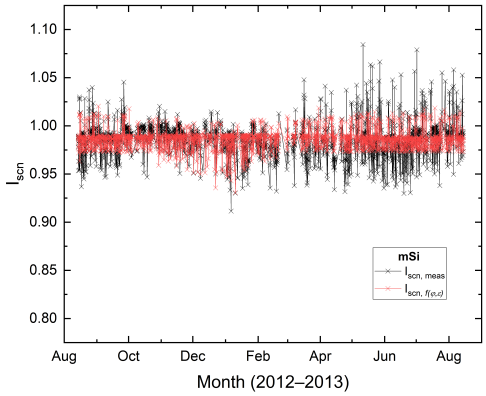

(c) Comparison of the measured and predicted values of I_{scn} (using $f(\varphi,\varepsilon)$) as a function of time for the mSi device.

Figure 6.7: Comparison of measured and predicted values for the three PV devices.

The seasonal variation in $I_{scn,meas}$ for the aSi-T and CdTe devices, identified in Section 6.3 is predicted accurately by the proposed model. The mean absolute errors (MAEs) for the winter months of October–February, during which time this drop in efficiency occurs, are 0.00967 and 0.01262 for the aSi-T and CdTe modules, respectively. $I_{scn,meas}$ for the mSi module exhibits a weaker seasonal trend, but this is still captured in the predictions by the model, which yields an MAE of 0.00936.

In addition to being able to model the long-term seasonal shift in efficiency due to the spectrum, high frequency changes in $I_{scn,meas}$ are also modelled accurately. In particular for the aSi-T device, high frequency fluctuations in $I_{scn,meas}$ above and below unity are captured by the model. The same is true for the mSi and CdTe devices, albeit to a lesser degree for the extreme values of $I_{scn,meas}$.

The prediction error increases for all three devices in the summer months. Whereas the model predicts a relatively stable efficiency in these months with only minor variations $\mathcal{O}(3\,\%)$, in reality $I_{scn,meas}$ exhibits variation $\mathcal{O}(10\,\%)$. Figures 6.8a, 6.8b, and 6.8c show the MAE for each 15-minute measurement and prediction, and the mean monthly MAE. Prediction errors in the summer months are the dominant contributor to the annual MAE values, which are 0.01018, 0.01343, and 0.01495 for the mSi, aSi, and CdTe devices, respectively. One cause of this may lie in the methodology used for the normalisation of I_{sc}. The influence of two factors — irradiance and temperature — were removed from the measured short-circuit current in the normalisation process, and it was assumed the resulting difference of I_{sc}^{*} from the reference current was due to the influence of the spectrum. In the summer, the relative contribution of the direct beam component of irradiance is greater, and thus the angle of incidence (AOI) has a greater effect on module efficiency [220]. However, changes in efficiency due to the AOI have not been considered because to do so would require information on the separate components of irradiance rather than just the global plane of array irradiance. Due to construction work around the meteorological weather station [6] in the summer of 2013, the measurements of the separate components of irradiance suffer from a relatively large number of missing values. Using these data would have impacted the reliability and accuracy of the derived model. Since the primary aim of this study is to present a new method to account for the spectral influence on the performance of PV devices, and demonstrate the relative power of an additional index in the single-

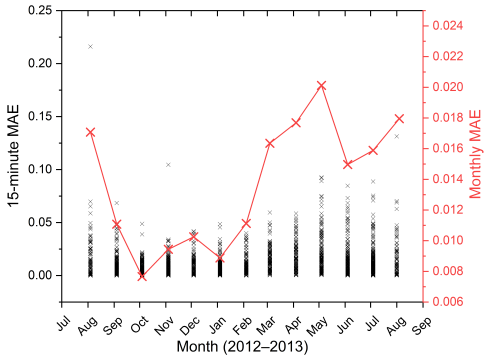

(a) 15-minute (crosses) and monthly MAE (line and crosses) values as a function of time for the aSi-T device. The annual MAE value is 0.0134

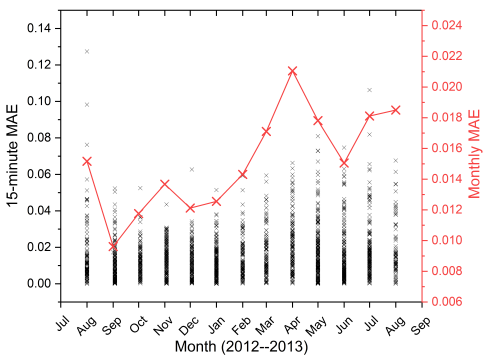

(b) 15-minute (crosses) and monthly MAE (line and crosses) values as a function of time for the CdTe device. The annual MAE value is 0.0149

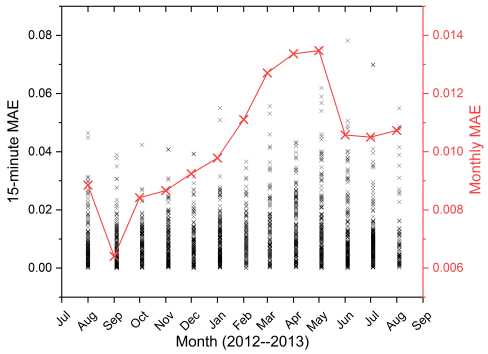

(c) 15-minute (crosses) and monthly MAE (line and crosses) values as a function of time for the mSi device. The annual MAE value is 0.0101

Figure 6.8: MAE values for the I_{scn} forecasts of the three PV devices.

variable APE spectral correction method, it was considered more appropriate to use the larger dataset. The resulting increase in prediction error for the summer months of 2013 is a systematic error present across all models for each device and does not impact the final conclusions of the study in terms of the relative performance of the different models and the parameters they include. There is another spike in the MAE for all models in the month of April 2013. This is likely to be a result of increased atmospheric aerosol during this month, as shown in Figure 3.15.

6.6.2 Comparison with existing models

In this section, the prediction accuracy of the proposed model, $f(\varphi, \varepsilon)$, is compared with that of the APE model, $f(\varphi)$, presented in Section 6.4.1, and a proxy-based alternative — the air mass and precipitable water content model, $f(AM_a, W)$ [2]. The latter is chosen for two reasons. First, as a proxy variable-based approach, it offers an insight into how the two methods — spectra– and proxy-based — compare in terms of accuracy. Second, it is chosen for its similarity in terms of inclusion of the effects of water vapour. The first subsection introduces the $f(AM_a, W)$ model and presents new coefficients for the model that have been derived for the aSi-T in this study. The following subsection compares the predictive accuracies of the different SCFs.

Air mass and precipitable water SCF

The functional form of $f(AM_a, W)$ is presented in Equation 2.30. The coefficients for the $f(AM_a, W)$ model have only been published for crystalline silicon and CdTe PV devices [2]. For the purpose of this study, an additional set of coefficients has been derived for the aSi-T device and these are summarised in Table 6.7.

	b0	b1	b2	b3	b4	b5
aSi-T	0.928	-0.103	-0.0597	0.0939	0.166	0.00656

Table 6.7: $f(AM_a, W)$ model coefficients for the aSi-T PV module.

6.6.3 Performance comparison

Time series plots of the same format as those which were presented in Section 5.3 are presented here for each device, where $I_{scn,calc} = f(AM, W)$. Figures 6.9a and 6.9b show that $f(AM_a, W)$ can accurately predict the seasonal shift

in I_{scn} for the CdTe and aSi-T devices. However, in the case of mSi device, although a decrease in I_{scn} is predicted in the winter months, this decrease is significantly overestimated. The mSi MAEs for the December, January, and February are 0.0151, 0.0144, and 0.0154, respectively.

A common observation across all three PV devices is that whereas $f(AM_a, W)$ is capable of modelling higher frequency variations in I_{scn} than the simple air mass function, with reference to the results reported in [180], the extreme values of I_{scn} are not accurately predicted. Figures 6.9a, 6.9b, and 6.9c show that although $f(AM_a, W)$ tends to estimate a change in I_{scn} correctly, the absolute prediction value is typically either an over– or underestimate. The reason for this may be the fact that W is a relatively simplistic indicator of atmospheric water vapour, without specific reference to its impact on the spectrum. Therefore, W may not be sufficiently sensitive to changes in the spectrum at specific wavelengths, caused by the presence of atmospheric water vapour, that are most significant for PV performance. On the other hand, in the proposed $f(\varphi, \varepsilon)$ SCF, the focus of ε on a specific water absorption band enables greater sensitivity to water vapour-induced changes in the spectrum that are the most influential on PV performance. This notion is supported by the annual values of MAE for all three devices, which are summarised to three significant figures in Table 6.8 for $f(AM_a, W)$, $f(\varphi)$, and $f(\varphi, \varepsilon)$. The proposed model reduces the MAE generated by $f(AM_a, W)$ by approximately 60% for both the mSi and aSi-T modules, and by around 20% for the CdTe module.

For all three PV devices, the new model also reduces the prediction error compared with $f(\varphi)$, albeit by a smaller margin than the improvements on $f(AM_a, W)$. Although the absolute value of the reduction in MAE appears small, the percentage change is around 10% for the mSi and aSi-T devices, and 2% for the CdTe device, which is significant. Although not the main focus of this study, it is still useful to compare the $f(\varphi)$ and $f(AM_a, W)$ SCFs. The

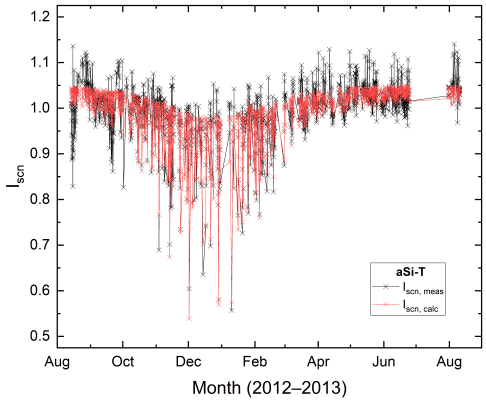

(a) Comparison of the measured and predicted values of $I_{scn} = f(AM, W)$ as a function of time for the aSi-T device.

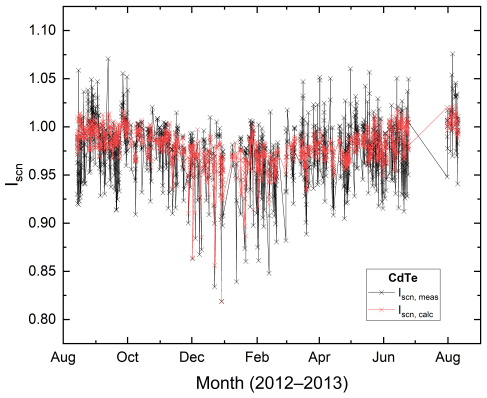

(b) Comparison of the measured and predicted values of $I_{scn} = f(AM, W)$ as a function of time for the CdTe device.

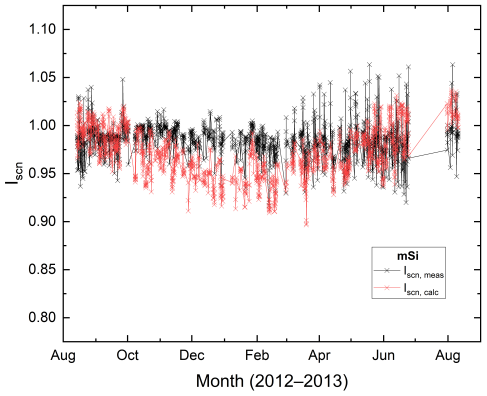

(c) Comparison of the measured and predicted values of $I_{scn} = f(AM, W)$ as a function of time for the mSi device.

Figure 6.9: Comparison of measured and predicted values for the three PV devices.

percentage improvements achieved through the inclusion of ε in the SCF for the aSi-T, CdTe, and mSi modules are around 10%, 2%, and 9%. It is worth bearing in mind that the additional information required for the new model, ε, is already present in data used to calculate φ. Therefore, there is no information cost associated with these improvements since no additional data are required. The only requirement is an extra calculation of the value for ε in the model, but this is relatively simple and does not add any significant computational cost to the overall modelling procedure. On the other hand, the parameterisation

DUT	MAE		
	$f(\varphi)$	$f(AM_a, W)$	$f(\varphi, \varepsilon)$
mSi	0.0112	0.0250	0.0102
CdTe	0.0152	0.0187	0.0149
aSi-T	0.0149	0.0224	0.0134

Table 6.8: Annual MAE values for the predictions made by $f(AM_a, W)$ and $f(\varphi, \varepsilon)$ for each DUT.

of $f(\varphi, \varepsilon)$ is somewhat more complex and if the user is working with a new or customised DUT, greater computational cost would be incurred to derive the model coefficients for this multivariable function. However, in the following section, it is shown that a balance between computational cost and accuracy can easily be struck. Even without the optimal parameterisation of $f(\varphi, \varepsilon)$, where a sub-optimal but simpler parameterisation is used instead, significant improvements in accuracy for all PV devices are still be achieved relative to existing SCFs.

6.6.4 Balancing model complexity and accuracy

It is clear that the proposed spectral correction based on the average photon energy and the depth of a water absorption band exceeds the accuracy of existing spectral corrections significantly. However, the analysis thus far finds that different functional forms of $f(\varphi, \varepsilon)$ offer better information criteria scores for different devices. From a computational complexity perspective, the functions are relatively simple and can easily be integrated into commercial software or other PV performance applications. Nevertheless, a simpler expression could save time for large-scale iterative calculations that may be required when analysing multiple modelling scenarios. Furthermore, from an end-user application perspective, it would be simpler to have a single functional form that only has device-specific coefficients, rather than a device-specific functional form with device-specific coefficients. It is also easier and more efficient to record and

share the model if its form is standardised. In this section, a single functional form is chosen to demonstrate how a high level of accuracy is still maintained even if the optimal functional expression, according to the statistical ranking, is not adopted for $f(\varphi, \varepsilon)$.

The simplest of the functions tested in Section 6.5.1 is the "Poly2D" equation, which takes the following form [332]:

$$z = z_0 + ax + by + cx^2 + dy^2 + fxy. \tag{6.1}$$

In this case, $x = \varphi$ and $y = \varepsilon$. The model coefficients (z_0, a, b, c, d, f) for each DUT are summarised in Table 6.9. The resulting MAE values for the comparison between $I_{scn,calc}$ and $I_{scn,meas}$ are summarised in Table 6.9.

DUT	R^2	Model coefficients					
		z_0	a	b	c	d	f
aSi-T	0.907	-21.94	22.62	-0.01393	-5.521	1.7341×10^{-4}	0.003860
CdTe	0.584	-0.5313	0.7208	0.02232	0.05321	1.629×10^{-4}	-0.01445
mSi	0.194	-0.3998	1.101	0.03366	-0.1837	1.493×10^{-4}	-0.02046

Table 6.9: Poly2D model coefficients for each DUT to four significant figures. R^2 values for the corresponding surface fitting functions are included to three significant figures.

The Poly2D model is used to predict values of I_{scn} in the same way as that which was presented in Section 6.6.3. The resulting annual MAE values for each DUT are summarised in Table 6.10

DUT	MAE
mSi	0.0101
CdTe	0.0150
aSi-T	0.0140

Table 6.10: Annual MAE values for the predictions made by $f(\varphi, \varepsilon)$ for each DUT. ε is set as the 650–670 nm spectral band. The model used is described in Equation 6.1 and the model coefficients for each DUT are summarised in Table 6.9.

The results in this section show that the proposed methodology is relatively flexible in terms of its functional form. It is also clear that the selection of the optimal functional form is a topic for further exploration to find a balance between not only model complexity and accuracy, but also usability. The two-dimensional polynomial function is a simple surface expression and, although it does not offer the highest level of accuracy possible for $f(\varphi, \varepsilon)$, it can still be used to derive an SCF for all three DUTs that improves the MAE value compared with $f(\varphi)$ and $f(AM_a, W)$. The coefficients of this model have been presented in Table 6.9.

6.7 Conclusion

For the Golden test site in the USA, changes in spectral irradiance can lead to variations in PV performance of up to 9%, 5%, and 2% on a monthly average timescale for the aSi-T, CdTe, and mSi devices, respectively. These values increase to 40%, 20%, and 5% on a 15-minute average timescale. A single-variable spectral correction function based on the average photon energy can account for most of this variation, but suffers from increased uncertainty for APE values between 1.85 eV and 1.90 eV. In this range of only 0.05 eV ($\pm$2.5%), the same or similar values of APE are correlated with a wide range ($\pm$10%) of I_{scn} values.

Including an additional parameter in the spectral correction, namely the depth of a water absorption band (ε) enables an association of the different I_{scn} values, which have the same APE value, to unique combinations of APE and ε instead. This work identifies the 650–670 nm spectral band to be optimal for all three devices investigated. Improvements in the prediction accuracy (reductions in the mean absolute error of prediction) of up to 10% are achieved with the new spectral correction. Furthermore, against a comparable two-variable proxy

spectral correction, the air mass and precipitable water SCF, improvements in the prediction accuracy of up to 60% are achieved.

The optimal parameterisation for the model appears to be device-dependent, but in this work it is shown that a compromise can be made between accuracy and complexity by adopting a simple and standard expression for the model for all devices. This expression is a two-dimensional polynomial (Poly2D), the device-specific coefficients for which are summarised in this study. The MAE for all three devices is still either the same or better when using the Poly2D expression rather than the optimal device-specific expression.

This work presents a new spectral correction model that addresses the question of bijectivity with the APE parameter that is used in some existing spectral correction methods. The methodology presented in this work has been demonstrated for three PV devices and the model accuracy has been validated for all three devices. Its benefits with respect to existing approaches have been shown and are manifested in particular through reductions in the normalised short-circuit current prediction error. However, the precise functional form of the model requires further investigation. Although multiple parameterisations have been investigated, further work should continue these investigations in more detail through the use of larger datasets from different climate regions, different statistical analyses, and a wider range of PV devices. The model coefficients in this study are limited by site-specific conditions such as the local climate, the specific technical characteristics of the PV devices, local measurement site set up, etc. Therefore, the precise coefficients presented in this study may not be universally applicable. Nevertheless, the standardised comparison between different SCF methodologies within this study shows that the proposed methodology — an SCF based on both φ and ε — addresses the shortfalls of $f(\varphi)$ and is thus the most accurate. This method should now be validated in different climate regions, PV devices, and so on.

Chapter 7

Geographic generalisation

7.1 Introduction

The data used in the previous chapters have been gathered from one test site in Golden, Colorado, USA. The climate characteristics, including the annual spectral irradiance variation, of this test site were introduced in Section 3.5.

The spectrum is known to vary significantly based on geographical location [333]. Even the performance of the most stable PV technology in terms of spectral response — crystalline silicon — can vary by up to 14% on a weekly basis due to spectral variation at different sites [52]. In a comparison between the climates of Eurasia and Western Africa, spectral variation was found to result in around ±6% variation in PV performance, depending on module type and location [334].

The unique climate characteristics of different locations may render different SCF approaches more or less suitable, in particular the proxy-variable SCFs that rely on a limited number of specific climate parameters. The APE and advanced APE SCF approaches presented in Chapters 5 and 6 may, in theory, be more generally applicable to a wider range of climates since the dependent vari-

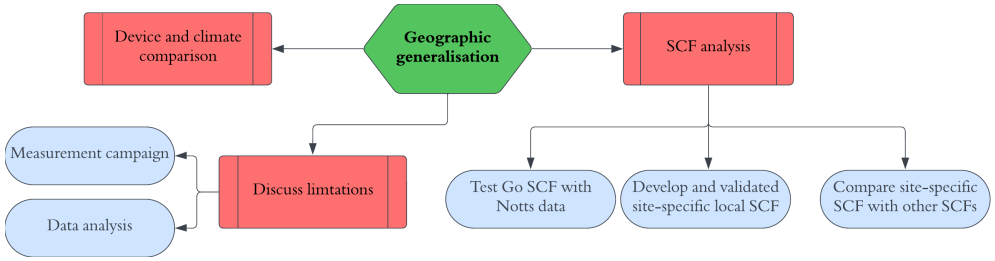

Figure 7.1: Structure of Chapter 7.

ables in the model are derived directly from the measured spectrum. However, uncertainty in the APE parameter resulting from variation in the atmospheric water vapour may mean that, in different locations where the typical annual variation in the spectrum is different, the accuracy of APE-based SCFs may vary. Therefore, it cannot reasonably be assumed that the results presented in this project for the single location of Go are universally applicable to all locations around the world.

The purpose of this chapter is to investigate the generalisability of the results presented in the previous chapters for a secondary location, namely Nottingham, United Kingdom (Notts). Since the PV devices used in Go are not available in the UK, the following subsection compares the available devices to determine whether or not the results from one can be representative of another. The Go model coefficients (Chapters 5 and 6) are then used to predict I_{scn} values for the Notts site to assess whether site-specific model coefficients are required. In the penultimate section, site-specific model coefficients are derived and tested using data from the Notts site. Finally, a summary of the results alongside a discussion of the limitations of the experiment is presented. The structure of this chapter is summarised in Figure 7.1.

	Notts		Go	
(10^{-4})	Slope	Intercept	Slope	Intercept
aSi	2.44	-302	102	-592
CdTe	2.50	-321	112	199
mSi	13.0	-384	98.9	-167

Table 7.1: Linear regression results to three significant figures of I_{sc} and G_{poa} for the three PV devices deployed at each of the two locations.

7.2 Device comparison

In this section, the PV devices deployed at the two test sites are compared. Although the semiconductor material is the same (aSi, mSi, CdTe), manufacturing differences for all three devices can result in differences in the material structure such as the presence of microcracks [335] and defect trapping states [336], which all influence the PV device spectral response [337]. Furthermore, the probability of defect occurrence also increases with device area [338]. Therefore, given the differences between the devices in terms of manufacturing, structure, and surface area, it is likely that properties such as defects, and therefore parameters affecting performance such as recombination probability, are also likely to differ between the devices. However, the significance of these differences is unknown and it is necessary to investigate whether the devices of the same semiconductor type (aSi, CdTe, and mSi) are comparable or not.

An ideal comparison would be between the spectral response curves of the devices. However, SR data is unavailable, hence the outdoor performances are compared. Figure 7.2 shows the relationship between I_{sc}^{*} (temperature– and AOI-normalised short-circuit current) and G_{poa} for the aSi, CdTe, and mSi devices at the Go test site. The linear regression curves plotted on each graph are compared to Figure 3.13 in Section 3.3.1. The slope and intercept values from the regression analysis for both sets of graphs are detailed in Table 7.1.

The results in Table 7.1 appear to show that the devices are not comparable,

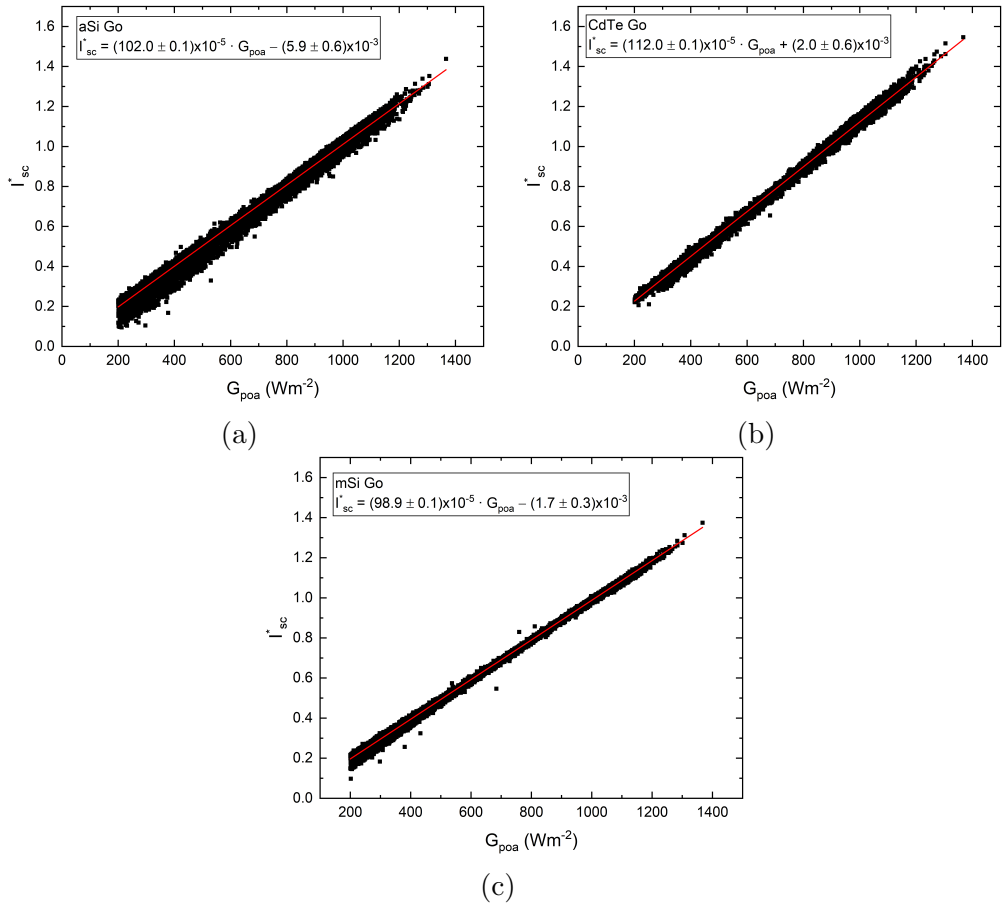

Figure 7.2: I^*_{sc} plots for the three devices deployed in Go along with a linear regression curve for each plot. This linear regression curve is used to assess the comparability between devices of the same semiconductor technology deployed at the two different test sites in this project.

primarily due to the slopes being different by a factor of around fifty for the thin film devices and around eight for the mSi device. This would suggest that the Go SCF coefficients may not be applicable to the UK devices at the UK test site. This hypothesis is tested in the following section, where the scale of the error resulting from using the Go coefficients in the UK is calculated.

7.3 Applying the Go model in Notts

The following analysis compares predictions of I_{scn} made using the Go model coefficients for each device, and the I_{scn} values calculated using data measured at the test site. The purpose of this section is to quantify the scale of the error resulting from the use of non-local model coefficients. Figure 7.3 presents the results of the comparison between the Go-calculated I_{scn} values ($I_{scn,calc,Go}$), and Notts-measured I_{scn} values ($I_{scn,meas,Notts}$).

For the aSi I_{scn} predictions, there is a strong cut off limit of the predicted I_{scn} values at around 1.06 for $f(\varphi)$. A similar but less distinct cut off is present for $f(\varphi, \varepsilon)$ with an almost-vertical column spanning $1.05 \leq I_{scn} \leq 1.10$. This is likely a result of the fact that the the larger I_{scn} values that are observed at the Notts site are beyond the range of the Go models presented in Chapters 5 and 6. The lower measured I_{scn} values that are a part of this vertical band are all from the summer period (after May). During this period, the range of observed φ values is significantly reduced compared with the winter, as discussed in Section 3.5. This φ range issue may be responsible for this mismatch between the I_{scn} values. The inclusion of ε in the model does not resolve the issue. The reason for this may be the fact that the water vapour scattering effects, which are encapsulated by ε, are highly location-specific and this environmental phenomenon may not be uniform across different geographies [339]. The CdTe device exhibits a similarly weak correlation between $I_{scn,calc}$

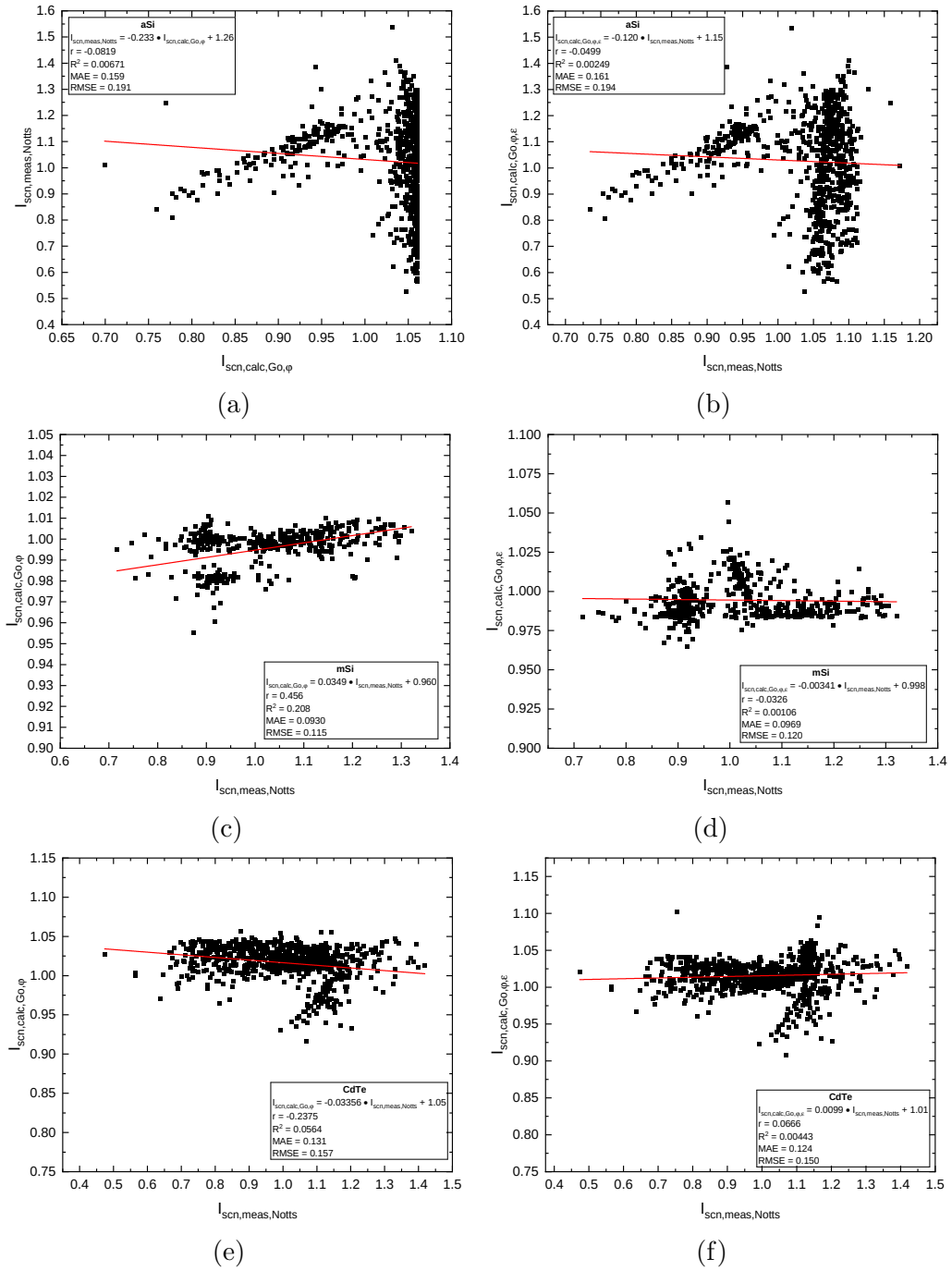

Figure 7.3: Relationship between values of I_{scn} measured in Nottingham and those calculated using the Go coefficients derived in Chapters 5 and 6 for the Golden test site. analysis. Results for the three devices — aSi (a, b), mSi (c, d), and CdTe (e, f) are presented

and $I_{scn,meas}$, although in this case the regression statistics do surpass 0.1 by a small margin.

I_{scn} values are predicted more accurately for the mSi module than for the aSi and CdTe modules. This may be due to there being less variation between mSi modules at the different test sites. However, the correlation is still weak, with values of only 0.456 and 0.208 for r and R^2, respectively. Furthermore, The I_{scn} values predicted by $f(\varphi, \varepsilon)$ do not correlate strongly with the measured values and the regression statistics — both r and R^2 — are below 0.1. This may be due to the effect described earlier of the geographic variation in atmospheric water absorption characteristics.

The RMSE and MAE values for all three devices reflect the weak correlations that have been discussed, exceeding 0.1 in all cases save for the RMSE of the mSi module. The likely cause of this increased error is the difference between the PV devices at the two test sites. To investigate whether the climate has any role in the I_{scn} prediction accuracy, new site-specific model coefficients are derived and validated using the Notts data. This removes the effect of using different PV devices from the analysis. If the trend of improved accuracy achieved by $f(\varphi)$ and $f(\varphi, \varepsilon)$ relative to the proxy-variable SCFs discussed earlier in this thesis is maintained, it may be concluded that the proposed direct-variable approach is a better method.

7.4 UK site-specific SCF development

New site-specific coefficients for the $f(\varphi)$ and $f(\varphi, \varepsilon)$ SCFs are presented here. Tables 6.2 and 7.3 contain the coefficients of the $f(\varphi)$ and $f(\varphi, \varepsilon)$ regressions in Figure 7.4. Although in this chapter an adjusted R^2 value that accounts for the number of predictor variables is used to asses the goodness of fit of the SCFs, no significant difference in the results was found between R^2 and R^2_{adj}. The

	a_0	a_1	a_2	a_3	a_4
aSi	-8346.594	17545.011	-13824.461	4839.855	-635.208
CdTe	188847.681	-391623.172	304428.103	-105134.267	13610.063
mSi	-10319.554	22105.855	-17741.604	6323.072	-844.328

Table 7.2: Notts site-specific model coefficients for the $f(\varphi)$ SCF.

	z_0	a	b	c	d	f
aSi	3.933	-3.251	-0.08884	0.8098	-7.225×10^{-4}	0.06647
CdTe	-25.67	24.175	0.12306	-5.545	-8.198×10^{-5}	-0.03676
mSi	20.47	-21.354	-0.06148	5.860	-2.307×10^{-5}	0.03139

Table 7.3: Notts site-specific model coefficients for the $f(\varphi, \varepsilon)$ SCF.

dominant metrics for assessing the predictive accuracy of the SCFs remains the MAE and RMSE.

In all three plots of $f(\varphi)$ (Figures 7.4a, 7.4c, 7.4e), there is a high degree of uncertainty in the fitting functions. The R^2_{adj} values for the aSi and CdTe modules are <0.1, indicating that variation in φ is incapable of explaining much of the variation in I_{scn}. Only for the mSi module does the R^2_{adj} value exceed 0.1, but is still extremely low at only 0.168. The primary issue appears to be for spectral irradiance conditions where the average photon energy lies between approximately 1.90 eV 1.95 eV. In this small range of φ, there is a large range of I_{scn}, which reaches up to around 0.7 in the case of the CdTe module. This phenomenon of the same φ values resulting in different I_{scn} values is similar to that which was observed in Chapter 6. Therefore, it would be expected that applying the same method proposed in Chapter 6 to minimise this error in the SCF may help with the UK SCF as well.

The $f(\varphi, \varepsilon)$ SCF for the three PV devices (Figures 7.4 (b), (d), and (f)) do in fact show a significant improvement in the fitting accuracy and thus the R^2_{adj} values. Relative to the $f(\varphi)$ parameterisations, the R^2_{adj} values for the aSi, mSi, and CdTe modules improve by factors of around 4.2, 1.4, and 12.5, respectively. The greatest percentage improvement is achieved for the CdTe

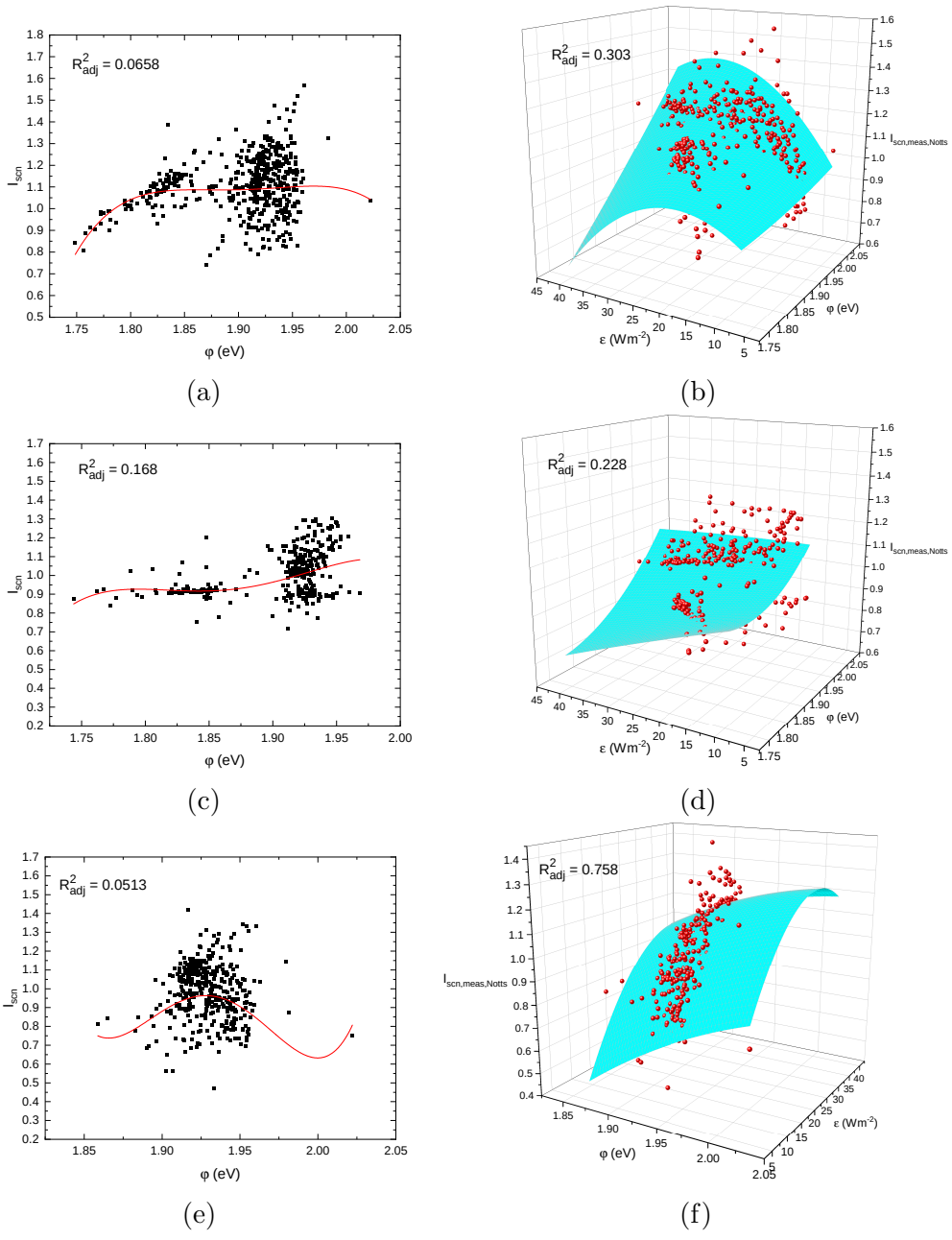

Figure 7.4: Relationship between values of I_{scn} measured in Nottingham and those calculated using the coefficients derived in Chapters 5 and 6 for the Golden test site. Results for the three devices — aSi (a, b), mSi (c, d), and CdTe (e, f) are presented

module, and although this may be expected considering its starting R^2_{adj} value ($f(\varphi)$) was the lowest of the three, its improved R^2_{adj} ($f(\varphi, \varepsilon)$) is also in fact the highest. Therefore, the inclusion of ε in the SCF for the CdTe module not only offers a significant improvement in the SCF fitting accuracy, but may be considered essential for modelling the spectral influence on CdTe PV performance in general. The benefits of including ε in the spectral correction model are apparent from inspection of the Figures 7.4 (b), (d), and (f) for all three devices as well. The crowding of data points around the 1.90 eV–1.95 eV range is spread out into the third dimension created by the additional variable. In this way, different I_{scn} values that are associated with the same φ value may now be distinguished through being associated with unique combinations of φ and ε.

The results presented in this section show that, when using local data from the Notts test site, the overall fitting accuracy of the SCFs is higher relative to the case when the Go coefficients are used with the Notts data. The single-variable APE model offers an extremely weak correlation between I_{scn} and φ compared to the Go data, but the trend in improvement resulting from the inclusion of ε in the module is maintained. In the following section, the prediction accuracies of the models presented in Figure 7.4 are calculated and analysed.

7.5 UK site-specific SCF validation

In this section, site-specific SCF coefficients (coefficients for the devices deployed at the Notts site) are derived for $f(\varphi)$ and $f(\varphi, \varepsilon)$ using data measured at the Notts test site. Validation of the proposed APE-based model in this project is conducted here in two main parts, the first of which is to compare the accuracy of predictions of I_{scn} made using the local SCF and the Go SCF. The second is to discuss the prediction accuracy in absolute terms, more gen-

erally. Further validation of the model is conducted in the following section through a comparison of its performance to a series of proxy-variable SCFs published in the literature previously.

Panels a–f in Figure 7.5 show the correlation between the measured values of I_{scn} and those calculated using the site-specific coefficients calculated in Section 7.4. Linear regression analysis and a series of statistical parameters are used to evaluate the strength of the correlation and predictive accuracy of the SCFs. The results of the regression analysis for each SCF and PV device are summarised in their respective figures.

The prediction accuracies of the Notts SCFs with site-specific coefficients are lower than those of the Go SCFs, also using site-specific coefficient, which were presented in Chapters 5 and 6. The MAE values are several times greater for the Notts data and the correlation between the predicted and measured I_{scn} values is weaker. Nevertheless, phenomena such as the APE bijectivity issue, and trends such as the mitigation of this issue using the depth of a water absorption band, which were first observed in the Go analysis, are upheld in the Notts analysis.

Figure 7.6 shows that the MAE and RMSE values achieved by the site-specific coefficients are lower than those achieved with non-local coefficients in all 20 cases — for both $f(\varphi)$ and $f(\varphi, \varepsilon)$ for all three PV panels. The greatest difference in the MAE and RMSE for $f(\varphi)$ is for the aSi panel, where reductions of over 30% are achieved when site-specific coefficients are used. For $f(\varphi, \varepsilon)$, the greatest improvements in accuracy as is for the CdTe panel, where the MAE is reduced by 62% and the RMSE is reduced by 52.4%. Albeit slightly smaller, the error reductions for the mSi device are still significant for both APE SCFs, with the MAE reductions exceeding 10% and 20%, and the RMSE reductions exceeding 4% and 12%, for $f(\varphi)$ and $f(\varphi, \varepsilon)$, respectively. Tables 7.4 and 7.5 summarise the percentage improvements in MAE and RMSE, respectively, for

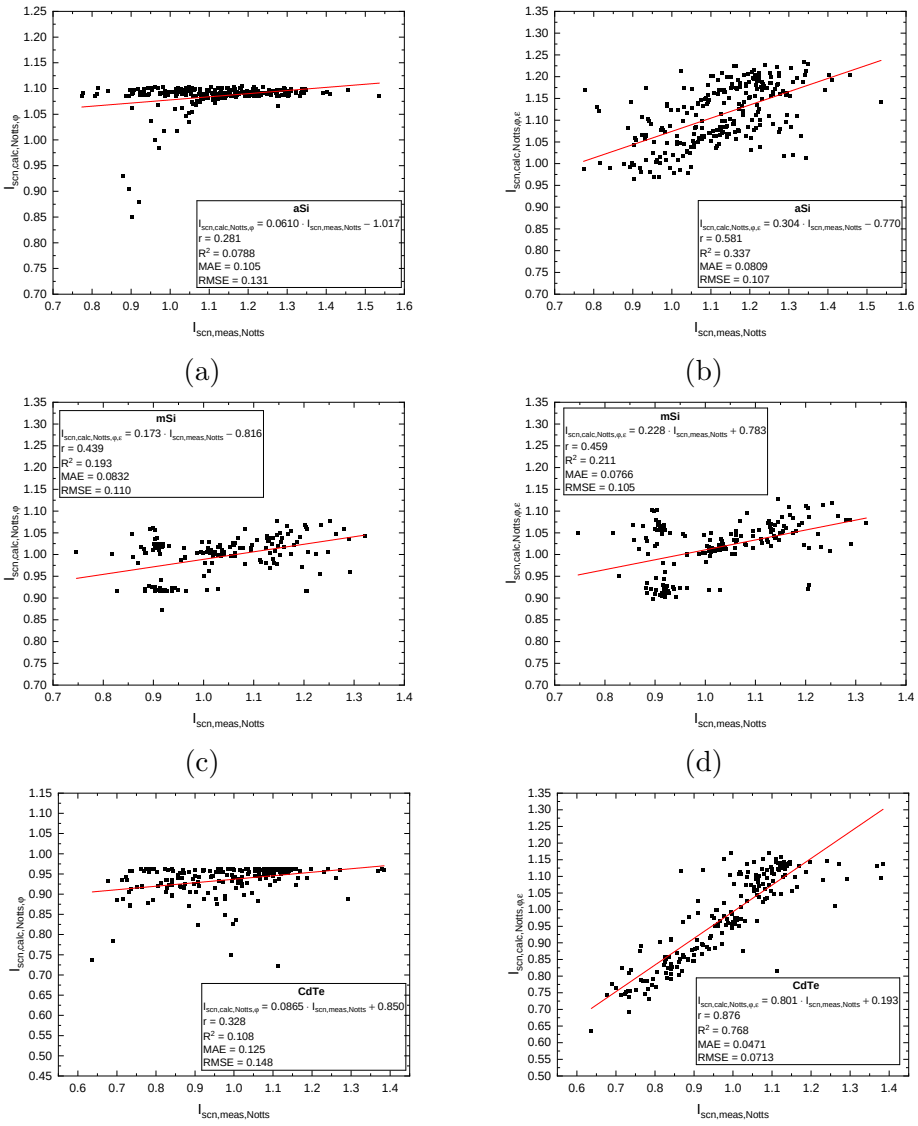

Figure 7.5: Relationship between values of I_{scn} measured in Nottingham and those calculated using device-specific (Nottingham) coefficients. Results for the three devices — aSi (a, b), mSi (c, d), and CdTe (e, f) are presented

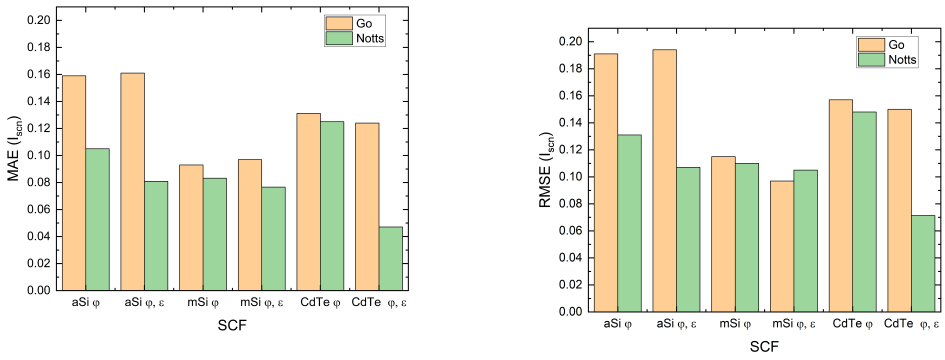

(a) (b)

Figure 7.6: MAE (a) and RMSE (b) comparison between predictions made using Go and Notts SCF coefficients for both APE models ($f(\varphi)$ and $f(\varphi, \varepsilon)$) and for all three PV panels (aSi, mSi, CdTe).

	$f(\varphi)$	$f(\varphi, \varepsilon)$
aSi	34.0	49.8
CdTe	4.73	62.0
mSi	10.5	20.9

Table 7.4: Percentage improvements in the MAE values achieved through using local (Notts) SCF coefficients for $f(\varphi)$ and $f(\varphi, \varepsilon)$ compared with the Go model coefficients. Note that a positive percentage improvement implies a reduction in the value of MAE.

each PV panel and for both $f(\varphi)$ and $f(\varphi, \varepsilon)$.

In addition to the consistent error reduction, as measured by the MAE and RMSE, the results of the linear regression also suggest that the site-specific coefficients are significantly more suited to the SCF analysis. Whereas in Figure 7.3 the r and R^2 values are close to zero, thus indicating that there is only a very weak correlation between $I_{scnmeas,Notts}$ and $I_{scncalc,Go}$. The use of site-specific

	$f(\varphi)$	$f(\varphi, \varepsilon)$
aSi	31.4	44.8
CdTe	5.73	52.4
mSi	4.35	12.5

Table 7.5: Percentage improvements in the RMSE values achieved through using local (Notts) SCF coefficients for $f(\varphi)$ and $f(\varphi, \varepsilon)$ compared with the Go model coefficients. Note that a positive percentage improvement implies a reduction in the value of RMSE.

coefficients to calculate predicted I_{scn} values leads to an improvement in almost all r and R^2 values by an order of magnitude. The final values are still relatively low, save for the CdTe device, but this may be part of the overall systematically higher error discussed earlier. The main result here is the relative difference between the local and non-local coefficients, from which it may be concluded that site-specific coefficients are essential for SCF analysis.

For the for the $f(\varphi, \varepsilon)$ model used with the CdTe panel, the r and R^2 values are 0.876 and 0.768, respectively. These values indicate a strong positive linear correlation between the predicted and measured values of I_{scn}. Alongside the lower MAE and RMSE values and greater error reduction compared with the other PV devices, it may be concluded that for the CdTe device in particular: a) $f(\varphi, \varepsilon)$ is the best choice, and (b) site-specific coefficients are essential. For the aSi and mSi devices, the $f(\varphi, \varepsilon)$ model also results in a lower error when compared with the $f(\varphi)$ model, although the difference is less significant than that which is observed for the CdTe panel.

Although the overall prediction errors are larger for each of the PV devices tested at the Notts site compared with the Go site, the trend of error reduction through the inclusion of an addition parameter — ε — in the $f(\varphi)$ model is maintained. In fact, the error reduction at the Notts site is significantly greater for all three modules. At the Go site, the mSi and CdTe MAE reductions were approximately 9% and 2%, while the aSi error reduction was negligible. While the mSi error reduction is similar, with a reduction in the MAE of 8% observed at the Notts site, that of the aSi and CdTe devices is significantly greater at 23% and 62%, respectively.

In this section, it has been shown that site-specific SCF coefficients are necessary. The use of local coefficients reduces both the MAE and RMSE of I_{scn} predictions by up to 62%. Improvements in accuracy are achieved for all PV panels and for both of the APE-based SCFs — $f(\varphi)$ and $f(\varphi, \varepsilon)$. However, the

	n_0	n_1	n_2	n_3	n_4
aSi	2.16687	-1.32628	0.52397	-0.08214	0.00437
CdTe	0.63367	0.59244	-0.24207	-0.01629	0.01097
mSi	0.58858	0.57755	-0.24626	0.03888	-0.00206

Table 7.6: Notts site-specific model coefficients for the $f(AM_a)$ SCF using the Sandia parameterisation of a fourth order polynomial function.

	k_1	k_2	k_3
aSi	1.27205	0.09914	-0.05941
CdTe	1.36913	0.28942	-0.14023
mSi	1.02015	-0.06538	-0.06538

Table 7.7: Notts site-specific model coefficients for the $f(AM_a, K_t)$ SCF using the PVSPEC parameterisation of a power function.

error values for these models are higher than those found for the Go-site data in Chapters 5 and 6. It is not clear at this stage whether the reduced levels of prediction accuracy for the Notts SCFs is a result of systematic site-specific characteristics, or an issue with the use of the APE-based SCF methodology at the test site. The following section will shed light on this through a comparison of the APE SCFs with other published SCFs in order to determine whether this increased prediction error is systematic across all models at the test site, or specific to the APE-based approaches.

7.6 Comparison with proxy-variable SCFs

The final stage of this analysis is to compare the performance of the spectra-based SCFs to that of proxy-based SCFs. The three proxy-variable functions examined in the previous chapters are tested here, namely $f(AM_a)$, $f(AM_a, K_t)$, and $f(AM_a, W)$. New model coefficients have been derived for each of these three SCFs using the Notts site data and are summarised in Tables 7.6, 7.7, and 7.8. Figure 7.7 presents the parameterisations.

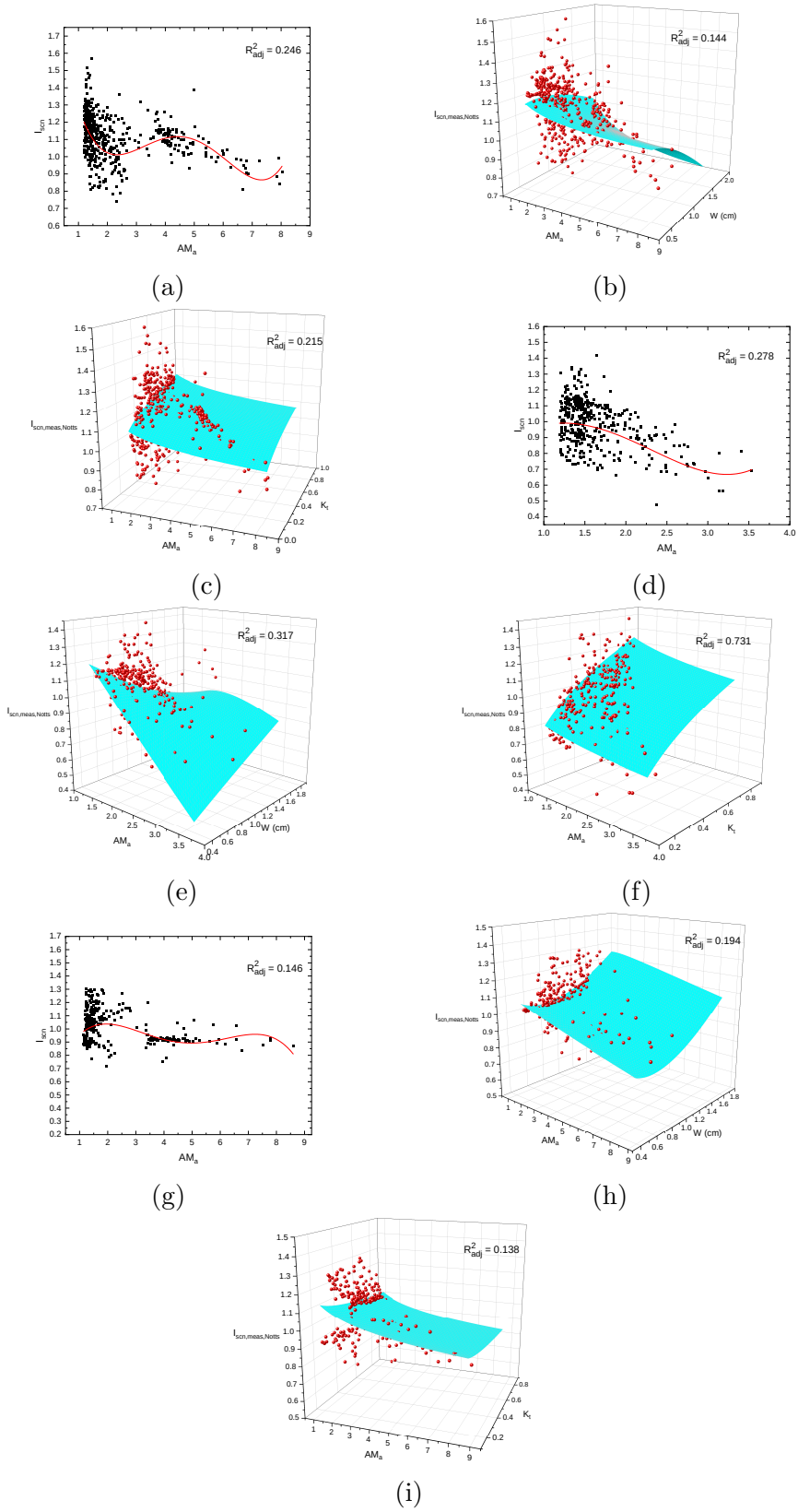

Figure 7.7: The three proxy-variable SCFs for the aSi (a–c), CdTe (d-f), and mSi (g-i) panels. The adjusted coefficient of determination (R^2_{adj}) value for each parameterisation is recorded on its respective figure. The model coefficients for each fit are recorded in Tables 7.6, 7.7, and 7.8.

	b0	b1	b2	b3	b4	b5
aSi	0.93528	-0.73621	0.01504	0.79982	-0.08325	0.26267
CdTe	2.73567	1.15685	-0.03139	0.08941	-1.26007	-1.70455
mSi	1.99287	1.28222	-0.01838	-2.07202	-0.06125	-0.0752

Table 7.8: Notts site-specific model coefficients for the $f(AM_a, W)$ SCF using the First Solar parameterisation of a two-dimensional polynomial function.

For the aSi and mSi modules, none of the SCF R^2_{adj} values exceed 0.3, indicating an existant but weak correlation. The AM_a variable, be it alone or combined with either K_t or W, is incapable of explaining up to around 70% of the variation in I_{scn}. For the CdTe module, although the R^2_{adj}value for $f(AM_a)$ is still just shy of 0.3, that of $f(AM_a, W)$ and $f(AM_a, K_t)$ reaches 0.317 and 0.731, respectively. The distinctly high value for $f(AM_a, K_t)$, but low value for $f(AM_a)$, suggests that the clearness index is a strong indicator of the variation in I_{scn} for the CdTe module. This is similar to the case with $f(\varphi)$ and $f(\varphi, \varepsilon)$, where $f(\varphi, \varepsilon)$ was found to have a significantly higher R^2_{adj} value (0.758 vs. 0.0513), which suggests that ε is the dominant explanatory variable of I_{scn}. Although these two parameters, ε and K_t, are representing different environmental phenomenon, it may be the case that these two are linked. The spectral variation that changes in cloud cover are being used to represent may be variation in the depth of water absorption bands in the spectrum. Figure 7.8 shows the correlation between K_t (indicator of cloud cover variation) and ε (indicator of water absorption band depth variation). The very strong positive correlation between the two variables supports the idea that variation in cloud cover, as represented by the clearness index, may be responsible for changes in the depth of the 650–670 nm water absorption band, which is at least one of the primary drivers of spectral mismatch variation for the CdTe PV module deployed at the Notts test site.

Figures 7.10, 7.11, and 7.12 show the correlation between the measured values of I_{scn} and those calculated using each of the three proxy-variable SCFs for the aSi, CdTe, and mSi panels, respectively. For the aSi module, all three SCFs

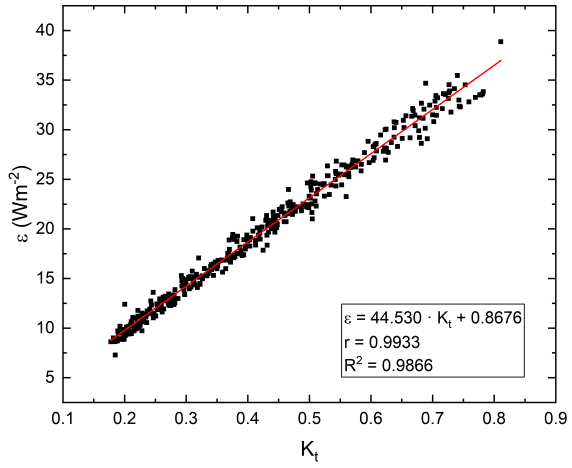

Figure 7.8: Linear regression between the spectral characterisation indices ε and K_t.

perform similarly, although $f(AM_a, K_t)$ does show some improvement with respect to the $f(AM_a)$ and $f(AM_a, W)$ SCFs. The r, R^2_{adj}, MAE, and RMSE values for the latter two are around 0.4, 0.144, 0.09, and 0.12, respectively. For $f(AM_a, K_t)$, these values are around 0.5, 0.215, 0.08, and 0.11. These results suggest that K_t is a more important driver of the spectral changes that influence aSi performance than W, and that a two-variable proxy -variable function offers an improvement of up to around 10% in terms of the MAE and around 7% in terms of the RMSE.

The results for the CdTe module are similar to those of the aSi module in that the $f(AM_a, K_t)$ SCF offers more accurate predictions of I_{scn} compared to the $f(AM_a)$ and $f(AM_a, W)$ SCFs. However, in the case of the CdTe module the $f(AM_a)$ SCF performs worse than with the aSi module, while the $f(AM_a, W)$ SCF performs better. This may be due to the importance of variation in W for the spectral mismatch of CdTe devices in general [2, 152]. Given that the importance of W for CdTe performance has been emphasised in the existing literature, it is somewhat surprising that the $f(AM_a, K_t)$ model outperforms the $f(AM_a, W)$ model. The reason for this may once again be the geographic variation in the effects of atmospheric water vapour content that was highlighted earlier, since the aforementioned studies are focused on US climates. In

addition, both K_t and W are relatively broad indicators. As alluded to earlier, changes in cloud cover indicated by K_t may be influencing specific features of the atmospheric water vapour content that are not conveyed by changes in W but, rather, changes in ε. However, deeper analysis of these atmospheric phenomena to verify this theory is beyond the scope of this study. In future work, this could be evaluated through sensitivity analysis of ε, potentially at different waveband intervals, to changes in K_t, W, and other atmospheric parameters. In terms of the $f(AM_a, K_t)$ performance specifically, the regression statistics indicate a stronger correlation between the measured and predicted values of I_{scn} for the CdTe module than for the aSi module, The r, R^2_{adj}, MAE, and RMSE values are 0.858, 0.736, 0.0538, and 0.0759. Although the MAE and RMSE values still exhibit the systematic increase in magnitude discussed earlier, the linear regression statistics suggest that the combination of AM_a and K_t is a good predictor of I_{scn} for the CdTe module at the Notts test site.

Finally, for the mSi module, $f(AM_a, W)$ performs slightly better than $f(AM_a, K_t)$. However, the difference between the single– and multivariable approaches are less significant for the mSi module than for the aSi and CdTe modules. Therefore, it may be concluded that AM_a is an important driver of spectral changes that influence the mismatch factor of mSi PV devices, which is consistent with reports in the literature [218]. Nevertheless, the two-variable approaches still offer a non-negligible improvement in the linear regression statistics and reduction in MAE and RMSE, which is consistent with the findings of previous research [2].

The MAE and RMSE values for all five SCFs are summarised in Figure 7.9. All SCFs exhibit higher error values than those reported in Chapters 5 and 6 for the SCFs derived using the Go data. This may suggest that the higher error values highlighted in the previous section may result from a systematic site error, rather than a specific issue with the use of the APE parameter, as all

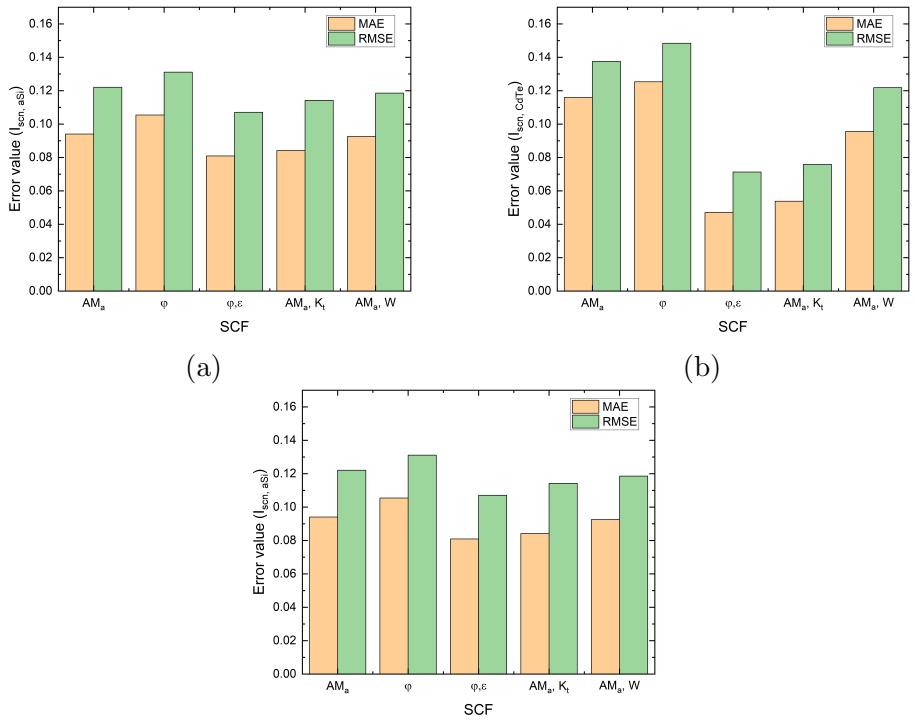

Figure 7.9: The mean absolute error (MAE) and root mean squared error (RMSE) calculated from predictions of I_{scn} using the Notts dataset for five SCFs and three PV panels. Panels (a), (b), and (c) present the results for the aSi, CdTe, and mSi devices, respectively. Each pair of bars indicates the MAE (left) and RMSE (right) for each SCF on the x-axis.

SCFs — including the proxy-variable SCFs — appear to be similarly affected. The systematic nature of this error means that a comparative analysis between the SCFs' errors remains unaffected.

The $f(\varphi, \varepsilon)$ function is shown in Figure 7.9 to outperform all other SCFs, both in terms of MAE and RMSE, for all three PV devices. The single-variable SCFs, namely $f(AM_a)$ and $f(\varphi)$ are the worst performing of the five, with over double the MAE and RMSE of $f(\varphi, \varepsilon)$ in the case of the CdTe module.

Tables 7.9, 7.10, and 7.11 summarise the improvement in MAE and RMSE achieved by $f(\varphi, \varepsilon)$ compared to the other SCFs for the aSi, CdTe, and mSi PV devices at the Notts test site. In terms of PV device, the greatest improvement in spectral mismatch modelling accuracy is achieved for the CdTe device. The mean improvement in MAE and RMSE across all SCFs is around 35% and

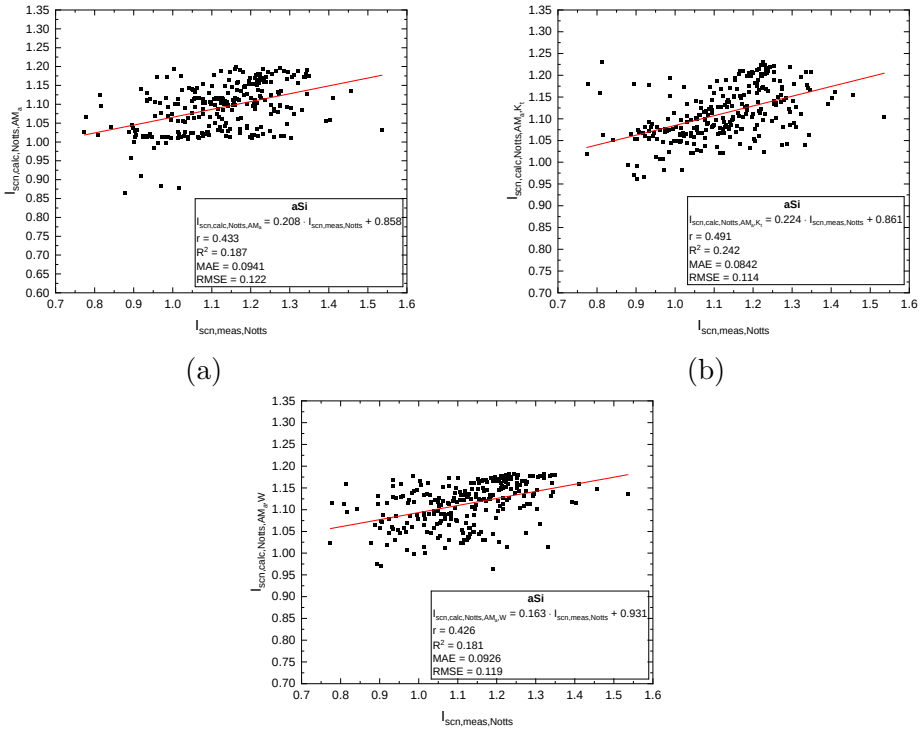

Figure 7.10: Linear regression analysis of the measured values of I_{scn} and those calculated using one of the proxy-variable SCFs for the aSi module.

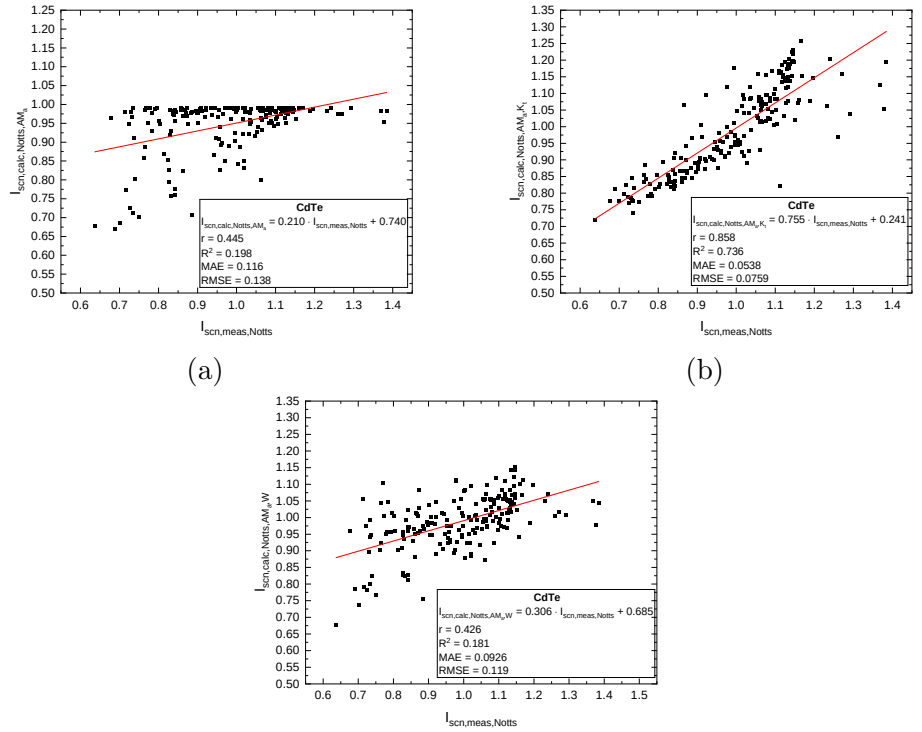

Figure 7.11: Linear regression analysis of the measured values of I_{scn} and those calculated using one of the proxy-variable SCFs for the CdTe module.

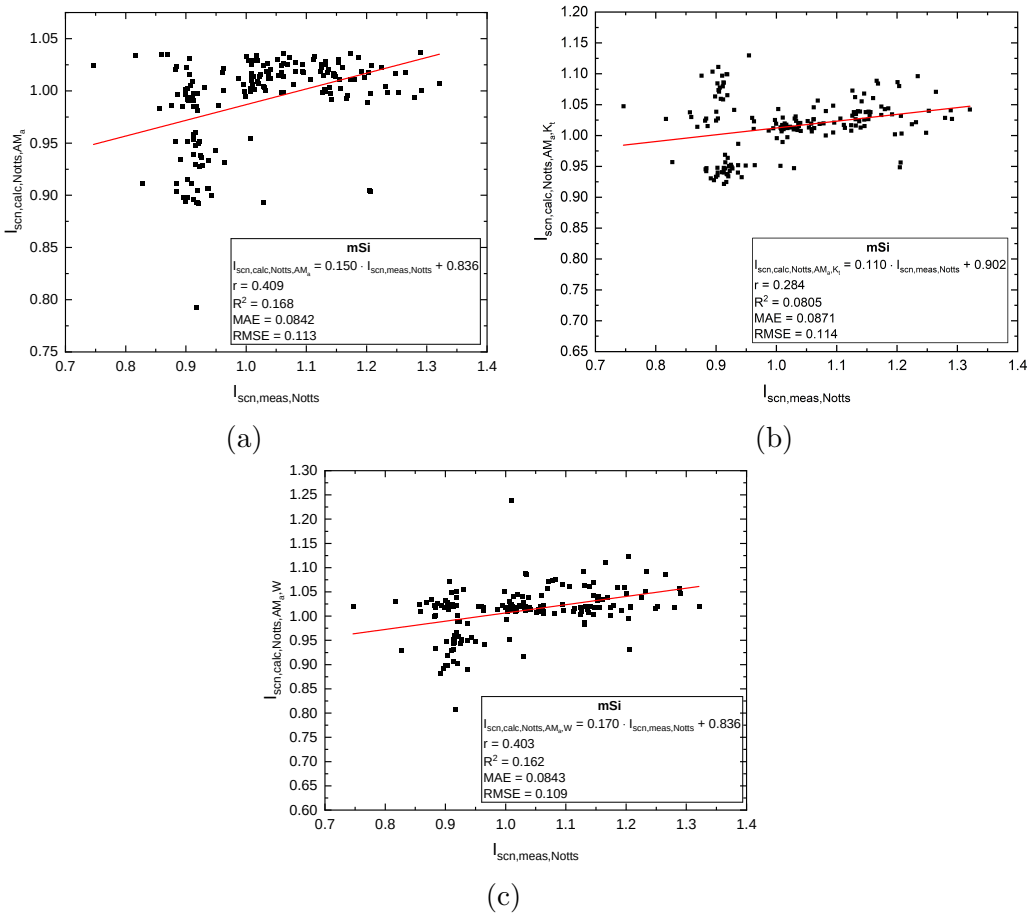

Figure 7.12: Linear regression analysis of the measured values of I_{scn} and those calculated using one of the proxy-variable SCFs for the mSi module.

37%, respectively. The greatest prediction error reductions are when $f(\varphi, \varepsilon)$ is compared to the single-variable SCFs, namely $f(AM_a)$ and $f(\varphi)$, for which improvements of up to around 60% and 50% are achieved for the MAE and RMSE, respectively. Overall, $f(\varphi, \varepsilon)$ exceeds the accuracy of all other SCFs in this analysis. The improvements in MAE and RMSE are of the order of at least 10% but often exceed this value. The closest SCF in terms of accuracy to $f(\varphi, \varepsilon)$ is $f(AM_a, K_t)$, which offers the advantage of not requiring spectral irradiance measurement in its calculation. However, broadband irradiance measurements are still required and, in the best case, the MAE/RMSE is still around 4%/6% greater, while in the worst case the values are 12%/8% greater. Therefore, $f(AM_a, K_t)$ should only be used in place of $f(\varphi, \varepsilon)$ in the complete absence of spectral irradiance data.

	% improvement by $f(\varphi, \varepsilon)$	
	MAE	RMSE
$f(AM_a)$	14	12
$f(\varphi)$	23	18
$f(AM_a, K_t)$	3.9	6.3
$f(AM_a, W)$	13	9.7

Table 7.9: Percentage improvement in MAE and RMSE achieved by $f(\varphi, \varepsilon)$ for the aSi module when compared with other SCFs.

	% improvement by $f(\varphi, \varepsilon)$	
	MAE	RMSE
$f(AM_a)$	59	48
$f(\varphi)$	62	52
$f(AM_a, K_t)$	12	6.0
$f(AM_a, W)$	5.1	41

Table 7.10: Percentage improvement in MAE and RMSE achieved by $f(\varphi, \varepsilon)$ for the CdTe module when compared with other SCFs at the Notts test site.

Overall, a mean reduction in the MAE/RMSE values for the aSi, CdTe, and mSi devices of around 13%/12%, 46%/37%, respectively. This is in line with the expectation that the improvements would be greatest for the thin film devices due in part to the greater susceptibility of their performance to spectral variation. Out of the two thin film devices, the greater improvement achieved for the CdTe module compared with the aSi module may be due to a combination of the particular dependence of CdTe performance on atmospheric water vapour variation, and the precise nature with which the $f(\varphi, \varepsilon)$ model includes water vapour effects through the use of a water absorption spectral band depth. This approach based on ε rather than W appears to serve modelling approach better and improve the overall accuracy with which the spectral mismatch is modelled, especially for the CdTe module.

	% improvement by $f(\varphi, \varepsilon)$	
	MAE	RMSE
$f(AM_a)$	9.0	7.0
$f(\varphi)$	8.0	5.0
$f(AM_a, K_t)$	12	7.9
$f(AM_a, W)$	9.1	3.4

Table 7.11: Percentage improvement in MAE and RMSE achieved by $f(\varphi, \varepsilon)$ for the mSi module when compared with other SCFs at the Notts test site.

7.7 Results summary and limitations

Overall, the design and execution of the experiment presented in this chapter has been a success. The new test site has been used for one year to generate data for the analysis of the spectral influence on PV performance. The results from this analysis, alongside some limitations of the experiment campaign, are discussed in this section.

7.7.1 Results summary

The data support the proposition of the advanced SCF based on the average photon energy and the depth of a water absorption band. For all three PV modules, the $f(\varphi, \varepsilon)$ SCF outperformed the four other SCFs. A mean reduction in the MAE/RMSE values for the aSi, CdTe, and mSi devices of around 13%/12%, 46%/37%, and 10%/6% is achieved by $f(\varphi, \varepsilon)$ compared with the alternative SCFs. Although the absolute values of the prediction accuracies reported in this chapter are lower than those reported in previous chapters that used the Go data, this appears to be a result of a systematic site error. Therefore, the comparative analysis between the SCFs is unaffected. Possible reasons for this increased uncertainty in the modelling at the Notts site are discussed in the following section.

7.7.2 Limitations of the experiment

A limited number of PV panels were tested in this investigation, which makes it hard to generalise the results for each PV technology. With only one year of data, it is also difficult to generalise the results for seasonal trends that may vary on a year-to-year basis. Although the data splicing method takes data from all seasons for both the model development and validation datasets, the final size of the dataset was relatively small compared to that of the Go dataset. Furthermore, the limited number of channels at the beginning of the experiment campaign exacerbated this issue as the mSi and CdTe devices shared the same channel and were therefore not measured for entire duration of the experiment. The upgrading of the equipment to the EKO system resolved this as six channels were set up, but this change in equipment led to a drop in the measurement accuracy. The sensitivity of the EKO equipment was fixed at a higher current and voltage rating that was not suitable for the low IV characteristics of the aSi and CdTe devices in particular. Another limitation related to the system is that the variation in the IV characteristics of the three devices over time was only taken into account in the analysis in a relatively simple way. Although two different values of I_{sc0}, which were calculated from the measured data at different times of the year, were used, this relatively simplistic mitigation measure does not directly address the more complex possibilities of variation in the IV characteristics due to degradation, thermal annealing (aSi), etc.

Chapter 8

Conclusion and scope for further work

8.1 Conclusion

This thesis set out to develop and validate a new method by which the spectral influence on PV performance can be accounted for in PV performance modelling to improve performance forecasting accuracy. The following research questions (**RQs**) were designed for this project:

1. What is the motivation for using spectral proxy variables in spectral correction functions?
2. Can metric(s) derived directly from measured spectral irradiance data offer an alternative basis for a spectral correction function?
3. How do proxy and direct variable spectral correction functions compare in terms of accuracy?
4. Is there value in collecting spectral irradiance data to facilitate the use of direct spectral correction functions in PV performance modelling?

Previous methods to account for this variation in PV performance models are based on one or a combination of proxy variables used to characterise the solar spectrum. Examples of such variables include the solar air mass, clearness index, and atmospheric precipitable water content. All of these variables each individually influence the spectral irradiance conditions measured on the surface. In answer to **RQ1**, historically, these spectral proxies have been used due to the ease with which they can be calculated in the absence of spectral irradiance data.

In this project, the use of parameters derived directly from measured spectra as a basis for a spectral correction function has been investigated. In answer to **RQ2**, this work finds that while a single variable SCF based on the average photon energy is possible, it carries with it a relatively high level of uncertainty since the APE is not a bijective index of the spectrum. In order to achieve unique characterisation of spectral distributions, a two-variable SCF based on the average photon energy and the depth of a water absorption band is proposed. A range of parameterisations were ranked according to their Bayesian and Akaike Information Criterion values, and the final SCF proposed in this work is a two-dimensional polynomial:

$$I_{scn} = f(\varphi, \varepsilon) = z_0 + a\varphi + b\varepsilon + c\varphi^2 + d\varepsilon^2 + f\varphi\varepsilon.$$

The model coefficients (z_0, a, b, c, d, f) for each DUT are summarised in Table 8.1. A range of spectral bands for ε (atmospheric windows and water absorption bands) were assessed, and ultimately the 650–670nm water absorption band was found to be optimal for all PV devices studied. The proposed model has been validated in two locations exhibiting distinct climatic conditions. One location is Golden, Colorado, USA, while the other is the University of Nottingham, Nottingham, UK. It was found that the use of device/site-specific coefficients

	z_0	a	b	c	d	f
aSi (N)	3.933	-3.251	-0.08884	0.8098	-7.225×10^{-4}	0.06647
CdTe (N)	-25.67	24.175	0.12306	-5.545	-8.198×10^{-5}	-0.03676
mSi (N)	20.47	-21.354	-0.06148	5.860	-2.307×10^{-5}	0.03139
aSi-T (G)	-21.94	22.62	-0.01393	-5.521	1.7341×10^{-4}	0.003860
CdTe (G)	-0.5313	0.7208	0.02232	0.05321	1.629×10^{-4}	-0.01445
mSi (G)	-0.3998	1.101	0.03366	-0.1837	1.493×10^{-4}	-0.02046

Table 8.1: $f(\varphi, \varepsilon)$ model coefficients (to four significant figures) for the devices deployed at the Notts (N) and Go (G) test sites.

at the Notts site improved on the use of the Go coefficients at the Notts site through a reduction in the MAE and RMSE for predictions of I_{scn}. For $f(\varphi, \varepsilon)$ applied to the aSi, CdTe, and mSi devices, the MAE values were reduced by 50%, 62%, and 21%, respectively, while the RMSE values were reduced by 45%, 52%, and 13% for these devices. In terms of the overall predictive accuracy, $f(\varphi, \varepsilon)$ SCF has been shown to improve the accuracy with which the PV spectral mismatch (I_{scn}) may be modelled by up to 60% in both Golden (Colorado, USA) and Nottingham (United Kingdom), when compared SCFs published in the existing literature. Tables 7.9, 7.10, and 7.11 in Chapter 7 summarise the percentage reduction in both the MAE and RMSE values achieved by using $f(\varphi, \varepsilon)$ rather than $f(\varphi)$, $f(AM_a)$, $f(AM_a, K_t)$, and $f(AM_a, W)$, for the aSi, CdTe, and mSi PV devices. A mean reduction in the MAE/RMSE values for the aSi, CdTe, and mSi devices of around 13%/12%, 46%/37%, and 10%/6% is achieved by $f(\varphi, \varepsilon)$. In answer to **RQ3**, these data show that $f(\varphi, \varepsilon)$ is consistently more accurate than traditional proxy SCFs. Therefore, this is a strong argument for the more widespread acquisition of spectral irradiance data in the field to improve the overall accuracy of PV performance models (**RQ4**). In the absence of accurate spectral irradiance data, the ranking results from the SCF comparison suggest that $f(AM_a, K_t)$ is used as a compromise. However, the role of simulated spectral distributions in place of measured data has not been explored in this study, which is one area of further work, among others, that is explored in the following section.

8.2 Scope for further work

Despite the increased rigour of the model validation through the use of two locations, this aspect of the investigation suffers from several limitations. The first is the similarity between the devices for the first part of the investigation in Section 7.3. The test used to check their comparability is relatively simple and it would have been ideal if the same device was available in both locations; then the test of whether the coefficients developed in Go work in the UK would have been more reliable. On the other hand, the main aim of this study is to develop a new SCF and the accuracy of the proposed SCF has still been validated in both locations. The analysis of "site-specific" coefficients may in fact be dominated by "device-specific" factors at the different test sites. The questions of whether device/site-specific model coefficients are required can be investigated in future work through the deployment of the same PV devices in different locations.

Another area for future investigation involves the acquisition of spectral irradiance data. In this project, a spectrometer that generates a spectral distribution based in part on spectral irradiance measurements and in part on modelling was used. However, such devices are not yet commonly deployed at PV measurement sites. On the one hand, this project serves as motivation for the wider deployment of spectral irradiance measurements at PV power plants and test sites to enable greater modelling accuracy of existing and future PV systems. On the other hand, testing the $f(\varphi)$ and $f(\varphi, \varepsilon)$ models using simulated spectral irradiance data, for example from the FARMS-NIT model [340], would be a useful line of inquiry. If the high level of accuracy demonstrated in this work is upheld with the use of simulated spectra, the applicability of the proposed model will be greatly enhanced as it would override one of the main arguments for the use of proxy variable SCFs, which is the ease with which their input parameters may be acquired.

Finally, in terms of the scope of analysis, there are two areas that could be explored. First, the proposed SCF could be integrated into different performance models to assess its compatibility with other submodels in the overall performance modelling pipeline. Second, deeper analysis of the performance of different SCFs on a broader range of timescales. Work is currently underway to investigate how different SCFs perform on shorter time scales when intraday weather variation under different sky conditions (clear, overcast, dynamic) are more important. The results of this future investigation would be useful for improving short-term PV performance forecasting accuracy.

References

[1] R. Daxini, R. Wilson, and Y. Wu, "Modelling the spectral influence on photovoltaic device performance using the average photon energy and the depth of a water absorption band for improved forecasting," *Energy*, vol. 284, p. 129046, 2023.

[2] M. Lee and A. Panchula, "Spectral correction for photovoltaic module performance based on air mass and precipitable water," in *2016 IEEE 43rd Photovoltaic Specialists Conference (PVSC)*, pp. 1351–1356, IEEE, 2016.

[3] T. Huld, T. Sample, and E. D. Dunlop, "A simple model for estimating the influence of spectrum variations on pv performance," in *Proceedings of the 24th European Photovoltaic Solar Energy Conference, Hamburg, Germany*, pp. 3385–3389, 2009.

[4] R. Takei, T. Minemoto, S. Yoshida, and H. Takakura, "Output energy estimation of si-based photovoltaic modules using clearness index and air mass," *Japanese Journal of Applied Physics*, vol. 51, no. 10S, p. 10NF10, 2012.

[5] T. Stoffel and A. Andreas, "NREL solar radiation research laboratory (SRRL): Baseline measurement system (BMS); Golden, Colorado (data)," tech. rep., National Renewable Energy Lab (NREL), Golden, CO (United States), 1981.

[6] W. Marion, A. Anderberg, C. Deline, S. Glick, M. Muller, G. Perrin, J. Rodriguez, S. Rummel, K. Terwilliger, and T. Silverman, "User's manual for data for validating models for PV module performance," tech. rep., National Renewable Energy Lab.(NREL), Golden, CO (United States), 2014.

[7] B. Marion, A. Anderberg, C. Deline, M. Muller, G. Perrin, J. Rodriguez, S. Rummel, T. Silverman, F. Vignola, and S. Barkaszi, "Data for validating models for pv module performance," tech. rep., EMN-DURMAT (EMN-DuraMAT); National Renewable Energy Lab.(NREL), Golden, CO ..., 2021.

[8] C. P. Cameron, J. Stein, and C. W. Hansen, "Evaluation of pv performance models and their impact on project risk.," tech. rep., Sandia National Lab.(SNL-NM), Albuquerque, NM (United States), 2011.

[9] M. Theristis *et al.*, "Blind photovoltaic modeling intercomparison: a multidimensional data analysis and lessons learned," *Progress in Photovoltaics: Research and Applications*, vol. tbd, no. tbd, p. tbd, 2023.

[10] American Society for Testing and Materials, *Standard solar constant and zero air mass solar spectral irradiance tables*. ASTM International, 2000.

[11] T. Ishii, K. Otani, A. Itagaki, and K. Utsunomiya, "A methodology for estimating the effect of solar spectrum on photovoltaic module performance by using average photon energy and a water absorption band," *Japanese Journal of Applied Physics*, vol. 51, no. 10S, p. 10NF05, 2012.

[12] B. R. Sutherland, "Solar materials find their band gap," *Joule*, vol. 4, no. 5, pp. 984–985, 2020.

[13] A. M. G. Amillo, T. Huld, P. Vourlioti, R. Müller, and M. Norton, "Application of satellite-based spectrally-resolved solar radiation data to pv performance studies," *Energies*, vol. 8, no. 5, pp. 3455–3488, 2015.

[14] H. Sai, T. Matsui, and K. Matsubara, "Stabilized 14.0%-efficient triple-junction thin-film silicon solar cell," *Applied Physics Letters*, vol. 109, no. 18, p. 183506, 2016.

[15] S. Pelland, C. Beswick, D. Thevenard, A. Côté, A. Pai, and Y. Poissant, "Development and testing of the pvspec model of photovoltaic spectral mismatch factor," in *2020 47th IEEE Photovoltaic Specialists Conference (PVSC)*, pp. 1258–1264, IEEE, 2020.

[16] NREL, "Outdoor Test Facility and Related Facilities." https://www.nrel.gov/pv/outdoor-test-facility.html Last accessed: 2023-05-23.

[17] NREL, "Nrel research facilities." Online, Last accessed 14 June 2023. https://www.nrel.gov/workingwithus/partnering-facilities.html Accessed 2023-06-14.

[18] Weather Spark, "Compare the Climate and Weather in Golden and Nottingham." https://weatherspark.com/compare/y/3539~41783/Comparison-of-the-Average-Weather-in-Golden-and-Nottingham. Last accessed: 2023-01-16.

[19] S. Bouckaert, A. F. Pales, C. McGlade, U. Remme, B. Wanner, L. Varro, D. D'Ambrosio, and T. Spencer, "Net zero by 2050: A roadmap for the global energy sector," tech. rep., International Energy Agency, 2021.

[20] J. Doerr, *Speed & scale: An action plan for solving our climate crisis now*. Penguin, 2021.

[21] M. Taylor, P. Ralon, A. Sonia, M. Jochum, and D. Gielen, *Renewable Power Generation Costs in 2021*. International Renewable Energy Agency, Abu Dhabi, 2022.

[22] A. Cherp, V. Vinichenko, J. Tosun, J. A. Gordon, and J. Jewell, "National growth dynamics of wind and solar power compared to the growth

required for global climate targets," *Nature Energy*, vol. 6, no. 7, pp. 742–754, 2021.

[23] N. Rathore and N. L. Panwar, "Strategic overview of management of future solar photovoltaic panel waste generation in the indian context," *Waste Management & Research*, vol. 40, no. 5, pp. 504–518, 2022.

[24] S. Ladislaw, E. Zindler, N. Tsafos, N. Goldie-Scot, L. Carey, P. Lezcano, J. Nakano, and J. Chase, "Industrial policy, trade, and clean energy supply chains," *Center for Strategic and International Studies. https://www.csis.org/analysis/industrial-policy-trade-and-cleanenergy-supply-chains*, 2021.

[25] R. D. Atkinson, "Why china needs to end its economic mercantilism," *The Huffington Post*, 2008.

[26] B. Frew, W. Cole, P. Denholm, A. W. Frazier, N. Vincent, and R. Margolis, "Sunny with a chance of curtailment: operating the us grid with very high levels of solar photovoltaics," *IScience*, vol. 21, pp. 436–447, 2019.

[27] E. O'Shaughnessy, J. Cruce, and K. Xu, "Rethinking solar pv contracts in a world of increasing curtailment risk," *Energy Economics*, vol. 98, p. 105264, 2021.

[28] E. O'Shaughnessy, J. R. Cruce, and K. Xu, "Too much of a good thing? global trends in the curtailment of solar pv," *Solar Energy*, vol. 208, pp. 1068–1077, 2020.

[29] M. M. Haque and P. Wolfs, "A review of high pv penetrations in lv distribution networks: Present status, impacts and mitigation measures," *Renewable and Sustainable Energy Reviews*, vol. 62, pp. 1195–1208, 2016.

[30] P. Chaudhary and M. Rizwan, "Voltage regulation mitigation techniques in distribution system with high pv penetration: A review," *Renewable and Sustainable Energy Reviews*, vol. 82, pp. 3279–3287, 2018.

[31] F. R. S. Sevilla, D. Parra, N. Wyrsch, M. K. Patel, F. Kienzle, and P. Korba, "Techno-economic analysis of battery storage and curtailment in a distribution grid with high pv penetration," *Journal of Energy Storage*, vol. 17, pp. 73–83, 2018.

[32] L. Bird, D. Lew, M. Milligan, E. M. Carlini, A. Estanqueiro, D. Flynn, E. Gomez-Lazaro, H. Holttinen, N. Menemenlis, A. Orths, *et al.*, "Wind and solar energy curtailment: A review of international experience," *Renewable and Sustainable Energy Reviews*, vol. 65, pp. 577–586, 2016.

[33] G. Notton, M.-L. Nivet, C. Voyant, C. Paoli, C. Darras, F. Motte, and A. Fouilloy, "Intermittent and stochastic character of renewable energy sources: Consequences, cost of intermittence and benefit of forecasting," *Renewable and sustainable energy reviews*, vol. 87, pp. 96–105, 2018.

[34] T. Ma, H. Yang, and L. Lu, "Solar photovoltaic system modeling and performance prediction," *Renewable and Sustainable Energy Reviews*, vol. 36, pp. 304–315, 2014.

[35] A. Mellit, A. M. Pavan, and V. Lughi, "Deep learning neural networks for short-term photovoltaic power forecasting," *Renewable Energy*, vol. 172, pp. 276–288, 2021.

[36] D. Koster, F. Minette, C. Braun, and O. O'Nagy, "Short-term and regionalized photovoltaic power forecasting, enhanced by reference systems, on the example of luxembourg," *Renewable Energy*, vol. 132, pp. 455–470, 2019.

[37] L. Ryan, J. Dillon, S. La Monaca, J. Byrne, and M. O'Malley, "Assessing the system and investor value of utility-scale solar pv," *Renewable and Sustainable Energy Reviews*, vol. 64, pp. 506–517, 2016.

[38] B. Espinar, J.-L. Aznarte, R. Girard, A. M. Moussa, G. Kariniotakis, *et al.*, "Photovoltaic forecasting: A state of the art," in *Proceedings 5th European PV-Hybrid and Mini-Grid Conference*, pp. 250–255, Citeseer, 2010.

[39] G. S. Kinsey, "Solar cell efficiency divergence due to operating spectrum variation," *Solar Energy*, vol. 217, pp. 49–57, 2021.

[40] Department for Energy Security and Net Zero, "Greenhouse gas reporting: conversion factors 2023: Conversion factors 2023: condensed set (for most users) - updated 28 june 2023," tech. rep., United Kingdom Government, 2023.

[41] M. Kerr and A. Cuevas, "Generalized analysis of the illumination intensity vs. open-circuit voltage of solar cells," *Solar Energy*, vol. 76, no. 1-3, pp. 263–267, 2004.

[42] B. V. Chikate, Y. Sadawarte, and B. Sewagram, "The factors affecting the performance of solar cell," *International journal of computer applications*, vol. 1, no. 1, pp. 0975–8887, 2015.

[43] K. Vidyanandan, "An overview of factors affecting the performance of solar pv systems," *Energy Scan*, vol. 27, no. 28, p. 216, 2017.

[44] S. Nann and K. Emery, "Spectral effects on pv-device rating," *Solar Energy Materials and Solar Cells*, vol. 27, no. 3, pp. 189–216, 1992.

[45] N. Chivelet, "Analysis of spectral factor of different commercial pv modules based on measured data," in *14th European PV Conference*, pp. 282–283, 1997.

[46] R. Rüther, G. Kleiss, and K. Reiche, "Spectral effects on amorphous silicon solar module fill factors," *Solar Energy Materials and Solar Cells*, vol. 71, no. 3, pp. 375–385, 2002.

[47] R. Gottschalg, T. Betts, D. Infield, and M. Kearney, "On the importance of considering the incident spectrum when measuring the outdoor performance of amorphous silicon photovoltaic devices," *Measurement Science and Technology*, vol. 15, no. 2, p. 460, 2004.

[48] N. Lindsay, Q. Libois, J. Badosa, A. Migan-Dubois, and V. Bourdin, "Errors in pv power modelling due to the lack of spectral and angular details of solar irradiance inputs," *Solar Energy*, vol. 197, pp. 266–278, 2020.

[49] Y. Hirata and T. Tani, "Output variation of photovoltaic modules with environmental factors—i. the effect of spectral solar radiation on photovoltaic module output," *Solar Energy*, vol. 55, no. 6, pp. 463–468, 1995.

[50] R. Gottschalg, T. R. Betts, D. Infield, and M. J. Kearney, "Experimental investigation of spectral effects on amorphous silicon solar cells in outdoor operation," in *Conference Record of the Twenty-Ninth IEEE Photovoltaic Specialists Conference, 2002.*, pp. 1138–1141, IEEE, 2002.

[51] T. Minemoto, M. Toda, S. Nagae, M. Gotoh, A. Nakajima, K. Yamamoto, H. Takakura, and Y. Hamakawa, "Effect of spectral irradiance distribution on the outdoor performance of amorphous si//thin-film crystalline si stacked photovoltaic modules," *Solar Energy Materials and Solar Cells*, vol. 91, no. 2-3, pp. 120–122, 2007.

[52] G. S. Kinsey, N. C. Riedel-Lyngskær, A.-A. Miguel, M. Boyd, M. Braga, C. Shou, R. R. Cordero, B. C. Duck, C. J. Fell, S. Feron, *et al.*, "Impact of measured spectrum variation on solar photovoltaic efficiencies worldwide," *Renewable Energy*, vol. 196, pp. 995–1016, 2022.

[53] R. A. Senthil, J. Theerthagiri, S. K. Pasha, M. Jagannathan, A. N. Grace, and S. Manickam, "Multijunction solar cells based on iii–v and ii–vi semiconductors," in *Oxide Free Nanomaterials for Energy Storage and Conversion Applications*, pp. 307–328, Elsevier, 2022.

[54] International Energy Agency, "Solar PV," tech. rep., International Energy Agency, 2022. Available at: https://www.iea.org/reports/solar-pv, License: CC BY 4.0.

[55] M. A. Green, E. D. Dunlop, J. Hohl-Ebinger, M. Yoshita, N. Kopidakis, K. Bothe, D. Hinken, M. Rauer, and X. Hao, "Solar cell efficiency tables (version 60)," *Progress in Photovoltaics: Research and Applications*, vol. 30, no. 7, pp. 687–701, 2022.

[56] O. Vigil-Galán, M. Courel, J. Andrade-Arvizu, Y. Sánchez, M. Espíndola-Rodríguez, E. Saucedo, D. Seuret-Jiménez, and M. Titsworth, "Route towards low cost-high efficiency second generation solar cells: current status and perspectives," *Journal of Materials Science: Materials in Electronics*, vol. 26, pp. 5562–5573, 2015.

[57] Z. Duan, X. Liang, Y. Feng, H. Ma, B. Liang, Y. Wang, S. Luo, S. Wang, R. E. Schropp, Y. Mai, *et al.*, "Sb2se3 thin-film solar cells exceeding 10% power conversion efficiency enabled by injection vapor deposition technology," *Advanced Materials*, vol. 34, no. 30, p. 2202969, 2022.

[58] P. Peumans, A. Yakimov, and S. R. Forrest, "Small molecular weight organic thin-film photodetectors and solar cells," *Journal of Applied Physics*, vol. 93, no. 7, pp. 3693–3723, 2003.

[59] K. Keis, E. Magnusson, H. Lindström, S.-E. Lindquist, and A. Hagfeldt, "A 5% efficient photoelectrochemical solar cell based on nanostructured zno electrodes," *Solar energy materials and solar cells*, vol. 73, no. 1, pp. 51–58, 2002.

[60] M. Law, L. E. Greene, J. C. Johnson, R. Saykally, and P. Yang, "Nanowire dye-sensitized solar cells," *Nature materials*, vol. 4, no. 6, pp. 455–459, 2005.

[61] L. Whittaker-Brooks, J. Gao, A. K. Hailey, C. R. Thomas, N. Yao, and Y.-L. Loo, "Bi 2 s 3 nanowire networks as electron acceptor layers in solution-processed hybrid solar cells," *Journal of Materials Chemistry C*, vol. 3, no. 11, pp. 2686–2692, 2015.

[62] M. Iqbal, *An introduction to solar radiation*. Elsevier, 2012.

[63] J. Balenzategui and F. Chenlo, "Measurement and analysis of angular response of bare and encapsulated silicon solar cells," *Solar Energy Materials and Solar Cells*, vol. 86, no. 1, pp. 53–83, 2005.

[64] D. Cheyns, B. Rand, B. Verreet, J. Genoe, J. Poortmans, and P. Heremans, "The angular response of ultrathin film organic solar cells," *Applied physics letters*, vol. 92, no. 24, p. 222, 2008.

[65] P. Faine, S. R. Kurtz, C. Riordan, and J. Olson, "The influence of spectral solar irradiance variations on the performance of selected single-junction and multijunction solar cells," *Solar cells*, vol. 31, no. 3, pp. 259–278, 1991.

[66] R. Eke, T. R. Betts, *et al.*, "Spectral irradiance effects on the outdoor performance of photovoltaic modules," *Renewable and Sustainable Energy Reviews*, vol. 69, pp. 429–434, 2017.

[67] J. Pascual, F. Martinez-Moreno, M. García, J. Marcos, L. Marroyo, and E. Lorenzo, "Long-term degradation rate of crystalline silicon pv modules at commercial pv plants: an 82-mwp assessment over 10 years," *Progress in Photovoltaics: Research and Applications*, vol. 29, no. 12, pp. 1294–1302, 2021.

[68] I. De la Parra, M. Muñoz, E. Lorenzo, M. García, J. Marcos, and F. Martínez-Moreno, "Pv performance modelling: A review in the light of quality assurance for large pv plants," *Renewable and Sustainable Energy Reviews*, vol. 78, pp. 780–797, 2017.

[69] S. Williams, T. Betts, R. Gottschalg, D. Infield, N. van der Borg, A. Burgers, H. De Moor, W. Warta, G. Friesen, D. Chianese, *et al.*, "Evaluating the state of the art of photovoltaic performance modelling in europe," in *20th European Photovoltaic Solar Energy Conference*, pp. 1937–1941, 2005.

[70] C. A. Gueymard, "Clear-sky irradiance predictions for solar resource mapping and large-scale applications: Improved validation methodology and detailed performance analysis of 18 broadband radiative models," *Solar Energy*, vol. 86, no. 8, pp. 2145–2169, 2012.

[71] B. C. Duck and C. J. Fell, "Comparison of methods for estimating the impact of spectrum on pv output," in *2015 IEEE 42nd Photovoltaic Specialist Conference (PVSC)*, pp. 1–6, IEEE, 2015.

[72] D. L. King, J. A. Kratochvil, and W. E. Boyson, "Field experience with a new performance characterization procedure for photovoltaic arrays," tech. rep., Sandia National Labs., Albuquerque, NM (US), 1997.

[73] M. Simon and E. L. Meyer, "The effects of spectral evaluation of c-si modules," *Progress in Photovoltaics: Research and Applications*, vol. 19, no. 1, pp. 1–10, 2011.

[74] C. Voyant, G. Notton, S. Kalogirou, M.-L. Nivet, C. Paoli, F. Motte, and A. Fouilloy, "Machine learning methods for solar radiation forecasting: A review," *Renewable Energy*, vol. 105, pp. 569–582, 2017.

[75] Z. Li, S. Rahman, R. Vega, and B. Dong, "A hierarchical approach using machine learning methods in solar photovoltaic energy production forecasting," *Energies*, vol. 9, no. 1, p. 55, 2016.

[76] P. Lauret, C. Voyant, T. Soubdhan, M. David, and P. Poggi, "A benchmarking of machine learning techniques for solar radiation forecasting in an insular context," *Solar Energy*, vol. 112, pp. 446–457, 2015.

[77] H. A. Kazem, J. H. Yousif, and M. T. Chaichan, "Modeling of daily solar energy system prediction using support vector machine for oman," *International Journal of Applied Engineering Research*, vol. 11, no. 20, pp. 10166–10172, 2016.

[78] M. P. Almeida, O. Perpinan, and L. Narvarte, "Pv power forecast using a nonparametric pv model," *Solar Energy*, vol. 115, pp. 354–368, 2015.

[79] J. H. Yousif, H. A. Kazem, N. N. Alattar, and I. I. Elhassan, "A comparison study based on artificial neural network for assessing pv/t solar energy production," *Case Studies in Thermal Engineering*, vol. 13, p. 100407, 2019.

[80] G. T. Klise and J. S. Stein, "Models used to assess the performance of photovoltaic systems," *Sandia National Laboratories*, 2009.

[81] L. H. Goldstein and G. R. Case, "Pvss—a photovoltaic system simulation program," *Solar Energy*, vol. 21, no. 1, pp. 37–43, 1978.

[82] J. K. Linn, "Photovoltaic system analysis program: Solcel," tech. rep., Sandia Labs., Albuquerque, N. Mex.(USA), 1977.

[83] E. R. Hoover, "Solcel-ii: An improved photovoltaic system analysis program," tech. rep., Sandia Labs., Albuquerque, NM (USA), 1980.

[84] D. Menicucci, "Pvform-a new approach to photovoltaic system performance modeling," tech. rep., Sandia National Labs., Albuquerque, NM (USA), 1985.

[85] M. K. Fuentes, "A simplified thermal model for flat-plate photovoltaic arrays," tech. rep., Sandia National Labs., Albuquerque, NM (USA), 1987.

[86] A. Mermoud and B. Wittmer, "Pvsyst user's manual," *Switzerland, January*, 2014.

[87] W. Marion and K. Urban, *User's Manual for TMY2s Typical Meteorological Years: Derived from the 1961-1990 National Solar Radiation Data Base*. National Renewable Energy Laboratory, 1995.

[88] A. P. Dobos, "Pvwatts version 1 technical reference," tech. rep., National Renewable Energy Lab.(NREL), Golden, CO (United States), 2013.

[89] A. P. Dobos, "Pvwatts version 5 manual," tech. rep., National Renewable Energy Lab.(NREL), Golden, CO (United States), 2014.

[90] A. H. Fanney, M. W. Davis, B. P. Dougherty, D. L. King, W. E. Boyson, and J. A. Kratochvil, "Comparison of photovoltaic module performance measurements," *Solar Energy Engineering*, 2006.

[91] T. U. Townsend, *A method for estimating the long-term performance of direct-coupled photovoltaic systems*. PhD thesis, University of Wisconsin - Madison, 1989.

[92] W. De Soto, S. A. Klein, and W. A. Beckman, "Improvement and validation of a model for photovoltaic array performance," *Solar energy*, vol. 80, no. 1, pp. 78–88, 2006.

[93] E. G. J. Brown, *Guidelines for California's Solar Electric Incentive Programs (Senate Bill 1): Sixth Edition*. California Energy Commission, 2016.

[94] A. H. Fanney, B. P. Dougherty, and M. W. Davis, "Evaluating building integrated photovoltaic performance models," in *Proceedings of the 29th IEEE photovoltaic specialists conference (PVSC), New Orleans, LA, USA*, pp. 194–9, Citeseer, 2002.

[95] C. W. Hansen, D. M. Riley, and M. Jaramillo, "Calibration of the sandia array performance model using indoor measurements," in *2012 38th IEEE Photovoltaic Specialists Conference*, pp. 003067–003072, IEEE, 2012.

[96] J. Peng, L. Lu, H. Yang, and T. Ma, "Validation of the sandia model with indoor and outdoor measurements for semi-transparent amorphous silicon pv modules," *Renewable energy*, vol. 80, pp. 316–323, 2015.

[97] G. R. North, J. A. Pyle, and F. Zhang, *Encyclopedia of atmospheric sciences*, vol. 1. Elsevier, 2014.

[98] D. Renné, "Resource assessment and site selection for solar heating and cooling systems," in *Advances in Solar Heating and Cooling*, pp. 13–41, Elsevier, 2016.

[99] E. Maxwell, W. Marion, D. Myers, M. Rymes, and S. Wilcox, "Final technical report, national solar radiation data base (1961-1990)," *National Renewable Energy Laboratory, Golden, CO, NREL/TP-463-5784*, 1995.

[100] M. Boxwell, *Solar Electricity Handbook: A Simple, Practical Guide to Solar Energy-Designing and Installing Photovoltaic Solar Electric Systems*. Greenstream Publishing, 2010.

[101] G. Stickler, "Educational brief-solar radiation and the earth system. national aeronautics and space administration," 2013.

[102] J. Meydbray, K. Emery, and S. Kurtz, "Pyranometers and reference cells, what's the difference?," tech. rep., National Renewable Energy Lab.(NREL), Golden, CO (United States), 2012.

[103] K. Lovegrove and J. Pye, "Fundamental principles of concentrating solar power (csp) systems," in *Concentrating solar power technology*, pp. 16–67, Elsevier, 2012.

[104] J. C. McVeigh, *Sun power: an introduction to the applications of solar energy*. Elsevier, 2013.

[105] A. Martinez-Gracia, "Solar energy availability," in *Solar Hydrogen Production*, pp. 113–149, Elsevier, 2019.

[106] A. A. Siddiqi, "Optimization of landscape patterns for reflected radiation and the design of building facades/envelope," in *Passive and Low Energy Architecture*, pp. 507–516, Elsevier, 1983.

[107] B. Pon, "Pavement albedo, heat island group," 1999.

[108] T. Markvart, A. McEvoy, and L. Castaner, *Practical handbook of photovoltaics: fundamentals and applications*. Elsevier, 2003.

[109] B. Y. Liu and R. C. Jordan, "The interrelationship and characteristic distribution of direct, diffuse and total solar radiation," *Solar energy*, vol. 4, no. 3, pp. 1–19, 1960.

[110] J. Hay and J. Davies, "Calculations of the solar radiation incident on an inclined surface," in *Proceedings first Canadian Solar Radiation Data Workshop, Toronto. Ontario, Canada 1978*, 1980.

[111] D. T. Reindl, W. A. Beckman, and J. A. Duffie, "Diffuse fraction correlations," *Solar energy*, vol. 45, no. 1, pp. 1–7, 1990.

[112] R. Perez, R. Seals, P. Ineichen, R. Stewart, and D. Menicucci, "A new simplified version of the perez diffuse irradiance model for tilted surfaces," *Solar energy*, vol. 39, no. 3, pp. 221–231, 1987.

[113] R. Perez, R. Stewart, R. Seals, and T. Guertin, "The development and verification of the perez diffuse radiation model," tech. rep., Sandia National Labs., Albuquerque, NM (USA); State Univ. of New York ..., 1988.

[114] T. M. Klucher, "Evaluation of models to predict insolation on tilted surfaces," *Solar energy*, vol. 23, no. 2, pp. 111–114, 1979.

[115] K. Shukla, S. Rangnekar, and K. Sudhakar, "Comparative study of isotropic and anisotropic sky models to estimate solar radiation incident on tilted surface: A case study for bhopal, india," *Energy Reports*, vol. 1, pp. 96–103, 2015.

[116] M. S. Lave, A. P. Pohl, B. Hayes, and W. Hobbs, "Plane of array (poa) irradiance modeling.," tech. rep., Sandia National Lab.(SNL-CA), Livermore, CA (United States); Sandia National ..., 2014.

[117] D. R. Myers, K. Emery, and C. Gueymard, "Revising and validating spectral irradiance reference standards for photovoltaic performance evaluation," *J. Sol. Energy Eng.*, vol. 126, no. 1, pp. 567–574, 2004.

[118] J. Cañada, G. Pedrós, A. López, and J. Boscá, "Influences of the clearness index for the whole spectrum and of the relative optical air mass on uv solar irradiance for two locations in the mediterranean area, valencia and cordoba," *Journal of Geophysical Research: Atmospheres*, vol. 105, no. D4, pp. 4759–4766, 2000.

[119] C. Gueymard *et al.*, *SMARTS2: a simple model of the atmospheric radiative transfer of sunshine: algorithms and performance assessment*, vol. 1. Florida Solar Energy Center Cocoa, FL, 1995.

[120] T. R. Betts, R. Gottschalg, and D. Infield, "Aspire-a tool to investigate spectral effects on pv device performance," in *3rd World Conference on-*

Photovoltaic Energy Conversion, 2003. Proceedings of, vol. 3, pp. 2182–2185, IEEE, 2003.

[121] L. Feng, W. Qin, L. Wang, A. Lin, and M. Zhang, "Comparison of artificial intelligence and physical models for forecasting photosynthetically-active radiation," *Remote Sensing*, vol. 10, no. 11, p. 1855, 2018.

[122] P. Würfel and U. Würfel, *Physics of solar cells: from basic principles to advanced concepts*. John Wiley & Sons, 2016.

[123] F. Kasten and A. T. Young, "Revised optical air mass tables and approximation formula," *Applied optics*, vol. 28, no. 22, pp. 4735–4738, 1989.

[124] B. Marion, "Preliminary investigation of methods for correcting for variations in solar spectrum under clear skies," *University Libraries*, 2010.

[125] K. Rida, A. Al-Waeli, and K. Al-Asadi, "The impact of air mass on photovoltaic panel performance," *Eng. Sci. Rep*, vol. 1, no. 1, pp. 1–9, 2016.

[126] R. P. Kenny, A. Ioannides, H. Müllejans, W. Zaaiman, and E. D. Dunlop, "Performance of thin film pv modules," *Thin solid films*, vol. 511, pp. 663–672, 2006.

[127] A. H. Shnishil, S. S. Chid, M. J. Yaseen, and T. J. Alwana, "Influence of air mass on the performance of many types of pv modules in baghdad," *Energy Procedia*, vol. 6, pp. 153–159, 2011.

[128] C. A. Gueymard, "Parameterized transmittance model for direct beam and circumsolar spectral irradiance," *Solar Energy*, vol. 71, no. 5, pp. 325–346, 2001.

[129] K. Passow and M. Lee, "Effect of spectral shift on solar pv performance," in *2016 IEEE Conference on Technologies for Sustainability (SusTech)*, pp. 246–250, IEEE, 2016.

[130] B. Marion, "Influence of atmospheric variations on photovoltaic performance and modeling their effects for days with clear skies," in *2012 38th IEEE Photovoltaic Specialists Conference*, pp. 003402–003407, IEEE, 2012.

[131] D. L. King, "Photovoltaic module and array performance characterization methods for all system operating conditions," in *AIP conference proceedings*, vol. 394, pp. 347–368, American Institute of Physics, 1997.

[132] W. A. Peterson and I. Dirmhirn, "The ratio of diffuse to direct solar irradiance (perpendicular to the sun's rays) with clear skies–a conserved quantity throughout the day," *Journal of Applied Meteorology (1962-1982)*, pp. 826–828, 1981.

[133] J. Peng, L. Lu, and M. Wang, "A new model to evaluate solar spectrum impacts on the short circuit current of solar photovoltaic modules," *Energy*, vol. 169, pp. 29–37, 2019.

[134] E. Bauer, "The scattering of infrared radiation from clouds," *Applied Optics*, vol. 3, no. 2, pp. 197–202, 1964.

[135] U. Feister, N. Cabrol, and D. Häder, "Uv irradiance enhancements by scattering of solar radiation from clouds," *Atmosphere*, vol. 6, no. 8, pp. 1211–1228, 2015.

[136] H. H. Blau, R. P. Espinola, and E. C. Reifenstein, "Near infrared scattering by sunlit terrestrial clouds," *Applied Optics*, vol. 5, no. 4, pp. 555–564, 1966.

[137] J. Calbó, D. Pages, and J.-A. González, "Empirical studies of cloud effects on uv radiation: A review," *Reviews of Geophysics*, vol. 43, no. 2, 2005.

[138] B. Benabdelkrim, T. Ghaitaoui, and A. Benatillah, "Analysis and evaluation of climatic conditions effect on amorphous silicon pv module," *Journal of Nano- and Electronic Physics*, 2020.

[139] T. R. Betts, C. N. Jardine, R. Gottschalg, D. Infield, and K. Lane, "Impact of spectral effects on the electrical parameters of multijunction amorphous silicon cells," in *3rd World Conference onPhotovoltaic Energy Conversion, 2003. Proceedings of*, vol. 2, pp. 1756–1759, IEEE, 2003.

[140] C. N. Jardine, G. J. Conibeer, and K. Lane, "Pv-compare: direct comparison of eleven pv technologies at two locations in northern and southern europe," in *Seventeenth EU PVSEC*, 2001.

[141] T. Ishii, K. Otani, T. Takashima, and Y. Xue, "Solar spectral influence on the performance of photovoltaic (pv) modules under fine weather and cloudy weather conditions," *Progress in Photovoltaics: Research and Applications*, vol. 21, no. 4, pp. 481–489, 2013.

[142] Q. Zhao, Y. Yao, and W. Yao, "Studies of precipitable water vapour characteristics on a global scale," *International Journal of Remote Sensing*, vol. 40, no. 1, pp. 72–88, 2019.

[143] J. Wang, L. Zhang, A. Dai, T. Van Hove, and J. Van Baelen, "A near-global, 2-hourly data set of atmospheric precipitable water from ground-based gps measurements," *Journal of Geophysical Research: Atmospheres*, vol. 112, no. D11, 2007.

[144] C. H. Reitan, "Surface dew point and water vapor aloft," *Journal of Applied Meteorology (1962-1982)*, pp. 776–779, 1963.

[145] C. Gueymard, "Assessment of the accuracy and computing speed of simplified saturation vapor equations using a new reference dataset," *Journal of Applied Meteorology and Climatology*, vol. 32, no. 7, pp. 1294–1300, 1993.

[146] F. W. Murray, "On the computation of saturation vapor pressure.," tech. rep., Rand Corp Santa Monica Calif, 1966.

[147] S. Tabata, "A simple but accurate formula for the saturation vapor pressure over liquid water," *Journal of Applied Meteorology and Climatology*, vol. 12, no. 8, pp. 1410–1411, 1973.

[148] P. R. Lowe, "An approximating polynomial for the computation of saturation vapor pressure," *Journal of Applied Meteorology (1962-1982)*, pp. 100–103, 1977.

[149] W. Langlois, "A rational approximation for saturation vapor pressure over the temperature range of sea water.," *Journal of Applied Meteorology*, vol. 6, no. 2, pp. 451–452, 1967.

[150] G. L. Stephens, "On the relationship between water vapor over the oceans and sea surface temperature," *Journal of Climate*, vol. 3, no. 6, pp. 634–645, 1990.

[151] C. Gueymard, "Analysis of monthly average atmospheric precipitable water and turbidity in canada and northern united states," *Solar Energy*, vol. 53, no. 1, pp. 57–71, 1994.

[152] L. Nelson, M. Frichtl, and A. Panchula, "Changes in cadmium telluride photovoltaic system performance due to spectrum," *IEEE Journal of Photovoltaics*, vol. 3, no. 1, pp. 488–493, 2012.

[153] J.-P. Putaud, R. Van Dingenen, A. Alastuey, H. Bauer, W. Birmili, J. Cyrys, H. Flentje, S. Fuzzi, R. Gehrig, H.-C. Hansson, *et al.*, "A european aerosol phenomenology–3: Physical and chemical characteristics of particulate matter from 60 rural, urban, and kerbside sites across europe," *Atmospheric Environment*, vol. 44, no. 10, pp. 1308–1320, 2010.

[154] L. A. Remer, R. G. Kleidman, R. C. Levy, Y. J. Kaufman, D. Tanré, S. Mattoo, J. V. Martins, C. Ichoku, I. Koren, H. Yu, *et al.*, "Global aerosol climatology from the modis satellite sensors," *Journal of Geophysical Research: Atmospheres*, vol. 113, no. D14, 2008.

[155] B. N. Holben, T. F. Eck, I. a. Slutsker, D. Tanre, J. Buis, A. Setzer, E. Vermote, J. A. Reagan, Y. Kaufman, T. Nakajima, *et al.*, "Aeronet—a federated instrument network and data archive for aerosol characterization," *Remote sensing of environment*, vol. 66, no. 1, pp. 1–16, 1998.

[156] A. Ångström, "On the atmospheric transmission of sun radiation and on dust in the air," *Geografiska Annaler*, vol. 11, no. 2, pp. 156–166, 1929.

[157] I. Dincer, *Comprehensive energy systems*. Elsevier, 2018.

[158] S. Kalogirou, *McEvoy's handbook of photovoltaics: fundamentals and applications*. Academic Press, 2017.

[159] C. Stark and M. Theristis, "The impact of atmospheric parameters on the spectral performance of multiple photovoltaic technologies," in *2015 IEEE 42nd Photovoltaic Specialist Conference (PVSC)*, pp. 1–5, IEEE, 2015.

[160] M. Theristis, E. F. Fernández, C. Stark, and T. S. O'Donovan, "A theoretical analysis of the impact of atmospheric parameters on the spectral, electrical and thermal performance of a concentrating iii–v triple-junction solar cell," *Energy conversion and management*, vol. 117, pp. 218–227, 2016.

[161] J. Gómez-Amo, M. Freile-Aranda, J. Camarasa, V. Estellés, M. Utrillas, and J. Martínez-Lozano, "Empirical estimates of the radiative impact of an unusually extreme dust and wildfire episode on the performance of a photovoltaic plant in western mediterranean," *Applied Energy*, vol. 235, pp. 1226–1234, 2019.

[162] X. Li, F. Wagner, W. Peng, J. Yang, and D. L. Mauzerall, "Reduction of solar photovoltaic resources due to air pollution in china," *Proceedings of the National Academy of Sciences*, vol. 114, no. 45, pp. 11867–11872, 2017.

[163] E. Liang and V. Kargatis, "Dependence of the spectral evolution of γ-ray bursts on their photon fluence," *Nature*, vol. 381, no. 6577, pp. 49–51, 1996.

[164] C. Tillman, S. Å. Johansson, B. Erlandsson, M. Grätz, B. Hemdal, A. Almén, S. Mattsson, and S. Svanberg, "High-resolution spectroscopy of laser-produced plasmas in the photon energy range above 10 kev," *Nuclear Instruments and Methods in Physics Research Section A: Accelerators, Spectrometers, Detectors and Associated Equipment*, vol. 394, no. 3, pp. 387–396, 1997.

[165] G. B. Armen and H. Wang, "Incident-photon energy-distribution effects on radiationless resonant raman scattering," *Physical Review A*, vol. 51, no. 2, p. 1241, 1995.

[166] G. Neugebauer, W. Wales, and R. Walker, "Photoproduction of negative and positive pions from deuterium for photon energies 500 to 1000 mev," *Physical Review*, vol. 119, no. 5, p. 1726, 1960.

[167] C. N. Jardine, T. Betts, R. Gottschalg, D. Infield, and K. Lane, "Influence of spectral effects on the performance of multijunction amorphous silicon cells," in *Proc. Photovoltaic in Europe Conference*, pp. 1756–1759, 2002.

[168] T. Minemoto, Y. Nakada, H. Takahashi, and H. Takakura, "Uniqueness verification of solar spectrum index of average photon energy for evaluating outdoor performance of photovoltaic modules," *Solar Energy*, vol. 83, no. 8, pp. 1294–1299, 2009.

[169] C. Cornaro and A. Andreotti, "Influence of average photon energy index on solar irradiance characteristics and outdoor performance of photovoltaic modules," *Progress in Photovoltaics: Research and Applications*, vol. 21, no. 5, pp. 996–1003, 2013.

[170] R. Moreno-Sáez and L. Mora-López, "Modelling the distribution of solar spectral irradiance using data mining techniques," *Environmental modelling & software*, vol. 53, pp. 163–172, 2014.

[171] T. Rodziewicz and M. Rajfur, "Numerical procedures and their practical application in pv modules' analyses. part ii: Useful fractions and ape," *Opto-Electronics Review*, vol. 27, no. 2, pp. 149–160, 2019.

[172] M. Piliougine, D. Elizondo, L. Mora-López, and M. Sidrach-de Cardona, "Multilayer perceptron applied to the estimation of the influence of the solar spectral distribution on thin-film photovoltaic modules," *Applied energy*, vol. 112, pp. 610–617, 2013.

[173] G. Nofuentes, B. García-Domingo, J. Muñoz, and F. Chenlo, "Analysis of the dependence of the spectral factor of some pv technologies on the solar spectrum distribution," *Applied energy*, vol. 113, pp. 302–309, 2014.

[174] S. R. Williams, T. R. Betts, T. Helf, R. Gottschalg, H. Beyer, and D. Infield, "Modelling long-term module performance based on realistic reporting conditions with consideration to spectral effects," in *3rd World Conference onPhotovoltaic Energy Conversion, 2003. Proceedings of*, vol. 2, pp. 1908–1911, IEEE, 2003.

[175] G. Nofuentes, C. Gueymard, J. Aguilera, M. Pérez-Godoy, and F. Charte, "Is the average photon energy a unique characteristic of the spectral distribution of global irradiance?," *Solar Energy*, vol. 149, pp. 32–43, 2017.

[176] T. Minemoto, S. Fukushige, and H. Takakura, "Difference in the outdoor performance of bulk and thin-film silicon-based photovoltaic modules," *Solar Energy Materials and Solar Cells*, vol. 93, no. 6-7, pp. 1062–1065, 2009.

[177] T. Minemoto, S. Nagae, and H. Takakura, "Impact of spectral irradiance distribution and temperature on the outdoor performance of amorphous

si photovoltaic modules," *Solar energy materials and solar cells*, vol. 91, no. 10, pp. 919–923, 2007.

[178] S. Nagae, M. Toda, T. Minemoto, H. Takakura, and Y. Hamakawa, "Evaluation of the impact of solar spectrum and temperature variations on output power of silicon-based photovoltaic modules," *Solar Energy Materials and Solar Cells*, vol. 90, no. 20, pp. 3568–3575, 2006.

[179] T. Ishii, K. Otani, and T. Takashima, "Effects of solar spectrum and module temperature on outdoor performance of photovoltaic modules in round-robin measurements in japan," *Progress in Photovoltaics: Research and Applications*, vol. 19, no. 2, pp. 141–148, 2011.

[180] R. Daxini, Y. Sun, R. Wilson, and Y. Wu, "Direct spectral distribution characterisation using the average photon energy for improved photovoltaic performance modelling," *Renewable Energy*, vol. 201, pp. 1176–1188, 2022.

[181] W. Shockley, "The theory of p-n junctions in semiconductors and p-n junction transistors," *Bell System Technical Journal*, vol. 28, no. 3, pp. 435–489, 1949.

[182] N. Pearsall, *The performance of photovoltaic (PV) systems: modelling, measurement and assessment*. Woodhead Publishing, 2016.

[183] S. Hubbard, "Recombination," *Photovoltaic Solar Energy: From Fundamentals to Applications*, pp. 39–46, 2016.

[184] Z. I. Alferov, V. Andreev, and V. Rumyantsev, "Solar photovoltaics: Trends and prospects," *Semiconductors*, vol. 38, pp. 899–908, 2004.

[185] D. M. Bierman, A. Lenert, W. R. Chan, B. Bhatia, I. Celanović, M. Soljačić, and E. N. Wang, "Enhanced photovoltaic energy conversion using thermally based spectral shaping," *Nature Energy*, vol. 1, no. 6, pp. 1–7, 2016.

[186] S. Sharma, M. Kumar, A. Laref, J. Siqueiros, and O. R. Herrera, "Recent advances in interfacial engineering and band-gap tuning of perovskite multiferroic heterostructures for high performance photovoltaic applications," *Materials Letters*, p. 133490, 2022.

[187] C. H. Henry, "Limiting efficiencies of ideal single and multiple energy gap terrestrial solar cells," *Journal of applied physics*, vol. 51, no. 8, pp. 4494–4500, 1980.

[188] F. ISE, "Fraunhofer ise develops the world's most efficient solar cell with 47.6 percent efficiency," tech. rep., Fraunhofer Institute for Solar Energy Systems ISE, May 2022.

[189] P. Schygulla, P. Beutel, S. Heckelmann, O. Höhn, M. Klitzke, J. Schön, E. Oliva, F. Predan, M. Schachtner, G. Siefer, *et al.*, "Quadruple junction solar cell with 47.6% conversion efficiency under concentration," in *20th International Conference on Metal Organic Vapor Phase Epitaxy, Stuttgart, Germany*, 2022.

[190] G. Peharz, G. Siefer, and A. Bett, "A simple method for quantifying spectral impacts on multi-junction solar cells," *Solar Energy*, vol. 83, no. 9, pp. 1588–1598, 2009.

[191] M. Bonnet-Eymard, M. Boccard, G. Bugnon, F. Sculati-Meillaud, M. Despeisse, and C. Ballif, "Optimized short-circuit current mismatch in multi-junction solar cells," *Solar energy materials and solar cells*, vol. 117, pp. 120–125, 2013.

[192] M. A. Green and S. P. Bremner, "Energy conversion approaches and materials for high-efficiency photovoltaics," *Nature materials*, vol. 16, no. 1, pp. 23–34, 2017.

[193] T. Trupke, M. Green, and P. Würfel, "Improving solar cell efficiencies by up-conversion of sub-band-gap light," *Journal of applied physics*, vol. 92, no. 7, pp. 4117–4122, 2002.

[194] T. Trupke, P. Wurfel, and M. A. Green, "Up-and down-conversion as new means to improve solar cell efficiencies," in *3rd World Conference onPhotovoltaic Energy Conversion, 2003. Proceedings of*, vol. 1, pp. 67–70, IEEE, 2003.

[195] E. Klampaftis, D. Ross, K. R. McIntosh, and B. S. Richards, "Enhancing the performance of solar cells via luminescent down-shifting of the incident spectrum: A review," *Solar Energy Materials and Solar Cells*, vol. 93, no. 8, pp. 1182–1194, 2009.

[196] M. Rafiee, S. Chandra, H. Ahmed, and S. J. McCormack, "An overview of various configurations of luminescent solar concentrators for photovoltaic applications," *Optical Materials*, vol. 91, pp. 212–227, 2019.

[197] G. Brito-Santos, B. Gil-Hernández, C. Hernández-Rodríguez, B. González-Díaz, R. Guerrero-Lemus, and J. Sanchiz, "Degradation analysis of highly uv-resistant down-shifting layers for silicon-based pv module applications," *Materials Science and Engineering: B*, vol. 288, p. 116207, 2023.

[198] W. Yang, X. Li, D. Chi, H. Zhang, and X. Liu, "Lanthanide-doped up-conversion materials: emerging applications for photovoltaics and photocatalysis," *Nanotechnology*, vol. 25, no. 48, p. 482001, 2014.

[199] F. Capasso, "Band-gap engineering: from physics and materials to new semiconductor devices," *Science*, vol. 235, no. 4785, pp. 172–176, 1987.

[200] Z. Hu, Z. Lin, J. Su, J. Zhang, J. Chang, and Y. Hao, "A review on energy band-gap engineering for perovskite photovoltaics," *Solar Rrl*, vol. 3, no. 12, p. 1900304, 2019.

[201] R. Caballero, I. Victorov, R. Serna, J. M. Cano-Torres, C. Maffiotte, E. Garcia-Llamas, J. Merino, M. Valakh, I. Bodnar, and M. León, "Band-gap engineering of cu2znsn1- xgexs4 single crystals and influence of the surface properties," *Acta materialia*, vol. 79, pp. 181–187, 2014.

[202] H. Ferhati and F. Djeffal, "Graded band-gap engineering for increased efficiency in czts solar cells," *Optical materials*, vol. 76, pp. 393–399, 2018.

[203] R. Gottschalg, T. Betts, D. Infield, and M. Kearney, "The effect of spectral variations on the performance parameters of single and double junction amorphous silicon solar cells," *Solar energy materials and solar cells*, vol. 85, no. 3, pp. 415–428, 2005.

[204] R. Gottschalg, D. Infield, and M. Kearney, "Experimental study of variations of the solar spectrum of relevance to thin film solar cells," *Solar Energy materials and solar cells*, vol. 79, no. 4, pp. 527–537, 2003.

[205] T. Rodziewicz, J. Teneta, A. Zaremba, and M. Wacławek, "Analysis of solar energy resources in southern poland for photovoltaic applications/analiza struktury zasobów energii słonecznej obszaru polski południowej do zastosowań fotowoltaicznych," *Ecological Chemistry and Engineering S*, vol. 20, no. 1, pp. 177–198, 2013.

[206] D. Magare, O. Sastry, R. Gupta, T. R. Betts, R. Gottschalg, A. Kumar, B. Bora, and Y. Singh, "Effect of seasonal spectral variations on performance of three different photovoltaic technologies in india," *International Journal of Energy and Environmental Engineering*, vol. 7, no. 1, pp. 93–103, 2016.

[207] M. Simon and E. L. Meyer, "Spectral distribution on photovoltaic module performance in south africa," in *2008 33rd IEEE Photovoltaic Specialists Conference*, pp. 1–5, IEEE, 2008.

[208] B. H. King, C. W. Hansen, D. Riley, C. D. Robinson, and L. Pratt, "Procedure to determine coefficients for the sandia array performance model (sapm)," *SAND2016-5284*, vol. 1256510, 2016.

[209] IEC, "Photovoltaic devices — part 9: Classification of solar simulator characteristics," *IEC 60904-9*, 2020.

[210] R. W. Andrews and J. M. Pearce, "The effect of spectral albedo on amorphous silicon and crystalline silicon solar photovoltaic device performance," *Solar Energy*, vol. 91, pp. 233–241, 2013.

[211] M. Alonso-Abella, F. Chenlo, G. Nofuentes, and M. Torres-Ramírez, "Analysis of spectral effects on the energy yield of different pv (photovoltaic) technologies: The case of four specific sites," *Energy*, vol. 67, pp. 435–443, 2014.

[212] C. H. Seaman, "Calibration of solar cells by the reference cell method—the spectral mismatch problem," *Solar Energy*, vol. 29, no. 4, pp. 291–298, 1982.

[213] Y. Liang, Z. Xu, J. Xia, S.-T. Tsai, Y. Wu, G. Li, C. Ray, and L. Yu, "For the bright future—bulk heterojunction polymer solar cells with power conversion efficiency of 7.4%," *Advanced materials*, vol. 22, no. 20, pp. E135–E138, 2010.

[214] Y. Hishikawa, T. Doi, M. Higa, K. Yamagoe, and H. Ohshima, "Precise outdoor pv module performance characterization under unstable irradiance," *IEEE Journal of Photovoltaics*, vol. 6, no. 5, pp. 1221–1227, 2016.

[215] J. Chantana, H. Mano, Y. Horio, Y. Hishikawa, and T. Minemoto, "Spectral mismatch correction factor indicated by average photon energy for precise outdoor performance measurements of different-type photovoltaic modules," *Renewable Energy*, vol. 114, pp. 567–573, 2017.

[216] H. Müllejans, A. Ioannides, R. Kenny, W. Zaaiman, H. A. Ossenbrink, and E. D. Dunlop, "Spectral mismatch in calibration of photovoltaic reference devices by global sunlight method," *Measurement Science and Technology*, vol. 16, no. 6, p. 1250, 2005.

[217] K. M. Armijo, R. K. Harrison, B. H. King, and J. B. Martin, "Spectral derates phenomena of atmospheric components on multi-junction cpv technologies," in *AIP Conference Proceedings*, vol. 1616, pp. 264–271, American Institute of Physics, 2014.

[218] M. Braga, L. R. do Nascimento, and R. Rüther, "Spectral modeling and spectral impacts on the performance of mc-si and new generation cdte photovoltaics in warm and sunny climates," *Solar Energy*, vol. 188, pp. 976–988, 2019.

[219] E. Mouhib, P. M. Rodrigo, L. Micheli, E. F. Fernández, and F. Almonacid, "Quantifying the rear and front long-term spectral impact on bifacial photovoltaic modules," *Solar Energy*, vol. 247, pp. 202–213, 2022.

[220] D. L. King, J. A. Kratochvil, and W. E. Boyson, "Measuring solar spectral and angle-of-incidence effects on photovoltaic modules and solar irradiance sensors," in *Conference Record of the Twenty Sixth IEEE Photovoltaic Specialists Conference-1997*, pp. 1113–1116, IEEE, 1997.

[221] D. L. King, J. A. Kratochvil, and W. E. Boyson, *Photovoltaic array performance model*, vol. 8. United States. Department of Energy, 2004.

[222] C. J. Riordan, R. Hulstrom, and D. Myers, "Influences of atmospheric conditions and air mass on the ratio of ultraviolet to total solar radiation," tech. rep., Solar Energy Research Inst., Golden, CO (USA), 1990.

[223] W. F. Holmgren, C. W. Hansen, and M. A. Mikofski, "pvlib python: A python package for modeling solar energy systems," *Journal of Open Source Software*, vol. 3, no. 29, p. 884, 2018.

[224] S. Wilcox and W. Marion, "Users manual for tmy3 data sets," *TP-581-43156*, 2008.

[225] M. Lee, L. Ngan, W. Hayes, J. Sorensen, and A. F. Panchula, "Understanding next generation cadmium telluride photovoltaic performance due to spectrum," in *2015 IEEE 42nd Photovoltaic Specialist Conference (PVSC)*, pp. 1–6, IEEE, 2015.

[226] C. Rigollier, O. Bauer, and L. Wald, "On the clear sky model of the esra—european solar radiation atlas—with respect to the heliosat method," *Solar energy*, vol. 68, no. 1, pp. 33–48, 2000.

[227] Solar radiation Data (SoDa), "Linke turbidity (tl) factor worldwide." Online, Last accessed 30 March 2023. https://www.soda-pro.com/help/general-knowledge/linke-turbidity-factor.

[228] N. Martin and J. Ruiz, "A new method for the spectral characterisation of pv modules," *Progress in photovoltaics: Research and Applications*, vol. 7, no. 4, pp. 299–310, 1999.

[229] Y. Nakada, H. Takahashi, K. Ichida, T. Minemoto, and H. Takakura, "Influence of clearness index and air mass on sunlight and outdoor performance of photovoltaic modules," *Current Applied Physics*, vol. 10, no. 2, pp. S261–S264, 2010.

[230] M. Theristis, E. F. Fernández, F. Almonacid, and P. Pérez-Higueras, "Spectral corrections based on air mass, aerosol optical depth, and precipitable water for cpv performance modeling," *IEEE Journal of Photovoltaics*, vol. 6, no. 6, pp. 1598–1604, 2016.

[231] J. Caballero, E. Fernández, M. Theristis, F. Almonacid, and G. Nofuentes, "Spectral corrections based on air mass, aerosol optical depth, and precipitable water for pv performance modeling," *IEEE Journal of Photovoltaics*, vol. 8, no. 2, pp. 552–558, 2018.

[232] H. Xie, J. Zhao, K. Wang, and H. Peng, "Long-term variations in solar radiation, diffuse radiation, and diffuse radiation fraction caused by aerosols in china during 1961–2016," *PloS one*, vol. 16, no. 5, p. e0250376, 2021.

[233] H. Li, M. Zhang, L. Wang, Y. Ma, W. Qin, and W. Gong, "The effect of aerosol on downward diffuse radiation during winter haze in wuhan, china," *Atmospheric Environment*, vol. 265, p. 118714, 2021.

[234] M. L. Roderick and G. D. Farquhar, "Hazy, cool and well fed?," *Nature Climate Change*, vol. 2, no. 2, pp. 76–77, 2012.

[235] J. D. Garrison and G. P. Adler, "Estimation of precipitable water over the united states for application to the division of solar radiation into its direct and diffuse components," *Solar Energy*, vol. 44, no. 4, pp. 225–241, 1990.

[236] G. Pfister, R. McKenzie, J. Liley, A. Thomas, B. Forgan, and C. N. Long, "Cloud coverage based on all-sky imaging and its impact on surface solar irradiance," *Journal of applied meteorology and climatology*, vol. 42, no. 10, pp. 1421–1434, 2003.

[237] I. Zanesco and A. Krenzinger, "The effects of atmospheric parameters on the global solar irradiance and on the current of a silicon solar cell," *Progress in Photovoltaics: Research and Applications*, vol. 1, no. 3, pp. 169–179, 1993.

[238] C. Hansen, K. Klise, J. Stein, Y. Ueda, and K. Hakuta, "Calibration of photovoltaic module performance models using monitored system data," in *29th European PV Solar Energy Conference*, 2014.

[239] K. A. Klise, C. W. Hansen, and J. S. Stein, "Dependence on geographic location of air mass modifiers for photovoltaic module performance models,"

in *2015 IEEE 42nd Photovoltaic Specialist Conference (PVSC)*, pp. 1–5, IEEE, 2015.

[240] D. R. Myers and C. A. Gueymard, "Description and availability of the smarts spectral model for photovoltaic applications," in *Organic Photovoltaics V*, vol. 5520, pp. 56–67, SPIE, 2004.

[241] C. A. Gueymard, "The smarts spectral irradiance model after 25 years: New developments and validation of reference spectra," *Solar Energy*, vol. 187, pp. 233–253, 2019.

[242] B. C. Duck and C. J. Fell, "Improving the spectral correction function," in *2016 IEEE 43rd Photovoltaic Specialists Conference (PVSC)*, pp. 2647–2652, IEEE, 2016.

[243] R. Ohtani and I. Naito, "Comparisons of gps-derived precipitable water vapors with radiosonde observations in japan," *Journal of Geophysical Research: Atmospheres*, vol. 105, no. D22, pp. 26917–26929, 2000.

[244] A. E.-K. Mousa, M. Rabah, A. Saber, M. Zhran, *et al.*, "Analysis of spatial and temporal variation of precipitable water vapor using cosmic radio occultation observations over egypt," *The Egyptian Journal of Remote Sensing and Space Science*, vol. 25, no. 3, pp. 751–764, 2022.

[245] J. A. Ruiz-Arias, C. A. Gueymard, F. J. Santos-Alamillos, and D. Pozo-Vázquez, "Worldwide impact of aerosol's time scale on the predicted long-term concentrating solar power potential," *Scientific reports*, vol. 6, no. 1, pp. 1–10, 2016.

[246] I. Pvps, "Trends 2015 in photovoltaic applications," *Report No. IEA-PVPS T1-27*, 2015.

[247] L. V. Mercaldo, M. L. Addonizio, M. Della Noce, P. D. Veneri, A. Scognamiglio, and C. Privato, "Thin film silicon photovoltaics: Architectural

perspectives and technological issues," *Applied Energy*, vol. 86, no. 10, pp. 1836–1844, 2009.

[248] E. H. Rusnindyo, E. A. Karuniawan, A. A. Setiawan, and F. D. Wijaya, "Building integrated thin film photovoltaic performance modelling on conventional building," in *AIP Conference Proceedings*, vol. 2255, p. 070023, AIP Publishing LLC, 2020.

[249] M. Piliougine, P. Sánchez-Friera, G. Petrone, F. J. Sánchez-Pacheco, G. Spagnuolo, and M. Sidrach-de Cardona, "New model to study the outdoor degradation of thin–film photovoltaic modules," *Renewable Energy*, 2022.

[250] E. Calabrò, "An algorithm to determine the optimum tilt angle of a solar panel from global horizontal solar radiation," *Journal of Renewable Energy*, vol. 2013, 2013.

[251] A. G. Siraki and P. Pillay, "Study of optimum tilt angles for solar panels in different latitudes for urban applications," *Solar energy*, vol. 86, no. 6, pp. 1920–1928, 2012.

[252] H. Yang and L. Lu, "The optimum tilt angles and orientations of pv claddings for building-integrated photovoltaic (bipv) applications," *Journal of Solar Energy Engineering*, 2007.

[253] Y.-M. Chen, C.-H. Lee, and H.-C. Wu, "Calculation of the optimum installation angle for fixed solar-cell panels based on the genetic algorithm and the simulated-annealing method," *IEEE Transactions on Energy Conversion*, vol. 20, no. 2, pp. 467–473, 2005.

[254] H. Hussein, G. Ahmad, and H. El-Ghetany, "Performance evaluation of photovoltaic modules at different tilt angles and orientations," *Energy conversion and management*, vol. 45, no. 15-16, pp. 2441–2452, 2004.

[255] T. Chow and A. Chan, "Numerical study of desirable solar-collector orientations for the coastal region of south china," *Applied Energy*, vol. 79, no. 3, pp. 249–260, 2004.

[256] M. Benghanem, "Optimization of tilt angle for solar panel: Case study for madinah, saudi arabia," *Applied Energy*, vol. 88, no. 4, pp. 1427–1433, 2011.

[257] Viridian Solar Ltd, "1.3 Tilt and Orientation." https://www.viridiansolar.co.uk/resources-1-3-tilt-and-orientation.html#:~:text=1.3%20Tilt%20and%20Orientation&text=The%20position%20that%20maximises%20the,35%20degrees%20from%20the%20horizontal. Last accessed: 2023-01-08.

[258] A. R. Wilshaw, N. M. Pearsall, and R. Hill, "Installation and operation of the first city centre pv monitoring station in the united kingdom," *Solar Energy*, vol. 59, no. 1-3, pp. 19–26, 1997.

[259] J. A. Duffie and W. A. Beckman, *Solar Engineering of Thermal Processes*, vol. 53. John Wiley & Sons, 2013.

[260] P. J. Lunde, "Solar thermal engineering: space heating and hot water systems," *U.S. Department of Energy Office of Scientific and Technical Information*, 1980.

[261] J. Kern and I. Harris, "On the optimum tilt of a solar collector," *Solar Energy*, vol. 17, no. 2, pp. 97–102, 1975.

[262] R. K. Cheng, *Inside Rhinoceros 5*. Cengage Learning, 2013.

[263] M. Piliougine, J. Carretero, L. Mora-López, and M. Sidrach-de Cardona, "Experimental system for current–voltage curve measurement of photovoltaic modules under outdoor conditions," *Progress in photovoltaics: research and applications*, vol. 19, no. 5, pp. 591–602, 2011.

[264] T. Geballe and G. Hull, "Seebeck effect in silicon," *Physical Review*, vol. 98, no. 4, p. 940, 1955.

[265] V. Tatsiankou, K. Hinzer, J. Haysom, H. Schriemer, K. Emery, and R. Beal, "Design principles and field performance of a solar spectral irradiance meter," *Solar Energy*, vol. 133, pp. 94–102, 2016.

[266] K. Menoufi, "Dust accumulation on the surface of photovoltaic panels: introducing the photovoltaic soiling index (pvsi)," *Sustainability*, vol. 9, no. 6, p. 963, 2017.

[267] S. Toth, M. Muller, D. C. Miller, H. Moutinho, B. To, L. Micheli, J. Linger, C. Engtrakul, A. Einhorn, and L. Simpson, "Soiling and cleaning: Initial observations from 5-year photovoltaic glass coating durability study," *Solar Energy Materials and Solar Cells*, vol. 185, pp. 375–384, 2018.

[268] B. Nimmo and S. A. Said, "Effects of dust on the performance of thermal and photovoltaic flat plate collectors in saudi arabia: preliminary results," *Altern. Energy Sources;(United States)*, vol. 1, no. CONF-791204-, 1981.

[269] S. A. Kalogirou, R. Agathokleous, and G. Panayiotou, "On-site pv characterization and the effect of soiling on their performance," *Energy*, vol. 51, pp. 439–446, 2013.

[270] H. Haeberlin and J. Graf, "Gradual reduction of pv generator yield due to pollution," *Power [W]*, vol. 1200, p. 1400, 1998.

[271] D. Dahlioui, B. Laarabi, and A. Barhdadi, "Review on dew water effect on soiling of solar panels: Towards its enhancement or mitigation," *Sustainable Energy Technologies and Assessments*, vol. 49, p. 101774, 2022.

[272] A. Livera, M. Theristis, E. Koumpli, S. Theocharides, G. Makrides, J. Sutterlueti, J. S. Stein, and G. E. Georghiou, "Data processing and

quality verification for improved photovoltaic performance and reliability analytics," *Progress in Photovoltaics: Research and Applications*, vol. 29, no. 2, pp. 143–158, 2021.

[273] S. Lindig, A. Louwen, D. Moser, and M. Topic, "Outdoor pv system monitoring—input data quality, data imputation and filtering approaches," *Energies*, vol. 13, no. 19, p. 5099, 2020.

[274] S. Lindig, D. Moser, A. J. Curran, K. Rath, A. Khalilnejad, R. H. French, M. Herz, B. Müller, G. Makrides, G. Georghiou, *et al.*, "International collaboration framework for the calculation of performance loss rates: Data quality, benchmarks, and trends (towards a uniform methodology)," *Progress in Photovoltaics: Research and Applications*, vol. 29, no. 6, pp. 573–602, 2021.

[275] L. Deville, M. Theristis, B. H. King, T. L. Chambers, and J. S. Stein, "Open-source photovoltaic model pipeline validation against well-characterized system data," *Progress in Photovoltaics: Research and Applications*, 2023.

[276] M. Drif, P. Perez, J. Aguilera, and J. Aguilar, "A new estimation method of irradiance on a partially shaded pv generator in grid-connected photovoltaic systems," *Renewable energy*, vol. 33, no. 9, pp. 2048–2056, 2008.

[277] R. Platon, J. Martel, N. Woodruff, and T. Y. Chau, "Online fault detection in pv systems," *IEEE Transactions on Sustainable Energy*, vol. 6, no. 4, pp. 1200–1207, 2015.

[278] S. Theocharides, G. Makrides, V. Venizelou, P. Kaimakis, and G. Georghiou, "Pv production forecasting model based on artificial neural networks (ann)," in *33rd Eur. Photovolt. Sol. Energy Conf*, no. September, pp. 1830–1894, 2017.

[279] S. Theocharides, G. Makrides, A. Livera, M. Theristis, P. Kaimakis, and G. E. Georghiou, "Day-ahead photovoltaic power production forecasting methodology based on machine learning and statistical post-processing," *Applied Energy*, vol. 268, p. 115023, 2020.

[280] I. Hughes and T. Hase, *Measurements and their uncertainties: a practical guide to modern error analysis*. OUP Oxford, 2010.

[281] A. Ranganathan, "The levenberg-marquardt algorithm," *Tutoral on LM algorithm*, vol. 11, no. 1, pp. 101–110, 2004.

[282] Y. Viswanadham, "The relationship between total precipitable water and surface dew point," *Journal of Applied Meteorology and Climatology*, vol. 20, no. 1, pp. 3–8, 1981.

[283] NASA Jet Propulsion Laboratory, "Understanding the climate: air and water." Online, Last accessed 16 February 2023. https://sealevel.jpl.nasa.gov/ocean-observation/understanding-climate/air-and-water/.

[284] W. Spark, "The weather year round anywhere on earth," 2021.

[285] G. Nofuentes, J. De la Casa, M. Torres-Ramírez, and M. Alonso-Abella, "Solar spectral and module temperature influence on the outdoor performance of thin film pv modules deployed on a sunny inland site," *International Journal of Photoenergy*, vol. 2013, 2013.

[286] T. Stocker, *Climate change 2013: the physical science basis: Working Group I contribution to the Fifth assessment report of the Intergovernmental Panel on Climate Change*. Cambridge university press, 2014.

[287] C. H. Reitan, "Distribution of precipitable water vapor over the continental united states," *Bulletin of the American Meteorological Society*, vol. 41, no. 2, pp. 79–87, 1960.

[288] M. D. King, "A method for determining the single scattering albedo of clouds through observation of the internal scattered radiation field," *Journal of Atmospheric Sciences*, vol. 38, no. 9, pp. 2031–2044, 1981.

[289] M. D. King, L. F. Radke, and P. V. Hobbs, "Determination of the spectral absorption of solar radiation by marine stratocumulus clouds from airborne measurements within clouds," *Journal of Atmospheric Sciences*, vol. 47, no. 7, pp. 894–908, 1990.

[290] J. G. Estupiñán, S. Raman, G. H. Crescenti, J. J. Streicher, and W. F. Barnard, "Effects of clouds and haze on uv-b radiation," *Journal of Geophysical Research: Atmospheres*, vol. 101, no. D11, pp. 16807–16816, 1996.

[291] J. Schafer, V. Saxena, B. Wenny, W. Barnard, and J. De Luisi, "Observed influence of clouds on ultraviolet-b radiation," *Geophysical research letters*, vol. 23, no. 19, pp. 2625–2628, 1996.

[292] J. Sabburg and J. Wong, "The effect of clouds on enhancing uvb irradiance at the earth's surface: a one year study," *Geophysical Research Letters*, vol. 27, no. 20, pp. 3337–3340, 2000.

[293] J. Sabburg, A. Parisi, and M. G. Kimlin, "Enhanced spectral uv irradiance: a 1 year preliminary study," *Atmospheric Research*, vol. 66, no. 4, pp. 261–272, 2003.

[294] R. McKenzie, W. Matthews, and P. Johnston, "The relationship between erythemal uv and ozone, derived from spectral irradiance measurements," *Geophysical Research Letters*, vol. 18, no. 12, pp. 2269–2272, 1991.

[295] R. McKenzie, G. Bodeker, D. Keep, M. Kotkamp, and J. Evans, "Uv radiation in new zealand: north-to-south differences between two sites, and relationship to other latitudes," *Weather and Climate*, pp. 17–26, 1996.

[296] S. Nann and C. Riordan, "Solar spectral irradiance under overcast skies (solar cell performance effects)," in *IEEE Conference on Photovoltaic Specialists*, pp. 1110–1115, IEEE, 1990.

[297] C. J. Riordan, D. R. Myers, and R. L. Hulstrom, "Spectral solar radiation data base documentation," tech. rep., Solar Energy Research Inst.(SERI), Golden, CO (United States), 1990. Available at: https://www.nrel.gov/grid/solar-resource/spectral-solar.html.

[298] A. Souka and H. Safwat, "Determination of the optimum orientations for the double-exposure, flat-plate collector and its reflectors," *Solar Energy*, vol. 10, no. 4, pp. 170–174, 1966.

[299] E. Sjerps-Koomen, E. Alsema, and W. Turkenburg, "A simple model for pv module reflection losses under field conditions," *Solar energy*, vol. 57, no. 6, pp. 421–432, 1996.

[300] A. Standard, "93-77, methods of testing to determine the thermal performance of solar collectors. american society of heating," *Refrigeration and Air Conditioning Engineers, Inc., New York, NY*, vol. 9, 1977.

[301] M. A. Abella, E. Lorenzo, and F. Chenlo, "Effective irradiance estimation for pv applications," in *3rd World Conference onPhotovoltaic Energy Conversion, 2003. Proceedings of*, vol. 2, pp. 2085–2089, IEEE, 2003.

[302] N. Martin and J. Ruiz, "Calculation of the pv modules angular losses under field conditions by means of an analytical model," *Solar energy materials and solar cells*, vol. 70, no. 1, pp. 25–38, 2001.

[303] B. H. King and C. D. Robinson, "Angle of incidence characterization of six laminated solar cells for 2020 dtu fotonik inter-laboratory comparison study," tech. rep., Sandia National Lab.(SNL-NM), Albuquerque, NM (United States), 2020.

[304] M. A. Muñoz-García, O. Marin, M. C. Alonso-García, and F. Chenlo, "Characterization of thin film pv modules under standard test conditions: Results of indoor and outdoor measurements and the effects of sunlight exposure," *Solar Energy*, vol. 86, no. 10, pp. 3049–3056, 2012.

[305] A. E. Delahoy, J. Britt, and Z. Kiss, "Cis photovoltaic technology; final technical report 12 january 1997-15 april 1998," tech. rep., National Renewable Energy Laboratory (NREL), 1998.

[306] L. Fanni, A. Virtuani, and D. Chianese, "A detailed analysis of gains and losses of a fully-integrated flat roof amorphous silicon photovoltaic plant," *Solar Energy*, vol. 85, no. 9, pp. 2360–2373, 2011.

[307] E. Meyer and E. Van Dyk, "Characterization of degradation in thin-film photovoltaic module performance parameters," *Renewable Energy*, vol. 28, no. 9, pp. 1455–1469, 2003.

[308] J. P. Enríquez and X. Mathew, "Influence of the thickness on structural, optical and electrical properties of chemical bath deposited cds thin films," *Solar Energy Materials and Solar Cells*, vol. 76, no. 3, pp. 313–322, 2003.

[309] J. Kuurne, A. Tolvanen, and J. Hyvarinen, "Sweep time, spectral mismatch and light soaking in thin film module measurement," in *2008 33rd IEEE Photovoltaic Specialists Conference*, pp. 1–3, IEEE, 2008.

[310] J. Chantana, Y. Imai, Y. Kawano, Y. Hishikawa, K. Nishioka, and T. Minemoto, "Impact of average photon energy on spectral gain and loss of various-type pv technologies at different locations," *Renewable Energy*, vol. 145, pp. 1317–1324, 2020.

[311] M. Tsuji, J. Chantana, K. Nakayama, Y. Kawano, Y. Hishikawa, and T. Minemoto, "Utilization of spectral mismatch correction factor for es-

timation of precise outdoor performance under different average photon energies," *Renewable Energy*, vol. 157, pp. 173–181, 2020.

[312] V. Tatsiankou, K. Hinzer, J. Mohammed, A. Muron, M. Wilkins, J. Haysom, H. Schriemer, and S. Myrskog, "Reconstruction of solar spectral resource using limited spectral sampling for concentrating photovoltaic systems," in *Photonics North 2013*, vol. 8915, p. 891506, International Society for Optics and Photonics, 2014.

[313] V. Tatsiankou, K. Hinzer, H. Schriemer, S. Kazadzis, N. Kouremeti, J. Gröbner, and R. Beal, "Extensive validation of solar spectral irradiance meters at the world radiation center," *Solar Energy*, vol. 166, pp. 80–89, 2018.

[314] L. A. Neves, G. C. Leite, R. C. MacKenzie, R. A. Ferreira, and M. P. Porto, "A methodology to simulate solar cells electrical response using optical-electrical mathematical models and real solar spectra," *Renewable Energy*, vol. 164, pp. 968–977, 2021.

[315] Y. Yang, A. Yu, B. Hsu, W. Hsu, A. Yang, and C. Lan, "Development of high-performance multicrystalline silicon for photovoltaic industry," *Progress in Photovoltaics: Research and Applications*, vol. 23, no. 3, pp. 340–351, 2015.

[316] M. E. Meral and F. Dincer, "A review of the factors affecting operation and efficiency of photovoltaic based electricity generation systems," *Renewable and Sustainable Energy Reviews*, vol. 15, no. 5, pp. 2176–2184, 2011.

[317] L. A. Conde, J. R. Angulo, M. Á. Sevillano-Bendezú, G. Nofuentes, J. A. Töfflinger, and J. de la Casa, "Spectral effects on the energy yield of various photovoltaic technologies in lima (peru)," *Energy*, vol. 223, p. 120034, 2021.

[318] M. Tsuji, M. M. Rahman, Y. Hishikawa, K. Nishioka, and T. Minemoto, "Uniqueness verification of solar spectrum obtained from three sites in japan based on similar index of average photon energy," *Solar Energy*, vol. 173, pp. 89–96, 2018.

[319] D. Dirnberger, G. Blackburn, B. Müller, and C. Reise, "On the impact of solar spectral irradiance on the yield of different pv technologies," *Solar Energy Materials and Solar Cells*, vol. 132, pp. 431–442, 2015.

[320] J. Polo, M. Alonso-Abella, J. A. Ruiz-Arias, and J. L. Balenzategui, "Worldwide analysis of spectral factors for seven photovoltaic technologies," *Solar Energy*, vol. 142, pp. 194–203, 2017.

[321] N. Kriegeskorte, "Crossvalidation," in *Brain Mapping* (A. W. Toga, ed.), pp. 635–639, Waltham: Academic Press, 2015.

[322] D. M. Hawkins, "The problem of overfitting," *Journal of chemical information and computer sciences*, vol. 44, no. 1, pp. 1–12, 2004.

[323] R. D. Cook and S. Weisberg, *Applied regression including computing and graphics*. John Wiley & Sons, 2009.

[324] T. Soga, *Nanostructured materials for solar energy conversion*. Elsevier, 2006.

[325] D. L. King, J. A. Kratochvil, and W. E. Boyson, "Stabilization and performance characteristics of commercial amorphous-silicon pv modules," in *Conference Record of the Twenty-Eighth IEEE Photovoltaic Specialists Conference-2000 (Cat. No. 00CH37036)*, pp. 1446–1449, IEEE, 2000.

[326] R. Gottschalg, J. Del Cueto, T. R. Betts, S. R. Williams, and D. Infield, "Investigating the seasonal performance of amorphous silicon single-and multi-junction modules," in *3rd World Conference onPhotovoltaic Energy Conversion, 2003. Proceedings of*, vol. 2, pp. 2078–2081, IEEE, 2003.

[327] Y. K. Ramgolam and K. M. S. Soyjaudah, "Modelling the impact of spectral irradiance and average photon energy on photocurrent of solar modules," *Solar Energy*, vol. 173, pp. 1058–1064, 2018.

[328] I. M. Peters, L. Haohui, T. Reindl, and T. Buonassisi, "Global comparison of the impact of temperature and precipitable water on cdte and silicon solar cells," in *2017 IEEE 44th Photovoltaic Specialist Conference (PVSC)*, pp. 1140–1142, IEEE, 2017.

[329] A. Guechi, M. Chegaar, and e. A. Merabet, "The effect of water vapor on the performance of solar cells," *Physics procedia*, vol. 21, pp. 108–114, 2011.

[330] B. Sierk, S. Solomon, J. Daniel, R. Portmann, S. Gutman, A. Langford, C. Eubank, E. Dutton, and K. Holub, "Field measurements of water vapor continuum absorption in the visible and near-infrared," *Journal of Geophysical Research: Atmospheres*, vol. 109, no. D8, 2004.

[331] OriginLab Corporation, "OriginPro 2020." Online, Last accessed 16 February 2023. https://www.originlab.com/ Accessed 2022-12-29.

[332] OriginLab Corporation, "30.3.16 Poly2D." Online, Last accessed 16 February 2023. https://www.originlab.com/doc/Origin-Help/Poly2D-FitFunc Accessed 2023-02-16.

[333] G. Bel and M. M. Bandi, "Geographic dependence of the solar irradiance spectrum at intermediate to high frequencies," *Physical Review Applied*, vol. 12, no. 2, p. 024032, 2019.

[334] T. Huld and A. M. Gracia Amillo, "Estimating pv module performance over large geographical regions: The role of irradiance, air temperature, wind speed and solar spectrum," *Energies*, vol. 8, no. 6, pp. 5159–5181, 2015.

[335] R. H. Plante, *Solar energy, photovoltaics, and domestic hot water: A technical and economic guide for project planners, builders, and property owners*. Academic Press, 2014.

[336] X. Wen, Y. Feng, S. Huang, F. Huang, Y.-B. Cheng, M. Green, and A. Ho-Baillie, "Defect trapping states and charge carrier recombination in organic–inorganic halide perovskites," *Journal of Materials Chemistry C*, vol. 4, no. 4, pp. 793–800, 2016.

[337] J. A. Duffie, W. A. Beckman, and N. Blair, *Solar engineering of thermal processes, photovoltaics and wind*. John Wiley & Sons, 2020.

[338] L. Mao, J. Tong, S. Xiong, F. Jiang, F. Qin, W. Meng, B. Luo, Y. Liu, Z. Li, Y. Jiang, *et al.*, "Flexible large-area organic tandem solar cells with high defect tolerance and device yield," *Journal of Materials Chemistry A*, vol. 5, no. 7, pp. 3186–3192, 2017.

[339] M. A. Obregón, M. J. Costa, A. M. Silva, and A. Serrano, "Spatial and temporal variation of aerosol and water vapour effects on solar radiation in the mediterranean basin during the last two decades," *Remote Sensing*, vol. 12, no. 8, p. 1316, 2020.

[340] Y. Xie, M. Sengupta, and C. Wang, "A fast all-sky radiation model for solar applications with narrowband irradiances on tilted surfaces (farms-nit): Part ii. the cloudy-sky model," *Solar Energy*, vol. 188, pp. 799–812, 2019.

[341] OriginLab Corporation, "30.3 non-linear surface fitting." Online, Last accessed 16 February 2023. https://www.originlab.com/doc/Origin-Help/Non-linear-Surface-Fitting-FitFunc Accessed 2023-06-02.

Appendices

Appendix A

Parameterisations

The functional forms of the six parameterisations used in this study, which are referenced in Tables 6.3, 6.4, and 6.5, are summarised this appendix. Further information on the fitting functions listed here, including the meanings behind each of the coefficients in the models, can be found in Ref. [341].

1. LogNormal2D :

$$z(x,y) = z_0 + B\exp\left\{-\frac{\left(\ln\frac{x}{C}\right)^2}{2D^2}\right\} + E\exp\left\{-\frac{\left(\ln\frac{y}{F}\right)^2}{2G^2}\right\} + H\exp\left\{-\frac{\left(\ln\frac{x}{C}\right)^2}{2D^2} - \frac{\left(\ln\frac{y}{F}\right)^2}{2G^2}\right\} \tag{A.1}$$

2. ExtremeCum:

$$z(x,y) = z_0 + B\exp\left\{-\exp\left\{\frac{C-x}{D}\right\}\right\} + E\exp\left\{-\exp\left\{\frac{F-y}{G}\right\}\right\} + H\exp\left\{-\exp\left\{\frac{C-x}{D}\right\} - \exp\left\{\frac{F-y}{G}\right\}\right\} \tag{A.2}$$

3. RationalTaylor:

$$z(x,y) = \frac{z_0 + A_{01}x + B_{01}y + B_{02}y^2 + C_{02}xy}{1 + A_1x + B_1y + A_2x^2 + B_2y^2 + C_2xy} \tag{A.3}$$

4. DoseResp2D:

$$z(x,y) = z_0 + \frac{B}{\left[1 + \left(\frac{x}{C}\right)^{-D}\right]\left[1 + \left(\frac{y}{E}\right)^{-F}\right]} \tag{A.4}$$

5. Parabola2D:

$$z(x,y) = z_0 + ax + by + cx^2 + dy^2 \tag{A.5}$$

6. Poly2D

$$z(x,y) = z_0 + ax + by + cx^2 + dy^2 + fxy \tag{A.6}$$